

TRINITY COLLEGE DUBLIN
THE UNIVERSITY OF DUBLIN

SCHOOL OF PHYSICS

Examining How Planets Interact With The
Stellar Wind Using 3D Numerical Models

STEPHEN CAROLAN

A thesis submitted for the degree of
DOCTOR OF PHILOSOPHY IN ASTROPHYSICS

2022



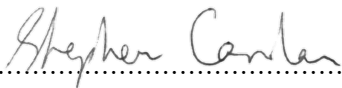
Declaration

I declare that this thesis has not been submitted as an exercise for a degree at this or any other university and it is entirely my own work.

I agree to deposit this thesis in the University's open access institutional repository or allow the Library to do so on my behalf, subject to Irish Copyright Legislation and Trinity College Library conditions of use and acknowledgement.

I consent to the examiner retaining a copy of the thesis beyond the examining period, should they so wish (EU GDPR May 2018).

Name: Stephen Carolan

Signature:  **Date:** 29/07/2022

Abstract

The majority of planets do not exist in empty space, but are embedded in the stellar wind, which consists of mostly ionised Hydrogen ejected from the host star. Understanding stellar wind-planet interactions is of huge importance to the scientific community today, given the effect they have on the lifetime of a planet's atmosphere, and consequently the planet's habitability.

In this thesis I explore the various ways planets interact with the stellar wind using advanced 3D numerical models. I start with the interaction between Earth's magnetic field and the solar wind. Given that the solar wind has evolved over the Sun's main-sequence lifetime, I investigate how this evolving wind has affected Earth's magnetosphere, the volume around the Earth dominated by its magnetic field. To do this, I demonstrate the technique of using stellar wind and 3D magnetosphere simulations in tandem, changing the stellar wind properties to obtain the corresponding magnetospheric structure. I find that Earth's magnetosphere in the young system was significantly smaller than it is today, and as the solar wind relaxes further, will continue to grow.

I then move to planets on close-in systems (< 0.1 au). The high-energy radiation that close-in planets receive from their host stars can lead to strong photoevaporation. The stellar wind exerts pressure on the expanding atmosphere and, if sufficiently strong, confines it close to the planet. Using 3D isothermal models which ignore magnetic fields, I show that this confinement can limit both the rate of escape and its observational signatures, placing importance on considering the conditions of the stellar wind when interpreting observational data.

I continue by applying these models to a test system: the newly discovered exoplanet AU Mic b. This young close-in system presents an interesting dichotomy. While the planet is expected to be highly irradiated by the host star, which can cause significant photoevaporation, the stellar wind could be strong enough to reduce or even inhibit atmospheric escape. I show that stellar wind mass-loss rates on the upper end of those proposed in literature ($< 1000\dot{M}_{\odot}$, where

$\dot{M}_\odot = 2 \times 10^{-14} M_\odot/\text{yr}$ is the solar mass-loss rate) completely remove detection signatures of atmospheric escape, while those on the lower end ($> 10\dot{M}_\odot$) yield blue-shift dominant absorption. These models demonstrate that the wind-atmosphere interaction can also inform us of the stellar wind conditions, depending on what follow up observational missions detect.

I then investigate how magnetic fields change the wind-atmosphere interaction. Magnetic fields alter the previous picture, resulting in a new structure. I now find a dead-zone of low velocity material trapped in the closed field lines, and polar flows where escaping material is funnelled along the open field lines, resulting in the novel finding of a double-tail structure. This new structure affects the observational signatures of atmospheric escape, with larger magnetic field strengths yielding both increased line centre absorption, and more asymmetry between transits above and below mid-disc.

Finally, I present preliminary work on the inclusion of two processes in these 3D models: charge exchange and radiation pressure, both of which are thought to contribute to the high velocity absorption observations have found. Though it does not change the geometry of the escaping atmosphere, I find that charge exchange can greatly alter the absorption profile in Ly- α , with relatively small changes in stellar wind density and velocity causing large changes in blue wing absorption. The current implementation of radiation pressure in my model yields a departure from the findings in literature. With a tail oriented more radially away from the star, the line profile is changed significantly, with increased blue-shifted absorption. This can be attributed to the current lack of self-shielding in my model, a process which attenuates the radiation as it passes through the atmosphere, reducing its effect on the dynamics of the atmosphere.

Although I investigate a variety of different wind-planet interactions in this thesis, my research consistently illustrates that considering the properties of the stellar wind is incredibly important in order to correctly interpret the structure of the planet's local environment, and how it affects the planet's atmosphere.

Acknowledgements

I have been incredibly fortunate to work with such a fantastic group of people throughout my PhD. First and foremost, I have to thank my supervisor, Aline Vidotto. You encouraged me at every step along the way, kept me motivated through the pandemic, and gave guidance and feedback whenever I needed it. I have learned so much from you (except how to spot typos!) and will forever be thankful that I had you as my PhD supervisor.

I also would like to extend my gratitude to the post-docs in our group. All of you helped me with different presentations and posters throughout the years, both answering and asking questions, allowing me to continuously learn from you and improve. I of course owe special thanks to both Carolina and Gopal. Our weekly meetings with Aline have been some of the best learning experiences of my life, and I will forever be grateful for your ideas and advice.

I will be eternally thankful for my fellow PhD students with whom I shared an office. I will always feel nostalgic for those first 18 months before the pandemic, for all the coffees drank, lunches ate, pints had, and board games played. They truly were some of the best times of my life.

Of course I have to thank all of my family and friends. Thank you all for keeping me sane, for offering support, for making me laugh, and for listening to the seemingly never-ending stream of nonsense that comes out of my mouth. You have all helped me more than you know.

Last, but certainly not least, Clare. I will never forget your continuous support during all of this. You made the bad days good and the good days better. This truly would have been impossible without you.

Finally, I must also address my various golf and gaming addictions, without which my PhD would have probably been far more productive, yet far less enjoyable.

Contents

List of Publications	v
List of Figures	vii
List of Tables	x
1 Introduction	1
1.1 Evidence Of Atmospheric Escape In Exoplanetary Systems	3
1.1.1 Indirect Evidence Of Atmospheric Escape	3
1.1.2 Spectroscopic Transits: Lyman- α Absorption	4
1.1.3 Spectroscopic Transits: Heavier Elements	8
Fundamental Concepts	10
1.2 Fundamentals Of Modelling Photoevaporation	10
1.2.1 Fundamentals Of Gas Dynamics	10
1.2.2 1D Photoevaporation Model	12
1.3 Stellar Wind Models	15
1.3.1 1D Isothermal Wind	15
1.3.2 Polytropic Winds	18
1.3.3 3D Stellar Wind Models	20
1.4 Planet-Wind Interactions	22
1.4.1 Solar System Planets	22
1.4.2 Close-In Systems	24
1.5 Matching Spectroscopic Transit Observations With 3D Models	26
Computational Models	29

CONTENTS

1.6	My Base 3D MHD Computational Model	29
1.7	Ly- α Transit Calculations	34
	Overview Of The Thesis	37
2	The Evolution Of Earth's Magnetosphere	39
2.1	Context	40
2.2	1.5D Stellar Wind Simulations	42
2.2.1	Choice Of Stellar Wind Parameters	42
2.2.2	The Rotation Rate Of The Young Sun	46
2.2.3	Global Properties Of The Young Solar Wind	47
2.3	Magnetosphere Model	49
2.4	The Magnetopause	51
2.5	The Bow Shock And Magnetosheath	57
2.6	Very Fast Rotating Young Sun	60
2.7	Conclusions	64
2.8	Appendix	66
2.8.1	Stellar Wind Fits	66
2.8.2	Open And Closed Magnetospheres	68
3	The Effects Of The Stellar Wind On Ly-α Transits	72
3.1	Context	73
3.2	Developing A 3D Model Of Photoevaporation In Close-In Systems	75
3.2.1	New Coordinate System	75
3.2.2	Launching A Planetary Wind	76
3.2.3	Informing The <i>Inner Boundary</i> Conditions: 1D Model	78
3.2.4	Stellar Gravity	78
3.2.5	Orbital Effects: Coriolis & Centrifugal Forces	80
3.2.6	New Outer Boundaries	82
3.3	Simulations Of Reduced Atmospheric Escape From Close-In Planets	84
3.4	Reduced Ly- α Transit Depth Due To Stellar Wind Confinement	90
3.5	Discussion	94
3.5.1	Implications For Interpreting Ly- α Signatures	94
3.5.2	Model Limitations	96

3.6	Conclusions	98
4	The Dichotomy Of Atmospheric Escape In AU Mic b	101
4.1	Context	101
4.2	Atmospheric Escape And Synthetic Ly- α Transit Models	103
4.3	Variation Of The Stellar Wind Strength	104
4.4	Discussion And Conclusions	109
5	The Effects Of Magnetic Fields On Ly-α Transits	112
5.1	Context	113
5.2	3D Self-Consistent Radiative MHD Simulations	113
5.3	Effect Of Magnetic Fields: Atmospheric Escape	118
5.4	Effect Of Magnetic Fields: Observational Signatures	125
5.5	Discussion	129
5.5.1	Magnetic Field Geometries	129
5.5.2	No Significant Change In Escape Rate	129
5.5.3	Implications On Observations	130
5.6	Conclusions	131
5.7	Appendix: Quasi Steady-State Solutions	133
6	Modelling Charge-Exchange & Radiation Pressure	135
6.1	Context	136
6.2	Simulating Charge Exchange And Radiation Pressure	136
6.2.1	Charge Exchange	137
6.2.2	Radiation Pressure	140
6.2.3	Charge Exchange And Radiation Pressure	142
6.3	Effects On The Transit Line Profiles	143
6.4	Discussion	145
6.5	Next Steps	147
6.6	Conclusions	149
7	Summary & Future Work	152
7.1	Future Work	152
7.2	Summary	158

CONTENTS

References	165
Appendix A Published Works	178

List of Publications

First-Authored Publications

1. **Carolan, S.**, Vidotto, A. A., Loesch, C. & Coogan, P.
“The evolution of Earth’s magnetosphere during the solar main sequence”,
Monthly Notices of the Royal Astronomical Society, Volume 489, Issue 4, p.5784-5801,
(2019)
2. **Carolan, S.**, Vidotto, A. A., Plavchan, P., Villarreal D’Angelo, C. & Hazra, G.
“The dichotomy of atmospheric escape in AU Mic b”,
Monthly Notices of the Royal Astronomical Society: Letters, Volume 498, Issue 1,
p.L53-L57, (2020)
3. **Carolan, S.**, Vidotto, A. A., Villarreal D’Angelo, C. & Hazra, G.
“Effects of the stellar wind on the Ly- α transit of close-in planets”,
Monthly Notices of the Royal Astronomical Society, Volume 500, Issue 3, p.3382-3393
(2021)
4. **Carolan, S.**, Vidotto, A. A., Villarreal D’Angelo, C., Hazra, G. & Kubyskhina, D.
“The effects of magnetic fields on observational signatures of atmospheric escape in
exoplanets: Double tail structures”,
Monthly Notices of the Royal Astronomical Society, Volume 508, Issue 4, p.6001-6012
(2021)

Co-Authored Publications

1. Hazra, G., Vidotto, A. A., **Carolan, S.**, Villarreal D'Angelo, C., Manchester, W.
“The impact of coronal mass ejections and flares on the atmosphere of the hot Jupiter HD189733b”,
Monthly Notices of the Royal Astronomical Society, Volume 509, Issue 4, p.5858-5871,
(2022)
2. Kubyshkina, D., Vidotto, A. A., Villarreal D'Angelo, C., **Carolan, S.**, Hazra, G.,
Carleo, I.
“Atmospheric mass-loss and stellar wind effects in young and old systems - I. Com-
parative 3D study of TOI-942 and TOI-421 systems”,
Monthly Notices of the Royal Astronomical Society, Volume 510, Issue 2, p.2111-2126,
(2022)
3. Kubyshkina, D., Vidotto, A. A., Villarreal D'Angelo, C., **Carolan, S.**, Hazra, G.,
Carleo, I.
“Atmospheric mass loss and stellar wind effects in young and old systems - II. Is
TOI-942 the past of TOI-421 system?”,
Monthly Notices of the Royal Astronomical Society, Volume 510, Issue 2, p.3039-3045,
(2022)

List of Figures

1.1	Exoplanet Population - Mass	2
1.2	Exoplanet Population - Radius	4
1.3	HD209458b Ly- α Observation	5
1.4	GJ436b Ly- α Observation	6
1.5	Transit Schematic	7
1.6	Helium Observation	9
1.7	Escaping Atmosphere Structure	14
1.8	1D Parker Wind	18
1.9	Parker Spiral	21
1.10	Earth's Magnetospheric Structure	23
1.11	Types Of Wind-Atmosphere Interactions	24
1.12	Modelling The Ly- α Transit	27
1.13	My Simulation Setup	31
1.14	My Synthetic Transit Setup	36
2.1	Stellar Wind Values At 1 au	44
2.2	Models Of Stellar Rotation With Time	47
2.3	Simulation Grid	50
2.4	Stellar Wind Orientation	51
2.5	3D Model	52
2.6	Slow And Medium Rotation Models	53
2.7	Contributing Pressure Comparisons	54
2.8	Standoff Distances	55
2.9	Bow Shock Distance And Density Profiles	58

LIST OF FIGURES

2.10	Velocity, Current, And Magnetic Field Components On The Subsolar Line	61
2.11	Fast Rotating Models	62
2.12	Currents In The Fast Rotating Models	63
2.13	Open And Closed Magnetosphere Structures	69
2.14	Density And Pressure Structures In Open And Closed Magnetospheres	71
3.1	HJ And WN Planets In The Catalogue Of Exoplanets	74
3.2	The Coordinate System Of My Simulations	76
3.3	Planetary Wind	77
3.4	Escaping Atmosphere Velocity Structures	80
3.5	3D View Of My HJ Model	84
3.6	Orbital Slice In My Models (Zoom In)	86
3.7	Orbital Slice In My Models (Zoom Out)	87
3.8	Model Escape Rates	89
3.9	Ly- α Line Profiles	92
3.10	Percentage Absorptions Of The Blue And Red Wings	93
3.11	Escape Rate vs Percentage Absorption	95
4.1	3D View Of AU Mic b	105
4.2	Orbital Plane Of The AU Mic b Models	106
4.3	Ly- α Line Profiles And Percentage Absorption Of The AU Mic b Models	108
5.1	3D View Of The Polar Flows And Dead-Zone	115
5.2	Orbital Plane Of The Magnetic Models	120
5.3	Polar Plane Of The Magnetic Models	121
5.4	Escape Rates Of Magnetic Models	123
5.5	Pressure Structure For 2 Different Magnetic Field Strengths	124
5.6	Ly- α Line Profiles Of The Magnetic Models	126
5.7	Percentage Absorption For Different Impact Parameters	128
5.8	Quasi-Steady State Variation Of The 1G Model	134
6.1	Base Model	137
6.2	Charge Exchange Model	139
6.3	β Profile	141
6.4	Radiation Pressure Model	142

LIST OF FIGURES

6.5	Radiation Pressure & Charge Exchange Model	143
6.6	Line Profiles	144
6.7	Solar Wind Model With Charge Exchange	147
6.8	Charge Exchange Models - Line Profile Comparison	148

List of Tables

2.1	Stellar Wind Values At 1 au	45
2.2	Standoff Distances And Latitudes Of Open Field Lines	56
2.3	Stellar Wind Fits For $\Omega < 1.4\Omega_{\odot}$	67
3.1	HJ And WN Model Parameters	79
3.2	Summary Of HJ And WN Model Results	88
4.1	Simulation Results Of AU Mic b Models	107
5.1	Parameters Of The Magnetic Models	118
5.2	Summary Of Magnetospheric Structure In Magnetic Models	122



Introduction

Three decades ago, we only knew of the planets in the solar system. From small rocky planets like Mercury, to large gas giants like Jupiter, we assumed we lived in a typical planetary system. Today, thanks to observational missions like *Kepler*, we have found nearly 5000 confirmed exoplanets, which paint a very different picture. Figure 1.1 shows the current mass-orbital distance distribution of confirmed planets, suggesting that the solar system planets could to be outliers. In reality this may not be true, as our detection techniques are biased towards close-in planets (eg. Kipping & Sandford, 2016). The more extreme “Hot Jupiters” (Jupiter sized planets on close-in orbits) were the first to be discovered (Mayor & Queloz, 1995), however they are thought to be quite rare, with an occurrence rate of about 1% (Cumming et al., 2008; Howard et al., 2010, 2012). The so called “Super-Earths” or “Sub-Neptunes” (planets with masses/radii between that of Earth and Neptune) have been found to be quite common in FGK stellar systems, with many containing at least one of this class of planets (Fressin et al., 2013), and are even more common around M dwarf stars (Dressing & Charbonneau, 2013). Though we have discovered planets with a broad range of characteristics, and have found some are more common than others, one thing they all have in common is that they are embedded in the stellar wind.

The stellar wind is the process through which stars lose mass. An outflow of particles is ejected from the star, consisting mainly of ionised Hydrogen, with small amounts of heavier elements (Helium, Carbon, Oxygen etc.). This wind flows into the interplanetary medium, filling the environment around the star with hot accelerating gas. The stellar wind is chief among ways in which stars and planets interact. From the surface of the Earth this interaction can be seen through the aurora, caused by stellar wind particles

1. INTRODUCTION

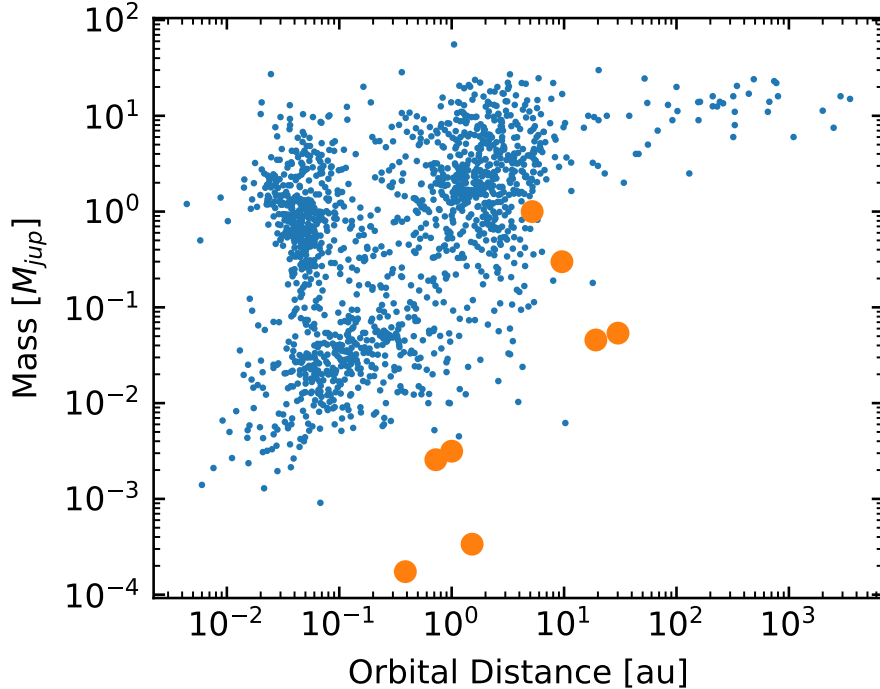


Figure 1.1: Planetary mass vs orbital distance for all known planets. All confirmed exoplanets are marked by blue points (<https://exoplanets.nasa.gov/discovery/exoplanet-catalog/>), while the solar system planets are marked with orange circles.

that are funnelled onto our atmosphere through the open planetary magnetic field lines. This phenomenon is not unique to the Earth, with the gas giants of our solar system evidencing it through cyclotron maser emission (Treumann, 2006). However no confirmed extrasolar detection has been made to date (a tentative detection has been found by Turner et al., 2021).

For close-in planets, the interaction with the stellar wind is more extreme. Close to the star stellar winds are denser, hotter and have higher ambient magnetic fields (eg. Vidotto et al., 2015). Many planets are known to exist where the stellar wind is still accelerating, and if close enough can enhance stellar activity (eg. Cuntz et al., 2000). As well as this, giant close-in planets are known to exhibit extreme atmospheric escape (eg. HD209458b, Vidal-Madjar et al., 2003). Like the stellar wind, these exoplanets have the capability of launching their own winds, due to high atmospheric temperatures and high levels of irradiation from their host stars (Lammer et al., 2003; Baraffe et al., 2004; Yelle, 2004). This yields another process through which planets interact with the stellar wind,

1.1 Evidence Of Atmospheric Escape In Exoplanetary Systems

with the dynamics of the interaction of these two outflows ultimately shaping the planet's local environment. Understanding these interactions is crucial, not only in order to better understand the population of planets we have discovered, but also due to their implications on planetary atmospheres and habitability (Dong et al., 2018; Lingam & Loeb, 2018).

In this thesis I study both wind-magnetosphere and wind-atmosphere interactions, focussing on how the stellar wind affects their observational signatures. This chapter is presented as follows. I will begin by discussing both the indirect and direct evidence of atmospheric escape in exoplanetary systems in section 1.1. I will then introduce how this atmospheric escape can be modelled in section 1.2, followed by stellar wind models in section 1.3. In section 1.4, I will describe the various planet-wind interactions considered in this thesis, before discussing how 3D models of these interactions can be used to interpret observational data in section 1.5. Finally, I will discuss the base 3D model which I build upon in this thesis in section 1.6, as well as the ray-tracing calculations performed to synthetically observe these models in section 1.7.

1.1 Evidence Of Atmospheric Escape In Exoplanetary Systems

Though the extreme atmospheric escape of close-in systems is alien to our solar system, there are a variety of methods to both detect it observationally and to infer its affect from the exoplanet population.

1.1.1 Indirect Evidence Of Atmospheric Escape

The left panel of figure 1.2 shows the radius-orbital distance distribution of confirmed Kepler exoplanets, where the effects of atmospheric escape can be seen. On this plot we see two distinct populations of exoplanets: a population of Jupiter sized planets orbiting $< 0.1\text{au}$ from their host stars, known as Hot Jupiters; and planets with radii from approximately 1 to 4 R_{\oplus} (Earth radii) on slightly longer orbits, containing the Warm Neptunes and Super Earths. This population of Hot Jupiters and the gap in the distribution of exoplanets have been attributed to a combination of orbital migration, where larger orbit planets move closer to their host stars, and atmospheric escape (Owen & Lai, 2018). Planets in this gap have insufficient gravity to support their atmospheres, and as a result

1. INTRODUCTION

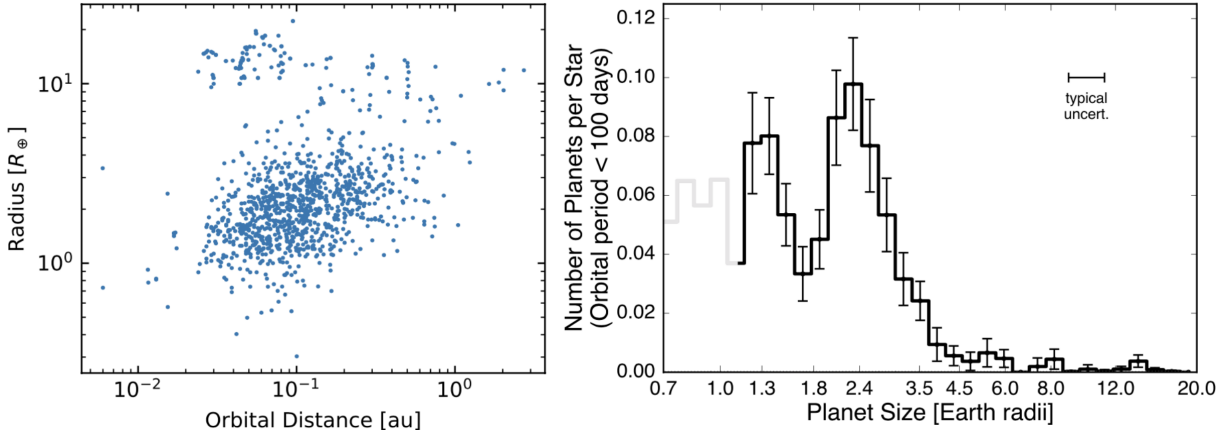


Figure 1.2: **Left:** Planetary radii vs orbital distance for confirmed Kepler exoplanets (<https://exoplanets.nasa.gov/discovery/exoplanet-catalog/>). **Right:** Number of Kepler planets in different radius bins for sub-Neptune exoplanets after correction for detection biases (Fulton et al., 2017, Figure 7).

the Hydrogen dominated gas evaporates off the planet. With the atmosphere escaping, the radius of the planet begins to decrease, causing the planet to move towards the lower population in the plot.

Within the lower population of exoplanets exists more subtle evidence of atmospheric escape. This becomes more obvious when these planets are separated into radius bins, as shown in the right panel of figure 1.2 (Fulton et al., 2017). Here there again exists two over-populations: planets with radii $< 1.5R_{\oplus}$ and those with radii $> 2.0R_{\oplus}$. The under-population between these two groups has again been attributed to atmospheric escape (Owen & Wu, 2017; Jin & Mordasini, 2018; Gupta & Schlichting, 2019, 2020). Planets in the population on the right-hand side hold a few % of their mass, but a substantial amount of their radius as Hydrogen atmospheres, while those in the gap were unable to retain their atmospheres and transitioned to the population on the left-hand side, which consists of rocky cores.

1.1.2 Spectroscopic Transits: Lyman- α Absorption

As well as this indirect evidence of atmospheric escape, there have also been direct observations. At first these missions targeted escaping Hydrogen, looking for excess absorption in the Lyman- α line (Ly- α hereafter) during the exoplanet's transit. Figure 1.3 shows the

1.1 Evidence Of Atmospheric Escape In Exoplanetary Systems

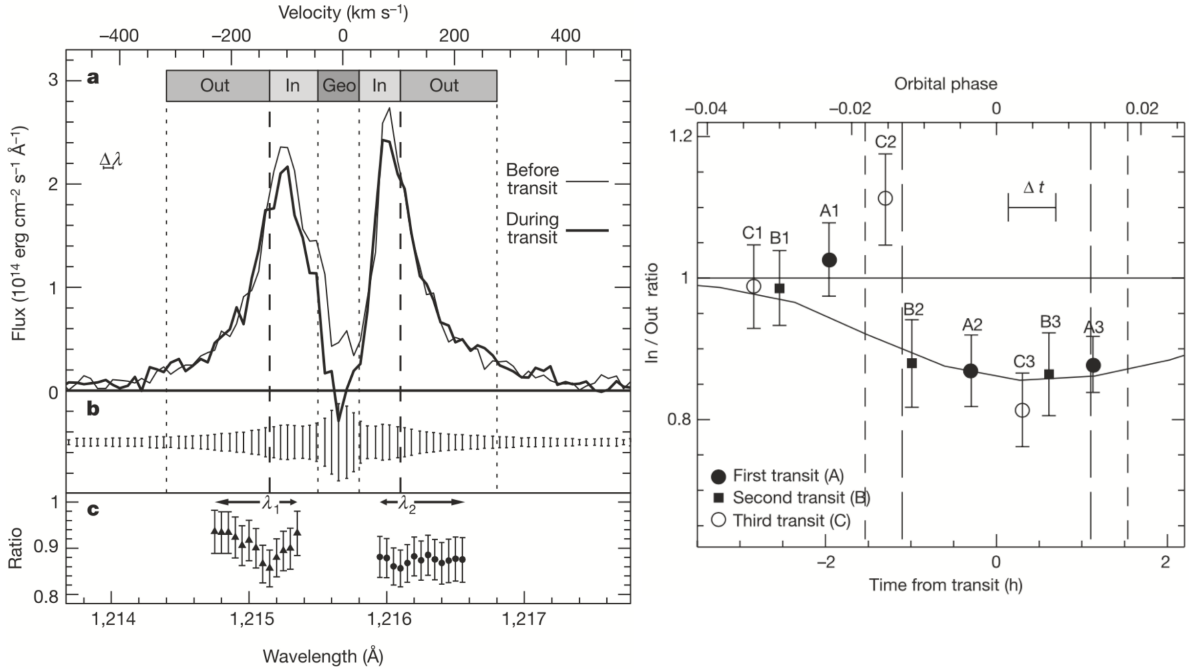


Figure 1.3: **Left:** The observed Ly- α line before (thin line) and during (thick line) the transit of HD209458b. **Right:** The relative flux of Ly- α as a function of transit time (Figures from Vidal-Madjar et al., 2003).

first such observation from Vidal-Madjar et al. (2003). When observing the Ly- α transit of the Hot Jupiter HD209458b, excess absorption was found in the blue and red wings, shown in the left panel. This suggests the presence of an extended escaping neutral Hydrogen atmosphere around the planet, containing material with high velocity (100km/s) along the line of sight. The right panel shows the change in relative flux with time from the transit of the planet. Here we can observe slight asymmetry in the observed flux, with more absorption after transit than before (this asymmetry is more obvious for other planets, eg. in GJ 436 b figure 1.4). This suggests that as the Hydrogen escapes the planet, and as the planet continues in its orbit, the escaped Hydrogen forms a comet-like tail, trailing the planet in its orbit.

The phenomenon of observed atmospheric escape is not exclusive to Hot Jupiter sized planets. Perhaps the most famous smaller planet to exhibit direct evidence of atmospheric escape is the Warm Neptune GJ 436 b shown in figure 1.4 (Ehrenreich et al., 2015). Again in the left panel we see significant high blue-shifted absorption in the Ly- α line before,

1. INTRODUCTION

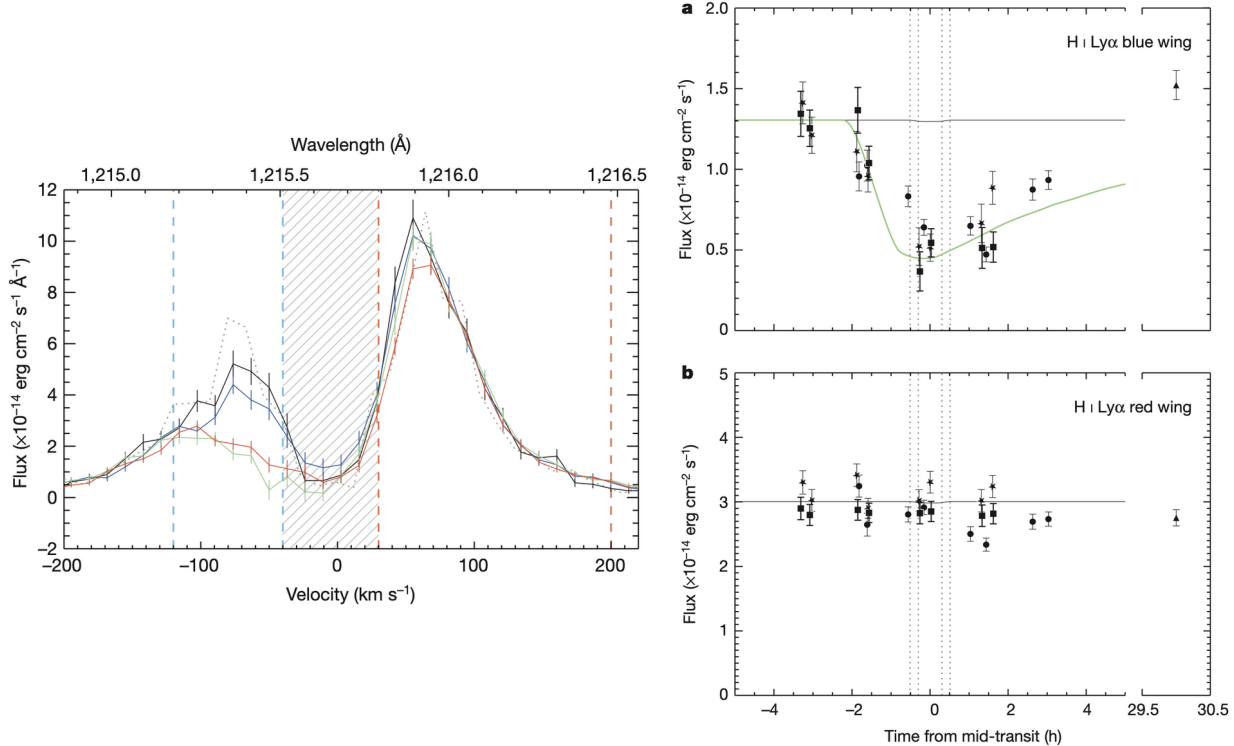


Figure 1.4: **Left:**The observed Ly- α transits out of transit (black), pre-transit (blue), in transit (green) and post transit (red) of GJ 436 b. **Right:** The relative flux of Ly- α line in the red and blue wings as a function of transit time (Figures from Ehrenreich et al., 2015).

during and after the optical transit of the planet. Integrating the observed flux in the blue and red wings of these line profiles yields the right panel, showing the relative flux of each wing of the Ly- α line for different observations. We again see clear evidence of significant absorption in the Ly- α line starting approximately 1 hour before the beginning of the optical transit, and lingering for more than 3 hours after transit, where absorption gradually decreases. This evidences the presence of absorbing neutral Hydrogen in front of the planet which begins to cover the stellar disc 1 hour before the planet, as well as a “giant comet-like cloud” of escaping Hydrogen following the planet in its orbit, the density of which decreases further away from the planet leading to a gradual drop off in absorption with time after transit (Ehrenreich et al., 2015).

Figure 1.5 demonstrates this structure, illustrating the transiting planet and comet-like tail which follows it in its orbit, as well as the Ly- α transit line profile obtained at different stages of the orbit (Owen et al., 2021). As the density and velocity of Hydrogen

1.1 Evidence Of Atmospheric Escape In Exoplanetary Systems

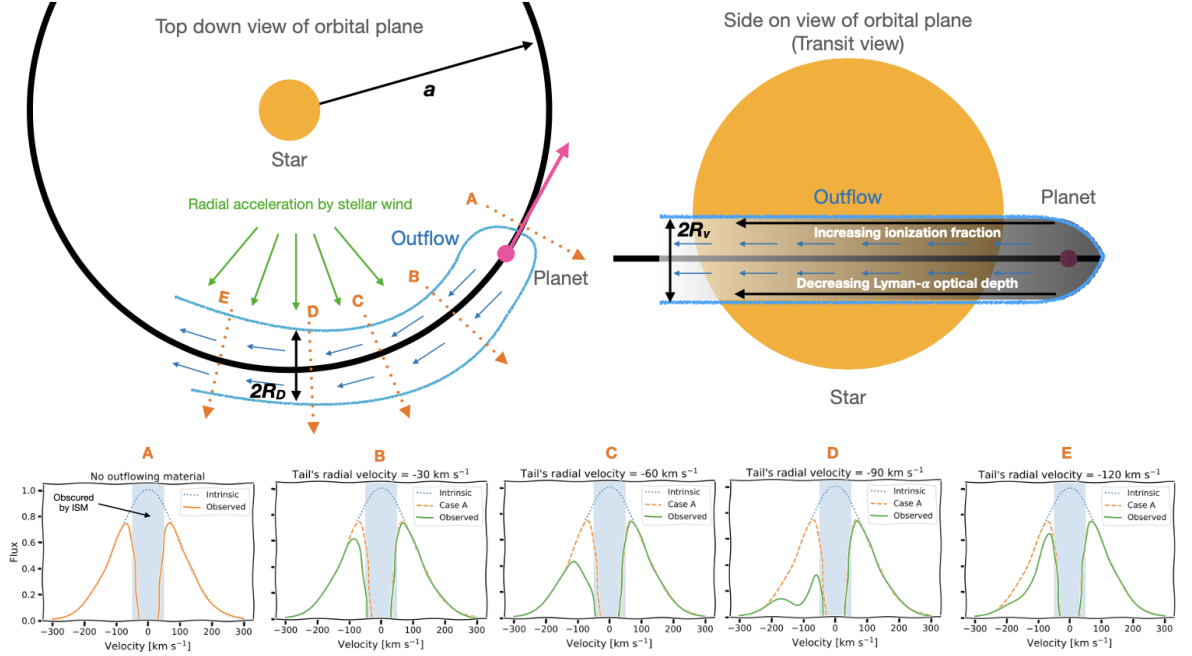


Figure 1.5: Schematic of the comet-like tail, and its effect of Ly- α transits (Owen et al., 2021, Figure 1).

are not uniform throughout the tail, the transit line profile will look vastly different at different stages of the transit. At mid transit, the low velocity dense region of the escaping atmosphere lies over the stellar disc, resulting in significant absorption close to line centre (which for Ly- α is not observable due to interstellar absorption and geocoronal emission). Further away from the planet the density of the escaping gas decreases, while the gas is accelerated to greater velocities. This results in absorption at higher velocities after mid-transit, leading to asymmetry in the transit line profiles before and after mid-transit, as illustrated in figure 1.5. To understand transit line profile observations we therefore need a model which encompasses the planetary tail containing the accelerating gas within the computational grid, and so therefore require a 3D model.

Though observations of transits in Ly- α have proven successful in detecting escaping atmospheres, it is not without its challenges. The line centre of Ly- α is not observable, due to both interstellar absorption and geocoronal emission. Therefore, escaping Hydrogen atmospheres at low velocities are difficult to detect with this line, as only absorption far from line centre can be found. As a result there have been significant efforts put into

1. INTRODUCTION

observing the escape of heavier elements using other spectral lines.

1.1.3 Spectroscopic Transits: Heavier Elements

At other wavelengths in the ultraviolet (UV), escape has been detected from HD209458b namely from Oxygen, Carbon and Sulphur lines, though contrasting results can be found in literature (Vidal-Madjar et al., 2004; Linsky et al., 2010; Ballester & Ben-Jaffel, 2015). Though the far UV shows promise, with several resonance lines from abundant elements, the low stellar flux accompanied by variability across the stellar disc can cause inconsistencies to be obtained if there is significant short term variability in the light curve (Llama & Shkolnik, 2015, 2016). The near UV offers a solution to these problems, with a higher stellar flux and a more uniform background, though elements absorbing at these wavelengths are less abundant and so makes detection challenging (Fossati et al., 2010; Haswell et al., 2012). Nevertheless there have been successes, such as in WASP-12b, where atmospheric escape was detected as well as the presence of MgII and FeII in the upper atmosphere of the planet, with a bow-shock ahead of the planet, supported by either a planetary magnetic field or by the escaping atmosphere of the planet (Fossati et al., 2010; Lai et al., 2010; Vidotto et al., 2010; Haswell et al., 2012; Bisikalo et al., 2013; Fossati et al., 2013; Nichols et al., 2015). As well as WASP-12b, more recent efforts have led to the discovery of heavy elements in the atmospheres of WASP-121b (Sing et al., 2019; Gibson et al., 2020), HD209458b (Cubillos et al., 2020), KELT-9b (Hoeijmakers et al., 2018, 2019) and others. Currently, a popular theory explains the presence of heavier elements at higher altitudes by suggesting that the escaping Hydrogen bulk flow drags these elements with it. This results in a higher abundance of heavier elements in hotter temperatures, leading to increased absorption from these elements (Cubillos et al., 2020). However simulating these elements poses some difficulty, which will be discussed in section 1.2.

As well as the near UV, recently the Helium 10833Å triplet in the near infra-red has been identified as a useful tool for the detection of escaping atmospheres, given its greater abundance when compared to the heavy metals in the near UV and its observability with ground-based instruments (Oklopčić & Hirata, 2018). This has led to many detections of Helium in the upper atmosphere, one of which is shown in figure 1.6 for WASP-107b (Spake et al., 2018), as well as HAT-P-11b (Allart et al., 2018; Mansfield et al., 2018), WASP-69b (Nortmann et al., 2018), HD189733b (Salz et al., 2018; Guilluy et al., 2020)

1.1 Evidence Of Atmospheric Escape In Exoplanetary Systems

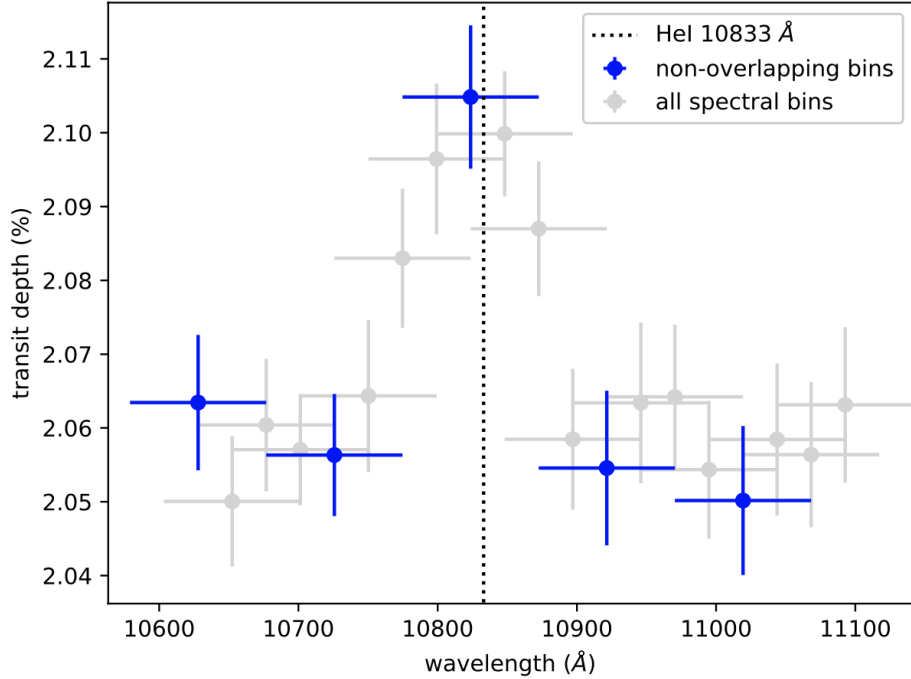


Figure 1.6: Observation of excess absorption in the 10833Å Helium line in the transit spectra of WASP-107b (Spake et al., 2018, Figure 3).

and HD209458b (Alonso-Floriano et al., 2019). Investigations into the dependence on the stellar radiation have found that this works best for larger planets around active K-type stars, but there has been some success in other systems (Oklopčić, 2019).

Observations can show the presence of escaping elements in the upper atmosphere, and allow for estimates on the escape rate of the planet to be made, but cannot provide a clear picture of what is happening in the planet’s environment. To do this we need models capable of simulating atmospheric escape in these close-in systems. Next, I will discuss the fundamentals of these models, and how they can be used to simulate the escaping atmosphere, as well as the stellar wind.

Fundamental Concepts

1.2 Fundamentals Of Modelling Photoevaporation

There are two main mechanisms that have been proposed to cause the atmospheric escape evidenced in section 1.1: photoevaporation and core-powered mass loss. Photoevaporation occurs when close-in planets receive high levels of irradiation from their host stars (EUV and X-ray) which heats their upper atmospheres through photoionisation, inducing hydrodynamic escape (Lammer et al., 2003; Baraffe et al., 2004; Yelle, 2004). Contrary to this, core-powered mass loss is driven by the combination of insulating stellar bolometric flux and the thermal energy in the core of the planet, generated during the planet's formation (Ginzburg et al., 2016, 2018; Gupta & Schlichting, 2019, 2020). Which of these mechanisms caused the sub-jovian desert and radius gap discussed in section 1.1 is not clear, with both being likely candidates, and both probably contributing over the lifetime of the planet (Rogers et al., 2021). In later chapters I will focus on the photoevaporative outflows from close-in exoplanets, using advanced 3D models. However before discussing these simulations we must address some fundamentals of gas dynamics.

1.2.1 Fundamentals Of Gas Dynamics

I will begin by deriving the equations for mass conservation and the mass-loss rate. We can define the total mass (M) within a volume (V) as:

$$M = \int_V \rho dV \quad (1.1)$$

where ρ is the mass density. The change in this mass with time, or the mass-loss rate, can then be written as:

$$\dot{M} = \frac{dM}{dt} = \frac{\partial}{\partial t} \int_V \rho dV. \quad (1.2)$$

We can also write the mass-loss rate in terms of the mass flux which leaves the surface (S) of the volume, and then using the divergence theorem:

1.2 Fundamentals Of Modelling Photoevaporation

$$\frac{dM}{dt} = - \oint_A \rho \mathbf{u} dS = - \oint_V \nabla \cdot (\rho \mathbf{u}) dV, \quad (1.3)$$

where \mathbf{u} is the velocity of the outflow at the surface S , with the negative sign arising from the mass leaving the volume. Equating the above equations:

$$\frac{\partial}{\partial t} \int_V \rho dV = - \oint_V \nabla \cdot (\rho \mathbf{u}) dV. \quad (1.4)$$

We can therefore derive:

$$\frac{\partial \rho}{\partial t} + \nabla \cdot (\rho \mathbf{u}) = 0. \quad (1.5)$$

This is known as the mass continuity equation or the mass conservation equation written in “conservative form”. Essentially this states that a change in density in a volume (with respect to time) must equate the flux of mass through the surface of the volume, if there are no other sources to add or remove mass from the volume.

If we assume that the gas is time independent (i.e. $\partial/\partial t = 0$), and spherically symmetric we find:

$$\nabla \cdot (\rho \mathbf{u}) = 0. \quad (1.6)$$

$$\frac{1}{r^2} \frac{\partial}{\partial r} (r^2 \rho u_r) = 0. \quad (1.7)$$

$$r^2 \rho u_r = \text{constant} \quad (1.8)$$

where u_r is the radial velocity (spherical coordinates). When we consider the volume to be a concentric sphere surrounding the body, we can write the change in mass of said sphere, or the mass-loss rate as:

$$\dot{M} = 4\pi \rho u_r r^2 \quad (1.9)$$

Next, to derive the momentum equation, the motion of the gas is described by Newtons second law, which can be written as:

$$\rho \frac{D\mathbf{u}}{Dt} = \sum \mathbf{f}, \quad (1.10)$$

where the right side represents the sum of the forces per unit volume \mathbf{f} . The derivative on

1. INTRODUCTION

the left is the total derivative, defined as:

$$\frac{D}{Dt} = \frac{\partial}{\partial t} + \mathbf{u} \cdot \nabla. \quad (1.11)$$

Recall that we assumed a time independent fluid ($\partial/\partial t = 0$), as well as spherical symmetry, so the above operator becomes:

$$\frac{D}{Dt} = u \frac{d}{dr}. \quad (1.12)$$

Using this operator we can derive the momentum equation of the gas which depends on the forces acting on the outflow. As was shown by Parker (1958) this can be used to derive an analytical solution for the velocity structure of the stellar wind, which will be discussed in section 1.3. Next, as demonstrated by Yelle (2004); García Muñoz (2007); Murray-Clay et al. (2009); Koskinen et al. (2013a) and others, I will show how these equations can be used to model photoevaporative outflows.

1.2.2 1D Photoevaporation Model

For photoevaporation, the momentum conservation equation accounting for the forces acting on the escaping atmosphere can then be written as follows:

$$\rho u \frac{du}{dr} = -\frac{dP_T}{dr} - \frac{GM_p \rho}{r^2} + \frac{3GM_* \rho r}{a^3} \quad (1.13)$$

where P_T is the thermal pressure, G is the gravitational constant, M_p is the mass of the planet, M_* is the mass of the star and a is the semi-major axis of the planets orbit. The first and second terms on the right hand side are the forces due to the pressure gradient and planetary gravity, while the last term is the “tidal gravity”. This is the sum of the stellar gravity and centrifugal force along the line joining the star and the planet, which is necessary when simulating the planet’s reference frame.

Additionally an equation for the energy of the evaporating atmosphere is solved, written as:

$$\rho u \frac{d}{dr} \left(\frac{k_B T}{(\gamma - 1)\mu} \right) = \frac{k_B T u}{\mu} \frac{d\rho}{dr} + \Gamma + \Lambda, \quad (1.14)$$

where $\gamma = 5/3$ is the adiabatic index, T is the temperature, μ is the mean mass per particle (in units of the mass of Hydrogen m_H), and k_B is the Boltzmann constant (Murray-Clay

1.2 Fundamentals Of Modelling Photoevaporation

et al., 2009). The left hand side in the above equation tracks the internal thermal energy of the fluid, while the first term on the right hand side tracks the cooling due to the work done by the expanding gas. Γ is the heating due to photoionisation, while Λ is the radiative cooling.

Assuming that the ionising radiation is centred at one photon energy ($h\nu_0 = 20\text{eV}$), Γ can then be written as:

$$\Gamma = \epsilon F_{\text{UV}} \sigma_{\nu_0} n_n e^{-\tau}. \quad (1.15)$$

ϵ is the fraction of energy deposited as heat ($\epsilon = (h\nu_0 - 13.6\text{eV})/h\nu_0$), F_{UV} is the UV flux, σ_{ν_0} is the cross section for photoionisation of Hydrogen, and n_n is the number density of neutral Hydrogen. τ is the optical depth of the UV radiation:

$$\tau = \sigma_{\nu_0} \int_r^\infty n_n dr. \quad (1.16)$$

Λ is the cooling due to Ly- α emission. Ly- α radiation is emitted when neutral Hydrogen atoms that are collisionally excited by electrons return to the ground state, which takes the form:

$$\Lambda = -7.5 \times 10^{-19} n_p n_n e^{118348/T} \quad (1.17)$$

where n_p is the number density of ionised Hydrogen (Black, 1981). Though there are many other cooling mechanisms, such as collisional ionisation, radiative recombination, free-free emission and thermal conduction, Murray-Clay et al. (2009) find that their contribution to the cooling of the escaping atmosphere is negligible.

As we can see above, in order to model photoionisation self-consistently one needs to track the density of ionised and neutral Hydrogen. To do this we calculate the ionisation balance. Equilibrium is achieved when the rate of photoionisation balances the rate of radiative recombinations and the rate at which ions are advected away:

$$n_n \frac{F_{\text{UV}} e^{-\tau}}{h\nu_0} \sigma_{\nu_0} = n_p^2 \alpha_{\text{rec}} + \frac{1}{r^2} \frac{d}{dr} (r^2 n_p u) \quad (1.18)$$

where $\alpha_{\text{rec}} = 2.7 \times 10^{-13} (T/10^4\text{K})^{-0.9}$ is the Case-B radiative recombination coefficient for Hydrogen (Storey & Hummer, 1995). Case-B includes all recombination channels except direct recombination to the ground state. Direct ground state recombinations release a

1. INTRODUCTION

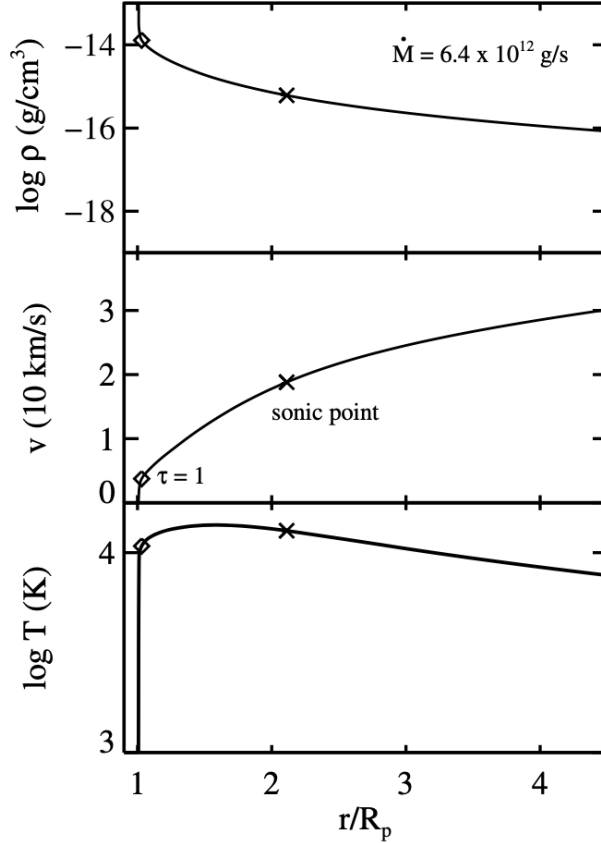


Figure 1.7: The density, velocity and temperature structure of a 1D escaping atmosphere (Murray-Clay et al., 2009, Figure 4).

photon with enough energy to ionise a neighbouring neutral Hydrogen atom. As a result, this recombination channel does not yield a net change in the total number of neutrals, and so can be ignored. The Case-B coefficient therefore only considers recombinations to excited states, which can then reach the ground state by emitting spectral lines.

Figure 1.7 shows the density, velocity and temperature profiles from one such 1D model. Incoming high energy flux penetrates the atmosphere of the planet, with the point where the optical depth reaches unity marked on each panel. This radiation is energetic enough to liberate the electron from the Hydrogen atom, with the excess energy contributing to the heating the gas, as discussed above. This causes an increase in temperature and the accelerating expansion of the gas (accompanied with decreasing density), seen in the middle panel of the velocity structure. The gas then adiabatically cools through this expansion, resulting in a decrease in the temperature profile with altitude. This process drives the

escaping atmosphere, resulting in mass-loss rates from 10^9 to 10^{13} g/s in extreme systems (Murray-Clay et al., 2009; Owen & Jackson, 2012; Johnstone et al., 2015c; Kubyshkina et al., 2018; Allan & Vidotto, 2019; Carolan et al., 2021a).

As photoionisation requires ionising flux to induce escape, and as close-in planets are thought to be mostly tidally locked (Kasting et al., 1993; Edson et al., 2011), it is clear that this escape mechanism will not be spherically symmetric. Instead, the day-side will be highly irradiated, while the night-side receives no flux. Though 1D codes are incredibly useful in understanding the conditions of the planet’s day-side, it is clear that in order to correctly treat atmospheric escape in close-in exoplanets we require a 3D model, which encompasses both day and night sides of the planet. The stellar wind, which I will discuss next, is another important factor to consider using 3D models, as it will ultimately shape the structure of the escaping atmosphere around the planet.

1.3 Stellar Wind Models

In order to consider the effect of the stellar wind on the escaping atmosphere we need to know what structure the stellar wind takes. To find this we again employ numerical models. Here I will discuss a few of these, including Parker’s isothermal model (Parker, 1958), the Weber-Davis model (Weber & Davis, 1967), as well as more advanced 3D Magnetohydrodynamic solutions (Goedbloed & Poedts, 2004).

1.3.1 1D Isothermal Wind

Parker (1958) developed the most basic model of the solar wind, which showed that a non-rotating sun could produce an isotropic, isothermal stationary wind. Continuing from equation 1.12, Parker (1958) assumed the only forces acting on the stellar wind are the forces due to the gas pressure and stellar gravity. This yields the following momentum equation:

$$u \frac{du}{dr} = -\frac{1}{\rho} \frac{dP_T}{dr} - \frac{GM_*}{r^2}. \quad (1.19)$$

If the outflow behaves as an ideal gas, the pressure can be written as:

1. INTRODUCTION

$$P_T = \frac{\mathcal{R}\rho T}{\mu}, \quad (1.20)$$

where \mathcal{R} is the gas constant. Recall that this is an isothermal wind, and so the temperature T is assumed to be constant with distance. The force due to the pressure gradient can be written as:

$$\frac{1}{\rho} \frac{dP_T}{dr} = \frac{\mathcal{R}}{\mu} \frac{dT}{dr} + \frac{\mathcal{R}T}{\mu\rho} \frac{d\rho}{dr} = \frac{\mathcal{R}T}{\mu} \frac{1}{\rho} \frac{d\rho}{dr}. \quad (1.21)$$

Knowing that $r^2\rho u_r = \text{constant}$, we can express the density gradient in the equation above in terms of a velocity gradient:

$$\frac{1}{\rho} \frac{d\rho}{dr} = -\frac{1}{u} \frac{du}{dr} - \frac{2}{r}. \quad (1.22)$$

Subbing these into the momentum equation yields an equation for the velocity gradient of the isothermal stellar wind:

$$u \frac{du}{dr} + \frac{\mathcal{R}T}{\mu} \left(-\frac{1}{u} \frac{du}{dr} - \frac{2}{r} \right) + \frac{GM_*}{r^2} = 0, \quad (1.23)$$

which can also be expressed as:

$$u \frac{du}{dr} = \left(\frac{2c_s^2}{r} - \frac{GM_*}{r^2} \right) / (u^2 - c_s^2), \quad (1.24)$$

where c_s is the isothermal sound speed given by:

$$c_s = \sqrt{\frac{\mathcal{R}T}{\mu}}. \quad (1.25)$$

Though there are many solutions to equation 1.24 (see Figure 3.1, Lamers & Cassinelli 1999), only one of these is applicable to the solar wind. We can see from equation 1.24 that there is a critical point in this equation. First we can see that the denominator will equate to 0 when the velocity of the outflow reaches the isothermal sound speed (the sonic point). This will lead to a velocity gradient of $\pm\infty$, depending on the numerator. Similarly if we examine the numerator, we find it will equate to 0 at the critical radius (r_c):

$$\frac{2c_s^2}{r_c} = \frac{GM_*}{r_c^2}, \quad (1.26)$$

$$r_c = \frac{GM_*}{2c_s^2}. \quad (1.27)$$

In order to avoid an infinite velocity gradient, there are two possibilities: either the velocity remains subsonic everywhere (the “breeze” solution), or the velocity accelerates through the sonic point, and so we must force the numerator and denominator to equal 0 at that point.

The “breeze” solution is where the wind accelerates towards the sound speed, but remains sub-sonic with the velocity trending to zero at large distances ($u \propto 1/r^2$). From continuity, with the velocity trending to zero the density, as well as the pressure, tend to constant values. As this results in relatively high densities and pressures at large distances, the breeze solution is not applicable to the solar wind, as the ISM pressure is too small to contain it¹.

It is clear now that the only physical solution will be when the sonic point and critical radius coincide (ie. $u(r_c) = c_s$), resulting in a stellar wind with a positive velocity gradient everywhere. This solution is transonic: it starts subsonic close to the star and is accelerated through the critical point to supersonic velocities further away from the star.

Once equation 1.24 is solved the density structure of the wind can easily be found. Knowing that \dot{M} is a constant, the density profile can be found from the velocity profile:

$$\rho(r) = \frac{\dot{M}}{4\pi r^2 u(r)}. \quad (1.28)$$

An example of an isothermal solar wind profile is shown in figure 1.8. We see the velocity accelerates through the sonic point to close to 500 km/s at Earth’s orbit, while the density drops to approximately 10^{-23} g/cm³ at 1au, both of which are in reasonable agreement to observations of the solar wind at the Earth. Note that the velocity profile is independent of the density in the isothermal wind (i.e. changing the density at the base of the wind will have no impact on the resultant velocity profile). Therefore one can keep the velocity profile fixed while varying the density to control the stellar wind mass-loss rate of the model (we will use this method to control the wind in chapter 3).

Though the isothermal model is relatively simplistic, with the wind accelerated due to pressure gradients and stellar gravity, it performs quite well in estimating the overall

¹The breeze solution can be applicable to the escaping atmosphere, where the stellar wind can provide significant containing ambient pressure.

1. INTRODUCTION

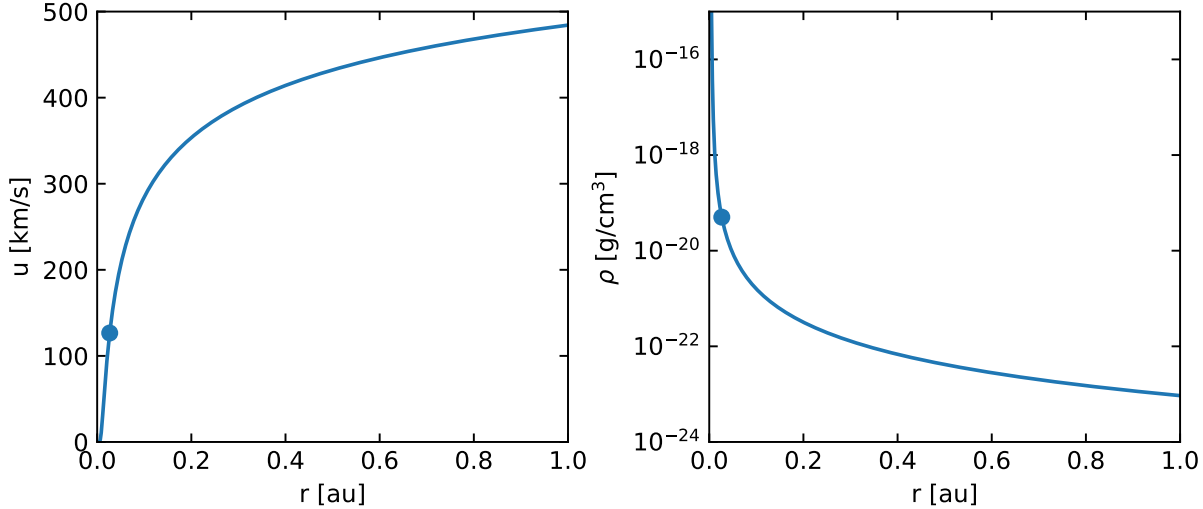


Figure 1.8: A 1D isothermal Parker wind model (Parker, 1958). Here $M_* = 1M_\odot$, $R_* = 1R_\odot$, $T = 1 \times 10^6$ K, and $\dot{M} = 2 \times 10^{-14}M_\odot/\text{yr}$. The left panel shows the velocity profile as a function of distance from the star, while the right shows the density. The point in each panel marks the critical point, where the wind is accelerated to the supersonic velocities.

structure of the stellar wind. However, stellar winds are not isothermal in reality, with Parker’s model requiring additional energy to be injected into the wind in order to keep the temperature constant as it expands. This issue can be tackled with a polytropic model.

1.3.2 Polytropic Winds

A polytropic model uses a polytropic index (α) to relate the temperature/pressure to the density of the wind:

$$T(r) = T_0 \left(\frac{\rho(r)}{\rho_0} \right)^{\alpha-1}, \quad P_T(r) = P_{T0} \left(\frac{\rho(r)}{\rho_0} \right)^\alpha, \quad (1.29)$$

where T_0 , ρ_0 and P_{T0} are the temperature, density and thermal pressure at the base of the stellar wind. When $\alpha = 1$ the relations for the isothermal wind are obtained. These relations can be enforced in the model, such that an energy equation does not need to be solved (Keppens & Goedbloed, 1999). Using these relations for pressure and temperature, and starting from momentum equation (1.19) we can derive the solution for the velocity structure of the polytropic wind. We again assume the outflow behaves like an ideal gas, however now the pressure depends on the density according to the above relation. Thus:

$$\begin{aligned}\ln\left(\frac{P_T}{P_{T0}}\right) &= \alpha \ln\left(\frac{\rho(r)}{\rho_0}\right), \\ \ln(P_T) - \ln(P_{T0}) &= \alpha(\ln(\rho) - \ln(\rho_0)), \\ d\ln(P_T) &= \alpha d\ln(\rho).\end{aligned}\tag{1.30}$$

Using the identity $d\ln(x)/dr = 1/x dx/dr$, we can write the force due to the pressure gradient as:

$$\frac{1}{\rho} \frac{dP_T}{dr} = \frac{P_T}{\rho} \frac{d\ln(P_T)}{dr} = \frac{\alpha \mathcal{R}T}{\mu} \frac{d\ln(\rho)}{dr} = \frac{\alpha \mathcal{R}T}{\mu} \left(-\frac{1}{u} \frac{du}{dr} - \frac{2}{r} \right).\tag{1.31}$$

By subbing this into the momentum equation we obtain:

$$u \frac{du}{dr} + \frac{\alpha \mathcal{R}T}{\mu} \left(-\frac{1}{u} \frac{du}{dr} - \frac{2}{r} \right) + \frac{GM_*}{r^2} = 0,\tag{1.32}$$

$$u \frac{du}{dr} = \left(\frac{2\alpha c_s^2}{r} - \frac{GM_*}{r^2} \right) / (u^2 - \alpha c_s^2).\tag{1.33}$$

Notice if $\alpha = 1$ we obtain the equation of motion for the isothermal wind. Just like the isothermal wind, the polytropic equation of motion contains a critical point. Again there are many solutions to this equation, though only one is physical: when the numerator and denominator go to zero simultaneously such that a positive velocity gradient is obtained everywhere. This solution is again transonic, with the wind accelerating through the critical point to supersonic velocities. The radius of the critical point is now given by:

$$r_c = \frac{GM_*}{2\alpha c_s^2}.\tag{1.34}$$

Unlike the isothermal wind, the position of the critical point cannot be determined before computation as the velocity and sound speed in the wind now depend on the polytropic index (the temperature no longer constant). In chapter 2, the polytropic index is assumed to be 1.05, which implies that the stellar wind temperature profile is nearly isothermal. This results in values for the solar wind velocity which are similar to those obtained from observations at the Earth (Johnstone et al., 2015a,b).

Both the isothermal and polytropic winds discussed above neglect two physical parameters: stellar rotation and magnetic fields. A Weber-Davis model includes these, where the magnetic field is treated as a split monopole, and the resultant wind is assumed to be

1. INTRODUCTION

axi-symmetric (Weber & Davis, 1967). In the initial condition of these models, the field is assumed to be purely radial and decays with distance-squared. As the simulation evolves, in addition to the radial magnetic field, an azimuthal component is created due to stellar rotation. This creates what is known as the Parker Spiral (illustrated in figure 1.9), where through stellar rotation the magnetic field lines are bent into a spiral like structure (Parker, 1958). One can show this magnetic field geometry is described by:

$$\frac{B_\phi}{B_r} = \frac{u_\phi - \Omega R}{u_r}, \quad (1.35)$$

where the subscripts r and ϕ denote the radial and azimuthal components respectively, R is the radial distance from the star, and Ω is the rotation rate of the star (eg. Vidotto, 2021). The tightness of the spiral is characterised by the spiral angle $\Psi = \arctan(B_\phi/B_r)$.

As the star rotates it will lose angular momentum through the stellar wind. The angular momentum-loss rate is given by:

$$\dot{J} = \frac{2}{3} \dot{M} r_A^2 \Omega \quad (1.36)$$

where r_A is the radius of the Alfvén point. This is another critical point in magnetised winds, which will be discussed in section 1.6. The stellar rotation effectively creates a 1.5D model, where the radial and azimuthal components are calculated along a radial line from the star. In chapter 2 I will employ a polytropic magnetised stellar wind model which considers stellar rotation to find the structure of the solar wind for different rotation rates (Johnstone et al. 2015a’s version of VAC: Tóth 1996). In section 2.2 I will discuss further the intricacies and exact setup of these models.

1.3.3 3D Stellar Wind Models

As previously discussed in section 1.2.2, it is important when modelling photoevaporation to consider the interaction with the stellar wind in 3D. Assuming that the gas is magnetic, time dependent ($\partial/\partial t$ terms are no longer negligible), and not spherically symmetric (considering 3 spatial dimensions), one obtains the set of Ideal Magnetohydrodynamic (MHD) equations that describe the wind (eg. Goedbloed & Poedts, 2004). These include the mass conservation equation:

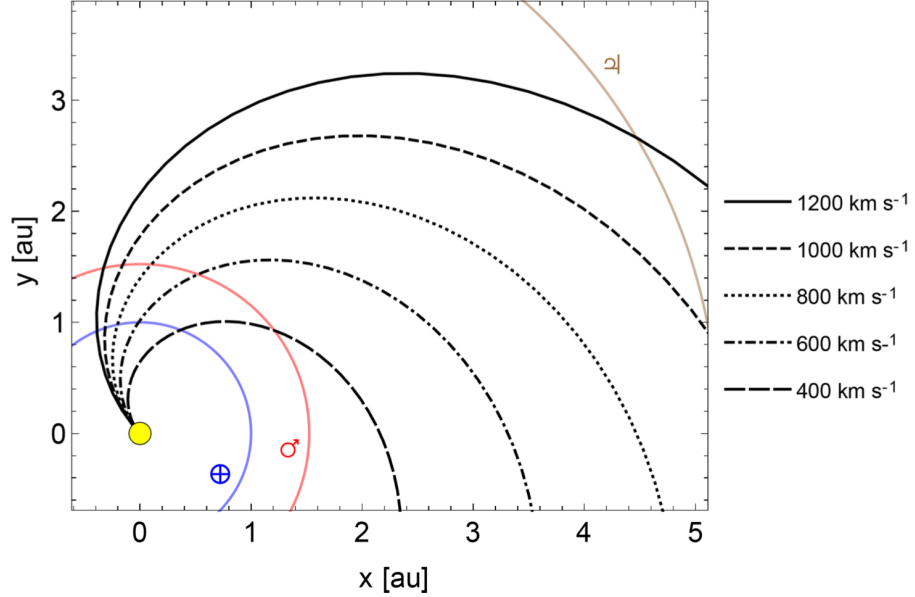


Figure 1.9: Illustration of the Parker Spiral of the Sun, where different lines represent the obtained Parker Spiral structure for different solar wind velocities (Figure 2 Lhotka & Narita, 2019).

$$\frac{\partial \rho}{\partial t} + \nabla \cdot (\rho \mathbf{u}) = 0, \quad (1.37)$$

the momentum conservation equation:

$$\frac{\partial(\rho \mathbf{u})}{\partial t} + \nabla \cdot \left[\rho \mathbf{u} \mathbf{u} + (P_T + \frac{B^2}{8\pi}) I - \frac{\mathbf{B} \mathbf{B}}{4\pi} \right] = \rho \mathbf{g}, \quad (1.38)$$

the magnetic induction equation:

$$\frac{\partial \mathbf{B}}{\partial t} + \nabla \cdot (\mathbf{u} \mathbf{B} - \mathbf{B} \mathbf{u}) = 0, \quad (1.39)$$

and the energy conservation equation

$$\frac{\partial \epsilon}{\partial t} + \nabla \cdot \left[\mathbf{u} \left(\epsilon + P_T + \frac{B^2}{8\pi} \right) - \frac{(\mathbf{u} \cdot \mathbf{B}) \mathbf{B}}{4\pi} \right] = \rho \mathbf{g} \cdot \mathbf{u}. \quad (1.40)$$

I denotes the identity matrix and \mathbf{g} the acceleration due to gravity. The total energy

1. INTRODUCTION

density ϵ is given by:

$$\epsilon = \frac{\rho u^2}{2} + \frac{P_T}{\gamma - 1} + \frac{B^2}{8\pi}, \quad (1.41)$$

where γ sets the adiabatic index. The induction equation defines the relationship between the velocity and magnetic field of the gas, which in the ideal MHD case, assumes negligible resistivity. Note that a set of Hydrodynamic (HD) equations can be found if we ignore magnetic fields in the above equations, setting $B = 0$. Both the MHD and HD equations are widely used in the study of escaping atmospheres and Space-Weather, including my base 3D magnetosphere model (the model I build upon in this thesis), which will be discussed in section 1.6.

1.4 Planet-Wind Interactions

With the capabilities of modelling both stellar and planetary outflows in the presence of magnetic fields, we can begin to study the various ways planets interact with the stellar wind. In this thesis, I will focus first on the interaction between the solar wind and Earth's magnetic field. Following this I move to close-in systems, where both non-magnetised and magnetised wind-atmosphere interactions will be investigated. Here, I will give a brief overview of these planet-wind interactions.

1.4.1 Solar System Planets

In the solar system, all of the giant planets and the Earth have intrinsic magnetic fields. These magnetic fields are largely dipolar, and create cavities in the solar wind, preventing it from reaching the surface directly (e.g. Bagenal, 2013). These cavities are known as magnetospheres, defined as the region where the planet's magnetic field dominates. The size of the magnetosphere is characterised by the magnetopause standoff distance, defined as the point on the line towards the star where the pressure due to the magnetic field balances the stellar wind ram pressure (Chapman & Ferraro, 1931):

$$r_M = \left(\frac{B_{p0}^2}{8\pi\rho_{sw}u_{sw}^2} \right)^{\frac{1}{6}} R_p, \quad (1.42)$$

where B_{p0} is the planet's magnetic dipole strength, ρ_{sw} and u_{sw} here are the stellar wind

density and velocity, and R_p is the radius of the planet.

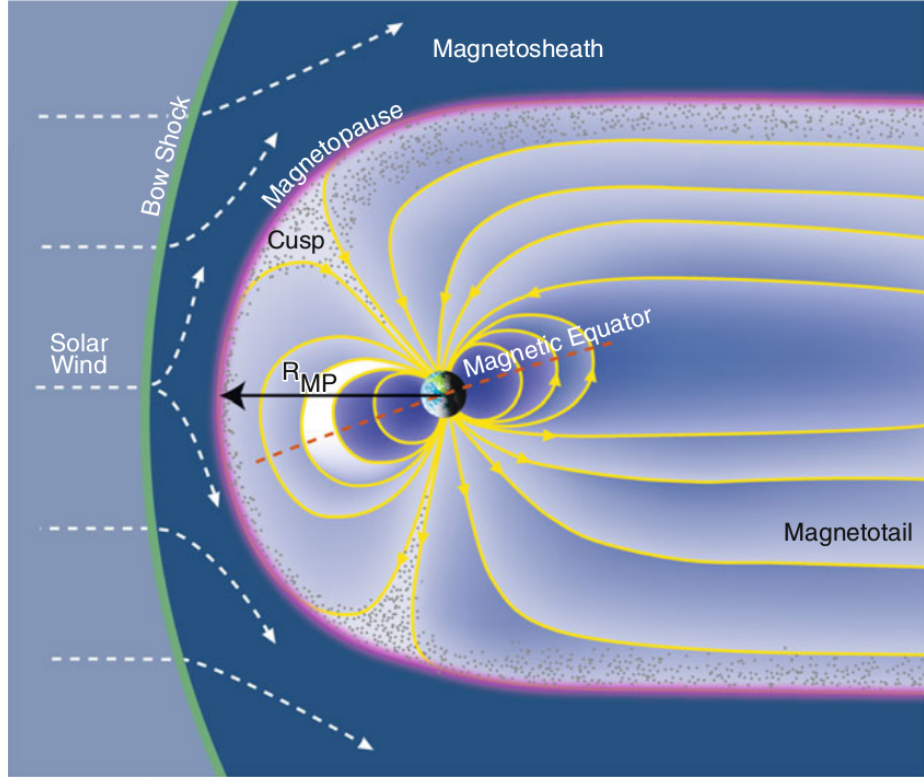


Figure 1.10: The Structure Of Earth's Magnetosphere (Bagenal, 2013).

The Chapman-Ferraro equation (equation 1.42) is a good approximation for the magnetopause standoff distance, but neglects the presence of two structures: the bow shock and magnetosheath, seen in figure 1.10. The bow shock is the shock wave formed when the supermagnetosonic (both supersonic and superalfvénic) stellar wind encounters an obstacle in its path, here the magnetic field of the planet. This is marked by the bow shock standoff distance. This is the distance from the centre of the planet towards the star where the stellar wind is shocked. The strength of the bow shock is determined by the upstream magnetosonic Mach number \mathcal{M} :

$$\mathcal{M} = \frac{u}{\sqrt{c_s^2 + v_a^2}}, \quad (1.43)$$

where v_a is the Alfvén velocity, which is discussed in section 1.6. As we will see in chapter 2, for large \mathcal{M} , the density across the shock can increase by as much as a factor of 4, while

1. INTRODUCTION

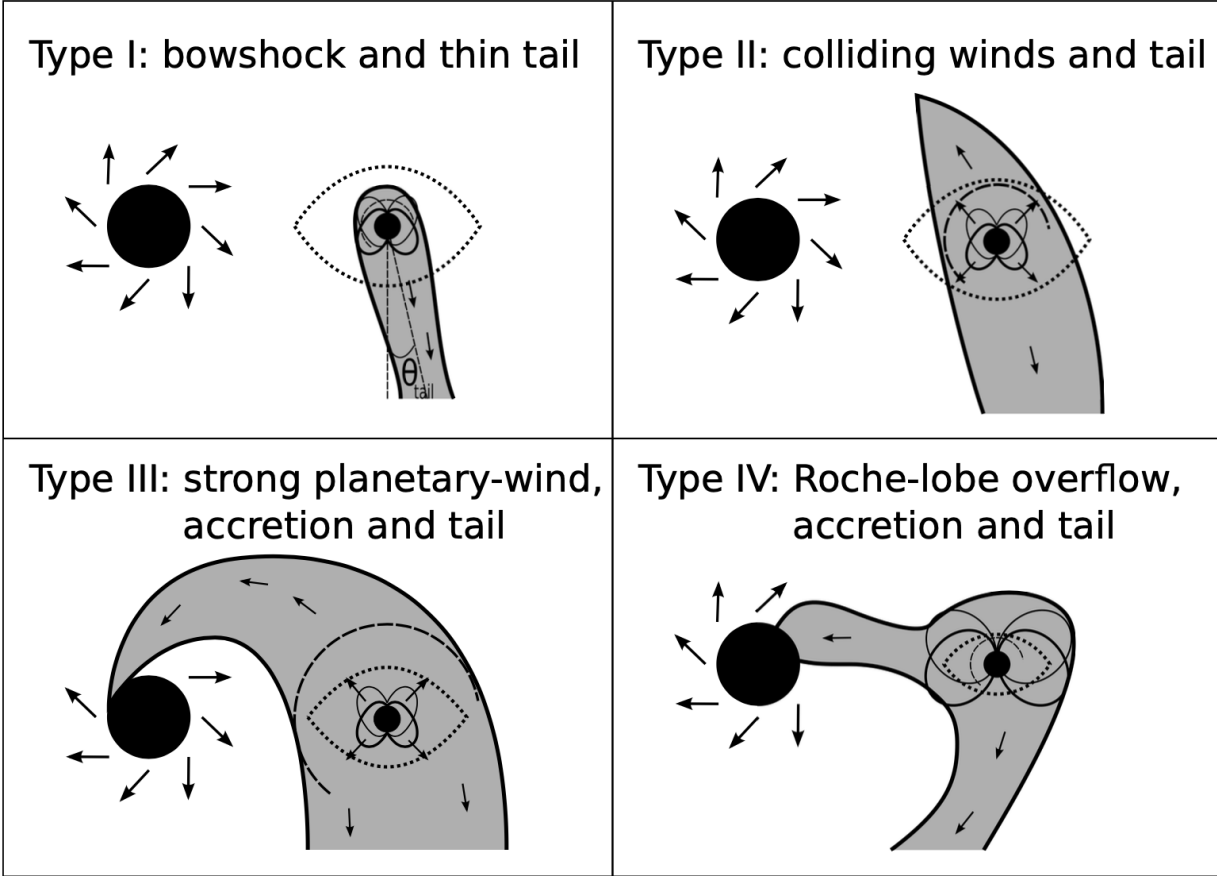


Figure 1.11: Schematic of different wind-planet interactions, showing the orbital plane (Matsakos et al., 2015, Figure 13).

the velocity can decrease by up to the same factor.

The region between the bow shock and magnetopause is known as the magnetosheath. This denser, hotter region is filled with shocked stellar wind material. Ram pressure is no longer the dominant pressure component in this region. Thermal pressure now dominates, as the velocity has fallen while the temperature and density has risen. The size and structure of the magnetosphere is important to understand, as it ultimately dictates how the stellar wind will interact with a planet's atmosphere (Blackman & Tarduno, 2018).

1.4.2 Close-In Systems

Understanding the bow shock and magnetosphere is not only crucial when studying solar system planets, but is also very relevant in close-in systems. While for solar system plan-

ets the magnetic field provides the primary force to oppose the solar wind, the escaping atmosphere from close-in exoplanets also contributes to the pressure balance. The interaction between the stellar wind and the planetary outflow shapes the comet-like tail which follows the planet in its orbit. The geometry and extent of the tail behind the planet are sensitive to several external parameters such as the ram pressure of the stellar wind, as well as the orbital velocity and tidal forces from the star, which arise from these close-in orbits (Matsakos et al., 2015; Pillitteri et al., 2015; Shaikhislamov et al., 2016). Figure 1.11 shows a schematic of the different star-planet interactions in close-in systems from Matsakos et al. (2015). If the stellar wind is weak, tidal forces are strong and/or there is strong atmospheric escape, a stream of planetary material can be created towards the star (accretion stream). This can alter the conditions of the stellar surface and ultimately the conditions of the stellar wind (Matsakos et al., 2015; Shkolnik & Llama, 2018). In the opposite scenario, when the stellar wind is strong and/or escape is weak, dayside material can be confined behind a bowshock, with a thin comet-like tail following the planet’s orbit. This confinement can affect the atmospheric escape rate, whereby a strong stellar wind can prevent the dayside escaping atmosphere from reaching supersonic velocities (Vidotto & Cleary, 2020). As a result the inner most regions of the escaping atmosphere can be affected, and the escape rate reduced due to a lack of dayside acceleration (Christie et al., 2016; Vidotto & Cleary, 2020). Though this “stellar wind confinement” has been studied in 1D, it had not yet been investigated in 3D, and so forms the basis for my investigation discussed in chapter 3.

The angle of the comet-like tail (θ_{tail} , illustrated in the top left panel of figure 1.11) depends strongly on the stellar wind conditions (Vidotto et al., 2010; Matsakos et al., 2015), and can be approximated by:

$$\theta_{tail} = \arctan\left(\frac{u_{sw}}{u_{orb}}\right) = \arctan\left(\frac{u_{sw}^2 a}{GM_*}\right)^{1/2} \quad (1.44)$$

where u_{orb} is the orbital velocity of the planet and a is the orbital distance of the planet. We can see from this equation that for a larger stellar wind velocity, we will obtain a tail that is oriented more radially away from the star. This will in turn affect the transit line profile, as the absorbing tail will be oriented more along the line-of-sight and so the line-of-sight velocity will increase. For a lower stellar wind velocity, or higher orbital velocity, the tail will be more perpendicular to the line of sight, and oriented behind the planet’s orbit.

1. INTRODUCTION

As a result the line-of-sight velocity will be smaller compared to the previous scenario, however the transit duration may increase as now absorbing material will cover the stellar disc for longer.

1.5 Matching Spectroscopic Transit Observations With 3D Models

Recently there has been an increasing number of 3D works which included the stellar wind (Bisikalo et al., 2013; Shaikhislamov et al., 2016; Schneiter et al., 2016; Carroll-Nellenback et al., 2017; Villarreal D’Angelo et al., 2018; McCann et al., 2019; Khodachenko et al., 2019; Esquivel et al., 2019; Carolan et al., 2020; Debrecht et al., 2020; Villarreal D’Angelo et al., 2021; Carolan et al., 2021a; MacLeod & Oklopčić, 2022; Hazra et al., 2022; Kubyshkina et al., 2022a). Many of these models have been compared to observations, such as the models by Villarreal D’Angelo et al. (2018), shown in figure 1.12. Using global simulations (computational grids which include both star and planet), they investigate the transit of GJ 436b (seen in figure 1.4). In total they present 6 models, varying the stellar EUV luminosity (low, medium, and high) and stellar wind temperature (1×10^6 and 3×10^6 K). As previously discussed in section 1.2.2, increasing the high energy stellar luminosity that the planet receives will cause increased heating of the planet’s atmosphere, resulting in strong atmospheric escape. Whereas increasing the temperature of the stellar wind will lead to increased acceleration of the wind and so greater velocities and ram pressures at the planet. As the geometry of the Ly- α line is dependent on the interaction between these two outflows, it is important to vary the conditions of both in order to fully cover the parameter space of the system. The top panels of figure 1.12 illustrate the different tail structures in these models. As discussed previously, we see a more radial tail in the models with faster stellar winds, as well as the formation of an accretion stream in the H1 model, where the combination of strong atmospheric escape and slower stellar wind lead to a stream of atmospheric material flowing towards the star.

Through radiative transfer calculations on these computational grids, the absorption signatures of these models in Ly- α can be found (we will return to such calculations in section 1.7). This allows for the authors to compare the synthetic observations of their models to the observational data of GJ 436b from Lavie et al. (2017). Despite the H1

1.5 Matching Spectroscopic Transit Observations With 3D Models

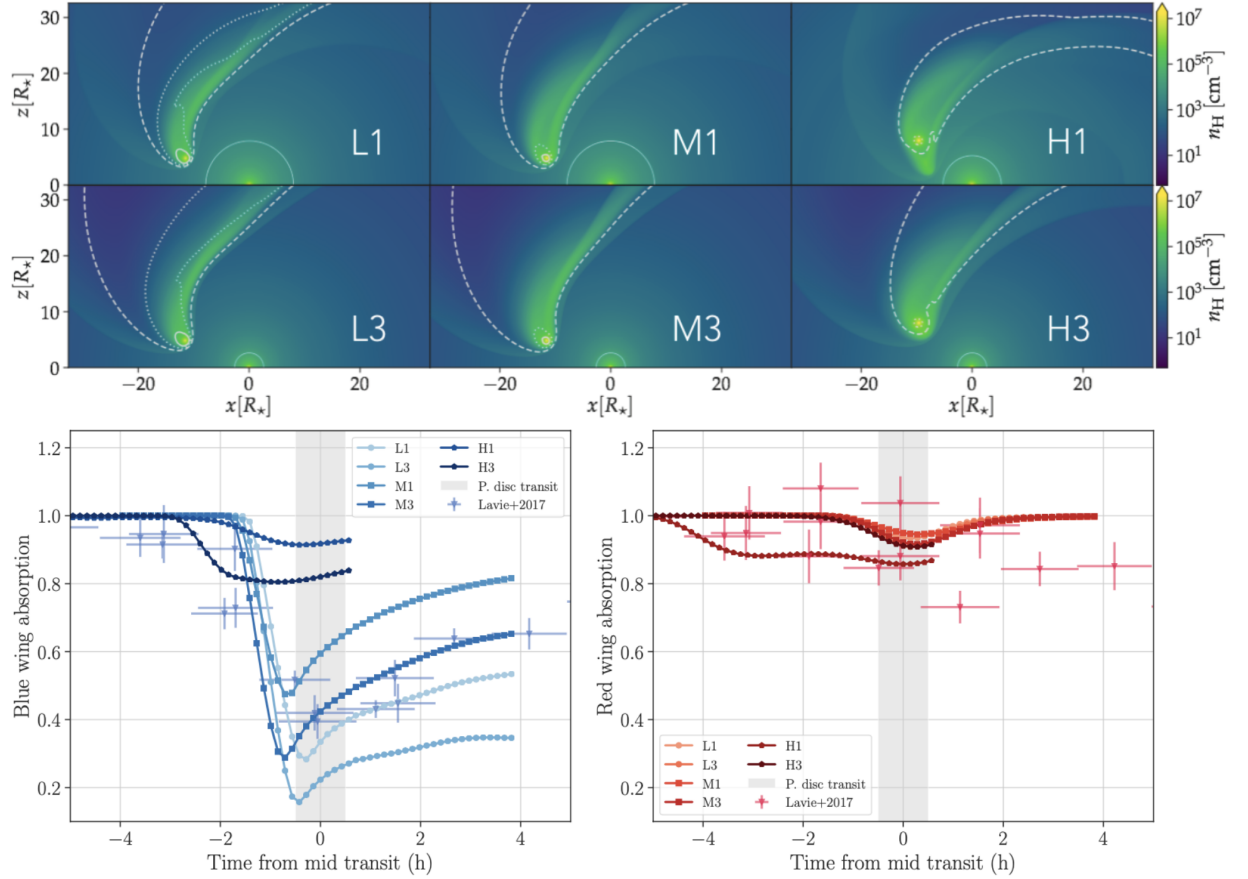


Figure 1.12: Top: 3D models of the escaping atmosphere - stellar wind interaction of GJ 436b. L, M and H stand for low medium and high stellar EUV luminosity, while 1 and 3 represent stellar wind temperatures of 1×10^6 and 3×10^6 K. The color shows the density on the orbital plane. The dashed lines mark ionisation fractions of 0.6, 0.8, and 0.99 from inside to out. **Bottom:** Blue and red wing absorption of the models in Ly- α as a function of time. The background points mark the observational data from Lavie et al. (2017). (Figures from Villarreal D’Angelo et al., 2021)

and H3 models containing the highest levels of stellar irradiation, and being able to match the early ingress in the transit line, these models produce the most shallow transits of the model sets. The authors attribute this to the higher ionisation fraction of the planetary tail caused by the increased photoionisation. The observational data can be best fit by the L1 and M3 models in the blue wing, which both produce similar absorption signatures after mid-transit. Though it may be difficult to disentangle this degeneracy between the strong stellar wind and EUV flux in the observational signatures, it does allow us to place bounds

1. INTRODUCTION

on the conditions of the system. Villarreal D'Angelo et al. (2021) constrain that the stellar wind velocity at the planet lies in the range of 250 – 460 km/s, with a stellar mass-loss rate of $2 \times 10^{-15} M_{\odot}/\text{yr}$, and planetary atmospheric escape rate of $6 - 10 \times 10^9$ g/s, while demonstrating both the importance and usefulness of 3D models in the investigation of exoplanetary mass loss, and its observational signatures. Next, I will introduce the base 3D model that I use in this thesis (which I will continue to build upon in later chapters to model atmospheric escape), as well as the ray-tracing calculations used to performed synthetic transit observations of these models.

Computational Models

1.6 My Base 3D MHD Computational Model

In this thesis I perform 3D MHD and HD simulations of interactions between planets and the stellar wind, to gain insights into various interactions and to contextualise observations. MHD models include magnetic fields, and will be used in chapters 2 and 5, while HD models discussed in chapters 3 and 4 do not include magnetic fields. Here I will discuss the base 3D model used in chapter 2, to which I will make several modifications and additions to in the chapters to follow.

There are several different methods capable of solving the ideal MHD equations. Here I use the most common of these: the finite-volume method. This involves defining the bounds of the computational domain in space (also called the “grid”) in which the simulation will be performed. Through Message Passing Interface (MPI) methods, this grid is split into subsections called “blocks” assigned to different processors for computational efficiency, which are themselves split into cells. The values of computed variables in a specific cell are defined by the average value in that cell. Over each iterative step (sometimes referred to as “time-step”) the cell-averaged values of computed variables are updated as the MHD equations are solved. One challenge with solving finite-volume conservation law equations in computational fluid dynamics is the Riemann problem, which is caused by discontinuities which occur in a continuous function over the cell boundary. Riemann solvers are used to solve these problems, which contain specific methods for computing the numerical flux across a discontinuity. For further discussion on Riemann solvers and the use of numerical methods in fluid dynamics, I refer the reader to Toro (2013).

In this setup, the ideal MHD equations need to be written in conservative form as:

$$\frac{\partial \mathcal{V}}{\partial t} + \nabla \cdot \mathbf{F} = \mathcal{S}, \quad (1.45)$$

where \mathcal{V} is now the conserved variable, \mathbf{F} and \mathcal{S} are the flux vector and source terms respectively which are explicit functions of \mathcal{V} .

In these simulations I do not perform “time accurate simulations” where real time advances during runtime. Instead the code evolves until a steady state is achieved, where

1. INTRODUCTION

a snapshot of a system is found. To do this local time stepping is used, which solves the equations 10 to 15 times faster than time accurate mode (Tóth et al., 2005). Local time stepping evolves each cell using a time step which is related to a local numerical stability criterion. Having different time steps for each cell requires the following modification:

$$\frac{1}{c} \frac{\partial \mathcal{V}}{\partial t} + \nabla \cdot \mathbf{F} = \mathcal{S}, \quad (1.46)$$

where c is an acceleration factor, which is a function of \mathcal{V} . Should a steady state solution be found (where the solution does not change with additional computational time) it is clear that the first term in the above two equations will equal 0, and so their solutions are equivalent. This is also true in discrete form, with the explicit 1-stage Euler discretisation of the above written as:

$$\mathcal{V}_{n+1} = \mathcal{V}_n + \Delta t(-\nabla \cdot \mathbf{F}_n + \mathcal{S}_n), \quad (1.47)$$

where Δt is the local time step. Again when a steady-state solutions is found ($\mathcal{V}_{n+1} = \mathcal{V}_n$), the divergence of the numerical flux must again balance the source terms exactly. So, once a steady-state solution is found, the value of the local time step will not matter given the accompanying 0 factor.

For this thesis, I use the BATS-R-US framework (Tóth et al., 2005) to solve the ideal MHD equations with the finite-volume method, using the “Linde” flux and “minmod” flux limiter to calculate the Riemann Problem (Linde et al., 1998; Linde, 1998). BATS-R-US is a modular code written in FORTRAN 90, optimised to run on High Performance Computing systems, such as ICHEC’s Kay system which was used for the models in this thesis. Model inputs, such as the planetary parameters, type of boundary conditions etc. are specified in the PARAM.IN, with the model outputting .DAT files containing variable values in each cell at a specific time-step. Desired changes to the existing framework can be made within the MODUSER module, before being selected for a given run in the PARAM.IN. These changes include additional source terms in the MHD equations, as well as new inner and outer boundary conditions (see chapter 3). As well as these, new variables for additional elemental species (see chapter 5), can be created within the MODEQUATION module.

BATS-R-US has previously been used to study various solar system objects (Stereberg et al., 2011; Ma et al., 2013; Jia et al., 2015; Jia & Kivelson, 2016; Carolan et al., 2019), the solar wind (e.g. Manchester et al., 2004; van der Holst et al., 2011) and stellar winds (e.g.

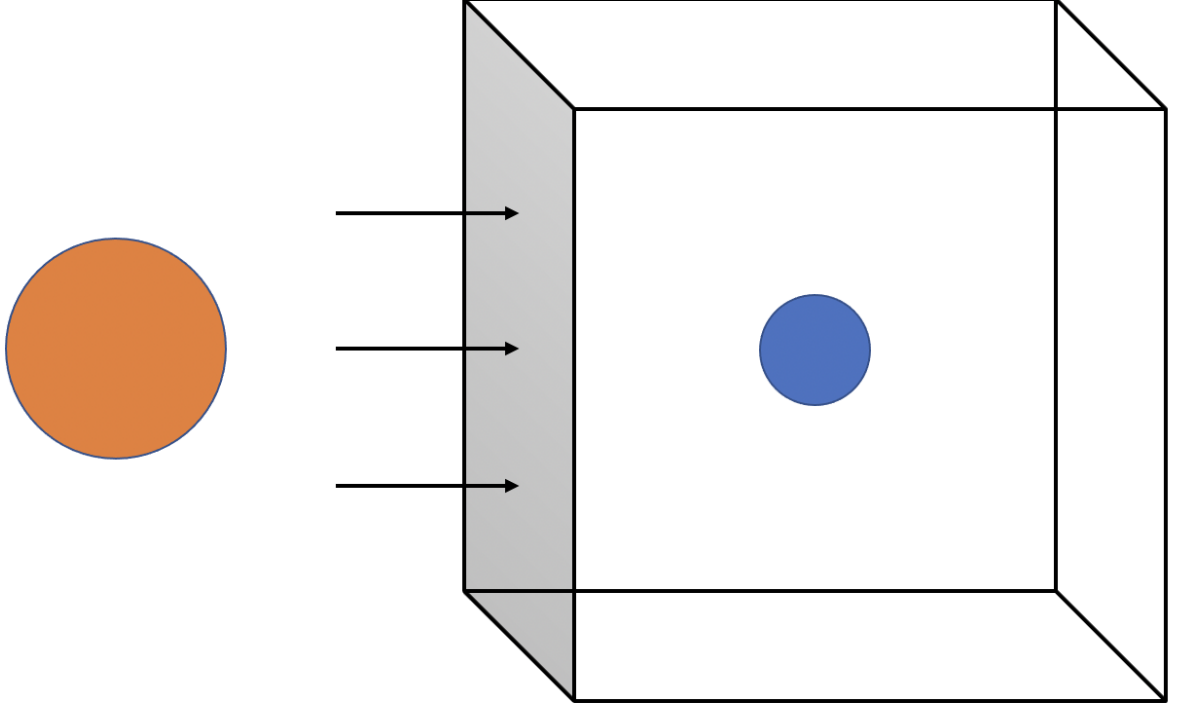


Figure 1.13: Schematic of the setup of my simulations. The orange circle represents the star, while the blue circle represents the planet which is located at the origin of the rectangular grid, outlined in black. There exists an inner boundary at the surface of the planet, and 6 outer boundaries, 1 for each face of the box. The stellar wind is injected through the boundary on the stellar side of the box, marked in grey. All other outer boundaries employ outflow conditions.

Vidotto et al., 2018; Kavanagh et al., 2019). The model solves for 8 parameters: the total mass density (ρ), thermal pressure (P_T), the velocity vector components (u_x, u_y, u_z) and magnetic vector components (B_x, B_y, B_z). The code solves the set of ideal MHD equations which represent the mass conservation, momentum conservation, induction, and energy conservation equations (Equations 1.37 to 1.40).

For each set of simulations, the grid is set up to be a Cartesian rectangular box, the size and orientation of which will be discussed within the relevant chapter. A schematic of this setup is shown in figure 1.13. In each simulation, the planet is located at the origin of the grid: $x, y, z = 0, 0, 0 R_p$, where R_p is the radius of the planet. At $1 R_p$ I place the inner boundary, with the boundary conditions again tailored for each set of simulations.

1. INTRODUCTION

Inside this boundary the density and temperature of the body are specified, which in turn set the thermal pressure at the boundary. Given the grid is a rectangular box surrounding the planet, there are 6 outer boundaries in total. Though again the conditions at these boundaries are specific to each simulation set, in general the boundary on the stellar side of the box is used to inject the stellar wind into the computational grid, with the remaining 5 boundaries employing outflow criteria to ensure material does not get trapped within the domain.

The size of the cells within the grid, otherwise known as the resolution of the grid, can be both uniform or non-uniform in the BATS-R-US framework. In general, the higher the resolution of the grid, the more cells in which the MHD equations must be solved, and so the longer the simulation will take to reach the steady-state solution. Non-uniform resolutions are therefore incredibly useful, as the user can utilize higher resolution where it is required, without wasting computational resources where it is not. In general, higher resolution is required in the grid where the gradient of density, pressure or velocity is large, or where the plasma $\beta = P_T/P_B = \frac{nk_B T}{B^2/8\pi}$ is low. Though again the resolution of the grid is dependent on the set of simulations, in general we require higher resolution close to the planet ($< 5R_p$), as an outflowing planetary atmosphere will present high gradients of the above criteria there, while in magnetic cases it is important to resolve the magnetic field lines close to the planet. An advantage of BATS-R-US is its ability to change the grid resolution using adaptive mesh refinement (AMR). This allows for the resolution of the grid to be changed during runtime, which is useful to save computational resources and time.

During runtime output files are generated containing values of density, velocity, pressure and magnetic field throughout the grid. This allows for steady state to be determined, before the characteristics of the system are investigated. In particular there are a number of important quantities to calculate in order to verify that the code is functioning properly: the sonic and Alfvén points, as well as the atmospheric escape rate.

The sonic point marks the position where the outflow reaches a super-sonic velocity. The more general equation for the sound speed is given by:

$$c_s = \sqrt{\frac{\gamma P_T}{\rho}}. \quad (1.48)$$

Note when $\gamma = 1$ we recover the isothermal sound speed. At velocities greater than the

1.6 My Base 3D MHD Computational Model

sound speed, sound waves are not able to propagate upstream in the flow of the gas, as the gas is travelling faster than the wave. As we will see in chapter 3, this is an important quantity in my simulations, as it determines if wind-atmosphere interactions can affect the conditions of the escaping atmosphere. The Alfvén point is another critical point in MHD fluids. This point is marked by the Alfvén velocity, the velocity at which Alfvén waves travel in the fluid. Alfvén waves are a type of MHD wave, while sound waves propagate through oscillations in density/pressure, Alfvén waves propagate in the presence of magnetic fields. The density of ions provides inertia, while the magnetic field line tension provides the restoring force, with the wave propagating in the direction of the magnetic field (Alfvén, 1942). The Alfvén velocity is given by:

$$v_A = \frac{B^2}{\sqrt{4\pi\rho}}. \quad (1.49)$$

Similar to the sonic point, the Alfvén point marks the position in the fluid where Alfvén waves can no longer travel upstream in the flow as the fluid is moving faster than the wave speed. A useful quantity when investigating the position of these critical points is the magnetosonic mach number \mathcal{M} (equation 1.43). When this value is greater than 1, neither sound nor Alfvén waves are capable of propagating upstream. Instead a standing wave is formed, known as a shock-wave or bow shock. As I will demonstrate in chapter 2, the bowshock is marked by a steep increase in the density, temperature and thermal pressure of the fluid, with the strength of the shock determined by the magnetosonic mach number of the upstream flow (note that in non-magnetic cases, the above magnetosonic mach number becomes the sonic mach number, with $v_A = 0$).

Another important characteristic to consider is the atmospheric escape rate (\dot{m}). This ultimately determines how fast a planet will lose its atmosphere, which is a key contributor to planetary habitability (Dong et al., 2018; Lingam & Loeb, 2018). This can be calculated in the grids as follows:

$$\dot{m} = \oint_S \rho \mathbf{u} \cdot d\mathbf{S}. \quad (1.50)$$

This is the integral of the mass flux ($\rho \mathbf{u}$) over a surface (S). Typically this surface is defined as a concentric sphere surrounding the planet, though it can be useful to examine the mass flux through specific planes (eg. a plane perpendicular to the magnetic poles, see chapter 5).

1. INTRODUCTION

1.7 Ly- α Transit Calculations

From chapter 3 onwards, I will model atmospheric escape in exoplanetary systems, and so am interested in investigating its observational signatures. For this I will use a ray-tracing model to compute the Ly- α transit line profiles, originally developed by Vidotto et al. (2018); Allan & Vidotto (2019), and modified here to perform these calculations on BATS-R-US grids.

I first extract the necessary variables from the computational grid: the density of neutral Hydrogen, temperature, and line of sight velocity (u_{LOS}), all of which affect the transit line profile. As the 3D simulations are performed in the co-orbiting, co-rotating reference frame (the star is always at negative x, and the planet is always centred at the origin), the line-of-sight velocity can be calculated by:

$$u_{\text{LOS}} = u_x - y\Omega_{\text{orb}}, \quad (1.51)$$

where Ω_{orb} is the orbital rotation rate. The above equation is found by converting the velocity vector from the computational grid (\mathbf{u}) to the inertial reference frame (\mathbf{u}_I):

$$\mathbf{u}_I = \mathbf{u} + \mathbf{\Omega}_{\text{orb}} \times \mathbf{R}, \quad (1.52)$$

where $\mathbf{\Omega}_{\text{orb}}$ is the orbital rotation vector (perpendicular to the orbital plane), and \mathbf{R} is the position vector relative to the star.

To speed up computation, I interpolate the non-uniform grid into a uniform grid with 201 points in each of the 3 dimensions (chosen to provide enough information from the grid, and ensuring a point exactly at the origin). With the uniform grid established, the frequency dependent optical depth (τ_ν) can now be found by integrating along the dimension corresponding to the line of sight, in this case x:

$$\tau_\nu = \int n_n \sigma \phi_\nu dx. \quad (1.53)$$

n_n is the number density of neutral Hydrogen, σ is the absorption cross section for Ly- α photons, and ϕ_ν is the frequency dependent Voigt line profile. σ is calculated for Ly- α as:

$$\sigma = \frac{\pi e^2 f}{m_e c}, \quad (1.54)$$

where f is the oscillator strength of the transition, m_e the electron mass, e the electron charge and c the speed of light. $f = 0.416410$ is obtained for Ly- α from the NIST catalogue¹. The Voigt line profile (ϕ_ν) is the convolution of the Gaussian and Lorentzian line profiles, which accounts for both Doppler and natural line broadening:

$$\phi_\nu = \frac{\lambda_0}{\sqrt{\pi}u_{\text{th}}} \frac{\chi}{\pi} \int_{-\infty}^{\infty} \frac{e^{-w^2}}{\chi^2 + (\Delta u/u_{\text{th}} - w)^2} dw, \quad (1.55)$$

where λ_0 is the wavelength at the line centre of Ly- α (1215.67Å), $u_{\text{th}} = \sqrt{2k_B T/m_H}$ and m_H is the atomic mass of Hydrogen. χ is the damping parameter given by $\chi = A_{ji}\lambda_0/4\pi u_{\text{th}}$. A_{ji} is the transition rate, for Ly- α this is $A_{ji} = 4.69860 \times 10^8 \text{ s}^{-1}$, taken again from the NIST catalogue¹. Δu is the velocity offset from the line centre, given by the difference between the channel and line of sight velocities $\Delta u = u_{\text{channel}} - u_{\text{LOS}}$, and $w = \sqrt{m_H u_{\text{LOS}}^2/2k_B T}$ (see Rybicki & Lightman 1986; Crivellari et al. 2019 for details).

With the optical depth calculated, the fraction of transmitted specific intensity can be found:

$$\frac{I_\nu}{I_*} = e^{-\tau_\nu}, \quad (1.56)$$

where I_* is the the specific intensity emitted from the star which at a given frequency is assumed to be uniform over the stellar disc. $1 - I_\nu/I_*$ therefore represents the fraction of specific intensity that is absorbed by the planet's disc and atmosphere. As the face of the uniform grid contains 201x201 cells (I integrate along the remaining dimension as the line of sight), I shoot 51 frequency dependent rays along each of these 201² cells. This is illustrated in figure 1.14. Here I also take into account the size of the stellar disc, setting the specific intensity of rays in pixels which do not cover the stellar disc to zero. Integrating over all rays, and dividing by the flux of the star allows for the frequency-dependent transit depth (ΔF_ν) to be calculated:

$$\Delta F_\nu = \frac{\iint (1 - e^{-\tau_\nu}) dydz}{\pi R_*^2}. \quad (1.57)$$

With the frequency/velocity dependent transit depth for a model determined, the observational characteristics of the system can be established. It is again important to note that for Ly- α , the line centre is contaminated by both geocoronal emission and interstellar

¹<https://www.nist.gov/pml/atomic-spectra-database>

1. INTRODUCTION

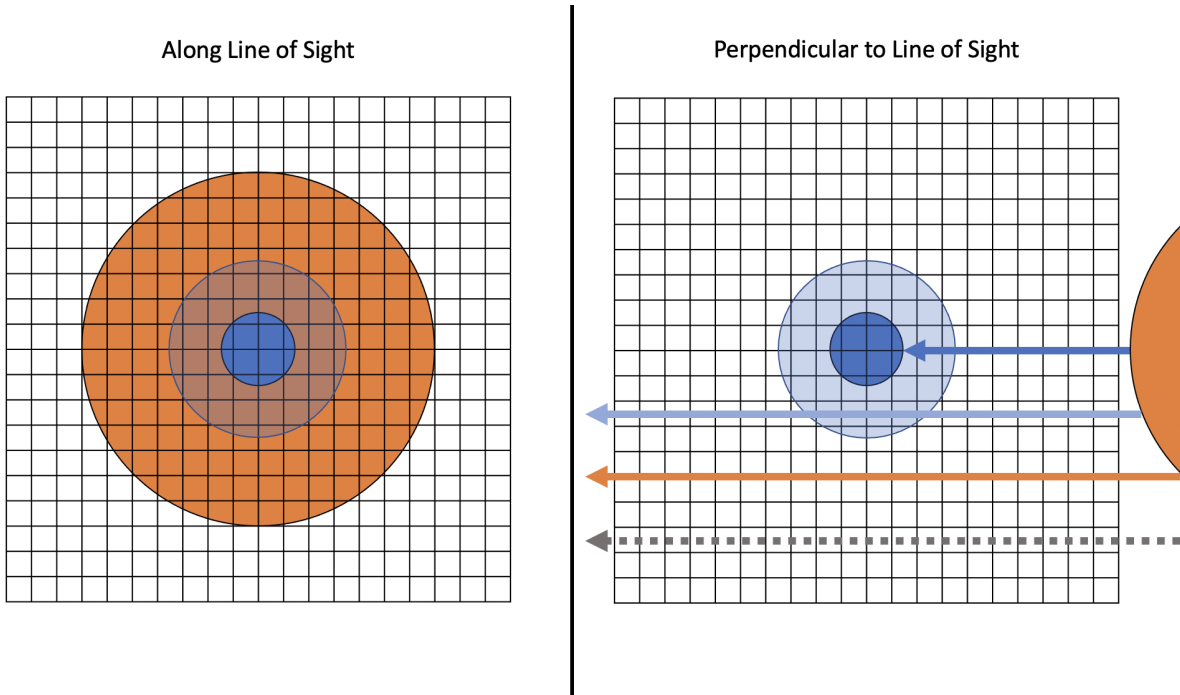


Figure 1.14: Schematic of the synthetic transit calculations. The left panel shows the view from along the line of sight, while the right shows the perpendicular view. The orange circle marks the stellar disc, the dark blue marks the planets surface, while the lighter blue traces the planets atmosphere (spherically symmetric in this example). Rays behind the planetary disc are fully absorbed during the calculation marked in dark blue, while the lighter blue rays which pass through the atmosphere will be somewhat absorbed by any neutral Hydrogen in the atmosphere. Orange rays from the stellar disc which do not pass through the atmosphere will be unaffected, while pixels which do not trace back to the stellar disc are not considered, marked with the dotted grey arrow.

absorption. Therefore I will use these models to identify how specific system characteristics affect these line profiles, and identify trends in the blue ($< -40\text{km/s}$), red ($> 40\text{km/s}$) and line centre absorption ($-40 \leq u_{\text{LOS}} \leq 40 \text{ km/s}$). One limitation of these calculations is that they currently do not account for the grid rotation needed before and after mid transit to correct the line-of-sight through the computational grid as the planet orbits. For a spherically symmetric (1D) escaping atmosphere, this rotation will not affect the resultant line-of-sight. However, for a 3D model capable of capturing the comet-like tail, this rotation could have a significant affect on the light curve. Because of this, in this thesis I will present transit line profiles at mid transit (where no rotation is required), and will leave the inclusion of grid rotation and light curve investigation to future work.

Overview Of The Thesis

In this chapter I have introduced and contextualised how planets interact with the stellar wind, covering both the Earth and exoplanetary system, magnetic and wind-atmosphere interactions. I have discussed both observational evidence of atmospheric escape, and the use of computational models over the last two decades to understand these observations. I introduced the base 3D MHD model, BATS-R-US, which I will continue to develop and make further additions to throughout this thesis. Finally I briefly introduced ray-tracing methods, and how they are used to synthetically observe these 3D simulations.

In chapter 2 I will discuss the Evolution of Earth’s Magnetosphere (published in Carolan et al. 2019) which employs the base model discussed previously in section 1.6. Here I combine stellar wind models with my magnetosphere simulations, in order to investigate how changes to the solar wind affect the size and structure of Earth’s magnetosphere. Given that the solar wind is not constant in time, but rather has evolved as the Sun spun-down over its evolution, this work contextualises how the changing wind can affect the Earth, and the evolution of this interaction.

In chapter 3 I present my work on how the stellar wind affects the Ly- α transits of close-in planets (published in Carolan et al. 2021a). Here I begin to make major additions to this version of BATS-R-US, adding the source terms necessary to model close-in exoplanets, as well as developing boundary conditions to launch an escaping atmosphere and to handle a radial stellar wind. For two typical exoplanets, I vary the strength of the stellar wind while keeping the planetary characteristics constant, investigating the differences between interactions of the escaping atmosphere with strong and weak stellar winds. I then perform ray-tracing calculations, determining the observational characteristics of these models, identifying the trends in their line profiles with stellar wind strength.

In chapter 4 I apply my model to the newly discovered Warm Neptune AU Mic b. AU Mic b provides an interesting dichotomy: the planet orbits a young M-dwarf and so one would expect the planet is highly irradiated and should exhibit strong atmospheric escape. However young M-dwarfs are thought to produce strong stellar winds, which as I will show in chapter 3 can confine the escaping atmosphere limiting its ability produce absorption signatures in Ly- α . This allows us to contextualise follow-up observations of this planet, and how they can be used to infer the conditions of the stellar wind in this system. (This

1. INTRODUCTION

work was published in Carolan et al. 2020)

In chapter 5, I will continue to make additions to this version of BATS-R-US, introducing magnetic fields to these now self-consistent simulations of photoevaporation. While keeping the conditions of the stellar wind constant, I increase the dipolar field strength of a typical Hot Juptier sized exoplanet. After first investigating how this affects the escaping atmosphere, its interaction with the stellar wind and the structure of the magnetosphere, I continue by performing ray-tracing calculations, to synthetically transit these planets. This allows me to investigate how the observational characteristics of close-in exoplanets change with the magnetic field strength of the planet (published in Carolan et al. 2021b).

In chapter 6 I introduce two new processes to my simulations, both of which are thought to produce the energetic neutral atoms required to match observations: Charge Exchange and Radiation Pressure. This involves ongoing extensive development and testing of modifications to this version of BATS-R-US. I will introduce these two processes as well as how they can be modelled, before showing preliminary simulations results, focusing again on their impact on transit absorption signatures.

Finally, in chapter 7 I will summarize the work presented in this thesis, before discussing the future work in this area.



The Evolution Of Earth's Magnetosphere

There have been numerical studies investigating present and past interactions between the solar wind and solar system planets, such as with Mars (Terada et al., 2009a; Ma et al., 2013, 2015; Sakai et al., 2018), Venus (Kulikov et al., 2007; Terada et al., 2009b) and Earth (Ridley et al., 2001; Vogt et al., 2004; Sterenborg et al., 2011). In this chapter, I examine the evolution of Earth's magnetosphere over the solar main-sequence. The novelty of my work is that I couple two sets of simulations: one set to characterise the evolving solar wind and another to characterise the evolution of Earth's magnetosphere, which uses the evolving solar wind as an input. To do this I use the base 3D MHD model presented in section 1.6, in combination with a 1.5D stellar wind model presented in 2.2 (VAC, Tóth, 1996; Johnstone et al., 2015c). My work on the interaction between the evolving solar wind and Earth is relevant for contextualising the atmospheric protection of our planet and exoplanets, which is likely linked to the evolution of life (Lammer et al., 2011, 2012; Zuluaga et al., 2013a; Blackman & Tarduno, 2018).

This chapter is presented as follows. In section 2.1 I contextualise our interest in Earth's interaction with the solar wind. I then simulate the evolution of the solar wind using empirical relations for base temperature, density and magnetic field strength (section 2.2). I use surface rotation as a proxy for age, in which case rotation of the young Sun is faster than the current rotation rate. This limitation is further discussed in section 2.2. I then simulate the interaction between the solar wind and Earth's magnetosphere at different ages (rotations) using 3D numerical simulations (section 2.3). I examine the variations in the day-side of Earth's magnetosphere and bow shock with rotation (section

2. THE EVOLUTION OF EARTH'S MAGNETOSPHERE

2.4). At a very early age, it is still unknown whether the sun was a fast, moderate or slow rotator. I explore the extreme environment around the young Earth in section 2.6 and present my conclusions in section 2.7. The work presented in this chapter has been published in Carolan et al. (2019).

2.1 Context

Recently, there have been discussions on whether smaller or larger magnetospheres can better protect the atmospheres of planets (Strangeway et al., 2010; Brain et al., 2013; Vidotto, 2013; Tarduno et al., 2014; Blackman & Tarduno, 2018). Some say that a large magnetosphere would act as a shield from stellar wind particles directly impacting the planet, and the larger the shield, the more protected the atmosphere is against erosion. On the other hand, others say that a larger magnetosphere would have a greater collecting area for stellar wind plasma, which would be channelled towards polar regions, through the cusps shown in figure 1.10. This inflow would generate local heating, which could induce atmospheric escape through polar flows (e.g. Moore & Horwitz, 2007). It is also possible that both effects co-exist, but they have different contributions depending on the physical characteristics of the system, such as planetary magnetic field strength and energy of stellar winds. Blackman & Tarduno (2018) suggested that it is the competition between low inflow speeds (from stellar winds) and large collecting areas (from magnetospheres) that define whether planetary magnetospheres can have protective effects in a planet's atmosphere.

Using energy conservation arguments, Blackman & Tarduno (2018) placed an upper limit on the stellar wind induced particle escape rate for the present day Earth of $2.62 \times 10^{27}(\mu/16)^{-1}\text{s}^{-1}$ (using momentum conservation yields a slightly lower value, on the order of 10^{26}). For oxygen ($\mu = 16$), these limits are comparable to the observed rates of O^+ escape from the poles ($7.2 \times 10^{25}\text{s}^{-1}$, Seki et al., 2001). The general formula of this upper limit (using energy conservation) takes the form $\dot{m} \propto \dot{M}(u^{sw})^2(r_M)^2$. From this equation it is clear that the upper limit on the atmospheric escape rate is very sensitive to the stellar wind conditions of the system and the size of the planet's magnetosphere (which itself is dependent on the stellar wind and planet's magnetic field). In particular, the above equation suggests that stellar wind induced escape is particularly important in the young system, when the stellar wind is known to be both fast and dense. However Blackman

& Tarduno (2018) found that for the Earth, even though the total amount of solar wind material captured in our magnetosphere is larger than that of a fictitious non-magnetic Earth, our magnetic field still has had a protective effect in protecting our atmosphere. This scenario however could be different in Earth's future, due to different solar wind characteristics.

Short term effects can impact the shape and size of the magnetosphere. Impulsive events, such as coronal mass ejections, may briefly increase the strength of the solar wind impacting the planet, causing a short-term variation in the magnetosphere, its surrounding bow shock, and atmosphere of the planet (Ngwira & Pulkkinen, 2014; Airapetian et al., 2016), which could alter atmospheric escape (Johnstone et al., 2019).

As well as these short-term events, the Sun is known to flip polarity on an 11-year cycle. As was seen by Bharati Das et al. (2019), the direction of the stellar wind's magnetic field can have large implications on the structure of the magnetosphere. The most extreme cases caused by this cyclical polarity flip are the open and closed magnetospheres. These occur when the magnetic field of the wind and the field lines on the day-side of the planet are aligned and anti-aligned respectively. In the case where they are parallel on the day-side (no reconnection), the magnetic field of the wind forces the planet's field lines to remain closed. Conversely, when they are anti-parallel (with reconnection), there is a much greater number of open field lines on the night-side and at the poles of the planets. This could lead to inflow/outflow of material at the polar regions, which has implications on the sustainability of a planets atmosphere as previously mentioned.

Though these relatively short-term cyclical variations are important, the long-term evolution of the solar wind will have a larger effect on Earth's magnetosphere. The magnetosphere is influenced by the conditions of the stellar wind, which depends on the magnetic activity of the star. Since stellar activity declines with both age and rotation (Skumanich, 1972; Ribas et al., 2005; Vidotto et al., 2014), the wind of the young sun is believed to have been stronger, which then declined with age (or rotation rate, Ó Fionnagáin & Vidotto, 2018; Ó Fionnagáin et al., 2019; Pognan et al., 2018). In a numerical study of the interaction between the paleo-Earth (~ 3.5 Gyr ago) and the young sun, Sterenborg et al. (2011) concluded that the young Sun's wind would have had easier access to the Earth's surface at that age. In this chapter, I quantify how the evolving solar wind has affected Earth's magnetosphere, using a combination of 1.5D stellar wind and 3D magnetosphere models.

2.2 1.5D Stellar Wind Simulations

To model the solar wind, I use a 1.5D Weber-Davis model (discussed in chapter 1, Weber & Davis, 1967). For that, I use the Versatile Advection Code (VAC, Tóth, 1996), based on the version of the code from Johnstone et al. (2015c). Here, I adopt a constant polytropic index of $\alpha = 1.05$ in my simulations, which implies that the stellar wind temperature profile, for each model, is nearly isothermal. Additionally, I consider the stars to be magnetised and rotating. The rotation rate Ω is varied from $0.8\Omega_{\odot}$ to $50\Omega_{\odot}$, where Ω_{\odot} is the current rotation rate of the sun, to mimic the solar wind evolution through the main-sequence. The wind temperature, density and magnetic field depend on rotation in my models. I describe next how I chose these wind parameters.

2.2.1 Choice Of Stellar Wind Parameters

Polytropic wind models have two important free parameters, namely the temperature and density at the base of the wind. The values of these parameters are typically assumed to be coronal values, which generate hotter and rarefied winds, similar to what is adopted for the present-day Sun (e.g. Pneuman & Kopp, 1971). However, these parameters are not easy to measure in stars other than the Sun. To derive the wind temperatures of low-mass stars, theoretical works have either assumed a relationship between temperature and X-ray fluxes (e.g., Holzwarth & Jardine, 2007; Johnstone et al., 2015c; Réville et al., 2016; Ó Fionnagáin & Vidotto, 2018) or that it is proportional to the square-root of the escape velocity (e.g., Matt et al., 2012). These two families of models have been discussed in depth by Johnstone et al. (2015c). They are, by definition, equivalent for the present-day Sun, but for other stars, they can lead to much different wind models (see also Vidotto, 2018, 2021). In the latter approach, for example, the escape velocity does not vary significantly in the main sequence, during which the stars spin down and become less active. This implies that wind temperatures in these models would be approximately constant throughout the main-sequence evolution. In my models, I use the former approach. Given that X-ray emission is seen to vary by several orders of magnitude for stars at different rotation rates (e.g., Pizzolato et al., 2003), I naively would expect that a high-temperature corona would lead to a high-temperature wind and, hence, I adopt in my models a correlation between the two. More specifically, I follow the approach by Ó Fionnagáin & Vidotto (2018), who

modelled the wind base temperature (T_0) by scaling the average coronal temperatures of Sun-like stars to current solar wind values following the X-ray flux–temperature relations of Johnstone & Güdel (2015). The base temperature is dependent on the stellar rotation rate Ω according to:

$$T_0 = \begin{cases} 1.5 \times 10^6 \left(\frac{\Omega}{\Omega_\odot}\right)^{1.2} \text{ K} & \text{for } \Omega < 1.4\Omega_\odot, \\ 1.98 \times 10^6 \left(\frac{\Omega}{\Omega_\odot}\right)^{0.37} \text{ K} & \text{for } \Omega \geq 1.4\Omega_\odot. \end{cases} \quad (2.1)$$

Ó Fionnagáin & Vidotto (2018) fit a broken power law to the X-ray data in light of other works suggesting a break in other activity quantities: rotation rates, lithium abundances and X-ray luminosity (Booth et al., 2017; Beck et al., 2017; van Saders et al., 2016).

For the base number density (n_0) I use a rotation-dependent density relation, derived by Ivanova & Taam (2003) from X-ray observations, and employed in other wind studies of solar-like stars (Holzwarth & Jardine, 2007; Réville et al., 2016; Ó Fionnagáin & Vidotto, 2018):

$$n_0 = 10^8 \left(\frac{\Omega}{\Omega_\odot}\right)^{0.6} \text{ g/cm}^3. \quad (2.2)$$

The magnetic field strength at the wind base $B_{r,0}^{\text{sw}}$ is derived from the empirical relation from Vidotto et al. (2014), based in observationally-derived magnetic maps:

$$B_{r,0}^{\text{sw}} = 1.29 \left(\frac{\Omega}{\Omega_\odot}\right)^{1.32} \text{ G}. \quad (2.3)$$

Note that the values from Vidotto et al. (2014) represent an average field strength of the large-scale magnetic field over the stellar surface and, here, is used as the radial component of the field strength.

These wind simulations extend to 1 au (equivalent to $215R_\odot$). For each of them, I compute the density, temperature, the radial (r) component of velocity u_r^{sw} and magnetic field, as well as the azimuthal (ϕ) component of velocity u_ϕ^{sw} and magnetic field with distance. The values of these quantities at 1 au, for each assumed rotation rate, are shown in figure 2.1 and listed in table 2.1.

These wind parameters at 1 au are the inputs of the magnetosphere simulations. The magnetosonic velocity at the interaction, together with the stellar wind velocity, determine

2. THE EVOLUTION OF EARTH'S MAGNETOSPHERE

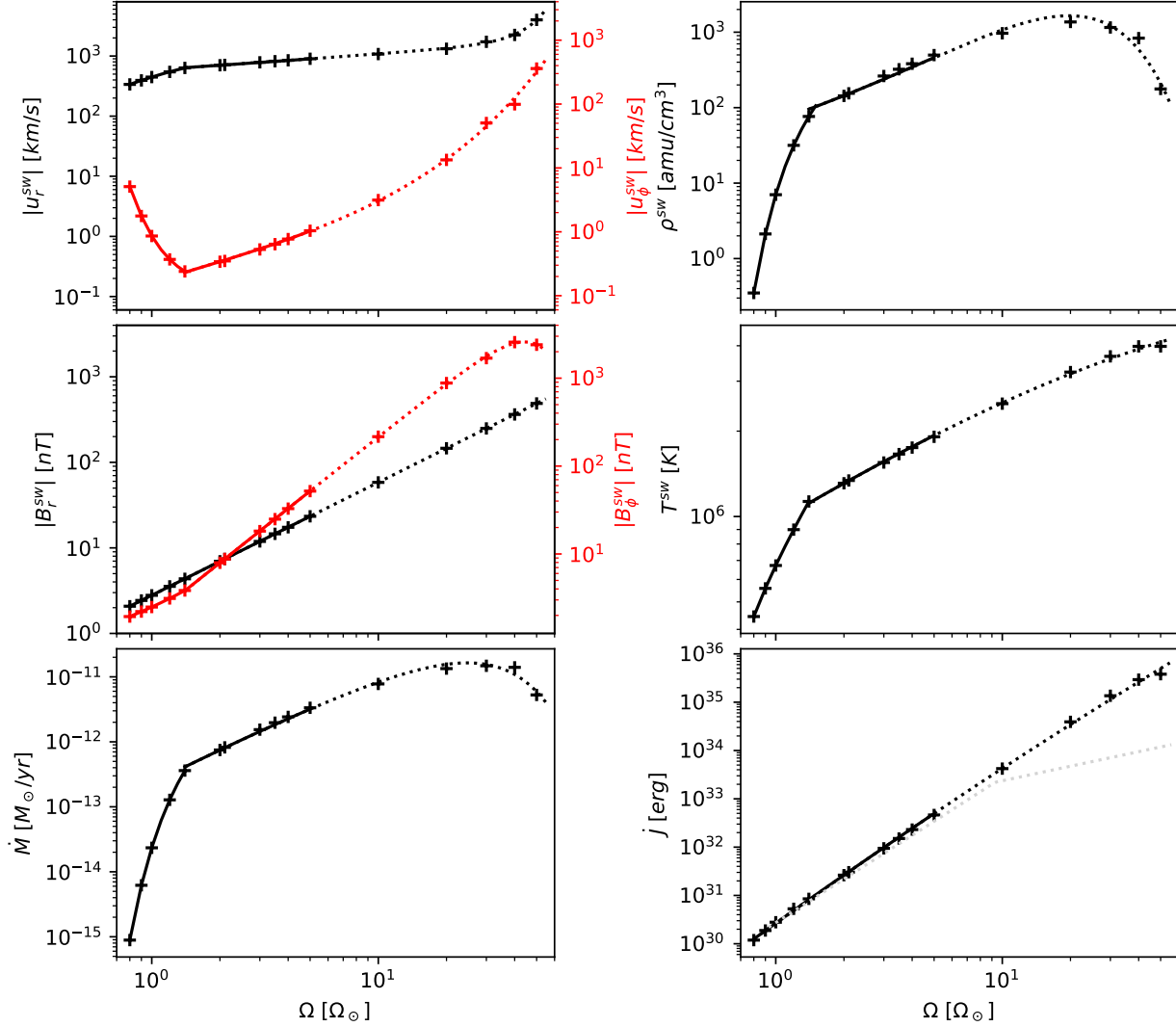


Figure 2.1: Stellar wind local velocity, density, magnetic field and temperature at 1au, and mass and angular momentum loss rate profiles for stellar rotation rates from $0.8 \Omega_{\odot}$ to $50 \Omega_{\odot}$. Fits are shown in black and red (when an azimuthal component is shown in the same panel). The crosses mark the results of a particular model and are also listed in table 2.1. To represent the uncertainty of whether the Sun would have rotated faster than $\sim 5\Omega_{\odot}$, part of the fits are shown as dotted lines. The grey dotted line in the last panel shows the break in angular-momentum loss rates one would expect if my models adopted saturation of the wind (see text for a discussion).

Table 2.1: The absolute magnitude of wind parameters for different stellar rotation rates Ω . The columns are: estimated age based on the rotation tracks from Gallet & Bouvier (2013), the mass- (\dot{M}) and angular momentum-loss rates (\dot{J}), the local radial and azimuthal components of the velocity ($u_r^{\text{sw}}, u_\phi^{\text{sw}}$), magnetic field ($B_r^{\text{sw}}, B_\phi^{\text{sw}}$), temperature (T^{sw}), proton number density (n_p^{sw}). \mathcal{M} is the local magnetosonic mach number and Ψ is the spiral angle of the wind. All the local quantities were computed at 1 au and are used as input in the 3D simulations of Earth’s magnetosphere.

Ω [Ω_\odot]	Age [Myr]	\dot{M} [M_\odot/yr]	\dot{J} [erg]	u_r^{sw} [km/s]	u_ϕ^{sw} [km/s]	B_r^{sw} [G]	B_ϕ^{sw} [G]	T^{sw} [$\times 10^5$ K]	n_p^{sw} [cm^{-3}]	\mathcal{M}	Ψ [$^\circ$]
0.8	7700	8.9×10^{-16}	1.2×10^{30}	337	5.1	2.1×10^{-5}	1.9×10^{-5}	4.4	0.35	2.5	47
0.9	6500	6.2×10^{-15}	1.9×10^{30}	393	1.8	2.4×10^{-5}	2.2×10^{-5}	5.6	2.1	3.6	48
1.0	5000	2.3×10^{-14}	2.8×10^{30}	446	0.86	2.8×10^{-5}	2.5×10^{-5}	6.7	7.0	4.0	48
1.2	3100	1.3×10^{-13}	5.3×10^{30}	545	0.37	3.5×10^{-5}	3.1×10^{-5}	9.0	32	4.3	49
1.4	2100	3.6×10^{-13}	8.5×10^{30}	634	0.24	4.4×10^{-5}	3.8×10^{-5}	11	76	4.5	49
2.0	1100	7.5×10^{-13}	2.6×10^{31}	702	0.34	7.0×10^{-5}	7.9×10^{-5}	13	143	4.6	41
5.0	40 – 440	3.3×10^{-12}	4.6×10^{32}	900	1.0	2.3×10^{-4}	5.2×10^{-4}	19	497	4.7	24
10	≤ 280	7.8×10^{-12}	4.2×10^{33}	1078	3.1	5.8×10^{-4}	0.0022	25	968	4.1	15
30	≤ 140	1.5×10^{-11}	1.4×10^{35}	1723	50.5	0.0025	0.017	37	1154	1.5	8
50	≤ 100	5.3×10^{-12}	3.8×10^{35}	3994	360	0.0049	0.024	40	177	0.99	11

2. THE EVOLUTION OF EARTH'S MAGNETOSPHERE

the magnetosonic mach number \mathcal{M} (as discussed in chapter 1). \mathcal{M} determines the strength of the shock. Given that a shock is only present around the Earth if $\mathcal{M} > 1$, I note a surprising result that, at rotation rate of $50\Omega_{\odot}$, my models do not predict the presence of a shock around the Earth. As we will see next, it is uncertain whether the Sun rotated that fast. If that indeed occurred, it happened only for a short amount of time, relative to the Sun's lifetime, and at an age $\lesssim 100$ Myr. We discuss age determination and the rotation-age relation next.

2.2.2 The Rotation Rate Of The Young Sun

To mimic the ageing Sun, I use rotation as a proxy for age, and compute stellar wind models at different rotation rates from $0.8\Omega_{\odot}$ to $50\Omega_{\odot}$. However, here, I am very careful at assigning an age to my models as the age-rotation relationship is only well constrained for stars older than ~ 800 Myr. Figure 2.2 shows the rotation evolution tracks for a $1M_{\odot}$ star during the main-sequence phase, extracted from the work of Gallet & Bouvier (2013). These tracks are the upper/lower envelopes of the observed rotation distributions from open clusters and they indicate the evolution of a slowly-rotating (red-dashed line) and a fast-rotating (solid blue) star. The convergence of the slow and fast rotator tracks happens at around ~ 800 Myr, after which, I can assign an age to a star from observed rotation rates (this forms the basis of the gyrochronology method Barnes 2003).

The symbols in figure 2.2 represent the selected rotation rates of which I perform simulations. As can be seen, for $\Omega \lesssim 2 \Omega_{\odot}$, there is a unique function between age and rotation and thus I can assign an age to the solar wind models. However, for $\Omega \gtrsim 2 \Omega_{\odot}$, there are ambiguities in age determination. For example, for the model with rotation rate of $5 \Omega_{\odot}$ (open symbols, connected by a dotted line), possible ages range from 40 to 440 Myr, depending whether the Sun used to be a slow or a fast rotator, respectively. Note that the Sun would only have rotated faster than $\sim 5 \Omega_{\odot}$, if it were not born as a slow rotator. Because of this, it is only possible to assign an upper limit on the age for the models with a given rotation rate $\gtrsim 2 \Omega_{\odot}$. For that, I assume that the Sun was in the fast rotator track. These age estimates and upper limits are listed in table 2.1 for each of the simulated rotation rates.

Given that we are unsure whether the Sun indeed rotated faster than $\sim 5 \Omega_{\odot}$, the computed quantities associated to these rotation rates are represented as dotted lines in

figure 2.1. The very fast rotating young Sun (30 and $50 \Omega_{\odot}$) will be discussed in section 2.6.

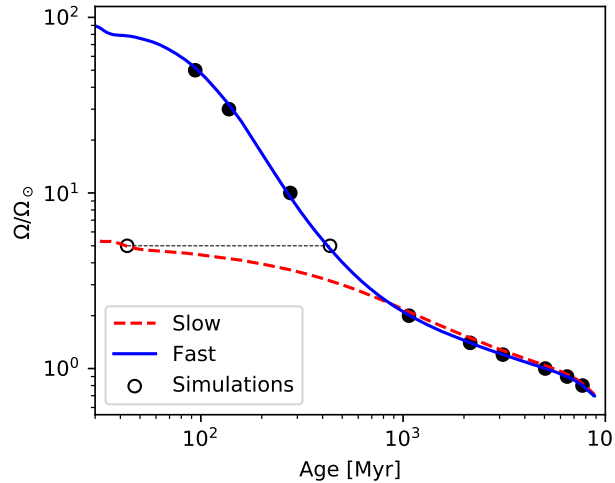


Figure 2.2: The evolution of stellar rotation rate (Ω) from Gallet & Bouvier (2013), for a $1 M_{\odot}$ star. The blue solid line tracks the evolution of a fast rotating solar like star, while the dashed red line tracks the slow rotator. The black points mark the values of Ω adopted in my simulations. The fast and slow models give a well constrained age for the $\lesssim 2.0 \Omega_{\odot}$ models. For higher rotation rates, ages are more uncertain. For example, the Sun could have rotated at $5 \Omega_{\odot}$ at any age between 40 and 440 Myr, depending whether it was a slow to fast rotator (connected by a dashed black line). Note that the Sun would only have rotated faster than $\sim 5 \Omega_{\odot}$, if it were not born as a slow rotator.

2.2.3 Global Properties Of The Young Solar Wind

In addition to the local conditions (at 1au) of the solar wind in time, I also present in the bottom panels of figure 2.1 and table 2.1 two global quantities of stellar winds: the mass-loss rate and the angular-momentum loss rate, discussed in chapter 1.

Mass-loss rates of solar type stars are challenging to derive from observations. The most successful technique to date has been the astrospheric Ly- α absorption (Wood et al., 2014, 2005), which has derived mass-loss rates for about a dozen stars. This technique has shown that mass-loss rates increase with X-ray fluxes (F_x), which also increase with Ω . For ages $\gtrsim 1000$ Myr ($\leq 10 \Omega_{\odot}$), the mass-loss rates of my models are very similar to those predicted by Wood et al. (2014). For example, my models predict that the Sun had a mass-loss rate of $7.5 \times 10^{-13} M_{\odot}/\text{yr}$, or about 40 times the present-day solar mass-loss

2. THE EVOLUTION OF EARTH'S MAGNETOSPHERE

rate, at a rotation rate of $2\Omega_{\odot}$. At a similar rotation rate, Wood et al. (2002) found that the star ϵ Eri shows a mass loss rate of $\sim 6 \times 10^{-13} M_{\odot}/\text{yr}$, similar to the value I find in my models.

For $F_x \gtrsim 10^6 \text{ erg cm}^{-2} \text{ s}^{-1}$, i.e., above approximately $15 \Omega_{\odot}$, Wood et al. (2014) predicted a break in the $\dot{M}-F_x$ relation, arguing that mass-loss rates of a very young Sun (high F_x) could actually have been very low ($\sim 10^{-14} M_{\odot}/\text{yr}$). This break, however, has been difficult to explain with other observations (e.g., Vidotto et al., 2016), and theoretically (e.g. Holzwarth & Jardine, 2007; See et al., 2014). It has been suggested that the low mass-loss rates of the ‘outlier’ stars in Wood’s sample (π^1 UMa, ξ Boo A) do not follow the $\dot{M}-F_x$ relation due to scattering, and that the relation between mass-loss rates and activity could extend to higher X-ray fluxes without a break (Jardine & Collier Cameron, 2019), albeit with some scatter. Recent studies of Wood et al. (2021) indeed point in the direction that this break does not exist.

Jardine & Collier Cameron (2019) estimated that AB Dor, a widely used proxy for the young Sun, has mass-loss rate $7 \times 10^{-12} M_{\odot}/\text{yr}$. With a rotation period of ~ 0.5 day, or $54\Omega_{\odot}$, their derived mass-loss rate is surprisingly similar to my $50\Omega_{\odot}$ model ($5.3 \times 10^{-12} M_{\odot}/\text{yr}$). Another clue that fast-rotating stars might actually have stronger stellar winds is that when we go to even younger stars (not studied in this chapter), mass-loss rates are observed to be $\sim 10^{-10}$ to $10^{-12} M_{\odot}/\text{yr}$ in the weak T Tauri phase, after disc clearing (Vidotto & Donati, 2017). Naively, one would expect that the wind of a young sun would have mass-loss rates that are intermediate between those of weak T Tauri stars and the current solar value. Altogether, these facts give support to the relatively high mass-loss rates, reaching $10^{-11} M_{\odot}/\text{yr}$, I obtain for very fast rotating Suns.

Our model, however, does not include saturation on the mass-loss rate nor on magnetic field at high rotation rates¹. Saturation is required to explain the spin down of the very fast rotators (e.g. Matt et al., 2015; Johnstone et al., 2015b). When considering saturation,

¹Although I do not impose a saturation in mass-loss rate, my models show a ‘levelling off’ of mass-loss rate for $\Omega \gtrsim 20\Omega_{\odot}$ (cf. the bottom left panel of figure 2.1). This inflection is more clearly seen in the local densities (top right panel of figure 2.1). Although the base densities are larger for larger rotation rates, the decrease in wind density with distance is steeper for $\gtrsim 20\Omega_{\odot}$. In the limit where the wind reaches terminal velocity, the density should fall with r^{-2} . The steeper decrease is thus an indication that the wind is still being accelerated for $\Omega \gtrsim 20\Omega_{\odot}$ at 1 au. In fact, I note that in these cases, the local magnetocentrifugal force (at 1au) is comparable or greater than the thermal pressure gradient in the wind radial momentum equation. Beyond $\gtrsim 20\Omega_{\odot}$, the thermal pressure gradient ceases to be the dominant force in my models.

the wind angular momentum-loss rate presents a break with Ω , which is illustrated by the grey dotted line in the bottom right panel of figure 2.1. This curve is from See et al. (2018), which is based on the torque formalism of Matt et al. (2015, I divided their curve by 2.9 to match the solar value). I note that for $\Omega \lesssim 10\Omega_{\odot}$, their trend is similar to ours, roughly obeying a cubic dependence with Ω . However, for $\Omega \gtrsim 10\Omega_{\odot}$, saturation requires an approximately linear dependence between \dot{J} and Ω , which is not seen my model.

2.3 Magnetosphere Model

To simulate Earth’s magnetosphere and its surrounding bow shock in a given stellar wind, I use the base 3D MHD model described in section 1.6. The wind is injected into the computation domain at a distance of $20 R_p$ on the dayside of the planet, as shown in figure 2.3. For the planetary parameters, I use present day values for magnetic dipole strength ($B_0 = -0.3$ G); radius ($R_p = 6.3 \times 10^8$ cm); and mass (5.976×10^{27} g) in my models. I assume that the Earth’s geodynamo has not changed during this evolution, although some works suggest that Earth’s dipolar field strength might have been 50% smaller ~ 3.5 Gyr ago (Tarduno et al., 2010). I discuss the effects that the hypothesis has on my simulations later in this chapter.

Since we are considering the dayside of the planet in this chapter, I choose a cubic grid of length $32 R_p$ ($x = [-44, 20] R_p$; $y = z = [-32, 32] R_p$) as seen in figure 2.3. The x axis points towards the star and the z axis is oriented perpendicular to the ecliptic plane. The y axis constructs the right-handed system. My simulations have a maximum resolution of $1/32 R_p$ within a radius of $5 R_p$, which gradually decreases to a minimum resolution of $2 R_p$ at the edges of the grid. I can achieve this high resolution by sacrificing grid space on the night side of the planet. I tested the effects of numerical resolution, by changing the highest resolution from $1/32 R_p$ to $1/64 R_p$ and $1/128 R_p$ at the inner regions of my simulations. I found no significant change in the position of pressure balances (used to identify the magnetopause) and so in this chapter, I present the results for the case of $1/32 R_p$. With this resolution, these simulations contain 22.6 million cells.

The inner boundary is set at $1R_p$ in my simulations. I chose values for base density (10 amu/cm^3), temperature (25000 K) and thermal pressure ($3.45 \times 10^{-11} \text{ dyn/cm}^2$) that are appropriate for the current ionosphere. Note that the ionospheric structure is not computed in my models. Since we are interested in the interaction region of the magne-

2. THE EVOLUTION OF EARTH'S MAGNETOSPHERE

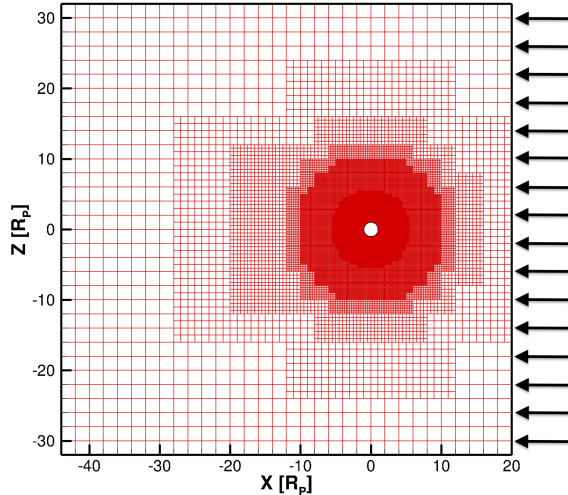


Figure 2.3: The refinement grid used in my models. A maximum resolution of $1/32 R_p$ is used within a radius of $5 R_p$, which slowly decreases outwards by a factor of 2 at each step as seen above. The arrows visualize the injection of the stellar wind into this domain.

tosphere with the stellar wind, which happens significantly above the planet, the values of pressure and density have no effects on the dynamics of the interaction (for example, for different values of density, I see no change in the position of thermal-magnetic and thermal-ram pressure balances). The boundary assumes that the density at $1R_p$ is fixed, and the magnetic field and thermal pressure have outflow conditions. The velocity vector is reflected upon reaching this boundary in the frame corotating with the planet. The outer boundary assumes an outflow of all parameters. Earth's rotation is kept at 1 day for all the simulations.

I align the magnetic axis of the Earth with the rotational axis, which is 23.5° inclined with respect to the orbital plane. All the simulations are thus at summer solstice. Presently, the Earth's magnetic axis is misaligned by $\sim 11^\circ$ to the rotational axis. However, as the magnetic tilt can vary on relatively short timescales compared to the evolutionary times considered here, and given that we do not know precisely how this variation would have occurred in the distant past, I chose to neglect the misalignment between magnetic and rotation axes in this chapter. The radial velocity u_r^{sw} of the solar wind is injected along the negative x direction in this coordinate system. u_ϕ^{sw} is aligned with the negative y direction such that the simulated 1.5D winds act in the xy plane. Note that I assume $B_r^{\text{sw}} > 0$. Hence $B_\phi^{\text{sw}} < 0$ in the stellar reference frame due to the trailing nature of the Parker spiral.

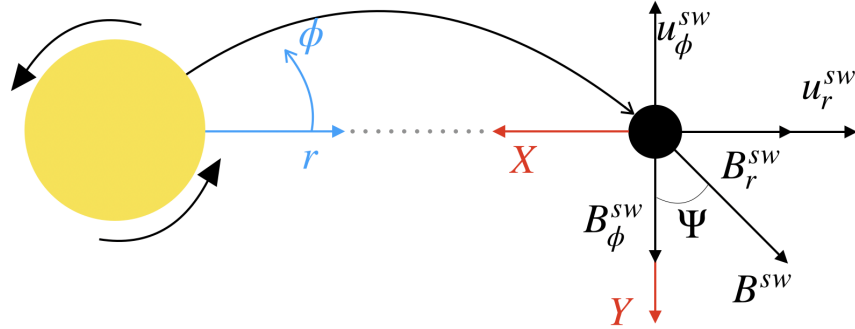


Figure 2.4: Illustration of how the stellar winds are oriented in my grid. The black circle represents the Earth, while the yellow represents the Sun. The magnetic and velocity vectors are drawn in the inertial frame of the star. The blue vectors show the stellar coordinate system, while the red show the orientation of the planetary coordinate system. Z constructs the right handed system, with the origin placed at the centre of the planet.

This is illustrated in figure 2.4.

As $u_r^{sw} \gg u_\phi^{sw}$ the wind is mainly radial at 1 au. This orientation yields a solar wind which enters the domain through the day-side of the box seen in figure 2.3 where it interacts with the planet's magnetic field. Once the wind reaches the magnetic field of the planet, it is shocked which is visualized in figure 2.5 by the density slice in the xy plane. The magnetic field from the planet deflects most incoming material.

As stellar rotation is a proxy for age (Skumanich, 1972), here I choose to sample 10 stages in the solar wind's evolution spanning a range of stellar rotation rates from $0.8\Omega_\odot$ to $50\Omega_\odot$ as seen in table 2.1, where Ω_\odot is the present day solar rotation rate. An example of a low and high stellar rotation model are shown in figure 2.6.

Here I examine how the dayside of Earth's magnetosphere varies in time, mainly focusing my analysis along the x axis in each of my 3D models (towards the star).

2.4 The Magnetopause

There are three main contributors to the total pressure in my models: thermal ($P_T = n_p k_B T$); magnetic ($P_B = B^2/8\pi$); and ram pressure ($P_{\text{ram}} = \rho u_r^2$). To examine which contributor dominates at a certain distance from the planet, these have been separated

2. THE EVOLUTION OF EARTH'S MAGNETOSPHERE

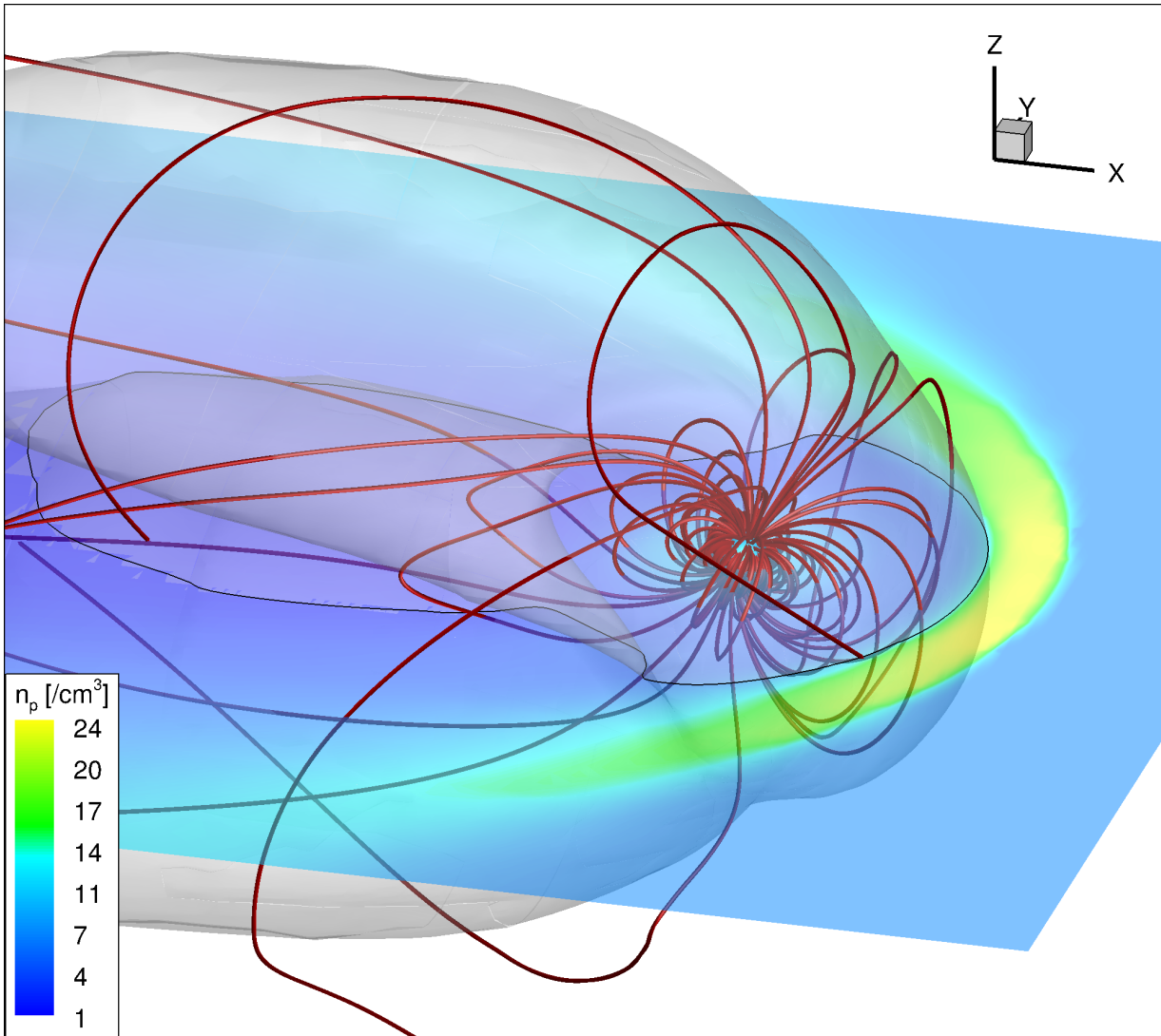


Figure 2.5: A 3D image of the Earth considering the star is rotating at $1.0 \Omega_{\odot}$. Red lines represent the magnetic field lines connected to the planet. The slice shows the density around the planet in the orbital plane. The surface marks a the boundary of the magnetosphere.

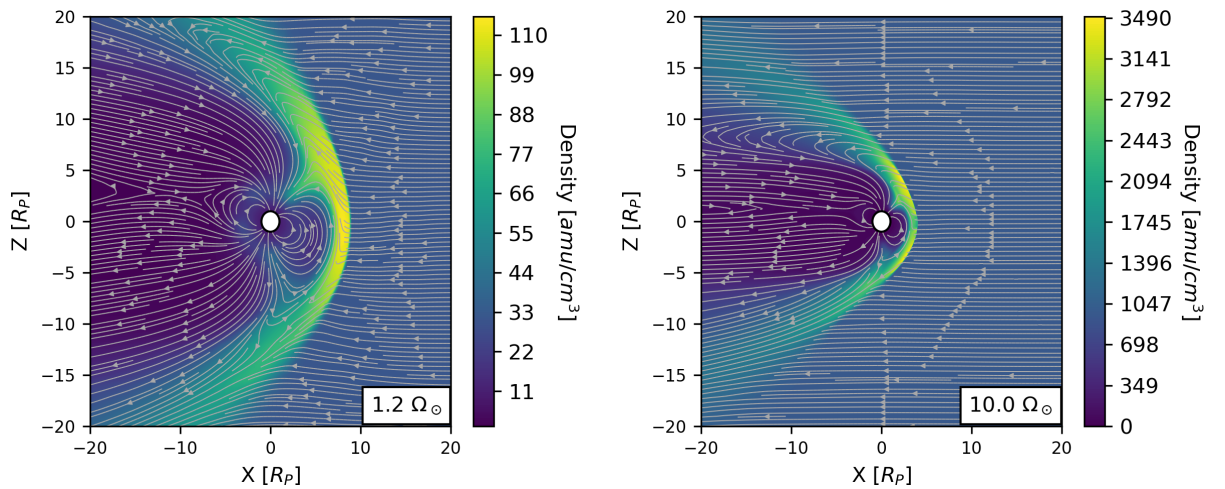


Figure 2.6: Earth’s magnetosphere for 2 different values of stellar rotation: $1.0 \Omega_{\odot}$ and $10 \Omega_{\odot}$. For each model the density distribution in the X-Z plane is shown as a colour. The streamtracers show the magnetic field lines, illustrating the magnetospheres in my models.

and plotted alongside density in figure 2.7, for two representative cases: low ($1.2 \Omega_{\odot}$) and high ($10 \Omega_{\odot}$) stellar rotation.

For both high and low stellar rotation rates, I see similar trends in the thermal, magnetic, and ram pressures. Inside the magnetosphere, magnetic pressure dominates due to the strong magnetic field of the planet. In the stellar wind, we see the dominant component is the ram pressure due to the high density, much higher velocity, and relatively low magnetic field and thermal components in the wind.

When the stellar wind is shocked, the majority of ram pressure is converted to thermal pressure (Cravens, 2004). In my models, this fraction is 75%. In the shock the velocity of the wind drops by a factor of 4 and the density increases by a factor of 4, for models with stellar rotation $< 10 \Omega_{\odot}$, which exhibit strong shocks.

The Chapman-Ferraro equation (equation 1.42) neglects the extent of the shock. It balances the magnetic pressure on the left side (inside magnetosphere) with the ram-pressure on the right side (in the stellar wind). In my simulations we can see that this transition is mediated by the presence of a finite shock (the magnetosheath), dominated by thermal pressure. The magnetopause standoff distance is marked by the point on the x axis where the magnetic and thermal pressures are balanced. Similarly, to identify the bow shock standoff distance I use the balance of thermal and ram pressures. These distances for the $1.2 \Omega_{\odot}$ model are marked in figure 2.7 and 2.8. We can see that the magnetopause

2. THE EVOLUTION OF EARTH'S MAGNETOSPHERE

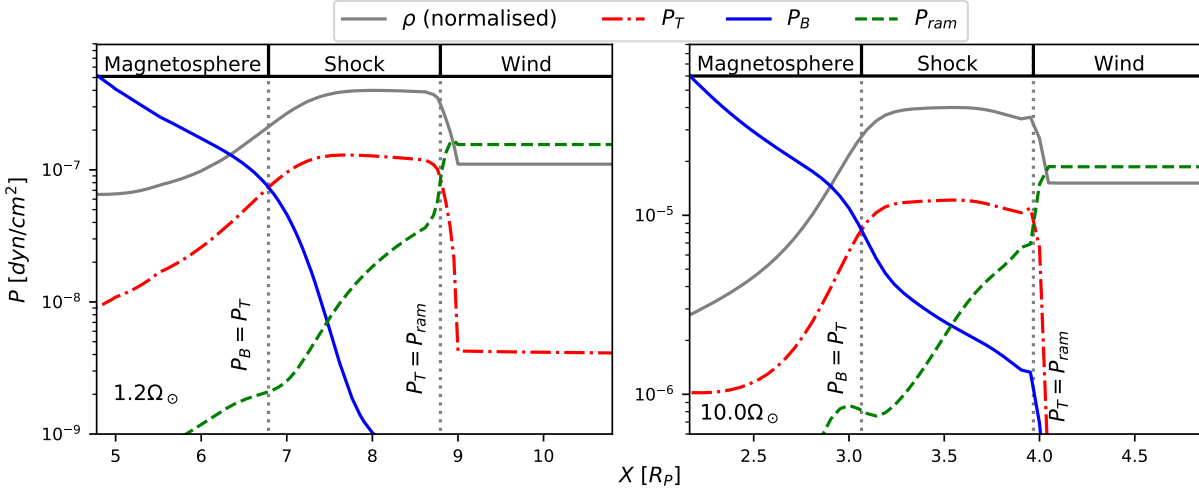


Figure 2.7: The variation of thermal, magnetic and ram pressures on the day side of the planet towards the star for the $1.2 \Omega_{\odot}$ and $10 \Omega_{\odot}$ models. The grey vertical dotted lines mark the points where thermal-magnetic and thermal-ram pressure balances occur, which represent the magnetopause and bow shock standoff distances. This allows for the size of the magnetosphere and magnetosheath to be established. The solid blue lines are the magnetic pressure, the dot-dashed red are the thermal pressures and the dashed green are the ram pressures.

corresponds to a local minimum in the velocity magnitude, with a density cavity just inside this. This cavity is carved by the large closed magnetic field lines in this region, which lead shocked material away.

As faster rotating stars are more active, they have stronger stellar winds, so we can expect a faster rotator to induce a smaller magnetosphere around the Earth. This is seen in figure 2.8, as we see a gradual decrease in standoff distance. There is a break in the trend of standoff distance with stellar rotation at approximately $1.4 \Omega_{\odot}$. This is due to how the base temperature of the wind is specified in equation 2.1, which is given by a piece-wise function about $1.4 \Omega_{\odot}$. To find a relation in terms of Ω I fit the data using a piece-wise function. I find the standoff distance varies with Ω according to equation 2.4.

$$r_M \propto \begin{cases} \Omega^{-2.04} & \Omega < 1.4\Omega_{\odot} \\ \Omega^{-0.27} & \Omega \geq 1.4\Omega_{\odot} \end{cases} \quad (2.4)$$

In my models, I adopted a dipolar field strength of the Earth that is constant in time (the same value across all my simulations). However, from analysis of single silicate

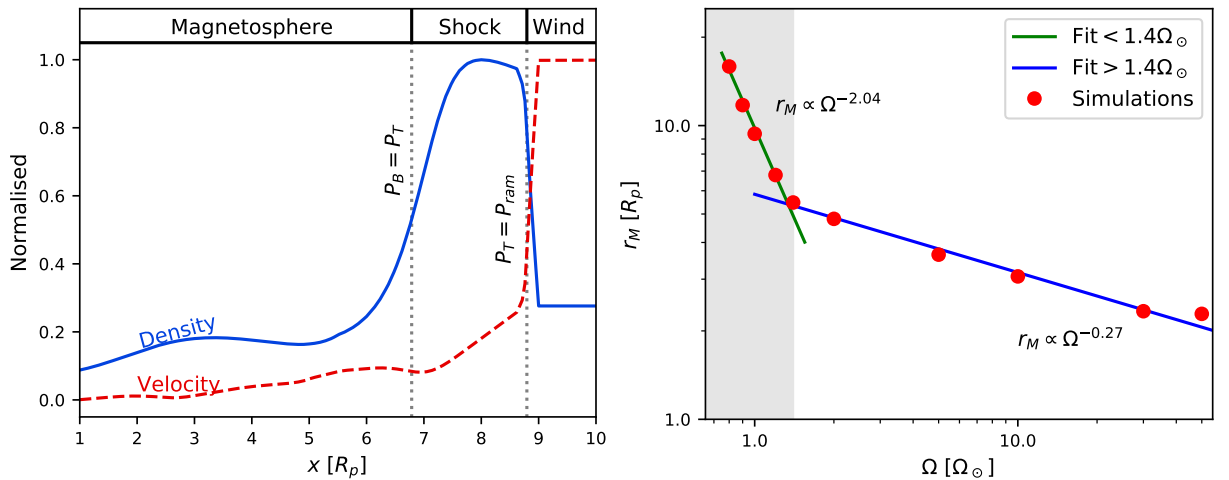


Figure 2.8: Left : The variation of normalized velocity magnitude and density towards the star in the $1.2 \Omega_\odot$ model. This verifies the pressure balance method for establishing the standoff distance and magnetosheath thickness from my models. **Right:** The variation in standoff distance with Ω for all magnetosphere models. As was seen in the stellar wind models, I see a different trend in r_M with Ω around $1.4 \Omega_\odot$. My fits are shown with the green line ($< 1.4 \Omega_\odot$) and blue line ($\geq 1.4 \Omega_\odot$), with the gray region marking the lower Ω domain.

crystals bearing magnetic inclusions, Tarduno et al. (2010) found that when the Earth was approximately 1 Gyr old, its magnetic dipole strength was lower than it is today, within the range from 0.5 to 0.7 times the present-day value. Zuluaga et al. (2013b) modelled the change in planetary dipole moment with time, suggesting that the magnetic field strength of the Earth averaged over its evolution is approximately 90% of its current value (i.e., during most of its evolution, the magnetic moment of the Earth has not changed). Given that r_M depends very weakly on the field strength ($r_M \propto B_0^{1/3}$), the evolving dipole moment would contribute a mean change of 3% to r_M over the magnetosphere’s evolution, when compared to models using present day values at all ages. Additionally, as can be seen in the piece-wise-function (equation 2.4), which has the same break seen in the assumption of stellar wind temperature, the variation in magnetospheric size is much more sensitive to the changing stellar wind than what would be expected due to an evolving planetary dipole (see also Ó Fionnagáin & Vidotto, 2018).

As was discussed in section 2.1, the shape and size of the magnetosphere has important implications on atmospheric loss. The area on the planet connected to open magnetic field lines determines the extent to which stellar wind material can reach the planet (henceforth referred to as “impact”). If this area is large, a greater amount of stellar wind material will

2. THE EVOLUTION OF EARTH'S MAGNETOSPHERE

Table 2.2: Properties of the magnetopause extracted from my simulations: the size of the magnetopause (r_M), calculated along the X axis, and the colatitude Φ of the last open field line on the dayside, which is calculated from the rotational axis of the planet (23.5° from the ecliptic).

Ω [Ω_\odot]	r_M [R_p]	Φ [$^\circ$]
0.8	15.9	11.1
0.9	11.7	10.2
1.0	9.4	10.3
1.2	6.8	10.5
1.4	5.5	11.3
2	4.8	12.1
5	3.6	13.4
10	3.1	17.1
30	2.4	26.2
50	2.3	31.8

impact the atmosphere, which could induce atmospheric loss. If this area is small, there are a greater number of closed field lines, which can collect stellar wind plasma and focus it onto the atmosphere (henceforth referred to as “collection”), which can also cause the same effect of enhancing atmospheric loss (Blackman & Tarduno, 2018).

Which of these two competing mechanisms (impact vs collection) causes more harm to the planet over its lifetime is currently still in debate. I do not model atmospheric loss here. However from my models we can examine the area on the planet connected to open field lines, which is quantified by the colatitude Φ of the last open field line on the dayside of the North pole in the xz plane. These are given in table 2.2.

In the young system, the area covered by open-field lines is much larger than for lower stellar rotation rates. This increased area could lead to a higher rate of stellar wind impact than in an old system. With the stellar wind gradually relaxing, the difference between young and old systems is further enhanced. As the magnetosphere is small in the earlier stages of the Earth’s evolution and the area of open field lines is large, we can expect that stellar wind impact will dominate over plasma collection in the young systems.

As the Sun spun down, this area gradually decreased, with a colatitude of open field lines of approximately 10.3° obtained for present day. Analytically, the colatitude of open field lines can be found from the magnetopause standoff distance through the following expression (Vidotto et al., 2013):

$$\Phi^{\text{analyt}} = \arcsin \left(\sqrt{\frac{R_p}{r_M}} \right). \quad (2.5)$$

Using this expression, I find $\Phi = 18.8^\circ$ for the present day, using r_M from my models. This value is significantly higher than what I obtain from my simulation. I attribute this difference to the orientation of the magnetic fields in the system.

With the magnetosphere gradually growing in size, the stellar wind gradually relaxing and the area of open field lines decreasing, it is clear that the amount of stellar wind inflow will decrease with time. Contrary to this, the collecting area for stellar wind plasma will increase through Earth's evolution, as the magnetospheric size and area covered by closed field lines increases. It is clear that of the two competing effects, stellar wind inflow will dominate in the young system, whilst plasma collection will dominate at old ages.

2.5 The Bow Shock And Magnetosheath

As outlined by Spreiter et al. (1966); Gombosi (2004); Balogh & Treumann (2013), the bow shock distance (r_{BS}) is related to the magnetopause standoff distance according to the following relation:

$$r_{BS} - r_M = \Delta r \approx 1.1 \frac{N_2}{N_1} r_M, \quad (2.6)$$

where the density compression factor $\frac{N_2}{N_1}$ (ratio of the density in front of the shock, and that in the shock) is given by the inverse of the equation below

$$\frac{N_1}{N_2} \approx \frac{\gamma + 1}{\gamma - 1} - 2 \frac{\gamma + 1}{\mathcal{M}^2(\gamma - 1)^2}, \quad (2.7)$$

In a strong shock this ratio is approximately 4, as the Mach number is large so the second term may be neglected. Using the above equations, a strong shock produces a magnetosheath thickness should be $0.275 r_M$ (Gombosi, 2004). This includes models with stellar rotation $\leq 10 \Omega_\odot$. Using the above relation we can predict the expected bow shock distance and compare this to what I obtain in my simulations.

The relationship between bow shock distance and standoff distance can be rationalized by considering the pressures and forces on the shocked material. On the planet-side of the

2. THE EVOLUTION OF EARTH'S MAGNETOSPHERE

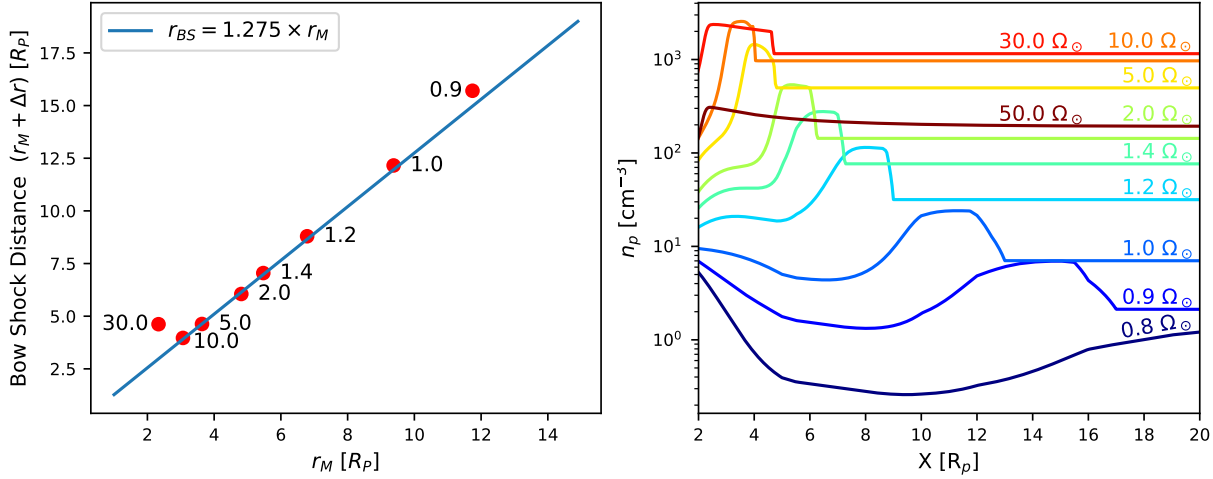


Figure 2.9: Left: The obtained bow shock distance (standoff distance + magnetosheath thickness) vs each magnetosphere standoff distance. We see the results from my models follow closely Equation 2.6 for a strong shock $\mathcal{M} \gg 1$. **Right:** Variation of density on the dayside of the planet, towards the star (X axis) for different values of stellar rotation Ω . This shows the relative change of density through each of my models, as well as illustrating the Rankine-Hugoniot shock conditions followed in my models (increase by factor of 4 in density).

star-planet line, the magnetic field of the planet is exerting a force on the shocked material directed away from the planet. On the star side, the wind is exerting a force directed in the opposite direction, as the wind particles that impact shocked material are themselves shocked. For the standoff distance to be smaller, the stellar wind ram pressure must be stronger. As a result, both the ram pressure and the magnetic pressure will be stronger as the shock is closer to the planet. Therefore the net force acting on the bow shock will act to reduce the thickness of the shock for a lower standoff distance. For a weaker wind the opposite effect is achieved.

In my models, a strong correlation between the bow shock distance and the prescribed relation in equation 2.6 for the strong shock ($\mathcal{M} \gg 1$) is found in the $< 10 \Omega_\odot$ models. This confirms that as the host star spins down during the main sequence the magnetosphere and magnetosheath both increase in size proportional to the piece-wise function in equation 2.4 for the majority of its evolution. The $30 \Omega_\odot$ model deviates from this trend. This is due to the weaker shock exhibited in this model, which is discussed in section 2.6.

Figures 2.6 and 2.8 show that the magnetosphere standoff distance moves closer to the planet for higher stellar rotation (stronger winds). As well as this I see a general decrease in thickness of the bow shock for higher values of Ω , as seen in figure 2.9, and an increase

2.5 The Bow Shock And Magnetosheath

in peak density up to $30 \Omega_{\odot}$ as seen in the right panel of the same figure. In this figure, we see the density distribution is constant at large x for different stellar rotation rates. This indicates the extent to which the stellar wind penetrates into the computational grid. There is a jump in density closer to the planet, signifying the formation of a bow shock. For most of my models these shocks follow the Rankine-Hugoniot jump conditions, which predict for an adiabatic shock a factor of 4 increase in density. The exceptions to this are the $30 \Omega_{\odot}$ and $50 \Omega_{\odot}$ models, exhibiting a weaker and no shock respectively. This is discussed in section 2.6.

In the case of large magnetospheres (lower stellar rotation) my models contain a low density cavity within the magnetosphere. To understand why this occurs I compare the density and velocity magnitude in the model, as seen in figure 2.8. This minimum in density occurs at the point where the velocity magnitude is at a local maximum. This region corresponds to where some of the largest closed magnetic field lines from the planet exist, seen in figure 2.6. The top panels of figure 2.10 shows the dominant components of velocity in this region are positive u_r and negative u_{θ} . (In the higher Ω models, u_{ϕ} begins to become significant). On the boundary of the magnetopause, the u_{θ} component is at a maximum magnitude. Along the x axis this corresponds to the z direction, which is perpendicular to the orbital plane of the planet in this instance. The high u_{θ} velocity here shows that the magnetic field lines lead a significant amount of material away. Just inside this region, the positive u_r component is moving material away from the planet and towards the sweeping θ component. As a result there is an under-density in this region. Figure 2.10 shows that the u_{ϕ} component is relatively negligible along the subsolar line. Finally outside the bow shock I can see u_r is at a maximum, which is to be expected as the stellar wind is mostly radial.

Across the shock, we see little variation in the radial component of the magnetic field (figure 2.10, bottom panel). In the B_{ϕ} component however we see a small shock-like behaviour in both low and high stellar rotation models, with an overall increase of a factor of 4 (adiabatic shock).

The largest variation in the magnetic field is observed in B_{θ} . Just inside the magnetosphere, this component is strong and positive, corresponding to a northward (positive z) direction of the dipolar field. This corresponds to the largest closed field lines in the x - z plane, which at this point on the x axis will be oriented in the positive z direction. This is true for all models. Through the bow shock, there is a steep decrease in this B_{θ} component

2. THE EVOLUTION OF EARTH'S MAGNETOSPHERE

for both high and low rotation models. This illustrates how the magnetic field lines across the magnetopause transition from closed to open field lines in the x-y plane.

The middle panel in figure 2.10 shows two notable trends in current, which are similar in both low and high Ω models. The j_ϕ component shows the “Chapman-Ferraro” current, also known as the magnetopause current. This current separates the shocked magnetosheath from the relatively empty magnetopause. This prevents the terrestrial dipole field from penetrating into the solar wind (Gombosi, 2004). At the boundary between the magnetopause and bow shock, there is a strong negative j_θ component. At the boundary between the stellar wind and bow shock, the j_θ component is strong and positive. This can be explained by the variation in B_ϕ . This tangential component to the shock surface itself shows shock-like behaviour, transitioning from low values in the magnetosphere, to shocked values in the magnetosheath before returning to low in the stellar wind. This variation in B_ϕ generates a perpendicular current component, with a negative j_θ generated by the difference the magnetic field orientation and strength on opposite side of the magnetopause (B_θ dominated inside, B_ϕ dominated outside), and a positive j_θ when it decreases across the shock.

2.6 Very Fast Rotating Young Sun

It is not currently known how the rotation rate of the Sun varied at early ages. Recently, a study based on the composition of volatile elements in lunar samples from Saxena et al. (2019) suggested that the Sun would have been a slow rotator. These authors argue that slow rotators are expected to generate lesser amount of energetic particles through coronal mass ejections (CME) and thus would not completely deplete the sodium and potassium still seen in the moon regolith. To reach such a conclusion, the authors rely on a correlation between solar flares and CMEs (e.g., Aarnio et al., 2011), and extend it to younger Sun-like stars using observed flare frequencies from solar analogues. As a consequence, a slowly rotating (less active) young Sun would present less frequent CMEs than a fast rotating young Sun. However, there has been some suggestions in the literature that the solar CME-flare relation might actually over-predict the number of CMEs in younger and more active stars (Drake et al., 2013). In this case, a fast rotating Sun could actually have had a lower frequency of CMEs (or more ‘failed CMEs’, see Alvarado-Gómez et al. 2018) for its predicted flare rate at young ages. This could have an impact in the calculated sputtering

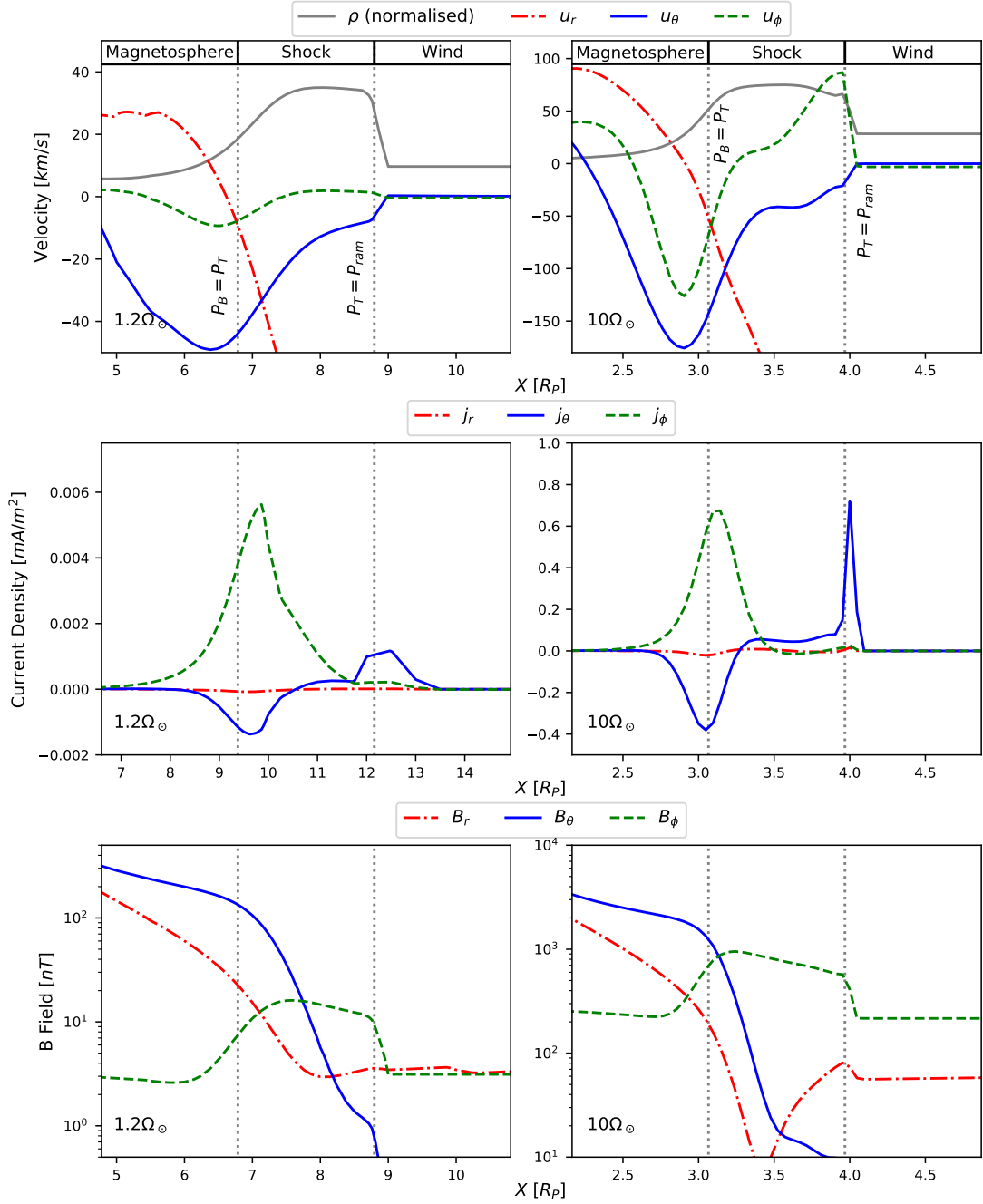


Figure 2.10: The variation velocity, current and B-field components along the x axis towards the star, for the $1.2\Omega_\odot$ and $10.0\Omega_\odot$ model. The grey vertical lines again mark the point where magnetic-thermal (left) and ram-thermal (right) pressures are balanced. The red dot-dashed line are the radial components, the solid blue are the θ components, and the dashed green are the ϕ components.

2. THE EVOLUTION OF EARTH'S MAGNETOSPHERE

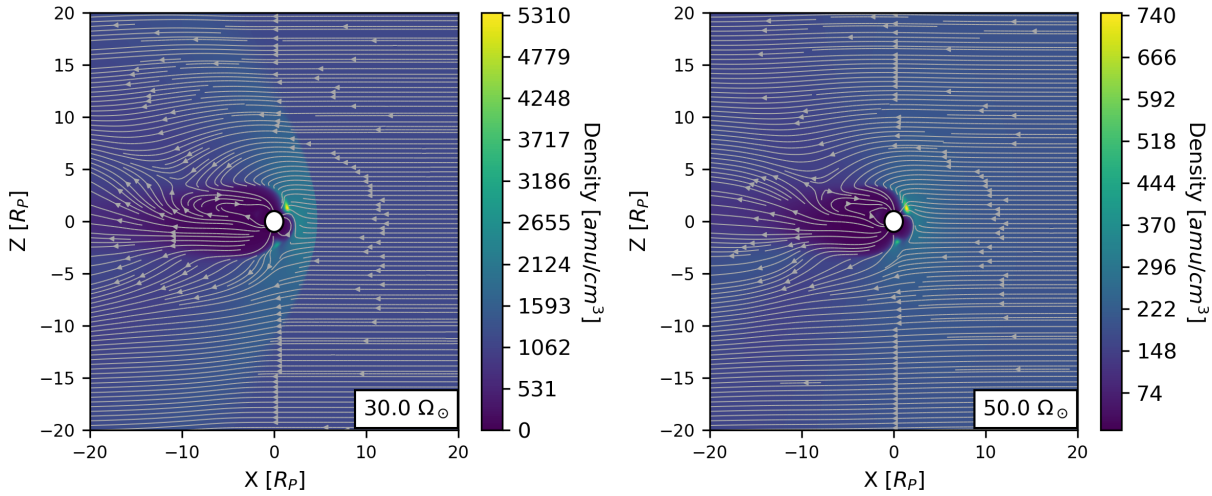


Figure 2.11: Earth’s magnetosphere in the wind of a very fast rotating young Sun. In the $30 \Omega_{\odot}$ model (left) we see a weaker shock than those in figure 2.6, with a comparably inflated magnetosheath. In the $50 \Omega_{\odot}$ model (right) there is no shock present, as the wind is submagnetosonic. Despite this, the magnetosphere is not completely crushed, though is reduced to a magnetopause standoff distance of $\approx 2.3 R_p$.

of volatile elements recorded in lunar data sample. Here, I speculate what would have happened to the Earth’s magnetosphere in the case that the young Sun was a fast rotator.

In the fast rotating regime it is possible for the young Sun to have a rotation rate as high as $100 \Omega_{\odot}$, while models of slow rotators suggest a maximum of approximately $5 \Omega_{\odot}$ (Gallet & Bouvier, 2013, see also figure 2.2). To understand the magnetosphere in the fast young system, I perform two additional simulations for stellar rotation rates of $30 \Omega_{\odot}$ and $50 \Omega_{\odot}$. The results of these models can be seen in figure 2.11.

In both of these models, the thermal pressure does not become large enough within the magnetosheath to balance either the magnetic or ram pressures, due to a weak shock for $30 \Omega_{\odot}$, and lack of shock for $50 \Omega_{\odot}$. We therefore cannot use the points of pressure balance to identify the magnetopause and bow shock standoff distances. Instead I use the j_{ϕ} current density as seen in figure 2.12. In all of my models, there is a positive j_{ϕ} component around the magnetopause. This is the Chapman-Ferraro or magnetopause current mentioned previously in this chapter. I use this current density to identify the position of the magnetopause in these fast rotating models. To identify the position of the bow shock in the $30 \Omega_{\odot}$ model, I use the point where ram pressure begins to dominate all other components.

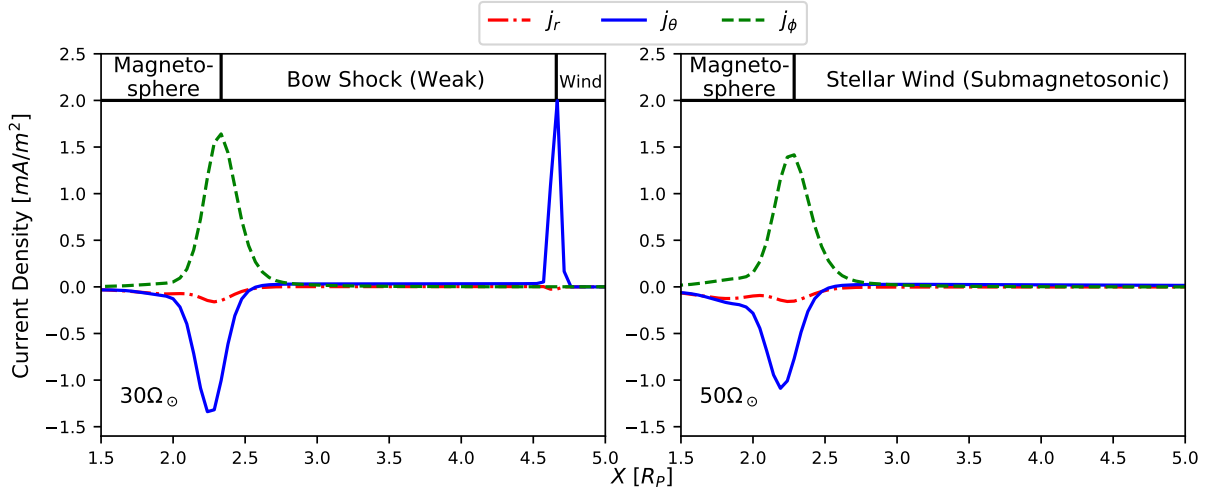


Figure 2.12: The current components along the subsolar line in the $30\Omega_\odot$ (left) and $50\Omega_\odot$ (right) models. The positive j_ϕ component is the magnetopause current, which is a current system flowing around the magnetosphere. The positive j_θ marks the position of the bow shock, and is generated from the change in magnetic field in the shock. As there is no shock in the $50.0\Omega_\odot$, this current density is not seen here.

Due to the lower magnetosonic Mach numbers (1.5 and 0.99 respectively), both these models exhibit some differences to those in figure 2.6. In the $30\Omega_\odot$ model there is a much weaker shock than for lower rotation rates. As a result the density jumps by only a factor of approximately 2 in the bow shock, whereas in the stronger shocks this factor was 4. Due to the larger N_1/N_2 compression ratio, resultant from the lower Mach number, the magnetosheath in this model is thicker than expected for a strong shock. This model therefore deviates from the expected equation for bow shock standoff distance shown in figure 2.9.

In the $50\Omega_\odot$ model, the wind is sub-magnetosonic so no bow shock is formed. However the magnetosphere still exists in this model, marked by the magnetopause current, and is not completely crushed. With the absence of a bow shock in this system, the magnetosheath thickness can no longer be quantified. These models suggest that if the Sun was a fast rotator, the young Earth would not have been surrounded by a bow shock. As the Sun spun down a weak shock would then form, followed by a strong shock for the remainder of the main sequence. The magnetopause would have had a minimum value of approximately $2.3 R_p$ in this system. For an intermediate or slow rotating Sun, the Earth would have been surrounded by a strong shock for the entirety of its evolution.

2.7 Conclusions

In this chapter, I studied the evolution of the Earth's magnetosphere over the main-sequence lifetime of our Sun (Carolan et al., 2019). The novelty of this work is that I coupled two sets of simulations: one to model the evolution of our solar wind and the other to model the evolution of Earth's magnetosphere. The results obtained in the former set were used as external boundary condition for the second set of simulations. I simulated the evolution of the solar wind using 1.5D stellar wind models of Sun-like stars with different stellar rotation rates. These winds were simulated out to 1 au. I see a split in stellar wind properties at 1 au around $1.4\Omega_{\odot}$, in line with how the base relations are specified. The resulting temperature, density, velocity and magnetic field vectors at 1au were then employed in my 3D magnetosphere models.

Using the balance of thermal and magnetic pressures, I found that the magnetopause standoff distance varies according to the following piece-wise function due to the break in stellar wind properties: $r_M(< 1.4\Omega_{\odot}) \propto \Omega^{-2.04}$ and $r_M(\geq 1.4\Omega_{\odot}) \propto \Omega^{-0.27}$. This suggests that given the early solar wind strength, the young Earth's magnetosphere was much smaller than it is today. As the Sun spun down, this size gradually increased, before experiencing a greater increase once the Sun's rotation rate dropped to $1.4\Omega_{\odot}$. Furthermore I can predict a much larger magnetosphere size in the future, according to the steep increase with magnetopause distance with decreasing Ω for $< 1.4\Omega_{\odot}$. My models yield a standoff distance of $9.4 R_p$ for the present day magnetosphere, which is within the bounds of observed values.

I found a linear relationship between magnetopause standoff distance and the thickness of the magnetosheath for stellar rotations $\leq 10 \Omega_{\odot}$. This is in line with the relation prescribed by Gombosi (2004) and Balogh & Treumann (2013), for a strong shock ($\mathcal{M} \gg 1$). These stellar wind models all have a $\mathcal{M} \gg 1$, allowing us to use equation 2.6 to predict that this thickness will be approximately $0.275 r_M$ for a given magnetopause distance (figure 2.9). Therefore, I can say that the magnetosheath thickness is proportional to stellar rotation rate in the same way as the magnetopause distance for the majority of its evolution, according to the following piece-wise function: $\Delta r(< 1.4\Omega_{\odot}) \propto \Omega^{-2.04}$ and $\Delta r(\geq 1.4\Omega_{\odot}) \propto \Omega^{-0.27}$.

I examined the variation of parameters along the subsolar line (line from the centre of the planet towards the star). I find that in my models the magnetosheath is dominated by

thermal pressure, while ram pressure dominates in the stellar wind and magnetic pressure dominates in the magnetosphere. I use the balance of magnetic and thermal pressures to define the magnetopause standoff distance, and the balance of thermal and ram pressures to define the boundary between the magnetosheath and the stellar wind. In my models, current densities also mark both of these positions well. I see strong ϕ and θ currents at the magnetopause boundary, corresponding to the ‘‘Chapman-Ferraro’’ current, with the θ component being strong and positive at the boundary of the stellar wind, due to the varying ϕ magnetic field at this boundary.

I examined the colatitude of the last open magnetic field line, to discuss whether stellar wind inflow or plasma collection poses a greater threat to Earth’s atmosphere at a certain stage of its evolution, which is currently in debate (Blackman & Tarduno, 2018). I found that this colatitude decreases through the evolution of Earth’s magnetosphere. This accompanied by the gradual increase in the size of the magnetosphere suggests that stellar wind inflow would pose the greatest threat in the young system before decreasing slowly with Ω , with the threat posed by plasma collection increasing with Ω .

It is possible that a young fast rotating Sun could have had a rotation rate as high as $50 \Omega_{\odot}$. It is uncertain whether the Sun rotated that fast. If that indeed occurred, it happened only for a short amount of time, relative to the Sun’s lifetime, and at an age $\lesssim 100$ Myr. I simulated the Earth’s magnetosphere in this extreme young system, modelling the wind of the Sun at speculative rotation rates of $30 \Omega_{\odot}$ and $50 \Omega_{\odot}$. For a fast-rotating Sun, the stellar wind models predict mass-loss rates of up to $10^{-11} M_{\odot}/\text{yr}$, which agrees with observations of mass-loss rates derived for fast rotators, like AB Dor (Jardine & Collier Cameron, 2019). However, these models do not consider wind saturation at very fast rotation rates. As a result, the wind models over-predict angular momentum-loss at high rotation rates ($> 10 \Omega_{\odot}$). Given the choice of parameters, at rotation rates of $30 \Omega_{\odot}$ and $50 \Omega_{\odot}$, my wind models have Mach numbers of 1.5 and 0.99, respectively. As a result, I expect Earth’s surroundings to exhibit differences between the young system and the majority of its evolution. As the wind is sub-magnetosonic in the $50 \Omega_{\odot}$ model, in our speculative scenario, there would not have been a bow shock surrounding the Earth in this fast young system. Once the rotation rate dropped to $30 \Omega_{\odot}$, a weak shock would then have formed, accompanied by a relatively inflated magnetosheath when compared to other models. With the Sun continuing to spin down, a strong shock would then surround the planet, and would remain for most of the duration of the solar main sequence.

2.8 Appendix

2.8.1 Stellar Wind Fits

For ease of use in future works, here I provide the fit parameters obtained for some physical quantities of the solar wind at 1au, as a function of rotation rate. The fits are shown as solid/dashed lines in figure 2.1 and take the form:

$$\log_{10} (F(\Omega)) = a \left(\frac{\Omega}{\Omega_{\odot}} \right)^b + c \left(\frac{\Omega}{\Omega_{\odot}} \right)^d + e \left(\frac{\Omega}{\Omega_{\odot}} \right)^f \quad (2.8)$$

The functions $F(\Omega)$ are computed at 1 au, and are the following: The stellar wind radial and azimuthal velocities in km/s; stellar wind radial and azimuthal magnetic field strengths in G; stellar wind mass density in g/cm^{-3} , temperature in MK; mass-loss rate in M_{\odot}/yr and angular momentum loss rate in erg. The parameters a - f for each of these functions are shown in table 2.3 for $\Omega < 1.4\Omega_{\odot}$ and for $\Omega \geq 1.4\Omega_{\odot}$.

To find the solar wind conditions at other orbital distances x , I use the values obtained at Earth's orbit x_E (i.e., from tables 2.3), with the following power-laws with distance

$$B_r^{\text{sw}}(x) = B_r^{\text{sw}}(x_E) \left(\frac{x_E}{x} \right)^2, \quad (2.9)$$

$$B_{\phi}^{\text{sw}}(x) = B_{\phi}^{\text{sw}}(x_E) \left(\frac{x_E}{x} \right), \quad (2.10)$$

$$u_r^{\text{sw}}(x) = u_r^{\text{sw}}(x_E), \quad (2.11)$$

$$u_{\phi}^{\text{sw}}(x) = u_{\phi}^{\text{sw}}(x_E) \left(\frac{x_E}{x} \right), \quad (2.12)$$

$$T^{\text{sw}}(x) = T^{\text{sw}}(x_E) \left(\frac{\rho(x)}{\rho(x_E)} \right)^{\alpha-1} = T^{\text{sw}}(x_E) \left(\frac{x_E}{x} \right)^{2(\alpha-1)}, \quad (2.13)$$

$$\rho^{\text{sw}}(x) = \rho^{\text{sw}}(x_E) \left(\frac{x_E}{x} \right)^2, \quad (2.14)$$

where $\alpha = 1.05$ is the polytropic index. Note that in these relations, I assume that u_r^{sw} does not depend on x , which implies that the wind has reached terminal velocity. This is

Table 2.3: The fitting parameters to derive the stellar wind properties at 1au for $\Omega < 1.4\Omega_{\odot}$ (top) and $\Omega \geq 1.4\Omega_{\odot}$ (bottom). Parameters a to f should be implemented in Equation (2.8) to derive the solar wind conditions.

Parameter	u_r^{sw}	u_{ϕ}^{sw}	B_r^{sw}	B_{ϕ}^{sw}	ρ^{sw}	T^{sw}	M	J
a	-8.50×10^1	-2.60×10^0	-1.32×10^2	1.09×10^2	-1.25×10^0	-7.17×10^{-2}	-1.21×10^0	-5.71×10^2
b	5.84×10^{-1}	-7.93×10^{-1}	-2.32×10^{-3}	2.80×10^{-1}	-2.93×10^0	-2.80×10^0	-2.95×10^0	-1.85×10^{-2}
c	8.77×10^1	2.54×10^0	1.32×10^2	-1.09×10^2	2.10×10^0	5.90×10^0	-1.24×10^1	6.01×10^2
d	5.72×10^{-1}	-1.82×10^0	2.02×10^{-3}	2.76×10^{-1}	3.37×10^{-1}	9.04×10^{-2}	-1.03×10^{-1}	-1.51×10^{-2}

Parameter	u_r^{sw}	u_{ϕ}^{sw}	B_r^{sw}	B_{ϕ}^{sw}	ρ^{sw}	T^{sw}	M	J
a	8.21×10^{-8}	2.01×10^{-1}	-1.32×10^2	-9.56×10^1	1.83×10^0	1.22×10^2	-1.26×10^1	-5.71×10^2
b	3.91×10^0	6.71×10^{-1}	-2.32×10^{-3}	-6.97×10^{-3}	2.56×10^{-1}	9.22×10^{-2}	-5.98×10^{-2}	-1.85×10^{-2}
c	2.77×10^0	-9.90×10^{-1}	1.32×10^2	-1.33×10^{-7}	-1.02×10^{-2}	-1.16×10^2	-1.24×10^{-3}	6.01×10^2
d	3.99×10^{-2}	-3.32×10^{-1}	2.02×10^{-3}	3.79×10^0	1.42×10^0	9.52×10^{-2}	1.76×10^0	-1.51×10^{-2}
e	-	-	-	9.59×10^1	-	-	-	-
f	-	-	-	2.39×10^{-3}	-	-	-	-

2. THE EVOLUTION OF EARTH'S MAGNETOSPHERE

valid for orbital distances approximately larger than Mercury's orbit.

2.8.2 Open And Closed Magnetospheres

In section 2.4, I discussed the various trends observed in Earth's magnetosphere with time, from 1.5D stellar wind simulations. It is also likely that the polarity of either the star's or planet's magnetic field will flip cyclically. This may lead to both "open" and "closed" magnetospheres (Cravens, 2004; Bharati Das et al., 2019). To examine this difference I perform two simulations, both with the same parameters as the $1.2 \Omega_{\odot}$ wind (see table 2.1), but now with a northward and southward magnetic field (positive and negative z). Instead of using a total magnetic field strength of $4.7 \times 10^{-5} G$ as in table 2.1, I use a strength of $1 \times 10^{-3} G$ so that the nightside magnetosphere is entirely contained in the numerical grid. These can be seen in figure 2.13.

For the positive case, the magnetic field is anti-aligned with the magnetic field of the planet. This creates a closed magnetosphere. For the negative case, the magnetic field in the wind is aligned with that of the planet. This creates an open magnetosphere. When the magnetic field lines of the wind and the magnetic field of the planet are anti-aligned, the planet's field lines remain closed on both the dayside and nightside of the planet, unlike what occurs in the models examined in section 2.4. This results in reduced inflow of material from the stellar wind, due to the lack of open field lines around the poles. Magnetic reconnection no longer occurs on the nightside of the planet, which can drive material towards the atmosphere (Bharati Das et al., 2019). However due to an increase in closed field lines surrounding the planet, there is a larger amount of material held within these loops, compared to models in section 2.4.

When the fields are aligned an open magnetosphere is observed. There is now a much lower number of closed magnetic field lines, which are mostly on the dayside of the planet. Open field lines now exist at much lower latitudes than seen in other models. This simulation gives a $\Phi = 23.3^{\circ}$, similar to the analytical value of 24.4° . As a result, there is now a much larger inflow of material, and a lower amount held by closed field lines. These two scenarios correspond to the two competing effects discussed by Blackman & Tarduno (2018). In one case we have a much larger region covered by closed field lines and so a larger collecting area for plasma. While in the other we see a greater potential for inflow of material directly from the stellar wind.

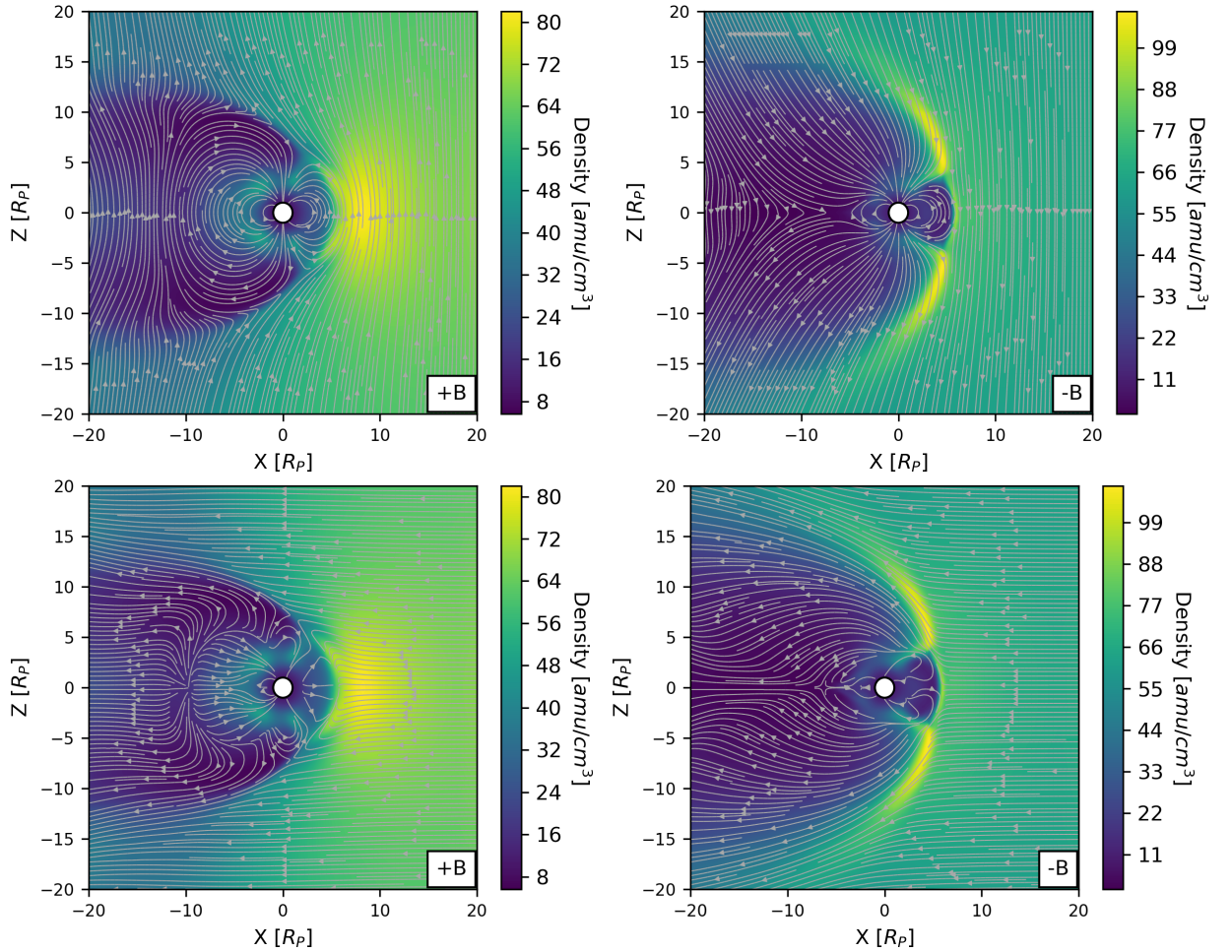


Figure 2.13: Closed (Left, northward stellar wind) and open (Right, southward stellar wind) magnetosphere. Top: The contour shows the density distribution in the models, while the streamtracers are magnetic field lines. Bottom: The contour shows the density distributions while the stream lines now show the velocity vectors. All parameters were kept constant between these models, except for the orientation of the stellar wind's magnetic field.

2. THE EVOLUTION OF EARTH'S MAGNETOSPHERE

As is clear in figure 2.13, there are significant differences in the dayside of open and closed magnetospheres. To examine these differences, I look at the subsolar line, in a similar way to section 2.4. The density and thermal pressure distributions along this line can be seen in figure 2.14.

In the open magnetosphere (negative z magnetic field) model, reconnection occurs on the dayside at a distance of $\sim 5 R_p$ from the planet. This corresponds to both an under and over density seen in this model along the x -axis. On the planet side of this reconnection, material is driven away from this point with the closed field lines trapping a portion of this material. On the wind side of the reconnection, material is driven away from the planet but the stellar wind acts as a resisting force creating the over-density seen in this model at $\sim 6 R_p$. As a result there is an increase in thermal pressure at $\sim 6 R_p$ as the forces from both reconnection and the stellar wind compress the material at this point.

In the closed magnetosphere there is a much smoother density profile on the dayside of the planet, as there is no reconnection on this side in the model. As a result the over and under densities observed in the open case are not seen here. We no longer see a bow shock with high density that extends northward and southward, but instead the closed planetary magnetic field lines focus material towards the subsolar line. This can be seen in figure 2.14, in the velocity streamlines. This forms a high density “bubble” on the dayside instead of an extended shock. In the open model, this is not the case. The open planetary field lines from the planet lead to the opposite effect, where we observe more inflow of material, but also a more extended shock northwards and southwards.

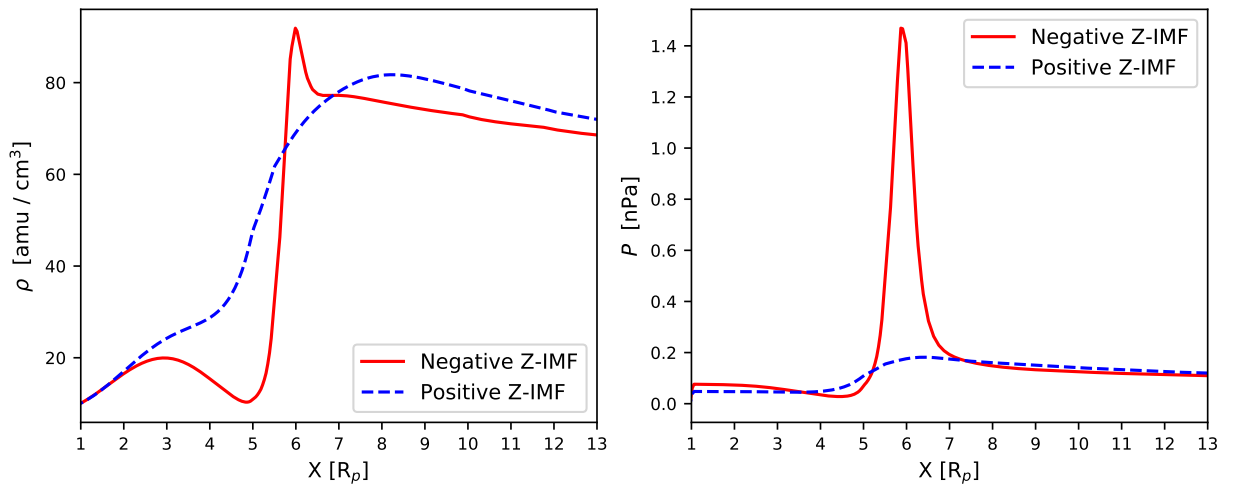


Figure 2.14: Left: The density distributions along the x axis for both a negative Z stellar wind (open) and a positive Z stellar wind (closed) case. Right: Variation in thermal pressure for both open and closed cases. We can see that the over density caused by magnetic reconnection on the dayside of the planet leads to a peak in thermal pressure.



The Effects Of The Stellar Wind On Ly- α Transits

Understanding how exoplanets lose mass is one of the most topical questions in astrophysics today. It determines the lifespan of a planet's atmosphere, which is a key contributor to a planet's habitability. In particular, being able to predict the mass loss of Earth-like planets around M dwarfs could greatly help identify targets for future and current missions, using the *James Webb Space Telescope (JWST)*, for example. Though terrestrial planets are of particular interest, understanding mass loss in the entire population of exoplanets is also important, given it is thought to shape the mass-radius distribution of exoplanets. The base BATS-R-US 3D model described in chapter 1, and used in chapter 2, is not suitable to model these systems by default, and requires a number of additions in order to be applicable. In this chapter I discuss the implementation and application of these additions to two test systems, investigating how the interaction between the stellar wind and escaping atmosphere affects the observational signatures of escape.

This chapter is presented as follows. In section 3.1 I will briefly contextualise this project, before discussing the necessary additions to model photoevaporation with BATS-R-US in section 3.2. The results of these new simulations are presented in section 3.3. I compute the synthetic transit observations in Ly- α in section 3.4, showing that properly accounting for the presence of the stellar wind can affect the interpretation of spectroscopic transits. In particular, not including the stellar wind interaction can lead to an underestimation of atmospheric escape rates. A discussion of my results is given in section 3.5, and finally, my conclusions are outlined in section 3.6. This work has been published in Carolan et al. (2021a).

3.1 Context

Using simulations we can model the interactions between the stellar and planetary outflows, gaining key insights into the characteristics of the system. In this chapter, I focus more specifically on the role the stellar wind has in this interaction, particularly on whether the stellar wind can affect the amount of atmospheric escape. One crucial point in the theory of astrophysical flows, such as stellar winds and accretion disk winds, is the presence of “critical points” (e.g. Parker, 1958; Weber & Davis, 1967). In the case of hydrodynamic outflows, such as the escaping atmospheres of close-in giants, one important critical point is the sonic point, which represents the location beyond which the planetary outflow becomes super-sonic. Planetary atmospheric escape models have suggested that the position of the sonic point (or surface, in the case of 3D geometries) in relation to the position where the interaction with the stellar wind occurs, can act to reduce planetary escape rate (Christie et al., 2016; Vidotto & Cleary, 2020). It has been suggested that if the stellar wind interacts with the super-sonic escaping atmosphere, the information cannot propagate upstream and it does not affect the inner regions of the planetary outflow. However, if this interaction occurs where the escaping atmosphere is sub-sonic, the inner outflow can be altered and therefore the escape rate can be affected (Vidotto & Cleary, 2020). In the latter scenario, the stellar wind would act to confine the planetary outflow and reduce/prevent escape (Christie et al., 2016).

Although an increase body of work on the 3D interaction between planetary atmospheres and stellar winds has become available recently (Bisikalo et al., 2013; Shaikhislamov et al., 2016; Schneiter et al., 2016; Carroll-Nellenback et al., 2017; Villarreal D’Angelo et al., 2018; McCann et al., 2019; Khodachenko et al., 2019; Esquivel et al., 2019; Debrecht et al., 2020; Villarreal D’Angelo et al., 2021), the effect of stellar wind ‘confinement’ of planetary atmospheres had not yet been studied in 3D (since the work in this chapter was carried out, MacLeod & Oklopčić 2022 has studied the affect of stellar wind confinement on Helium observational signatures in 3D). For that, the interaction must occur within the sonic surface of the planetary outflow, and to the best of my knowledge, the aforementioned 3D studies have focused on the interaction that happens when the planetary outflow has already reached super-sonic speeds. To model the confinement, the planetary outflow must be launched from the surface of the planet, as the inner regions of the escaping atmosphere must be examined in order to accurately quantify changes in the escape rate. This re-

3. THE EFFECTS OF THE STELLAR WIND ON LY- α TRANSITS

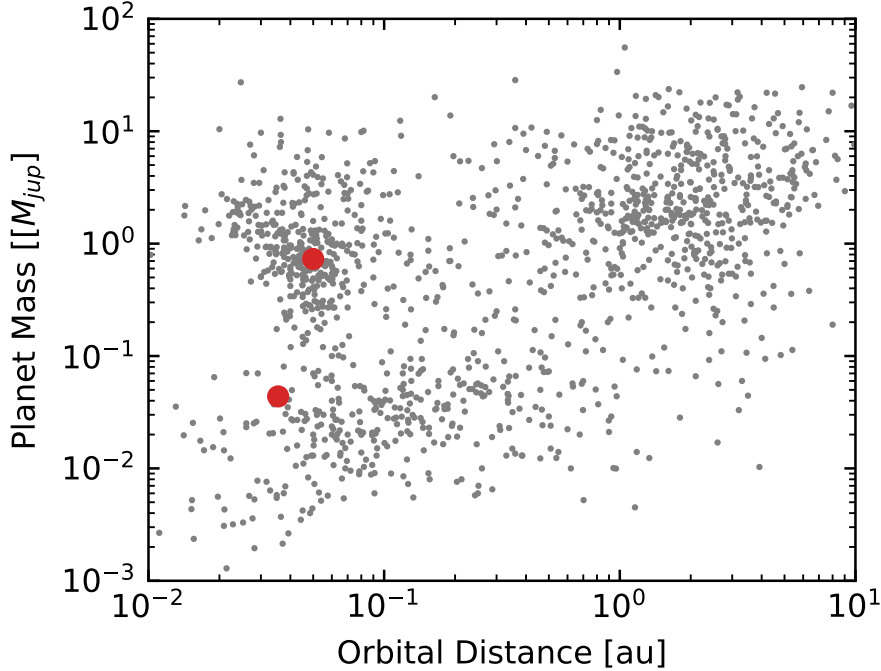


Figure 3.1: The masses vs orbital semi-major axis of all confirmed exoplanets are marked in grey (exoplanetarchive.ipac.caltech.edu). The red points mark the positions of the two planets examined in this work, they were chosen to have characteristics similar to GJ3470b, and HD209458b but orbiting a more active star.

quires high resolution close to the planet, in which case a planet-centric single body model is therefore preferred (‘local’ simulations), as opposed to ‘global’ models that incorporate both the star and the planet in the numerical grid.

In this chapter I perform 3D local hydrodynamic simulations of atmospheric escape in close-in exoplanets, including the interaction with the stellar wind. I vary the strength of the stellar wind to investigate how it confines the escaping atmosphere and the effect this has on the atmospheric escape rate. I chose two exoplanetary systems (shown in figure 3.1, similar to HD209458b but orbiting a more active star and GJ3470b) to represent typical close-in gas giants.

3.2 Developing A 3D Model Of Photoevaporation In Close-In Systems

In order to correctly model atmospheric escape in close-in systems, a number of additions must be made to the base model presented in chapter 1. This includes: a new coordinate system; modified inner boundary conditions to launch the escaping atmosphere; new source terms to account for orbital forces; and modified outer boundary conditions to account for the stellar wind. To simplify these simulations while I make these changes, I perform HD simulations, such that all magnetic fields are turned off. Fewer equations are now solved: the mass; momentum; and energy conservation equations, with the later two simplified by the omission of magnetic terms. I set $\gamma = 1.00001$ (to avoid numerical issues) making these simulations isothermal ($P^{1-\gamma} T^\gamma = \text{constant}$, results in constant temperature when $\gamma = 1$), and set $\mu = 0.5$ to model ionised Hydrogen, similar to the work of Bisikalo et al. (2013); Carroll-Nellenback et al. (2017).

3.2.1 New Coordinate System

In previous works, Hot Jupiters have been simulated using global simulation which include both the star and the planet in the computational domain (Carroll-Nellenback et al., 2017; Villarreal D’Angelo et al., 2018). There are downsides to such simulations, namely the computational time required and loss of resolution around the planet. As I wish to investigate exoplanetary mass loss, high resolution around the planet is preferable, and provided by a single-body simulation centred on the planet. These are also computationally less expensive than their global counterparts.

As shown in figure 3.2, I denote the stellar frame by capital letters, and the planet’s frame by lowercase. The planet’s circular orbit is described by orbital rotation rate Ω , which acts in the positive Z direction, such that the planet orbits about the star in the XY plane. The x axes are aligned in both frames, with the y and z axes being parallel. The simulations are performed in the planet’s reference frame, with the planet centred on the origin, and the star at $[-a, 0, 0]$, where a is the orbital separation of the planet and the star. A simple translation is required to go from the position in one frame to the other, however one must account for the rotational velocities due to the orbit when going from the planetary to the stellar frame.

3. THE EFFECTS OF THE STELLAR WIND ON LY- α TRANSITS

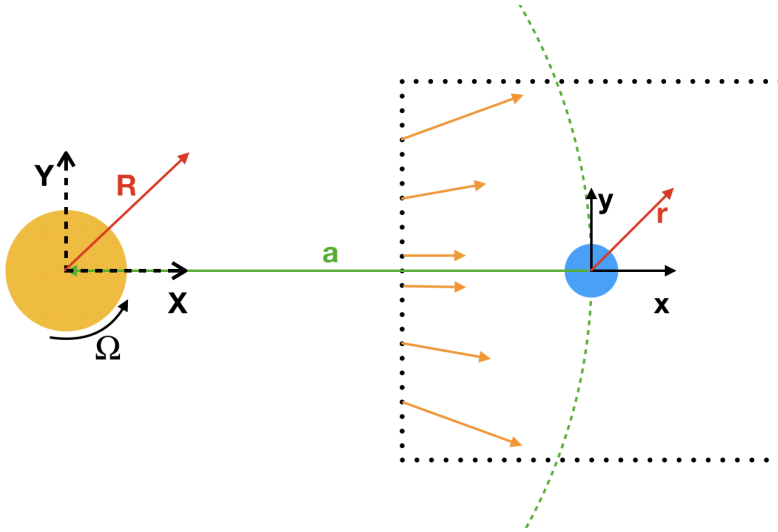


Figure 3.2: The coordinate system used in my simulations (not to scale). The orange circle represents the star, while the blue shows the planet. The uppercase letters show the direction of vectors in the stellar system, while the lowercase shows the axes in the planetary system. The black dotted square represents the computational grid, while the green dashed line shows the path of the planet’s orbit. The orange arrows represent the changing direction and magnitude of the stellar wind velocity as it enters the simulation grid. Note that, because of the close distance to the star, I cannot assume that the stellar wind is plane-parallel, as is done in simulations of planets that orbit far from their host stars (e.g. in chapter 2; Carolan et al., 2019).

The exoplanet is placed at the origin of a rectangular grid ($x, y = [-50, 50 R_p]$, $z = [-32, 32 R_p]$, where R_p is the radius of the planet) as seen in figures 3.2 and 3.5. These simulations contain 16 million cells and have a minimum cell size of $1/16 R_p$ within a radius of $5 R_p$, which gradually decreases towards the edge of the grid (We found increasing the maximum resolution of these simulations showed no significant change in the results).

3.2.2 Launching A Planetary Wind

As discussed in chapter 1, Hot Jupiters exist in close proximity to their host stars, they experience much higher base temperatures (temperature at the exobase), due to higher irradiation fluxes (Allan & Vidotto, 2019). If the temperature and density are high enough at the thermosphere, the planet can drive a wind against its own gravity, which acts similarly to a stellar wind. In this chapter I will model the escaping atmosphere (and stellar wind) as Parker winds (Parker, 1958). There are two unknowns in the Parker wind

3.2 Developing A 3D Model Of Photoevaporation In Close-In Systems

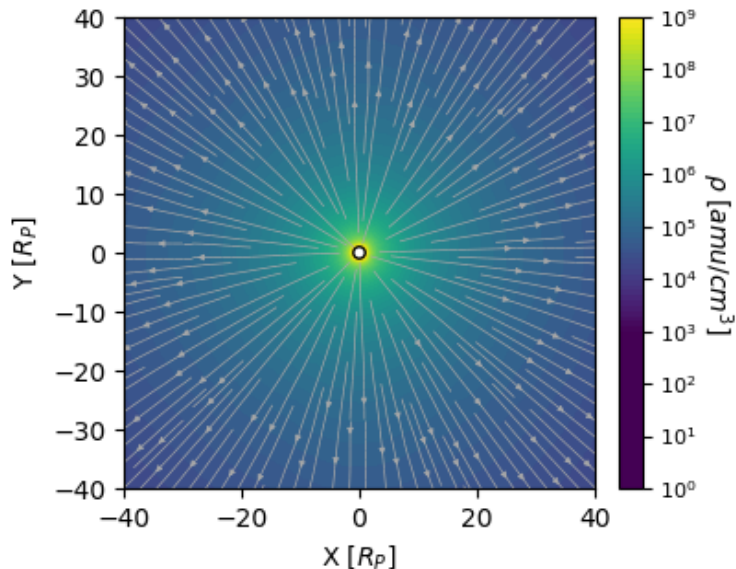


Figure 3.3: Example of the planet launching a wind in my simulations, using a modified inner boundary. The colour shows density, while the streamtracers show velocity.

model, the base density and temperature. To guide the selection of the temperature and density of the planetary outflow, I use information from the 1D model (Allan & Vidotto, 2019, see section 3.2.3).

To model atmospheric escape the inner boundary is modified in my 3D simulations. With the boundary placed at $1 R_p$, the temperature and density are fixed at user defined values, which set the pressure at the boundary. The velocity components are reflected ($u_{boundary} = -u_{real}$) where the velocity in the boundary cell has the same magnitude but opposite sign as the velocity in the real cell. This ensures that when one interpolates between the cells on either side of the boundary ($r = 1R_p$), a velocity of exactly 0 km/s will be obtained at the base of the wind. By setting a pressure at the boundary of the planet, a pressure differential is created between the boundary and the surrounding medium, which if strong enough to overcome the planet's gravity can drive an escaping atmosphere (see figure 3.3). One drawback of this setup is that this boundary does not launch an escaping atmosphere self-consistently (the implementation of self-consistent photoevaporation is discussed in chapter 5). Instead we need some way to inform the inner boundary conditions, for which I use a 1D code, discussed next, in section 3.2.3. The base values adopted for each of the modelled planets are shown in table 3.1. These values give rise to an escape

3. THE EFFECTS OF THE STELLAR WIND ON LY- α TRANSITS

rate \dot{m}_0 , which matches that found in the 1D model.

3.2.3 Informing The Inner Boundary Conditions: 1D Model

To inform the boundary conditions at the surface of the planet, I employ a 1D radiation hydrodynamic model similar to that discussed in section 1.2.2 (further discussed in Murray-Clay et al., 2009; Allan & Vidotto, 2019). This model takes the planetary parameters (table 3.1) as input, as well as the EUV flux from the host star: for the Hot Jupiter, I used $L_{\text{EUV,HJ}} = 2.06 \times 10^{-5} L_{\odot}$, (chosen to be 25 times larger than that assumed in Murray-Clay et al. 2009 to produce strong evaporation) and for the Warm Neptune, I used $L_{\text{EUV,WN}} = 3.73 \times 10^{-6} L_{\odot}$ (Bourrier et al. 2018). This yields an escape rate, as well as the velocity and ionisation fraction ($f_{\text{ion}} = n_p / (n_p + n_n)$) as a function of distance. With this information, I can constrain the two free parameters of the 3D isothermal model: the base density and temperature at the planetary radius (inner boundary). A unique temperature is chosen such that the velocity structure in 3D best matches the velocity structure from the 1D model, seen in figure 3.4. Similarly, the base density in the 3D simulations is adjusted, so that it and the matched velocity structure reproduce the escape rates resultant from the 1D model (\dot{m}_0 in table 3.1). By matching the velocity structure and escape rate, I ensure that the ram pressure of the escaping atmospheres in my 3D simulations without a stellar wind is close to that of the 1D model. The stellar wind can then be injected to examine the interaction between the stellar and planetary outflows, having vastly saved computational time by informing the 3D model with the 1D model.

Next I will discuss the additional forces one must include to simulate close-in systems.

3.2.4 Stellar Gravity

Given the main purpose of the base model is to study solar system objects, the effects of stellar gravity are ignored in the code, as no solar system planet is close enough to the Sun for this to be significant. For Hot Jupiters however, this cannot be ignored due to the short orbital distance to their hosts. To account for this, a new gravity term is added to the momentum conservation and energy equations, which acts towards the star:

$$\mathbf{g}_* = -\frac{GM_*}{R^2} \hat{\mathbf{R}} = -\frac{GM_*}{(r-a)^2} \hat{\mathbf{R}} \quad (3.1)$$

Table 3.1: The planet and stellar properties in each set of models. M_p and R_p describe the planet’s mass and radius, a is the orbital distance. \dot{m}_0 is the planetary atmospheric escape rate (with no stellar wind), u_{kep} is the Keplerian velocity of the system. T_p and $n_{0,p}$ are the temperature and base density of the planet’s outflowing atmosphere in the 3D model that were found to best match the results of the 1D model. \dot{M} , R_* and T_* describe the stellar mass, radius and stellar wind temperature, respectively, while the stellar wind radial velocity at each planet’s orbital distance is given as u_{local} . Finally, $F_{\text{EUV}}(a)$ is the EUV flux at the planet’s orbital distance.

Planet	M_p [M_{Jup}]	R_p [R_{Jup}]	a [au]	\dot{m}_0 [10^{10} g/s]	u_{kep} [km/s]	T_p [10^4 K]	$n_{0,p}$ [10^9 cm $^{-3}$]	M_* [M_{\odot}]	R_* [R_{\odot}]	T_* [10^6 K]	u_{local} [km/s]	$F_{\text{EUV}}(a)$ [erg/cm 2 /s]
HJ	0.7	1.4	0.050	58	147	1	3.86	1.00	1.00	2	400	1.12×10^4
WN	0.04	0.41	0.036	6.5	116	0.5	3.03	0.54	0.55	1	240	3.92×10^3

3. THE EFFECTS OF THE STELLAR WIND ON LY- α TRANSITS

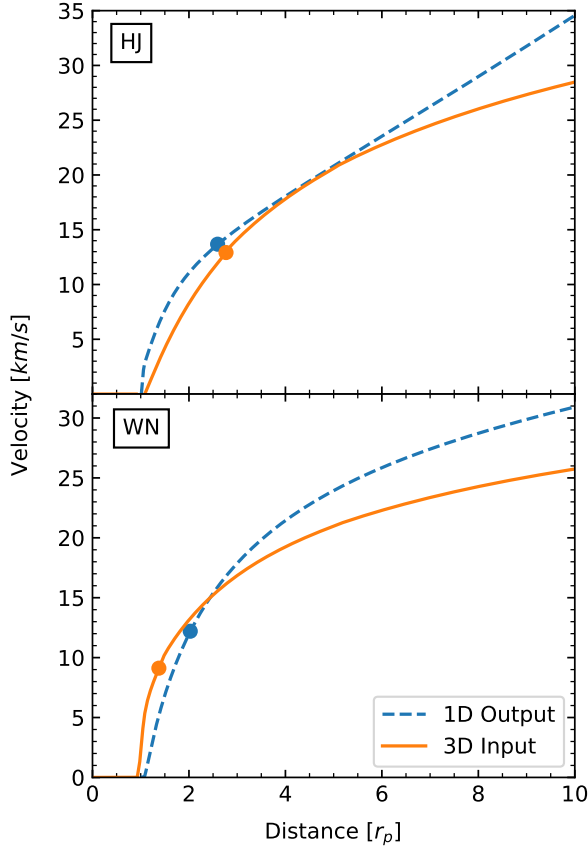


Figure 3.4: Velocity vs distance for the escaping atmosphere of both the Hot Jupiter (HJ) and Warm Neptune (WN) models. The dashed blue line shows the output of the 1D model, while the solid orange shows the initial condition I implement in my isothermal 3D model. The base density in the 3D model is then adjusted so that the same escape rate is obtained in both the 1D and 3D models. The circles mark the position of the sonic point in each model.

R is the position in the stellar frame, r is the position in the planetary frame, and a is the orbital separation between the star and planet.

3.2.5 Orbital Effects: Coriolis & Centrifugal Forces

For simplicity, I assume that the planet is tidally locked to the star, and perform these simulations in the co-rotating/co-orbiting reference frame. This approach is justified as many close-in planets are thought to be tidally locked to their host star (Kasting et al., 1993; Edson et al., 2011). This frame of reference insures that as the planet orbits, the

3.2 Developing A 3D Model Of Photoevaporation In Close-In Systems

star is always outside the grid at negative x, with the planet at the origin, which simplifies computation.

When simulating in the frame of the planet, additional terms must be included to account for orbital effects. These are the centrifugal force, which acts perpendicularly outward to the orbital motion; and the Coriolis force, which acts perpendicular to the orbital motion and towards the axis of rotation. These are fictitious forces that effectively bend the trajectory of material in the planets reference frame to account for orbital motion. They arise when one derives the acceleration in the stationary frame, relative to the rotating frame (Goldstein et al., 2002).

The velocity in the stationary frame can be written in terms of the velocity in the rotating frame as follows:

$$\mathbf{u}_s = \mathbf{u}_{rot} + \boldsymbol{\Omega} \times \mathbf{R}, \quad (3.2)$$

where \mathbf{u}_s and \mathbf{u}_{rot} are the velocities of a particle in the stellar and rotating axis, $\boldsymbol{\Omega}$ is the axis of rotation, and \mathbf{R} is the position in the stellar frame. The acceleration can be obtained using the operator below:

$$\left(\frac{d}{dt}\right)_s = \left(\frac{d}{dt}\right)_{rot} + \boldsymbol{\Omega} \times, \quad (3.3)$$

$$\left(\frac{d\mathbf{u}_s}{dt}\right)_s = \mathbf{a}_s = \left(\frac{d\mathbf{u}_s}{dt}\right)_{rot} + \boldsymbol{\Omega} \times \mathbf{u}_s, \quad (3.4)$$

$$\mathbf{a}_s = \left(\frac{d}{dt}(\mathbf{u}_{rot} + \boldsymbol{\Omega} \times \mathbf{R})\right)_{rot} + \boldsymbol{\Omega} \times (\mathbf{u}_{rot} + \boldsymbol{\Omega} \times \mathbf{R}). \quad (3.5)$$

As $R = r - a$, the following is true:

$$\frac{d}{dt}\mathbf{R} = \frac{d}{dt}\mathbf{r} = \mathbf{u}_{rot}. \quad (3.6)$$

Using this:

$$\mathbf{a}_s = \left(\frac{d}{dt}\mathbf{u}_{rot}\right)_{rot} + \boldsymbol{\Omega} \times \mathbf{u}_{rot} + \boldsymbol{\Omega} \times \mathbf{u}_{rot} + \boldsymbol{\Omega} \times (\boldsymbol{\Omega} \times \mathbf{R}), \quad (3.7)$$

$$\mathbf{a}_s = \mathbf{a}_{rot} + 2(\boldsymbol{\Omega} \times \mathbf{u}_{rot}) + \boldsymbol{\Omega} \times (\boldsymbol{\Omega} \times \mathbf{R}), \quad (3.8)$$

3. THE EFFECTS OF THE STELLAR WIND ON LY- α TRANSITS

where the second term on the right side is the acceleration due to the Coriolis force, and the final term is the acceleration due to the centrifugal force. The Coriolis term only affects the momentum, and so is added to the momentum conservation equation. The centrifugal term, like the stellar gravity term, affects the momentum and energy and so is added to the momentum and energy conservation equations.

With these new terms the HD equations become:

$$\frac{\partial \rho}{\partial t} + \nabla \cdot (\rho \mathbf{u}) = 0, \quad (3.9)$$

$$\frac{\partial(\rho \mathbf{u})}{\partial t} + \nabla \cdot \left[\rho \mathbf{u} \mathbf{u} + P_T \mathbf{I} \right] = \rho \left(\mathbf{g} - \frac{GM_*}{(r-a)^2} \hat{R} - \boldsymbol{\Omega} \times (\boldsymbol{\Omega} \times \mathbf{R}) - 2(\boldsymbol{\Omega} \times \mathbf{u}) \right), \quad (3.10)$$

$$\frac{\partial \epsilon}{\partial t} + \nabla \cdot \left[\mathbf{u} \left(\epsilon + P_T \right) \right] = \rho \left(\mathbf{g} - \frac{GM_*}{(r-a)^2} \hat{R} - \boldsymbol{\Omega} \times (\boldsymbol{\Omega} \times \mathbf{R}) \right) \cdot \mathbf{u}, \quad (3.11)$$

Where the total energy density ϵ is now

$$\epsilon = \frac{\rho u^2}{2} + \frac{P_T}{\gamma - 1}. \quad (3.12)$$

3.2.6 New Outer Boundaries

To complement the additional forces and new inner boundary, I define a new outer boundary for stellar wind injection. I also limit the inflow velocity from other outer boundaries as we will see below.

In the base version of BATS-R-US, the stellar wind is injected in a plane-parallel configuration with a constant velocity magnitude. For far-out planets, this is a good approximation, as the plane parallel configuration will be effectively radial from the star everywhere, and the stellar wind is most likely at terminal velocity. However in close-in systems, this is not the case, as the difference between the radial and plane parallel configuration at the edges of the grid will be quite significant, as shown in figure 3.2. We must therefore inject the stellar wind radially, which requires variation in the three velocity components depending on the coordinates of the outer boundary. As I am simulating in the co-orbiting frame, the stellar wind will appear to have a ϕ velocity component in this frame, due to the rotation. This arises naturally in my simulations from the addition of the Coriolis force.

3.2 Developing A 3D Model Of Photoevaporation In Close-In Systems

However this force will also act between the star and the beginning of the grid. This must be manually corrected for on the boundary, by adding a ϕ velocity component to the stellar wind, which is equal to $-\boldsymbol{\Omega} \times \mathbf{R}$.

As is also seen in figure 3.2, the velocity magnitude is not constant across the face of the boundary. When simulating close-in planets, it is important to consider how far a cell on the boundary is from the star, given that the stellar wind is accelerating in these regions. As a result, a cell at the edge of the boundary should have a larger velocity magnitude than one in the centre, given the stellar wind has accelerated over a greater distance to reach that cell. The variation in velocity magnitude across the boundary can be quite significant (up to a 100km/s difference between the edge and centre of the grid). To account for this, I first perform a 1D isothermal simulation of the stellar wind. I chose temperatures appropriate for stars hosting close-in exoplanets (see table 3.1), and vary the base density to control the stellar wind mass-loss rate. I then fit a ninth order polynomial to the solution (chosen to best fit the results of the 1D model), and input the resultant fit coefficients into my 3D simulations. In every cell on the boundary, the code then calculates the distance from the star and uses the fit coefficients to set the stellar wind velocity. The density is then set to ensure the mass-loss rate of the star remains constant. This implementation treats the stellar wind injection much more accurately in close-in systems than the constant plane-parallel boundary in the base version of the code.

When simulating in the rotating frame, the default outflow boundary conditions used in the Earth simulations cannot be used. This is mainly due to the effects of the Coriolis force which acts to bend the trajectory of material perpendicular to the direction of motion. When this occurs near an outer boundary which uses the default outflow conditions, it can cause an unregulated inflow from that boundary, which can have drastic effects on the simulation. It is particularly important to rectify this if the density in the region is quite high, as the inflow can change the structure of material in that region. We therefore want to limit the inflow from all outer boundaries except that which is injecting the stellar wind.

To do this, the code first checks the direction of the momentum of material at a boundary. If the relevant momentum component is directed into the grid, it is set to 0. If it is directed out of the grid, normal outflow conditions are applied. For example, on the negative y boundary, if the y component of the momentum is positive, then it is then set to 0, but if it is negative, the boundary allows the material to outflow.

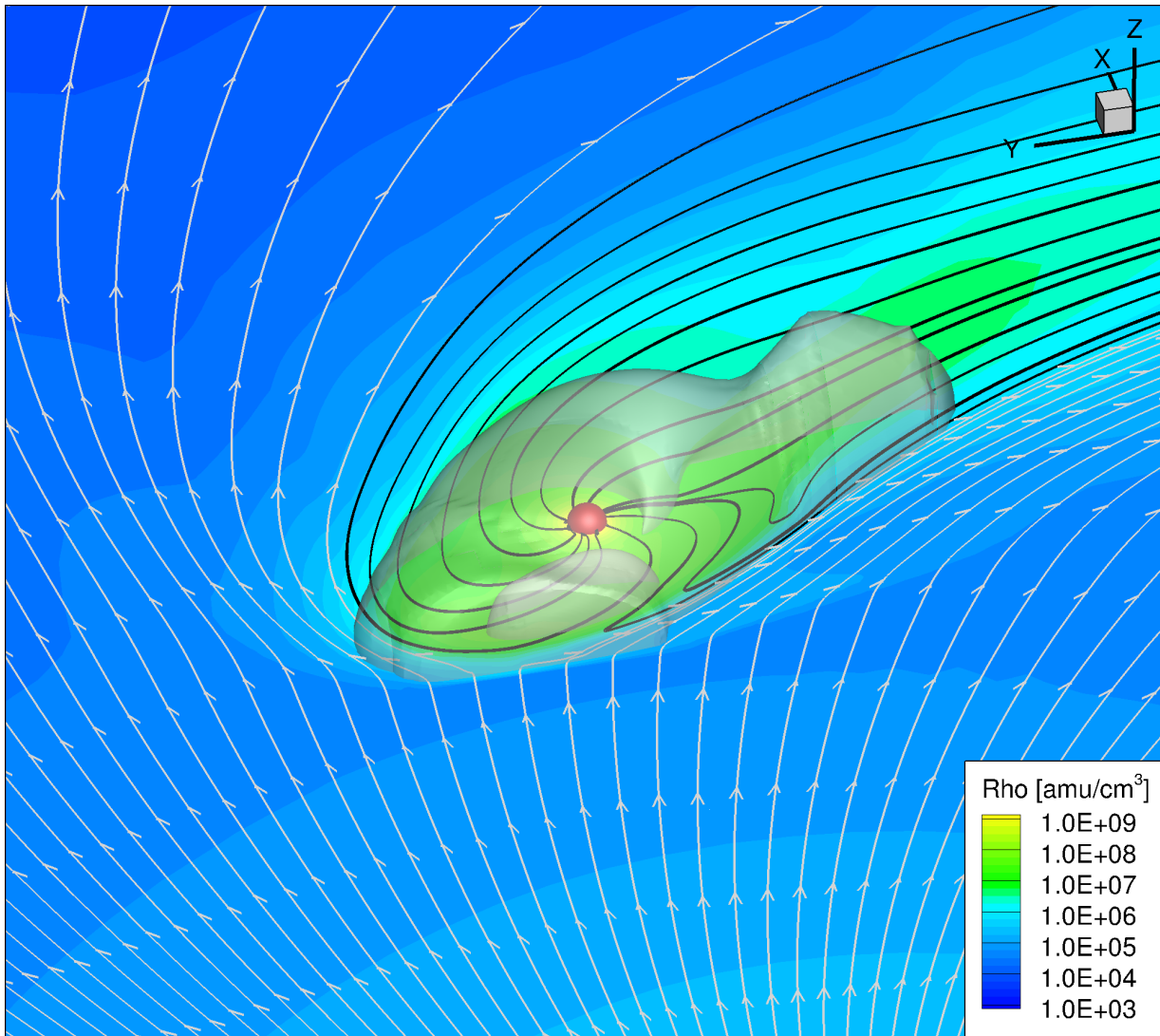


Figure 3.5: A 3D view of the HJ model for a stellar mass-loss rate of $10 \dot{M}_{\odot}$. The colour shows the density in the orbital plane. The gray surface marks the sonic surface around the planet. The grey streamlines show the flow of the stellar wind in the grid, while the black lines trace the escaping atmosphere of the planet.

3.3 Simulations Of Reduced Atmospheric Escape From Close-In Planets

Using this computational setup I model two exoplanets for a range of stellar wind conditions: a Hot Jupiter similar to HD209458b but orbiting a more active solar-like star

3.3 Simulations Of Reduced Atmospheric Escape From Close-In Planets

(labelled “HJ”); and a Warm Neptune similar to GJ3470b (labelled “WN”) which orbits an M dwarf. The relevant parameters used in the HJ and WN models are also provided in table 3.1.

For each planet I compute 13 and 14 models respectively, increasing the stellar wind mass-loss rate from 0 to 100 times the solar mass-loss rate ($\dot{M}_{\odot} = 2 \times 10^{-14} M_{\odot}/\text{yr}$). Given that it is difficult to measure the winds of cool dwarf stars, I chose this large range of stellar mass-loss rates to establish if and when neglecting the presence of the stellar wind as a contributing factor to signatures of atmospheric escape is appropriate. Note that this can only be achieved in multi-dimensional studies, as 1D models cannot account for the presence of a stellar wind. I chose to keep the temperatures of the isothermal stellar wind constant in each set ($T_{\star, \text{HJ}} = 2 \times 10^6 \text{ K}$, $T_{\star, \text{WN}} = 1 \times 10^6 \text{ K}$), retaining the same stellar wind velocity structure within each set of models. Varying the mass-loss rate, therefore, solely changes the stellar wind density. This setup allows me to investigate the effect that gradually increasing the stellar wind ram pressure ($\propto \dot{M} u_{\text{local}}$, where \dot{M} is the stellar wind mass-loss rate, and u_{local} is the velocity of the stellar wind at the planet’s orbit) has on the planet’s escaping atmosphere. The density and velocity in the orbital plane of three models from each set are shown in figure 3.6. As the stellar wind mass-loss rate is increased I see the transition from type 2 / “weak” to the type 1 / “strong” scenarios shown by Matsakos et al. (2015) / McCann et al. (2019) respectively.

In the left panels of figure 3.6 we can see a large sonic surface created when the supersonic stellar wind is shocked as it meets the super-sonic planetary outflow. As the ram pressure of the stellar wind increases this interaction happens closer to the planet. This confinement eventually affects the sonic surface of the escaping atmosphere, as seen in the changing white contour close to the planet from left to right panels in figure 3.6. The inner circular sonic surfaces in the left panels are unaffected (labelled “closed”). In the right panels the stellar wind has confined the outflow such that the sonic surface has been altered on all sides of the planet (labelled “open”). The middle panels show the transition between these two states, where the day-side sonic surface has changed, while the night-side surface remains largely unaffected.¹ Note that the inner sonic surface of the WN planet is

¹The additional $\mathcal{M} = 1$ transition, in figure 5 is due to the fact that both the stellar and planetary winds are supersonic. As a result there are two shocks, one outer “bow shock” where the stellar wind is shocked, and an inner “termination shock” where the supersonic escaping atmosphere is shocked. This is similar to what is shown in models of the interaction between the heliosphere and the ISM (eg. Zank & Müller, 2003), where instead it is the inner stellar wind and outer ISM forming two shockwaves.

3. THE EFFECTS OF THE STELLAR WIND ON LY- α TRANSITS

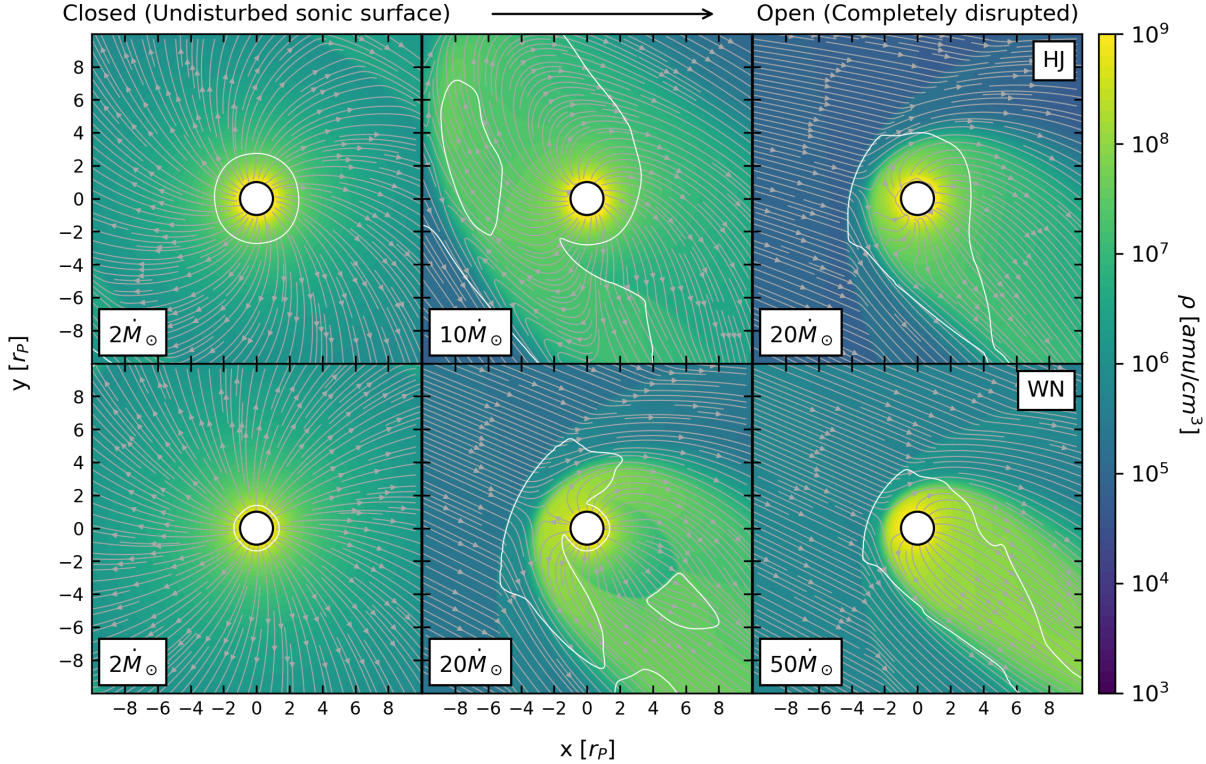


Figure 3.6: Top: The orbital slice of 3 Hot Jupiter (HJ, top) and 3 Warm Neptune (WN, bottom) models, chosen to illustrate transition from “closed” to “open” sonic surfaces for each planet. “Closed” refers to the scenarios where the inner (circular) sonic surface around the planet is not disturbed by the stellar wind. Contrary to that, “open” refers to the scenarios where this surface is disrupted. The planet is orbiting in the positive y direction, with the star at negative x . The colour shows the distribution of density around the planets, while the white contour marks a Mach number of 1, which shows the sonic surface around each planet. The streamlines trace the velocity of material in each model, in the planet’s reference frame. Bottom: A zoomed out version of this figure, showing the orbital plane from my grids. Here we can more clearly see the injection of the stellar wind from the negative x side of the grid, as well as the extension of material both ahead and behind the planet’s orbit.

at $1.1 R_p$. Published models (eg. Villarreal D’Angelo et al., 2021) of GJ436b, also a Warm Neptune, have shown that the $\mathcal{M} = 1$ transition occurs farther out. The low position of the sonic point in my 3D models is due to my choice of temperature (see figure 3.4). I will come back to how a larger sonic surface would change my results when I further discuss the limitations of this model in section 3.5.2.

Previous models have shown that stellar wind confinement can affect the escape rate

3.3 Simulations Of Reduced Atmospheric Escape From Close-In Planets

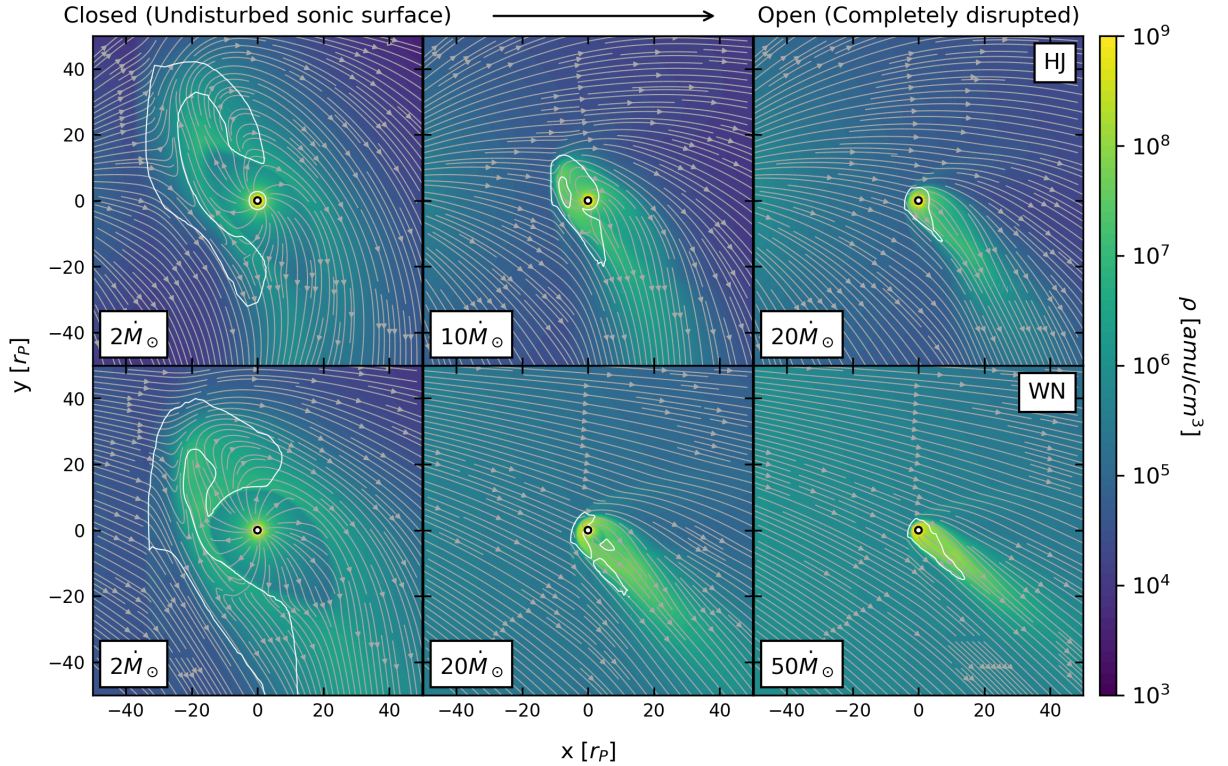


Figure 3.7: Zoom out of the orbital slices shown in figure 3.6

of the planets atmosphere (Christie et al., 2016; Vidotto & Cleary, 2020). To investigate the difference in escape rate between my closed and open 3D models, I integrate the mass flux through concentric spheres around the planet, obtaining the atmospheric escape rate. Table 3.2 shows a summary of the results of my simulations. The escape rate from each model is plotted in figure 3.8. Due to resolution, the escape rate can show small variations with distance from the planet, especially at the point where the stellar wind and escaping atmosphere meet. This small variation is quantified by the blue error bars in figure 3.8, which show one standard deviation from the mean escape rate in each model. Some models only reach a quasi-steady state solution, showing small periodic variability with increasing time step. For these models the maximum deviation is shown as a red error bar, while the average deviation over one period of the quasi-steady state variability is shown in blue. In both model sets, increasing the stellar wind mass-loss rate has reduced the atmospheric escape rate. For the HJ models, the escape rate has been reduced by 65% (from 5.8×10^{11} g/s to 2.1×10^{11} g/s, see table 3.2). The WN models show a more gradual change, with a

3. THE EFFECTS OF THE STELLAR WIND ON LY- α TRANSITS

Table 3.2: Summary of my simulation results. The stellar wind mass-loss rate (\dot{M}) is varied in each simulation, affecting the planetary atmospheric escape rate \dot{m} and Ly- α absorption at mid-transit computed in the blue [-300 to -40 km/s] plus red [40 to 300 km/s] wings (including the broad-band absorption due to the planetary disc). Here, the superscripts HJ and WN refer to the Hot Jupiter and Warm Neptune cases, respectively.

\dot{M} (HJ) (\dot{M}_{\odot})	\dot{m}^{HJ} (10^{10} g/s)	ΔF^{HJ} (%)	\dot{M} (WN) ($\dot{M}_{\odot}/\text{yr}$)	\dot{m}^{WN} (10^{10} g/s)	ΔF^{WN} (%)
0	58	20.7	0	6.5	8.8
2	56	12.0	1	6.6	7.3
4	55	8.6	2	6.4	5.3
6	55	6.9	4	6.5	4.0
8	57	6.4	10	6.4	3.7
10	51	6.0	15	6.4	3.7
12	40	5.9	20	6.5	3.7
14	37	5.8	25	6.4	3.7
16	35	5.8	30	6.2	3.6
20	30	5.5	35	6.0	3.5
30	27	5.1	40	5.8	3.4
60	22	4.2	50	5.4	3.2
100	21	3.9	75	4.6	2.8
-	-	-	100	3.9	2.4

maximum reduction of 40% (from 6.5×10^{10} g/s to 3.9×10^{10} g/s) over the range of stellar winds examined.

As the stellar wind mass-loss rate increases, the escaping atmosphere is confined to a reduced volume around the planet, which is clearly visible from the velocity streamlines in figure 3.6 (left to right). This decelerates material on the day-side of the planet, redirecting it towards the planetary tail as seen in figure 3.6. As the flow of the escaping atmosphere is further confined, this deceleration occurs closer to the planet, where it eventually inhibits the dayside flow from reaching super-sonic speeds. As a result, the atmospheric escape rate is gradually reduced as the flow’s sonic surface is further disrupted.

This change in escape rate occurs more suddenly in the HJ models than in the WN models as \dot{M} is increased. I propose this is related to the distance of the sonic point. In the closed HJ and WN models these are approximately $2.5 R_p$ and $1.1 R_p$ respectively. As a result the outflow in the WN models must be confined relatively closer to the planet in order for the sonic surface to be affected. This results in a more gradual reduction of

3.3 Simulations Of Reduced Atmospheric Escape From Close-In Planets

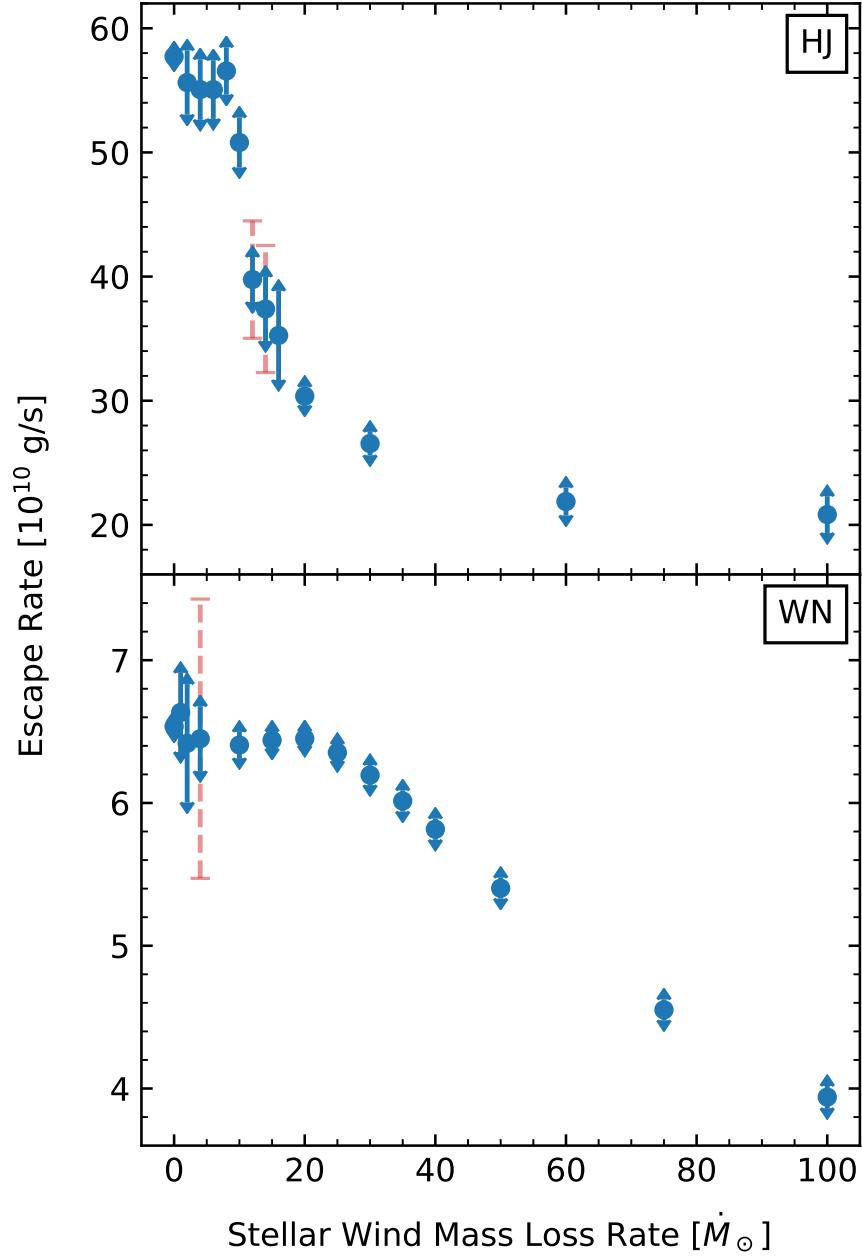


Figure 3.8: The variation of atmospheric escape rate with stellar mass-loss rate for each of my models. The points mark the mean escape rate, while the blue error bars illustrate one standard deviation from the mean. As some models reach a quasi-steady state solution, the average over several time steps is taken, and plotted in blue. For these models, the standard deviation at a single time step is shown in red.

3. THE EFFECTS OF THE STELLAR WIND ON LY- α TRANSITS

atmospheric escape in the WN models, as a stronger stellar wind is required to further confine this outflow and open the sonic surface. In the HJ models, this is not the case. The change from closed to open geometries happens over a much shorter range of \dot{M} , as the sonic surface is relatively further from the planet, and so can be more easily accessed by the stellar wind.

3.4 Reduced Ly- α Transit Depth Due To Stellar Wind Confinement

To compute the synthetic observations of my models, I use the ray-tracing model described in section 1.7. This requires the temperature, velocity and density of neutral Hydrogen atoms from my grid. This 3D model does not treat both the neutral and ionised portions of the planetary outflow, it simulates purely the ionised Hydrogen ($\mu = 0.5$). The 1D escape model from Allan & Vidotto (2019), which was used to inform the initial conditions of the 3D model, tracks both the neutral and ionised density, as outlined in section 3.2.3. This model can again be used to estimate the distribution of neutral Hydrogen within the 3D grids. Using the variation of ionisation fraction with radial distance $f_{\text{ion}}(r)$ from the 1D model, with the density of ionised Hydrogen (n_p) from the 3D model, the neutral density in 3D can be found as follows:

$$n_n = n_p \frac{1 - f_{\text{ion}}(r)}{f_{\text{ion}}(r)}. \quad (3.13)$$

Although this is not the most precise approach to calculate the neutral Hydrogen density, this post-processing technique is a work-around adopted when the ionisation balance equation is not solved self-consistently with the HD equations (similar approach has been used by Oklopčić & Hirata (2018) when calculating the population levels of Helium, and by Lampón et al. (2020) when modelling Helium in HD209458b's atmosphere). One limitation of this approach is that the 1D model computes the ionisation fraction along the star-planet line. Therefore, when I incorporate the ionisation fraction predicted in the 1D models in the 3D grid, the density of neutral material in the night side, or planetary tail, is not properly calculated. However, given that the inner regions of my 3D simulations are approximately spherically symmetric and contain most of the absorbing material, using the resultant ion fraction from the 1D model is an acceptable approximation for computing the synthetic observations.

3.4 Reduced Ly- α Transit Depth Due To Stellar Wind Confinement

With the neutral density found the synthetic transits can be calculated. For each of the models in the HJ and WN set, the transit depth as a function of velocity is shown in figure 3.9, and the integrated percentage absorption is given in table 3.2. As the Ly- α line centre is dominated by interstellar absorption and geocoronal emission, I omit the line centre $[-40, 40]$ km/s from these plots. In both model sets, the maximum transit depth decreases as the planetary outflow is further confined. This is due to the volume of absorbing planetary material around the planet decreasing as the escaping atmosphere is confined.

For most models, there is an obvious asymmetry in the line profile, with the blue wing showing more absorption than the red. In the low \dot{M} models, there is significant dayside (redshifted) outflow towards the star, similar to that seen by Matsakos et al. (2015) in their type 2 interaction, and in the “weak” stellar wind scenarios of McCann et al. (2019). As \dot{M} increases, this dayside stream is suppressed completely, as seen in figure 3.6. What remains is the planetary tail, containing mostly blue-shifted material (type 1 in Matsakos et al. 2015; “strong” stellar wind in McCann et al. 2019), leading to the line profile asymmetry we see in figure 3.9.

We quantify this asymmetry by integrating the modelled transit line profiles in figure 3.9 over velocity in the blue $[-300, -40]$ km/s and red $[40, 300]$ km/s wings. Note that this 3D model does not consider energetic neutral atoms (ENAs), and so the effect of these on the transit line profiles are not reflected in these calculations. For more discussion on this see section 3.5.2. The results of this are shown in figure 3.10. Note that even in the case with no stellar wind the line shows asymmetry due to the orbital motion and tidal forces. We can clearly see that in both models at low stellar mass-loss rates the absorption in the red wing dominates due to the significant dayside stream as mentioned above. As the stellar mass-loss rate is increased, the absorption in the blue wing begins to dominate as this dayside flow is further confined. There is a more sudden change in the WN model than with the HJ planet, as the HJ planet has a stronger outflow/higher escape rate. For both models the level of asymmetry is approximately constant within a certain range of stellar mass-loss rates. For the HJ models, the blue wing absorbs 1-2% more than the red for models between 10 and 30 \dot{M}_{\odot} . The WN models absorb roughly 0.25% more in the blue between 10 and 40 \dot{M}_{\odot} . Above these ranges the difference in absorption between the blue and red wing gradually decreases as the outflow becomes significantly more confined. For stellar wind mass-loss rates $< 10 \dot{M}_{\odot}$, despite the percentage absorption of each wing changing

3. THE EFFECTS OF THE STELLAR WIND ON LY- α TRANSITS

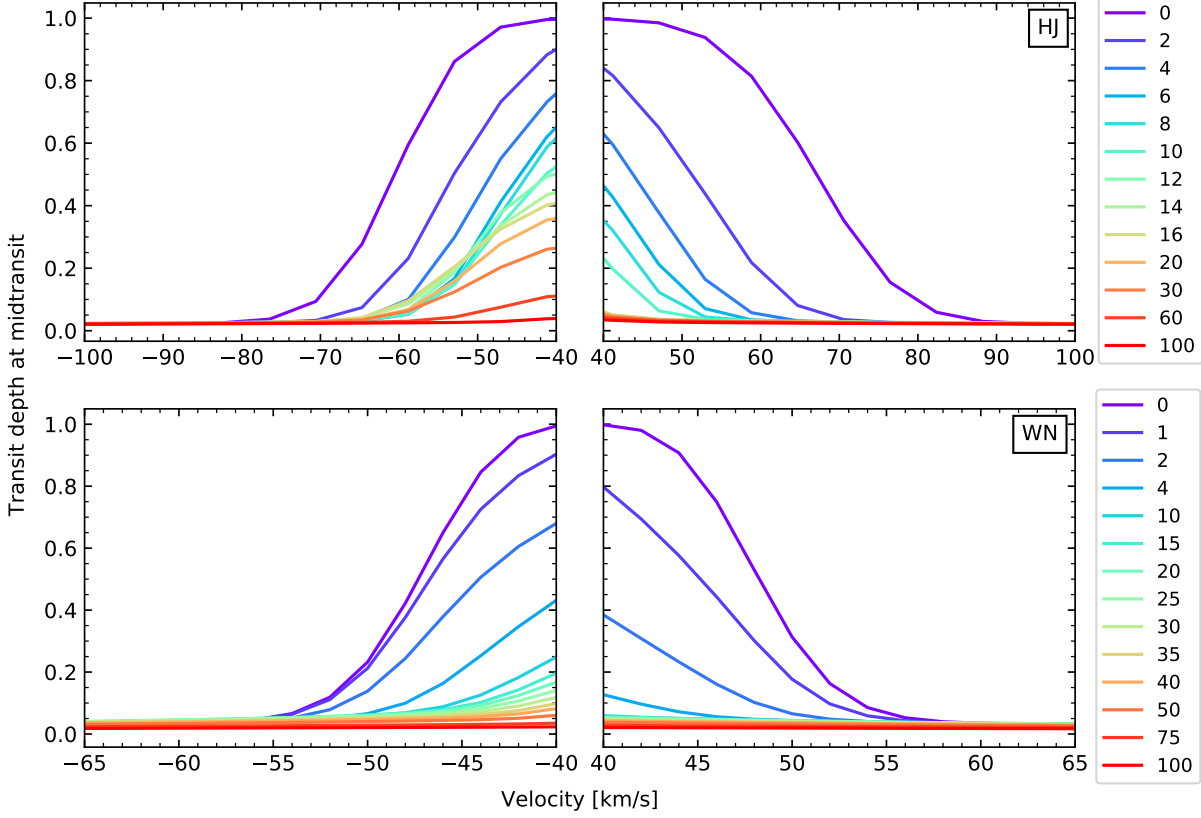


Figure 3.9: The blue (left) and red (right) wings of the in-transit Ly α line profile for each of my HJ (top) and WN (bottom) models. The colour shows the variation of stellar mass-loss rate from 0 to 100 \dot{M}_{\odot} . As the line centre is contaminated by interstellar absorption and geocoronal emission, I ignore the velocity range of -40 to 40 km/s. Note how the transit absorption is larger in the red wing for low stellar \dot{M} and larger in the blue wing for high stellar \dot{M} .

significantly (approximately 10% in the the HJ, 3% in WN) the atmospheric escape rate has not been affected as seen by the values on figure 3.10, and in figure 3.11. As mentioned in section 3.3, the stellar wind further confines the escaping planetary material, which in turn shapes the absorbing material around the planet. However for low stellar mass-loss rates the sonic surface of the atmospheric outflow is not yet affected, thus the escape rate remains unchanged.

We further investigate the relationship between total absorption (blue + red) and the atmospheric escape rate in figure 3.11. The filled and open circles represent the results for the HJ and WN models, respectively. The stellar wind mass-loss rate is increased from right

3.4 Reduced Ly- α Transit Depth Due To Stellar Wind Confinement

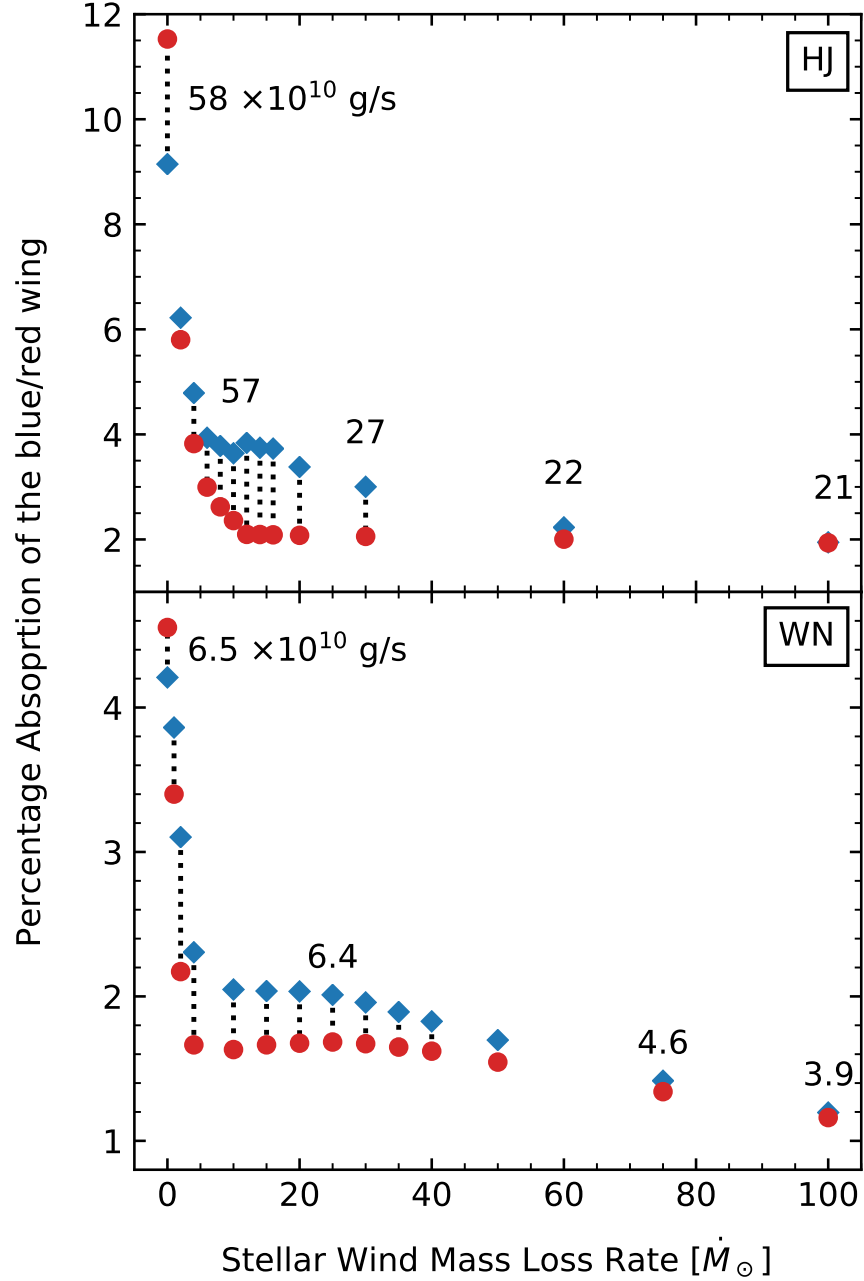


Figure 3.10: The percentage absorption in the blue (blue diamonds, -300 to -40 km/s) and red (red circles, 40 to 300 km/s) wings of Ly- α line as the stellar wind mass-loss rate is increased. The dotted line links points from the same model. The top panel shows the results for the HJ model while the bottom shows the WN models. At various points the atmospheric escape rate of the planet is marked in units of 10^{10} g/s.

3. THE EFFECTS OF THE STELLAR WIND ON LY- α TRANSITS

to left points, with the right-most point in each set being the one without the presence of a stellar wind (marked with an x). For each set of models, we see a region of the parameter space where, although the planetary escape rate is constant (marked with dotted lines), the transit absorption is not. As mentioned previously, this is due to stellar wind confinement, whereby the increasing ram pressure of the stellar wind confines absorbing material closer to the planet, therefore covering a decreased region on the stellar disc (Vidotto & Cleary, 2020). In the HJ model set, a constant planetary escape rate of approximately $\dot{m}_{\text{HJ}} \simeq 5.5 \times 10^{11}$ g/s produces 6% to 21% absorption, depending on the stellar wind conditions. For the WN planet, a constant planetary escape rate of $\dot{m}_{\text{WN}} \simeq 6.5 \times 10^{10}$ g/s produces 4% to 9% absorption. This reflects what is seen in figure 3.10, where the absorption of each wing has changed significantly, but the escape rate has not. As previously discussed in section 3.3, in the models showing absorption within the quoted ranges, the sonic surface remains intact (my ‘closed’ scenario), so the escape rate is unaffected by the changing stellar wind. Above a mass-loss rate of $10 \dot{M}_{\odot}$ (or $20 \dot{M}_{\odot}$ for the WN model), i.e., below an absorption of approximately 6% for the HJ models (or 4% for the WN models), the stellar wind begins to open the sonic surface, causing reduced atmospheric escape. In the range of WN models examined, the escape rate is reduced by approximately 40%, from 6.5×10^{10} to 4×10^{10} g/s, changing the total absorption by about 7%. For comparison, a similar 40% reduction in the HJ set, say, from 5.8×10^{11} to 3.3×10^{11} g/s, in escape rate occurs over a 15% range in total absorption.

3.5 Discussion

3.5.1 Implications For Interpreting Ly- α Signatures

The results presented in section 3.4 emphasise the importance of considering the stellar wind when interpreting transit observations. For example, suppose that a planet similar to the HJ model is observed with 5.5% of absorption in the Ly- α line. In the presence of a stellar wind, I would interpret this observational result as being caused by a planetary outflow that has an intrinsic escape rate of $\sim 3 \times 10^{11}$ g/s (see Figure 3.11). However, had I not considered the presence of a stellar wind, I would have predicted a lower planetary escape rate, in order to reproduce this 5.5% observed transit absorption. This is because, without stellar wind confinement, the absorbing material can now occupy a greater volume

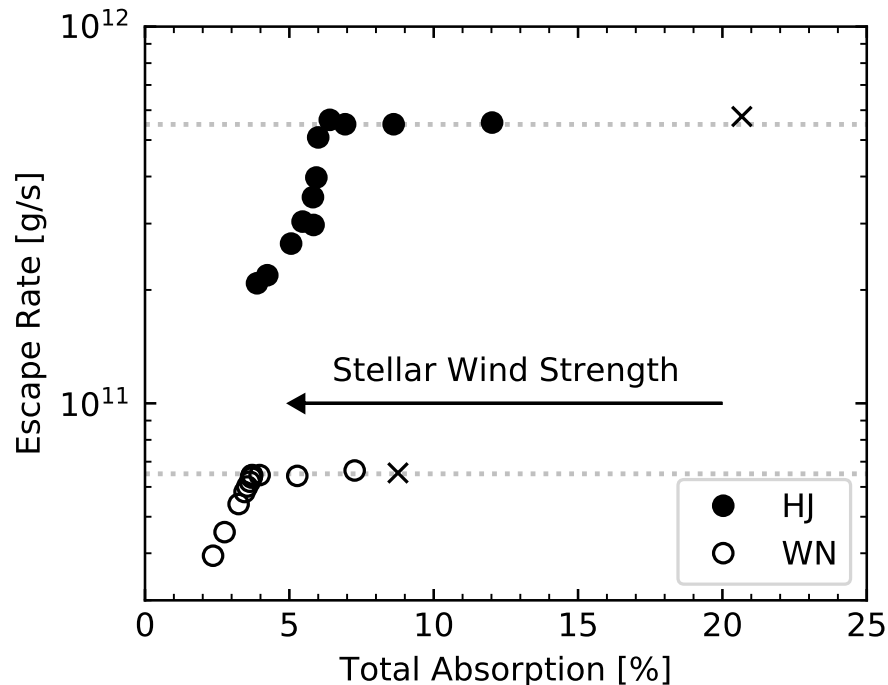


Figure 3.11: Atmospheric escape rate as a function of the percentage absorption of the blue+red wings of the Ly- α line at mid transit. The filled and open circles represent the HJ and WN models, respectively. For each set of models, we see a region where, although the escape rate is constant (marked with dotted lines), the transit absorption is not. The points marked with x are the models of each planet with no stellar wind, and from right to left, the stellar wind strength is increases (marked with an arrow).

around the planet, yielding the same percentage absorption for a lower escape rate. Therefore, given the degeneracy between planetary escape rates and stellar wind strengths for a same percentage absorption, I suggest that, in order to make a more accurate estimate of a planet’s atmospheric escape rate, one should also consider the presence of a stellar wind.

Another consequence found in this study is that stellar wind confinement can act to mask observational signatures of atmospheric escape in Ly- α . One instance of this could be with the sub-Neptune π Men c. The surprising lack of detection of Ly- α absorption led García Muñoz et al. (2020) to suggest a lack of Hydrogen in the atmosphere of π Men c. If this is indeed the case, they proposed that further observations of heavier elements, such as OI and CII lines, could still reveal a high atmospheric evaporation rate. An alternate explanation was proposed by Vidotto & Cleary (2020), who suggested that the atmosphere of π Men c could be Hydrogen-rich, but would remain undetected if a significant reduction

3. THE EFFECTS OF THE STELLAR WIND ON LY- α TRANSITS

in escape was caused by the stellar wind. They proposed that this could take place in π Men c as they found that the stellar wind interaction happened in the sub-sonic part of the planetary outflow.

As I showed here, the position where the interaction happens depends on the strength of the stellar wind and on the properties of the escaping atmosphere. One important parameter in atmospheric modelling is the stellar high-energy flux that is deposited on the planet's atmosphere. In Vidotto & Cleary (2020), they assumed a flux of $1340 \text{ erg cm}^{-2}\text{s}^{-1}$ and a stellar wind mass-loss rate of $1\dot{M}_{\odot}$ for π Men c. To investigate this further, Shaikhislamov et al. (2020) performed 3D simulations of the stellar wind of π Men c and, using a similar stellar wind condition and high-energy flux as those assumed in Vidotto & Cleary (2020), confirmed that the interaction was taking place in the sub-sonic regime, but did not obtain a significant reduction in the escape rate of the planet (only a reduction of 2.5% of the value obtained in their other simulations). I believe such a simulation performed by Shaikhislamov et al. (2020) falls in the partially-open scenario (middle panels in Figure 3.6).

Although I did not model the π Men system, I also found that the stellar wind might not necessarily lead to a significant reduction in escape rate, agreeing with Shaikhislamov et al. (2020). Nevertheless, when looking at the whole parameter space covered in my simulations, I found reduction in evaporation rates of up to 65% for the HJ simulations and 40% for the WN simulations. However, more importantly, I also found that this reduction is not linearly related to the depth of Ly- α transits. Even when the escape rate is not substantially reduced, the absorption signature of escaping atmosphere can be significantly affected. This is because the stellar wind confinement can change the volume of the absorbing material, without affecting too much the planetary escape rate.

3.5.2 Model Limitations

The aim of this chapter was to study in a systematic way how the stellar wind could affect atmospheric escape rates and how this would be observed in synthetic transits. This model is relatively fast to run, with a simulation taking about 8h to compute on 40 processors, although it could take longer in some cases. This enabled me to model nearly 30 different physical setups. However, this model can still be improved. For example, these 3D simulations model only the flow of ionised Hydrogen, and cannot capture the

asymmetry between day and night-side outflows. They are isothermal and ignore the effects of magnetic fields (included in chapter 5), radiation pressure and charge exchange (included in chapter 6).

A caveat of the 3D isothermal model is that I cannot match both the ram pressure and sonic point found in the 1D model¹. In this chapter, I chose to match the ram pressure of the escaping atmospheres, and as a result obtain sonic surfaces that are much closer to the planet than that predicted in the 1D model. To investigate how matching the sonic point would affect my results, I run one additional model of the WN planet in a $100 \dot{M}_{\odot}$ stellar wind, ensuring that the sonic point remains at the same position as the 1D model, ie., at $1.9 R_p$. This was done by reducing the temperature of the outflow from 5000 to 3100K, resulting in a sonic point that is further out, and a lower velocity outflow. I chose a base density such that escape rate for this model with no stellar wind matches that of the previous version, 6.5×10^{10} g/s. When the $100 \dot{M}_{\odot}$ stellar wind is injected into this model, I find that the atmospheric escape rate is reduced further than in the original, to 2.2×10^{10} g/s (previously 3.9×10^{10} g/s). This confirms that the further the sonic point is from the planet, the easier the stellar wind can disrupt this surface, with a greater reduction in escape rate being found. However it also places importance on advancing my 3D model, as although I have now matched the sonic point, the ram pressure of the outflow is lower than found in the 1D model. This lower ram pressure provides less resistance against the incoming stellar wind, which when accompanied by the higher sonic point means the stellar wind can more easily disrupt the inner regions of the escaping atmosphere and affect the escape rate.

As this model is isothermal, in the absence of orbital affects the outflow is isotropic: there is no difference between the day and night-side outflow (the self-consistent model in chapters 5 and 6 can capture this asymmetry). In reality this is not the case, as on a tidally locked planet the day-side will be highly illuminated, while the night-side, as the name suggests, will not be heated by stellar irradiation directly². This asymmetry will affect the structure of the outflow somewhat, with Carroll-Nellenback et al. (2017) showing using 3D HD simulations that the sonic surface of the escaping atmosphere is significantly different when assuming an isotropic versus an anisotropic temperature distribution at

¹It is a coincidence that the sonic point in the HJ simulation is at a similar distance in the 1D and 3D models

²Note that though there are mechanisms to transfer heat from the day to the night-side, such as day-night winds, the heating will still be largely asymmetric.

3. THE EFFECTS OF THE STELLAR WIND ON LY- α TRANSITS

the planetary boundary (their anisotropic model mimics a nightside of the planet). This obviously has implications on the atmospheric escape rate, with the anisotropic models of Carroll-Nellenback et al. (2017) showing an escape rate that was approximately 50% lower compared to the isotropic models. Temperature differences arise naturally in 3D models that solve for the radiative transfer of stellar photons through the planetary atmosphere (e.g. Debrecht et al., 2019; Carolan et al., 2021b; Hazra et al., 2022; Kubyshkina et al., 2022a). Although the day-night temperature differences are important to model, as they affect the planetary escape rate, I nevertheless expect that the hydrodynamic effects of the stellar wind on atmospheric escape is overall consistent to what I modelled here.

The presence of planetary magnetic fields, not included here yet, should also affect atmospheric escape. Owen & Adams (2014) demonstrated that magnetised exoplanets lose a factor of 4 to 8 times less mass than unmagnetised planets. This is because only a fraction of magnetic field lines around the planet remains open, along which ionised flows can escape. Khodachenko et al. (2015) found that a dipolar magnetic field of 1G around a HD209458b-analog planet was capable of reducing mass loss by up to an order of magnitude. Additionally, in the case of a magnetised planet, the planetary magnetic field can deflect the stellar wind (e.g. Carolan et al., 2019), which might no longer directly access the upper atmosphere of the planet.

Finally, my model neglects two physical processes, namely radiation pressure and charge exchange, both of which have been suggested to produce the population of neutral atoms that absorbs in the wing of Ly- α at high blue-shifted velocities (~ 100 km/s). I included both these processes in my model in chapter 6, where I will discuss their affect on the Ly- α transit line profile further.

3.6 Conclusions

We have seen significant progress in modeling atmospheric escape in close-in planets over the past two decades (Lammer et al., 2003; Murray-Clay et al., 2009; Bourrier & Lecavelier des Etangs, 2013; Villarreal D'Angelo et al., 2018; Debrecht et al., 2020). However, many current models still neglect the interaction of the planet's upper atmosphere with the wind of the host star. In particular, 1D hydrodynamic escape models are unable to treat the presence of the stellar wind – for that, multi-dimensional simulations are required. It has been demonstrated that the wind of the host star can affect atmospheric escape in

exoplanets (Matsakos et al., 2015; Shaikhislamov et al., 2016; Villarreal D’Angelo et al., 2018; McCann et al., 2019; Vidotto & Cleary, 2020). However, a current open question is in which systems the stellar wind would mostly likely affect atmospheric escape. One particular issue is that we do not have a full picture of how winds of cool dwarf stars vary from star to star. Cool dwarf stars are the most commonly known planet-hosts, but their winds are difficult to probe, with only a few techniques currently providing stellar wind measurements (e.g. Wood et al., 2005; Vidotto & Donati, 2017; Fichtinger et al., 2017; Jardine & Collier Cameron, 2019).

In this chapter (Carolan et al., 2021a), I systematically examined the effects of stellar winds on planetary atmospheric escape to determine whether and when neglecting the presence of the stellar wind is justified. I used 3D HD simulations to model the escaping planetary atmosphere interacting with the stellar wind, which was injected in the simulation domain through an outer boundary. We performed this study on two different gas giant planets, a Hot Jupiter similar to HD209458b but orbiting a more active star (HJ) and a Warm Neptune similar to GJ3470b (WN), and varied the stellar wind mass-loss rate from 0 to $100\dot{M}_{\odot}$, where $\dot{M}_{\odot} = 2 \times 10^{-14} M_{\odot}/\text{yr}$ is the present-day solar mass-loss rate. In total, I performed nearly 30 3D HD simulations of these systems.

For both planets, I found that as the stellar wind mass-loss rate was increased the planetary outflow was confined closer to the planet. As this confinement moved closer to the planet, planetary material could not properly accelerate, which eventually inhibited the dayside outflow from reaching super-sonic speeds. The inner regions of the escaping atmosphere were then affected, causing a reduced escape rate. For the HJ planet, the escape rate was reduced from 5.8×10^{11} g/s, when no stellar wind was considered, to 2.1×10^{11} g/s, when a wind with $100\dot{M}_{\odot}$ was considered. For the WN model, the planetary escape rates varied from 6.5×10^{10} g/s (no stellar wind) to 3.9×10^{10} g/s (strongest wind).

This reduction happened more suddenly in the HJ models than in the WN models, which I proposed is related to the distance of the sonic point. As the stellar wind strength increases, the escaping atmosphere is confined closer to the planet. This eventually disturbs the sonic surface of the outflowing atmosphere, transitioning from a “closed” to an “open” sonic surface configuration as seen in figure 3.6. This is ultimately what reduces the escape rate of the planet’s atmosphere, as the stellar wind now interacts with a subsonic planetary outflow and prevents an outflow from fully developing (Christie et al., 2016; Vidotto & Cleary, 2020). As the sonic point in the HJ models is further from the planet,

3. THE EFFECTS OF THE STELLAR WIND ON LY- α TRANSITS

the stellar wind can more easily affect it, so we see the escape rate of the HJ planet change over a short range in \dot{M} . In the WN planet, the sonic surface is very close to the planet. The stellar wind must now confine the escaping atmosphere much closer to the planet for the sonic surface to be affected, which results in a much more gradually transition from “closed” to “open” sonic surfaces in these models.

Using a ray-tracing technique, I investigated the possible observational signatures of this escape rate reduction in Ly- α transits. I found significant asymmetry towards the blue wing at mid-transit, which is to be expected when the day-side (redshifted) material is suppressed, and more material is funneled towards the planetary comet-like tail. This happens in the cases with larger stellar wind mass-loss rates. In the scenarios where only a weak wind (or no wind) were considered, the absorption in the red wing of the Ly- α line was larger, as some planetary material flows towards the star.

We also found that the changes caused in the atmospheric escape rate by the stellar wind affects Ly- α transits in a non-linear way. Across my set of models, the escape rate of the HJ planet was reduced from by 65% with the Ly- α absorption changing from 20.7 to 3.9%. For the WN planet, the escape rate was reduced by 40%, with a corresponding change in Ly- α absorption from 8.8% to 2.4%. However above 14% absorption in the HJ set (5% in the WN set) despite the percentage absorption changing significantly the atmospheric escape rate did not. These models represent the “closed” sonic surface models, where despite the volume of absorbing material changing, the sonic surface remains unaffected and so the escape rate does not vary. I concluded that the same atmospheric escape rate can therefore produce a range of absorptions depending on the strength of the stellar wind.

Neglecting the stellar wind when interpreting Ly- α observations can also lead to underestimations of the planet’s atmospheric escape rate. An unconfined escaping atmosphere can occupy a larger volume around the planet, and so a lower escape rate is required to produce significant absorption. Contrary to this, if the escaping atmosphere is confined by a strong stellar wind, a higher escape rate can produce the same absorption as the unconfined scenario, as the density of absorbing material increases. These degeneracies emphasise the importance of considering the stellar wind when interpreting transmission spectroscopic transits, in order to accurately estimate the atmospheric escape rate.



The Dichotomy Of Atmospheric Escape In AU Mic b

In the previous chapter, I discussed additions made to my 3D model in order to study close-in exoplanets, and their escaping atmospheres. I found that a strong stellar wind can confine the escaping atmosphere such that its observational signatures are removed, despite their still significant escape rates. Here I apply this model to AU Mic b. This newly discovered planet provides an interesting laboratory to test stellar wind confinement: on one hand AU Mic is a young M-dwarf and so AU Mic b should be highly irradiated and show strong atmospheric escape. On the other, a young M dwarf should produce a strong stellar wind, which I have shown can confine the escaping atmosphere.

This chapter is presented as follows. In section 4.1 I briefly contextualise this work and recap stellar wind confinement. I briefly discuss the setup of these models in section 4.2, before presenting the results of this study in section 4.3. Finally my conclusions are discussed in section 4.4. This work has been published in Carolan et al. (2020).

4.1 Context

AU Microscopii (AU Mic) is the second closest pre-main sequence star to the solar system (9.79 pc). With an age of approximately 22 Myr, it is orbited by an edge-on debris disk, within which lies the recently discovered planet, AU Mic b (Plavchan et al., 2020). AU Mic b is a Neptune sized planet ($R_p = 1.08R_{Nep}$, $M_p = 0.69M_{Nep}$), on a close-in orbit ($P_{orb} = 8.46\text{days}$, $a = 0.066\text{au}$). Two transits of the planet were detected in NASA's Transiting Exoplanet Survey Satellite (TESS) mission, where AU Mic was observed for the

4. THE DICHOTOMY OF ATMOSPHERIC ESCAPE IN AU MIC B

first 27 days of the survey (with the planetary mass obtained from an additional radial velocity measurement). Detections of such young exoplanets are still rare, given that young stars like AU Mic pose many observational challenges for planet detection, such as the presence of spots and frequent flares. AU Mic b can therefore provide unique insights into newly formed planets and their atmospheres.

Due to its youth and activity, AU Mic emits a large flux of high-energy photons in the extreme-ultraviolet (EUV). Combined with the small orbital distance (0.066 au), the estimated EUV flux impinging on AU Mic b is $4.7 \times 10^3 \text{ erg cm}^{-2} \text{ s}^{-1}$, and can be as high as $2.2 \times 10^4 \text{ erg cm}^{-2} \text{ s}^{-1}$ when the star is in flaring state (stellar fluxes from Chadney et al. 2015). These values are 10–50 times larger than the estimated flux received in HD209458b of $450 \text{ erg cm}^{-2} \text{ s}^{-1}$ (Murray-Clay et al., 2009), a Hot Jupiter that shows strong atmospheric evaporation (Vidal-Madjar et al., 2003). By analogy, one would expect that AU Mic b would be strongly evaporating. Additionally, due to the youth of the system, the planet likely still has its original atmosphere, which would be mainly composed of Hydrogen, if one formed with the planet. The strong evaporation of a Hydrogen-rich atmosphere, such as the one AU Mic b could host, is best probed in Hydrogen lines such as in Ly- α during the planet’s transit, as discussed in previous chapters. AU Mic b’s transit lends favourably to follow-up observations aimed at investigating the existence and extent of an escaping atmosphere, given that its relatively low impact parameter ($b = 0.16$) and star-planet radius ratio ($R_p/R_* = 0.0514$) leave a significant area of the stellar disc to be covered by the escaping atmosphere during the transit.

In chapter 3 I showed that one important point to consider when studying planetary evaporation is that the escaping atmospheres do not expand into an empty space, but rather the atmosphere pushes its way into the stellar wind. The stellar wind of cool dwarfs consists of a hot, ionised plasma, that is embedded in the stellar magnetic field (Vidotto et al., 2015). Stellar winds can affect atmospheric evaporation of close-in exoplanets (e.g., McCann et al., 2019; Shaikhislamov et al., 2020; Carolan et al., 2020, 2021a,b). In particular, the stronger the stellar wind is, the larger is the pressure it exerts in the planetary atmosphere. In a simplified way, we can think of this as the interaction of two fluids. The point where the two fluids meet is determined by pressure balance. Therefore, the stronger the stellar wind is, the point where balance is achieved is reached deeper in the evaporating atmosphere, which, as a consequence, is forced to occupy a smaller volume.

If the interaction happens so deep in the planetary atmosphere, where the planetary

4.2 Atmospheric Escape And Synthetic Ly- α Transit Models

outflow is still subsonic, the stellar wind can substantially reduce the evaporation (Christie et al., 2016; Vidotto & Cleary, 2020). Using 3D HD simulations, I performed a systematic study of the effects of the stellar wind on the evaporation rate of a typical Hot Jupiter (chapter 3, Carolan et al., 2021a). I showed that for weaker stellar winds, the reduction in planetary escape rate was very small. Nevertheless, because the atmosphere was forced to occupy a smaller volume, spectroscopic transit signatures were substantially affected. The atmospheric escape rates remained approximately constant ($\simeq 5.5 \times 10^{11}$ g/s), while its Ly- α transit absorption changed from 24% to 14% as the stellar wind mass-loss rate was only moderately increased from ‘no wind’ to a wind with a mass-loss rate that is 10 times the solar value of $\dot{M}_{\odot} = 2 \times 10^{-14} M_{\odot} \text{ yr}^{-1}$. However, in a stronger stellar wind, a more substantial reduction in evaporation rates was seen, particularly when this interaction started to occur below the sonic surface of the planetary outflow. For a stellar wind mass-loss rate of $100 \dot{M}_{\odot}$, the evaporation rate had reduced 65% and the absorption in the Ly- α line went down to less than 5%.

This leads to a dichotomy for the AU Mic system. While, due to the large EUV flux impinged on the atmosphere, the evaporation rate of a close-in planet is expected to be very strong during its youth, the stellar wind is also stronger at young ages (Vidotto & Donati, 2017; Carolan et al., 2019). AU Mic in particular is thought to have a wind mass-loss rate that is larger than solar. Theoretical estimates range from $10 \dot{M}_{\odot}$ (Plavchan et al., 2009) to $1000 \dot{M}_{\odot}$ (Strubbe & Chiang, 2006; Chiang & Fung, 2017).

To investigate what could be possibly happening in the AU Mic system and to guide whether strong evaporation could be detected in Ly- α transits, I study how the wind of AU Mic could affect the evaporation rate of AU Mic b and its predicted transit. For that, I use 3D HD simulations (see section 3.2) followed by synthetic line profile calculations (see section 1.7) that investigate the effect increasing the strength of the stellar wind has on Ly- α transits of AU Mic b. In section 4.2 I discuss the setup of my model for this system.

4.2 Atmospheric Escape And Synthetic Ly- α Transit Models

I use the model presented in chapter 3 (Carolan et al., 2021a) to study the effects of the stellar winds on AU Mic b. I assume a planetary mass of $0.69 M_{\text{Nep}}$ and radius of $1.08 R_{\text{Nep}}$.

4. THE DICHOTOMY OF ATMOSPHERIC ESCAPE IN AU MIC B

The stellar mass and radius are $M_* = 0.5 M_\odot$ and $R_* = 0.75 R_\odot$. The orbital distance is $a = 0.066$ au, transit duration is 3.5h and the impact parameter is $0.16R_*$. All these values are from Plavchan et al. (2020), with the planetary mass obtained from additional radial velocity measurements. Figure 4.1 shows the output of one of my simulations, after reaching steady state.

To calculate the Ly- α transit profiles, I use the same ray-tracing technique detailed in chapter 1 (Allan & Vidotto, 2019). Stellar rays are shot through the planetary material, which is represented by the volume entailed by the grey surface in figure 4.1. Because the 3D model does not treat the neutral material of the planetary outflow, I use a post-processing technique to estimate its ionisation fraction f_i (see chapter 3). This is done using the 1D atmospheric escape model of Allan & Vidotto (2019), where I assume an EUV luminosity of $1.5 \times 10^{-5} L_\odot$ appropriate for the quiescent state of AU Mic (Chadney et al., 2015). With this, I derive the density of neutrals as $n_n = n_p(1 - f_i)/f_i$, where n_p is the proton density from my 3D simulations.

Similar to chapter 3, the results of the 1D model are also used to constrain the free parameters in the 3D simulations, namely the atmospheric base temperature and density. The 1D model solves the energy equation of the planetary outflow assuming photoionisation by stellar EUV photons and Ly- α cooling (Allan & Vidotto, 2019). As a result, the atmospheric temperature varies from 1000K at $1R_p$ to nearly 8000 K at $\sim 2R_p$, and cools beyond that. I pick an intermediate temperature of 5300 K for the 3D model. I also chose the base density of the 3D simulations such that it matches the predicted escape rate of 6.5×10^{10} g/s from the 1D model.

4.3 Variation Of The Stellar Wind Strength

I perform 5 simulations where I systematically vary the stellar wind mass-loss rate: $\dot{M} = 0$ (no wind), 1, 10, 100 and 1000 \dot{M}_\odot . I use a temperature of 2MK for the stellar wind, so that the stellar wind is always injected with the same velocity (about 540 km/s). As this is a thermally-driven wind, the wind velocity is independent of the density, so changing \dot{M} while the velocity structure is constant solely changes the density profile of the injected stellar wind (see section 1.3).

Figure 4.2 shows the orbital slice of each of these simulations. We see that as the stellar wind mass-loss rate (and thus its ram pressure) is increased, the escaping atmosphere is

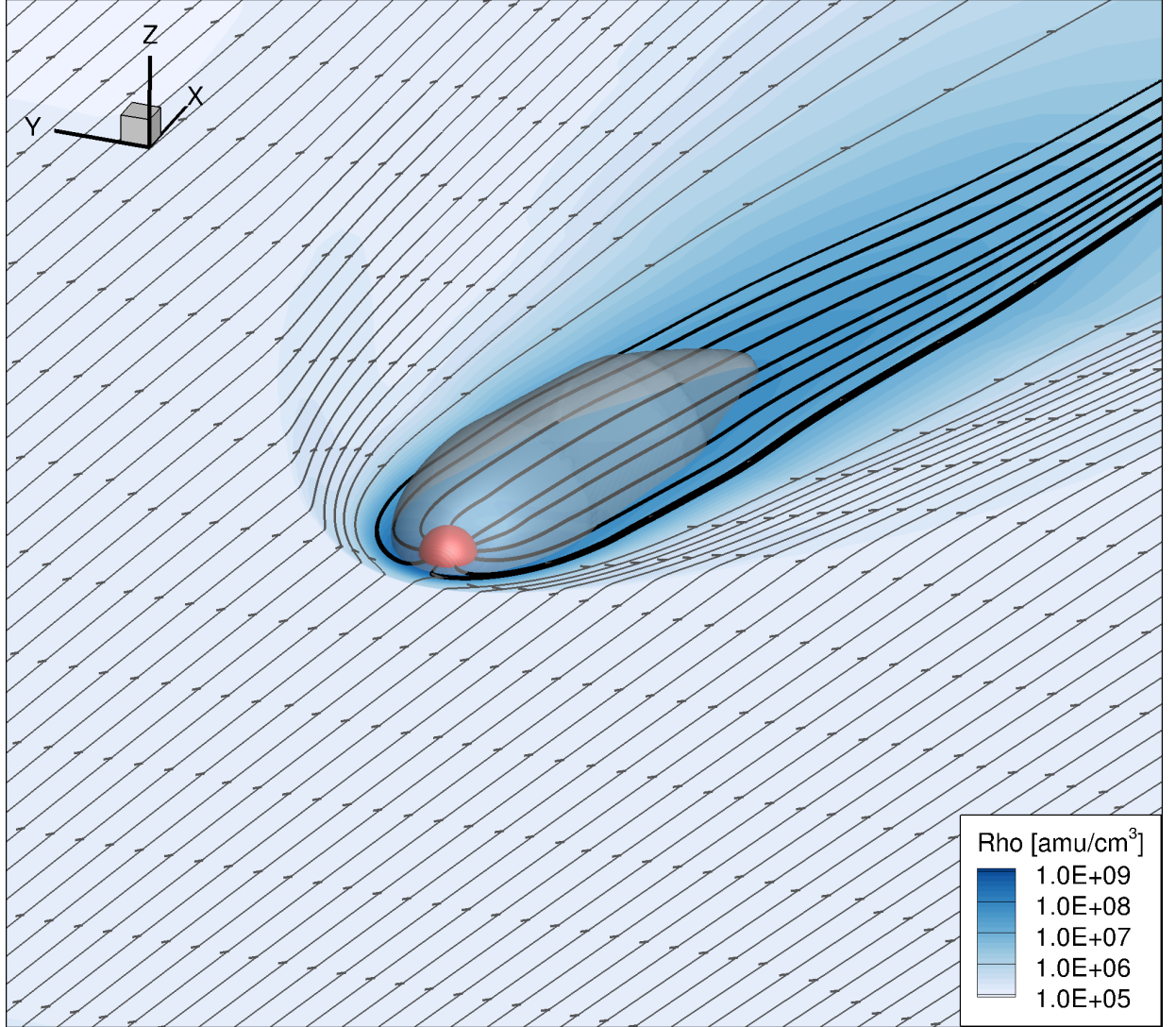


Figure 4.1: Atmospheric escape of AU Mic b, when it interacts with a stellar wind with $\dot{M} = 100\dot{M}_{\odot}$. The stellar wind is injected in the negative x . Its streamlines are shown in grey, while the black streamlines represent the velocity field of the planetary outflowing atmosphere. The density is shown in the equatorial plane and the grey surface around the planet shows the region used in the synthetic transits (with temperature $\lesssim 1.1T_p$, section 4.2).

4. THE DICHOTOMY OF ATMOSPHERIC ESCAPE IN AU MIC B

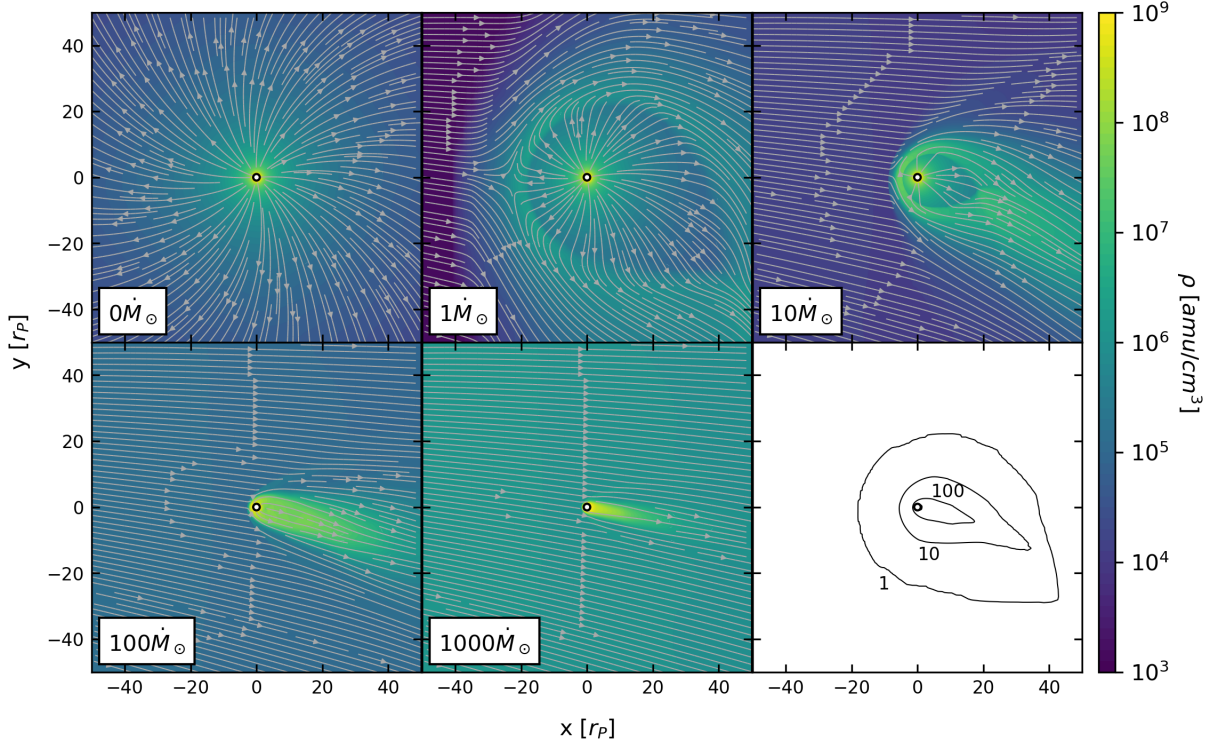


Figure 4.2: Density structure and velocity streamlines in the planet’s reference frame for the 5 simulations I run for varying stellar wind \dot{M} , quoted on the first five panels. The planet is shown at the center of the grid on the orbital plane. As the stellar wind that is injected in the negative x boundary has a larger \dot{M} , the escaping atmosphere of AU Mic b is forced into smaller volumes. The last panel shows the iso-contours of temperature at approximately the temperature I adopt for the planetary atmosphere. Material within these contours belong to the planet and are used in the synthetic calculations of the Ly- α transit profiles. The numbers shown next to each iso-contour represent the stellar wind mass-loss rate in \dot{M}_\odot . The inner-most contour is for the case with $1000\dot{M}_\odot$ (label not shown).

confined closer to the planet, and forced to occupy a smaller volume. The position where the interaction happens eventually disrupts the sonic surface (originally at $1.3R_p$) of the escaping atmosphere, such that parts of the planetary outflow, especially on the dayside, can no longer accelerate to supersonic speeds. When this happens, we see a stronger decrease in the escape rate of the planetary atmosphere.

I calculate the escape rate by integrating the mass flux through concentric spheres around the planet. These values are given in table 4.1, where we see that the escape rate is unaffected in the 1 and 10 \dot{M}_\odot models, and they are very similar to the values I

4.3 Variation Of The Stellar Wind Strength

Table 4.1: Simulation results showing the stellar wind mass-loss rate (\dot{M}), planetary atmosphere escape rate (\dot{m}), absorption in the blue ([-100,-36] km/s) and red ([36,100] km/s) wings of the Ly- α line and the sum of these absorptions.

\dot{M} (\dot{M}_\odot)	\dot{m} (10^{10} g/s)	ΔF_{blue} (%)	ΔF_{red} (%)	ΔF_{tot} (%)
0 (no-wind)	6.5	9.9	10	20
1	6.5	9.8	5.8	16
10	6.3	4.1	1.4	5.5
100	5.9	1.4	1.1	2.5
1000	3.2	0.25	0.25	0.5

obtain in the ‘no wind’ model. In the 100 \dot{M}_\odot model the escape rate has decreased slightly from 6.5×10^{10} to 5.9×10^{10} g/s. This is the first of my computed models where the wind is capable of sufficiently confining the escaping atmosphere such that the dayside sonic surface is disrupted. The dayside flow is no longer able to reach supersonic speeds. Material continues to outflow from the planet but they are funnelled back towards the comet-like tail (better seen in figure 4.1). The nightside sonic surface remains unaffected, so only a small decrease in escape rate is found in this model. This is not the case in the 1000 \dot{M}_\odot model, where the stellar wind confines the escaping atmosphere such that the sonic surface on all sides of the planet is affected. This results in a 50% lower escape rate, when compared to other models.

I investigate the effect this confinement has on the Ly- α transit by performing synthetic transit calculations. To ensure that the material I use in the ray-tracing computation is planetary, I use a temperature cut-off that is 10% higher than the planetary outflow and follow the description presented in section 4.2. The contours of this temperature cut-off are seen in the last panel of figure 4.2 for the orbital plane, further illustrating how the confinement of the planetary atmosphere varies in each model.

None of my models are saturated at line centre (i.e., 100% absorption), but models with 0 and 1 \dot{M}_\odot reach more than 95% absorption at line centre. However, given the line centre of the Ly- α line is contaminated by geocoronal emission and interstellar absorption (assuming the stellar and ISM radial velocities are $\simeq 0$), I do not consider the line centre [-36, 36] km/s in the results presented next. The blue [-100, -36] km/s and red [36, 100] km/s wings of the Ly- α line are shown in figure 4.3a and b, respectively. The absorption computed in these velocity intervals $\int_{v_i}^{v_f} \Delta F_v dv / (v_f - v_i)$ are shown in table 4.1 and figure 4.3c, where v_i and v_f are initial and final velocities in the ranges quoted above.

4. THE DICHOTOMY OF ATMOSPHERIC ESCAPE IN AU MIC B

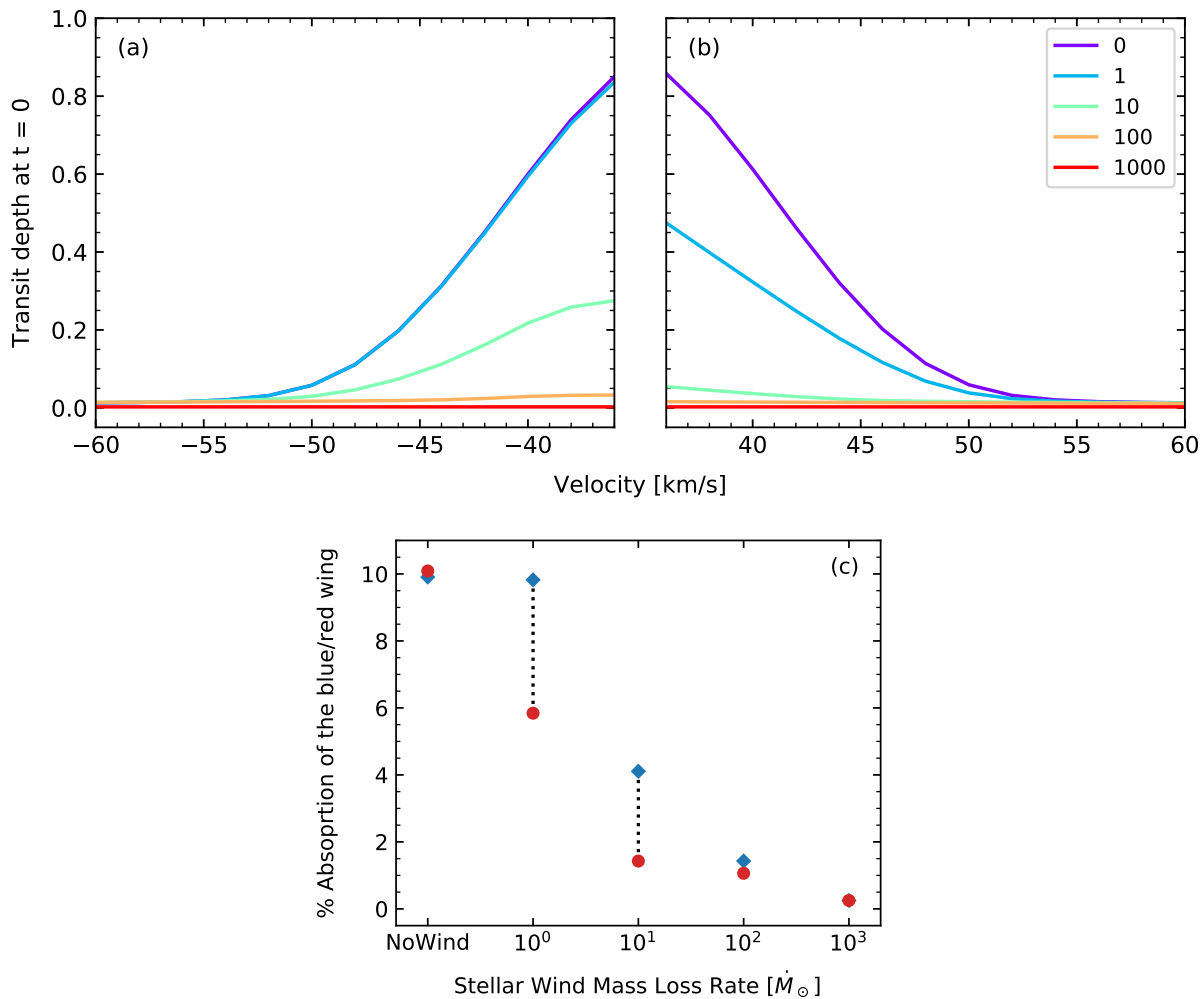


Figure 4.3: (a) and (b) Transit depth of the Ly- α line computed at mid-transit for the blue (≤ -36 km/s) and red (≥ 36 km/s) wings, respectively, as a function of Doppler velocity. (c) Integrated absorption in the blue (blue diamonds) and red (red circles) wings of the Ly- α line calculated at mid-transit, as a function of the stellar wind mass-loss rate. Table 4.1 shows these values and the total absorption.

The no-wind model is the only case where the line profile is nearly symmetric in both wings. Line asymmetry is already seen in model $1\dot{M}_\odot$. Despite the escape rate of the planet remaining unchanged for models 0, 1 and $10\dot{M}_\odot$, the Ly- α absorption has changed significantly when compared to the no-wind model. For the $10\dot{M}_\odot$ model, we see a greater reduction in the red wing absorption, as the planetary flow towards the star is suppressed by the stellar wind. Though we still see blue wing absorption in the $10\dot{M}_\odot$ model, it has been significantly reduced compared to the 0 and $1\dot{M}_\odot$ models. This is because the stronger stellar wind reduces the volume of the comet-like tail, which contains most of the blue-shifted absorbing material. The volume of absorbing material is further reduced in the $100\dot{M}_\odot$ model such that very little blue wing absorption is found, and essentially no detectable red wing absorption. The $1000\dot{M}_\odot$ stellar wind confinement has not only reduced the escape rate of the planet by 50% but also completely masked the observational signatures of this escape in Ly- α , as I find no red or blue wing absorption.

4.4 Discussion And Conclusions

I investigated here the dichotomy of atmospheric escape in the newly discovered exoplanet AU Mic b. On one hand, the high EUV flux from young host stars is expected to cause strong atmospheric escape (Kubyshkina et al., 2018). On the other hand, the star is expected to have a strong stellar wind (10 to $10^3\dot{M}_\odot$, Strubbe & Chiang, 2006; Plavchan et al., 2009), which can reduce the rate of atmospheric escape from the planet (Vidotto & Cleary, 2020; Carolan et al., 2021a). To investigate this dichotomy, I modelled the interaction between the wind of AU Mic with the escaping atmosphere of AU Mic b, by performing 3D HD simulations of the system. I considered a number of stellar wind mass-loss rates from $\dot{M} = 0$ to $10^3\dot{M}_\odot$. I found that increasing \dot{M} confines the escaping planetary atmosphere, which occupies a smaller volume. When this confinement disrupts the sonic surface of the planetary outflow, I see a more substantial reduction in the escape rate. For the models with 0, 1 and $10\dot{M}_\odot$ the escape rate is unaffected and remains 6.5×10^{10} g/s. In the $100\dot{M}_\odot$ model, the escape rate decreases slightly from 6.5×10^{10} to 5.9×10^{10} g/s. However, for the $1000\dot{M}_\odot$ model, escape rates is reduced by 50%, with a value of 3.2×10^{10} g/s. From an evolutionary point of view, a factor of 2 in the escape rate is negligible. The reduction is likely to be more important at young ages, when the stellar wind is stronger, but it is worth recalling that the evaporation of the planet is also stronger at younger ages,

4. THE DICHOTOMY OF ATMOSPHERIC ESCAPE IN AU MIC B

so investigating which process “wins” (wind vs EUV flux) is an important point to consider in future studies of planetary evolution.

The reduction in evaporation affects the Ly- α transit absorption differently. I calculated synthetic Ly- α line profiles at mid-transit and found that, although we still see blue wing absorption in the $10\dot{M}_{\odot}$ model, it is significantly smaller than the 0 and $1\dot{M}_{\odot}$ models. This happens even though no appreciable reduction is seen in the escape rate of these 3 models. This is because the stronger stellar wind reduces the volume of the comet-like tail, which contains most of the blue-shifted absorbing material. For the $10^3\dot{M}_{\odot}$ model, I found almost no Ly- α absorption, as most of the absorbing material is confined to a small volume around the planet. My models do not consider the charge-exchange process, which converts low velocity planetary neutral atoms to ions and, and high velocity stellar wind ions to energetic neutral atoms (Shaikhislamov et al., 2020). The net effect of this process is to shift absorption from the line centre to the blue wing. Given the already low absorption around line centre in the $> 100\dot{M}_{\odot}$ models (low volume occupied by absorbing material) shifting this to higher velocities by charge-exchange will not greatly alter absorption at line wings. Charge exchange can be more important for models with lower \dot{M} , given the volume containing neutrals is much larger than the higher \dot{M} models.

A few years ago, Chadney et al. (2015) predicted escape rates of a fictitious planet orbiting AU Mic. They assumed a Hot Jupiter planet similar to HD209458b at 0.2au, and obtained a strong evaporation rate of 1.2×10^{10} g/s. Due to differences in the planet parameters, a comparison between my results and theirs is not straightforward. If we were to ‘move’ their fictitious planet to the orbit of AU Mic b, I estimate a factor of $(0.2/0.066)^2 \simeq 9$ (i.e., linear with EUV flux) increase in their escape rates, bringing their estimates to 10^{11} g/s. This evaporation rate is about a factor of 2 larger than my ‘no wind’ model, but is on the same order of magnitude. Note though that we are comparing two different planets: a fictitious Hot Jupiter and AU Mic b, which is a Warm Neptune, and that the differences in planetary gravity will affect escape rates (Allan & Vidotto, 2019).

The numbers I quoted in this chapter should be used with care, as they are dependent on assumptions I made for the system, such as the planetary escape rate in the no-wind model, which I set from an assumed EUV flux, and the stellar wind temperature, which I assumed is a typical coronal-like temperature of 2 MK. For example, the evaporation rate of a planet that has a sonic surface at a larger distance is more easily affected by the stellar wind. Likewise, a stellar wind that has a larger ram pressure more easily

disrupts the planet’s sonic surface, having a greater effect on the evaporation (I provide a more detailed discussion in chapter 3 on how different system characteristics affect the reduction of escape rate and absorption, from Carolan et al. 2021a). Another assumption I made is that the stellar wind is spherically symmetric (purely radial velocity and isotropic mass flux). If the star has a complex magnetic field topology, the stellar wind will not be isotropic, as the field geometry leads to a non-homogeneous stellar wind along the planetary orbital path (Vidotto et al., 2015). Even if I were to adopt slightly different values for the planet escape rate or stellar wind properties, the general conclusions I found here should remain valid. Namely, I concluded that should future Ly- α observations detect solely blue wing absorption during the transit of AU Mic b (i.e., little or no red-shifted absorption), the stellar wind mass-loss rate of AU Mic can be estimated to be $\sim 10\dot{M}_{\odot}$. Red-shifted absorption would imply mass-loss rates $\lesssim 10\dot{M}_{\odot}$. Should future observations find a non-detection in Ly- α transits, I propose that this could be due to stellar wind confinement of the escaping atmosphere. In this case, my models would allow us to place a lower limit on the mass-loss rate of AU Mic of $\gtrsim 100\dot{M}_{\odot}$. This would help clarify whether AU Mic has a moderately strong wind ($10\dot{M}_{\odot}$) or substantially stronger ($10^3\dot{M}_{\odot}$).

5

The Effects Of Magnetic Fields On Ly- α Transits

In the previous chapters, I presented an isothermal 3D model, demonstrating its ability to study a variety of different close-in exoplanets, before using it to investigate the newly discovered Warm Neptune: AU Mic b. This model, however, is not self-consistent, and requires the use of a 1D code to inform the inputs of the 3D model, in order to set the properties of the escaping atmosphere. To improve upon this, we combined these two codes, developing a 3D code capable of self-consistently launching an escaping atmosphere, including both neutral and ionised Hydrogen. The implementation of this code was first described in Hazra et al. (2022), a publication I co-authored. However the work of Hazra et al. (2022) was unable to handle magnetic fields. Through extensive development and testing of new boundary conditions, I arrive at a self-consistent 3D model capable of tracking the escape of both ionised and neutral Hydrogen from a magnetised exoplanet. In this chapter I use this code to investigate how magnetic fields change the observational signatures of a atmospheric escape from a Hot Jupiter. While keeping all other parameters constant (see table 5.1) I vary the dipole strength of the planet's magnetic field from 0 to 10 G, examining the change in the magnetosphere and mid-transit absorption in Ly- α .

This chapter is presented as follows. In section 5.1 I briefly contextualise this work, before presenting the details of the 3D model in section 5.2. In section 5.3 I discuss the effects of the planetary magnetic field on the geometry of the escaping atmosphere, while in section 5.4 I discuss the implications of this on the observational signatures in Ly- α . A discussion of the impact of these results can be found in section 5.5, while I sum up my conclusions in section 5.6. This work is published in Carolan et al. (2021b).

5.1 Context

There have been a number of works that investigate different aspects of how the planet's magnetic field affects escape and its observational signatures. Using 2D models, Trammell et al. (2014) showed that the transit depth increases strongly with magnetic field strength when the Hydrogen ionisation layer is magnetically dominated, while in the same year Owen & Adams (2014) demonstrated that the strength and geometry of the stellar magnetic field is crucial to determine the fraction of open field lines around the planet. Khodachenko et al. (2015) found that the atmospheric escape rate is weakly affected by field strengths $< 0.3\text{G}$, but reduced by an order of magnitude for a 1G field, which could potentially have huge implications on the lifetime of the planet's atmosphere. Though these have all used 2D models, Matsakos et al. (2015) performed 3D simulations of close-in magnetic star-planet interactions, identifying 4 classifications: bowshock, colliding winds, strong planetary wind causing accretion, and Roche-lobe overflow. Arakcheev et al. (2017) found a 70% reduction in WASP-12's escape rate with a model containing the planet's magnetic field and stellar wind, though not the magnetic field of the stellar wind / star. Using 3D global simulations of HD 209458b, Villarreal D'Angelo et al. (2018) showed that the shape of the Ly- α line depends on both the stellar and planetary fields, as they control the geometry of the magnetosphere and the amount of neutrals inside it. Finally Harbach et al. (2021) used MHD models to demonstrate the dependence of the magnetosphere and Ly- α absorption on the stellar wind, though their model did not self-consistently calculate the heating and photoionisation due to stellar UV irradiation, and ignored close-in orbital forces. To the best of my knowledge, to date there has not been a 3D self-consistent radiative MHD model capable of resolving the inner most regions of the escaping atmosphere, which contains both the stellar and planetary magnetic fields. In this chapter I present such a model, and use it to investigate the effect of magnetic fields on the escaping atmosphere and their observational signatures.

5.2 3D Self-Consistent Radiative MHD Simulations

To model the escaping atmosphere in the presence of a magnetic field, I build upon the non-magnetised code presented in Hazra et al. (2022), which uses the BATS-R-US framework (Tóth et al., 2005). This model is an extensive update to that presented in chapter 3 (used

5. THE EFFECTS OF MAGNETIC FIELDS ON LY- α TRANSITS

in Carolan et al. 2020, 2021a), including new physics: the heating, cooling, ionisation and recombination of neutral and ionised Hydrogen, calculated during runtime. While the simulations of Hazra et al. (2022) were hydrodynamic, I adapt this model to investigate how magnetic fields affect atmospheric escape and its observational signatures. This is the first 3D self-consistent radiative MHD model of photoevaporation of an exoplanet using the BATS-R-US framework. The output of one such model is shown in figure 5.1.

I simulate the escaping atmosphere in a 3D Cartesian grid $[-30:50, -40:40, -30:30 R_p]$, with a maximum resolution of $1/16 R_p$ inside $5 R_p$. Similar to chapter 3, for simplicity I assume that the exoplanet is centered on the origin of the coordinate system, is tidally locked to its host star located outside the numerical domain at negative x , with the simulations performed in the co-rotating/ co-orbiting reference frame. The model now solves updated ideal MHD equations: the mass conservation; momentum conservation; energy conservation and induction equations respectively:

$$\frac{\partial \rho}{\partial t} + \nabla \cdot \rho \mathbf{u} = 0, \quad (5.1)$$

$$\frac{\partial(\rho \mathbf{u})}{\partial t} + \nabla \cdot \left[\rho \mathbf{u} \mathbf{u} + (P_T + \frac{B^2}{8\pi}) \mathbf{I} - \frac{\mathbf{B} \mathbf{B}}{4\pi} \right] = \rho \left(\mathbf{g} - \frac{GM_*}{|\mathbf{R}|^2} \hat{R} - \boldsymbol{\Omega} \times (\boldsymbol{\Omega} \times \mathbf{R}) - 2(\boldsymbol{\Omega} \times \mathbf{u}) \right), \quad (5.2)$$

$$\begin{aligned} \frac{\partial \epsilon}{\partial t} + \nabla \cdot \left[\mathbf{u} \left(\epsilon + P_T + \frac{B^2}{8\pi} \right) - \frac{(\mathbf{u} \cdot \mathbf{B}) \mathbf{B}}{4\pi} \right] = \\ \rho \left(\mathbf{g} - \frac{GM_*}{|\mathbf{R}|^2} \hat{R} - \boldsymbol{\Omega} \times (\boldsymbol{\Omega} \times \mathbf{R}) \right) \cdot \mathbf{u} + \mathcal{H} - \mathcal{C}, \end{aligned} \quad (5.3)$$

$$\frac{\partial \mathbf{B}}{\partial t} + \nabla \cdot (\mathbf{u} \mathbf{B} - \mathbf{B} \mathbf{u}) = 0. \quad (5.4)$$

The total energy density ϵ is

$$\epsilon = \frac{\rho u^2}{2} + \frac{P_T}{\gamma - 1} + \frac{B^2}{8\pi}, \quad (5.5)$$

γ is the adiabatic index, which I set to $5/3$. In the momentum equation 5.2, the source terms are the same as the isothermal model in chapter 3: the planet's gravity, the stellar gravity, the centrifugal and Coriolis forces. The energy conservation equation 5.3 now contains \mathcal{H} and \mathcal{C} terms, denoting the volumetric heating and cooling rates due to stellar radiation. The volumetric heating rate due to stellar radiation is given by:

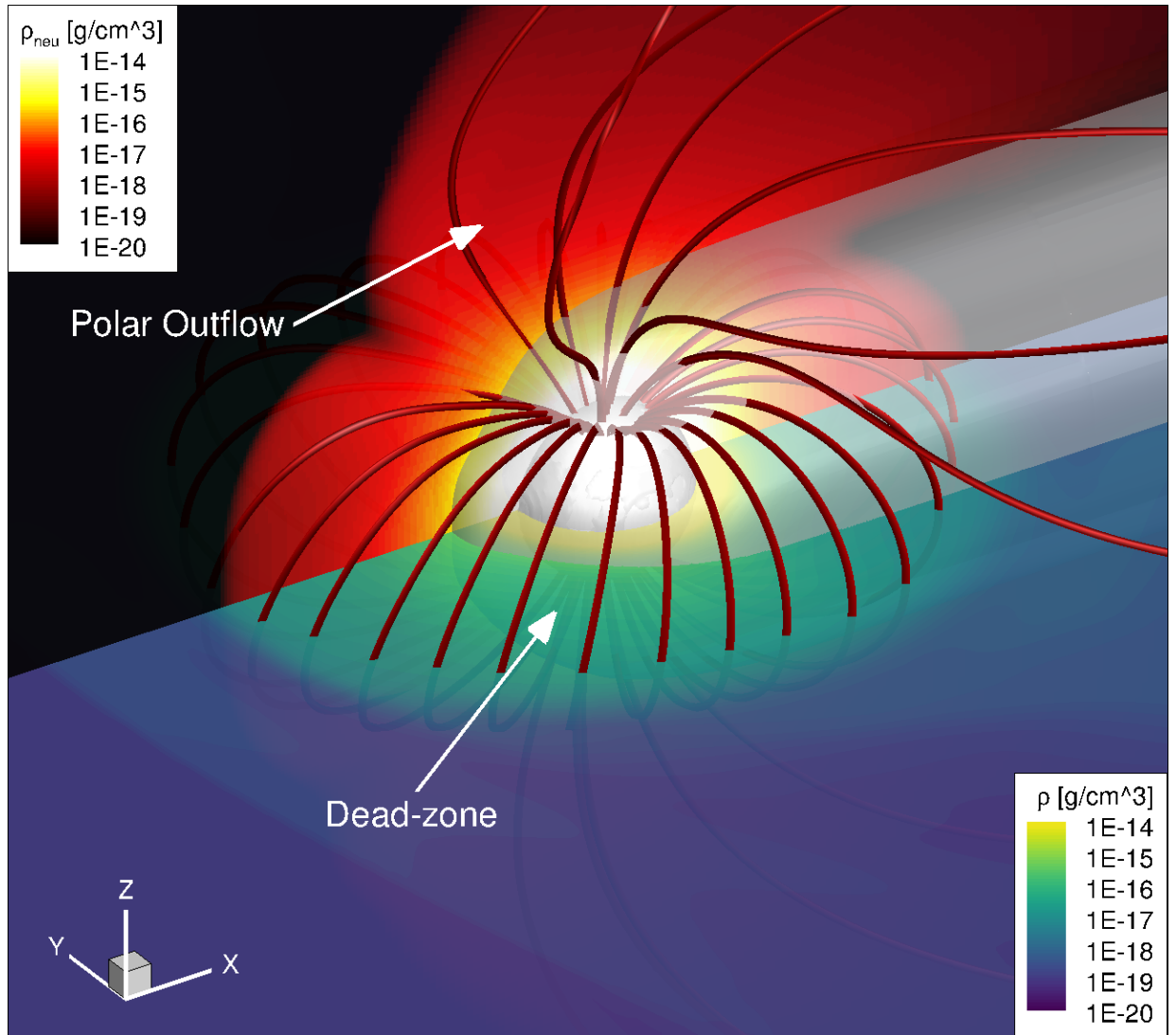


Figure 5.1: A 3D view of the 10G model. The white sphere is the planet, while the grey surface mark where the optical depth $\tau = 1$ of Ly- α photons. The black-red contour shows the density of neutrals on the polar plane, while the blue-green contour shows the total mass density on the orbital plane. The red lines trace the planetary magnetic field lines. Here we can clearly see a dead-zone of material trapped by the closed field lines, as well as a polar outflow where the field lines are open.

5. THE EFFECTS OF MAGNETIC FIELDS ON LY- α TRANSITS

$$\mathcal{H} = \eta \sigma n_n F_{\text{xuv}} e^{-\tau}, \quad (5.6)$$

here η is the excess energy released when a Hydrogen atom is ionised, n_n is the number density of neutrals, F_{xuv} is the incident XUV flux and τ is the optical depth. I assume that the incident XUV radiation is plane parallel, and that the entire XUV spectrum is concentrated at 20 eV. This yields $\sigma = 1.89 \times 10^{-18} \text{ cm}^{-2}$ and $\eta = 0.32$ (Murray-Clay et al., 2009; Allan & Vidotto, 2019; Hazra et al., 2020, 2022). The XUV flux is injected into the grid from the negative x boundary, such that the optical depth is calculated by:

$$\tau = \int_{x_{\text{boundary}}}^x n_n \sigma dx. \quad (5.7)$$

For the total volumetric cooling rate \mathcal{C} , the model contains the cooling due to Ly- α emission (Osterbrock, 1989):

$$\mathcal{C}_{\text{Ly}\alpha} = 7.5 \times 10^{-19} n_p n_n e^{(-1.183 \times 10^5 / T)}, \quad (5.8)$$

and the cooling due to collisions (Black, 1981):

$$\mathcal{C}_{\text{col}} = 5.83 \times 10^{-11} n_e n_n \sqrt{T} e^{(-1.578 \times 10^5 / T)} \chi_H, \quad (5.9)$$

where T is the temperature, $\chi_H = 2.18 \times 10^{-11} \text{ erg}$ is the ionisation potential of Hydrogen, and n_p and n_e are the number density of protons and electrons in cm^{-3} . This yields volumetric heating and cooling rates in units of $\text{erg cm}^{-3} \text{ s}^{-1}$.

In addition to these, the model solves two additional mass conservation equations, tracking the density of neutrals and ions:

$$\frac{\partial n_n}{\partial t} + \nabla \cdot n_n \mathbf{u} = \mathcal{R} - \mathcal{I}, \quad (5.10)$$

$$\frac{\partial n_p}{\partial t} + \nabla \cdot n_p \mathbf{u} = \mathcal{I} - \mathcal{R}, \quad (5.11)$$

where \mathcal{R} and \mathcal{I} are the recombination rate and ionisation rate due to photoionisation and collisional ionisation (Osterbrock, 1989) given by:

$$\mathcal{R} = 2.7 \times 10^{-13} (T/10^4 \text{ K})^{-0.9} n_e n_p, \quad (5.12)$$

5.2 3D Self-Consistent Radiative MHD Simulations

$$\mathcal{J} = \frac{\sigma n_n F_{\text{xuv}} e^{-\tau}}{h\nu} + 5.83 \times 10^{-11} n_e n_n \sqrt{T} e^{(-1.578 \times 10^5 / T)}. \quad (5.13)$$

where $\alpha_{\text{rec}} = 2.7 \times 10^{-13} (T/10^4 \text{K})^{-0.9}$ is the Case-B radiative recombination coefficient (see section 1.2.2 for details why this is a valid approximation), and \mathcal{R} and \mathcal{J} are in $\text{cm}^{-3} \text{s}^{-1}$.

We impose an inner boundary at $1R_p$. Here I fix the base temperature and density to 1000 K and $2.4 \times 10^{11}/\text{cm}^3$ respectively. Similar to the 1D models of Murray-Clay et al. (2009) I find that changing these values has no significant effect on the escape rate. For velocity, I use a reflective boundary (the velocity in the true and ghost cells have the same magnitude but the opposite sign), such that the velocity of material starts at ≈ 0 km/s at $1R_p$. In spite of the very small initial velocity, the planetary atmosphere is accelerated above the boundary according to the forces in the momentum equation. For the magnetic field I use BATS-R-US' default boundary (e.g., De Zeeuw et al., 2004; Tóth et al., 2005). This fixes the field strengths at $R = 0.5R_p$ such that the desired dipole strength is obtained at $R = 1R_p$, where a floating boundary condition is applied (the gradient of magnetic field is kept constant between true and ghost cells, such that the field lines can respond to changes in the outflow). For the outer boundaries (with the exception of the negative x boundary for the stellar wind) I use inflow limiting boundary conditions from chapter 3 (McCann et al., 2019; Carolan et al., 2020, 2021a). These are required when simulating in the co-rotating frame to remove any unwanted and uncontrolled inflows associated with the Coriolis force bending material near a boundary.

We initialise the computational domain with a 1D β profile of the escaping atmosphere, which is fit to a 1D model from Allan & Vidotto (2019). In the case studied here, this profile takes the form $u_r = u_\infty (1 - 1/r)^\beta$ where $u_\infty = 38$ km/s is the terminal velocity of the outflow, and $\beta = 2.97$ is found as the best fit to the 1D model. From mass conservation, I then initialise the density in the whole grid as $n(r) = n_0 u_0 / u_r$, where n_0 is the density at the boundary (see previous paragraph) and u_0 is derived from the 1D model. Initially, I assume a constant ionisation fraction throughout the grid (0.001%), but as the solution advances, the ionisation fraction is self-consistently obtained through Equations 5.10 and 5.11. This setup ensures that there is absorbing material (i.e. neutral Hydrogen) in the grid to absorb the ionising radiation from the star when the simulation begins. I note that the exact setup of the β profile does not affect the resulting steady-state solution. I begin these simulations with just planetary material, and once the escaping atmosphere has reached steady-state, I then turn on the orbital forces and inject the stellar wind, yielding

5. THE EFFECTS OF MAGNETIC FIELDS ON LY- α TRANSITS

Table 5.1: The parameters of my models. M_p and R_p are the mass and radius of the planet, while B_{0p} is the range of polar dipole field strength of the planet examined. a is the orbital distance from the star. F_{xuv} is the X-ray flux received by the planet. M_* and R_* are the mass and radius of the star. R_A is the Alfvén point of the stellar wind while \dot{M}_* is the stellar wind mass-loss rate. u_{r*} is the range of stellar wind velocities along the negative x boundary, with the minimum at the centre and increasing towards the edge of the grid-face. Finally B_{0*} is the stellar dipole strength.

M_p	R_p	B_{0p}	a	F_{xuv}	M_*	R_*	R_A	\dot{M}_*	u_{r*}	B_{0*}
$[M_J]$	$[R_J]$	[G]	[au]	$[\text{erg}/\text{cm}^2/\text{s}]$	$[M_\odot]$	$[R_\odot]$	$[R_*]$	$[M_\odot/\text{yr}]$	[km/s]	[G]
0.7	1.4	0-10	0.05	850	1	1	5.56	3.6×10^{-13}	327-368	2G

the resulting steady-state solutions seen in figures 5.2 and 5.3 respectively.

We inject the stellar wind at the negative x boundary. Here I use similar boundary conditions to chapter 3 (Carolan et al., 2020, 2021a), now adapted to also handle the stellar wind’s magnetic field. The boundary assumes a stellar wind velocity and magnetic field which is radial away from the star. I provide values of the stellar wind velocity, temperature, density and magnetic field which are derived from an external model, which describes the stellar wind using a 1D polytropic model. We use a similar model to that in chapter 2 (Carolan et al., 2019), which is based on Johnstone et al. (2015a)’s version of VAC (Tóth, 1996). I fix the stellar wind temperature and mass-loss rate at the boundary of the 3D simulations, the latter of which is used with the velocity solution from the 1D model to set the density along the boundary. Note that the stellar wind model is separate to the 3D simulations, and is not updated during runtime. For the purpose of this chapter, I use the same stellar wind in each simulation (see table 5.1 for details). The stellar wind is chosen as it is super-magnetosonic at the planet’s orbit, so that the magnetic interaction with the escaping atmosphere cannot travel upstream in the stellar wind and affect the boundary condition. This will allow us to more consistently examine the effect of magnetic fields on the planetary outflow, as varying the planet’s magnetic field cannot affect the injected stellar wind, ensuring the stellar wind is identical in all models. The model parameters for the planet and stellar wind can be found in table 5.1.

5.3 Effect Of Magnetic Fields: Atmospheric Escape

A recent study approximating the fractional energy released in the Calcium II K line, a

5.3 Effect Of Magnetic Fields: Atmospheric Escape

signature of magnetic star-planet interactions, suggested that surface magnetic fields of Hot Jupiters could reach 20-120 G, which is 10-100 times larger than the values dynamo scaling laws predict (Cauley et al., 2019). In this chapter I chose to run 5 models in total using the parameters in table 5.1, varying the magnetic field strength of the planet’s dipole from 0 to 10G, while keeping the stellar wind constant. This range is chosen to cover typical values employed by other studies (eg. Villarreal D’Angelo et al., 2018, assumed fields the from 0-5 G), Jupiter’s present day field (about 4.1G), as well as slightly larger field strengths to investigate how they affect the escaping atmosphere.

Figures 5.2 and 5.3 show the orbital and polar planes in each of my models, at steady-state (snapshot of quasi steady-state 1G model, see appendix 5.7). The 0G model resembles closely the strong stellar wind models from previous chapters (Carolan et al., 2020, 2021a), where the stellar wind funnels material into a tight comet-like tail centred on the orbital plane. We can see that this tail contains all of the low temperature neutral material, most of which has a line of sight velocity that will contribute to blue-shifted absorption in Ly- α (see section 5.4).

The presence of a planetary magnetic field leads to a different tail structure. Similar to other works (eg. Khodachenko et al., 2015), as the planetary magnetic field strength is increased, the structure moves away from an tail centred on the orbital plane. Where the magnetic field lines are open, we obtain two polar outflows, one above and below the orbital plane (as seen in the lower panels of figure 5.3). These are separated by a dead-zone around the planet where the field lines are closed, filled with mostly low velocity neutral material as seen in figure 5.1. In figure 5.3 we see that the size of the dead-zone increases with magnetic field strength, as a growing circle of low temperature and low velocity material is held around the planet on the orbital plane. In figures 5.2 and 5.3 we can see that as the size of the dead-zone increases the separation between the polar outflows also increases, until no singular comet-like tail is seen in the orbital plane of the 10G model. Instead we see two tail-like structures following the planet, one above and one below the orbital plane. Note that these two flows are asymmetric which will be discussed in section 5.4.

For lower magnetic field strengths ($<3G$), most of the absorbing material is at low to blue-shifted velocities. For stronger magnetic fields ($\geq 3G$), we see a small amount of red-shifted material on the night-side of the planet between the polar flows, as the magnetic field funnels some material back towards the planet.

In these models the $\tau = 1$ surface varies from $\approx 1.8R_p$ in the 10G model, to $\approx 1.2R_p$

5. THE EFFECTS OF MAGNETIC FIELDS ON LY- α TRANSITS

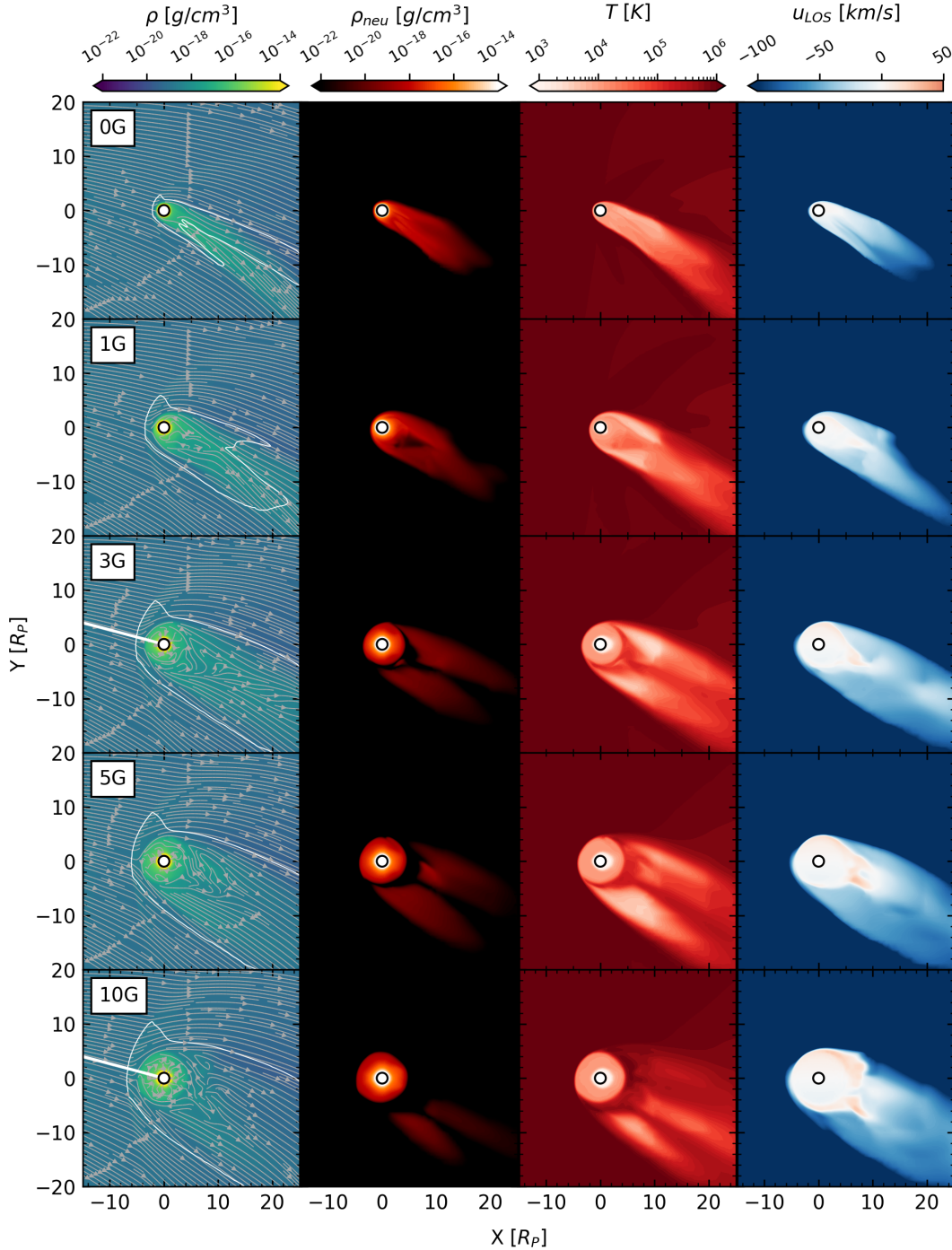


Figure 5.2: Cut at orbital plane of each of my models. Each row shows a different magnetic field strength of the planet, while each column shows the total density, neutral density, temperature and line of sight velocity respectively. The star is located at negative x , while the planet is marked by a circle centred on the origin. The grey streamlines in the left column trace the flow of material in each model (see figure 5.3 for stream-tracers of magnetic field). The white contour in the left column shows the position of the magnetosonic surface. The white line in the left middle panel is the line on which we examine different pressures in figure 5.5.

5.3 Effect Of Magnetic Fields: Atmospheric Escape

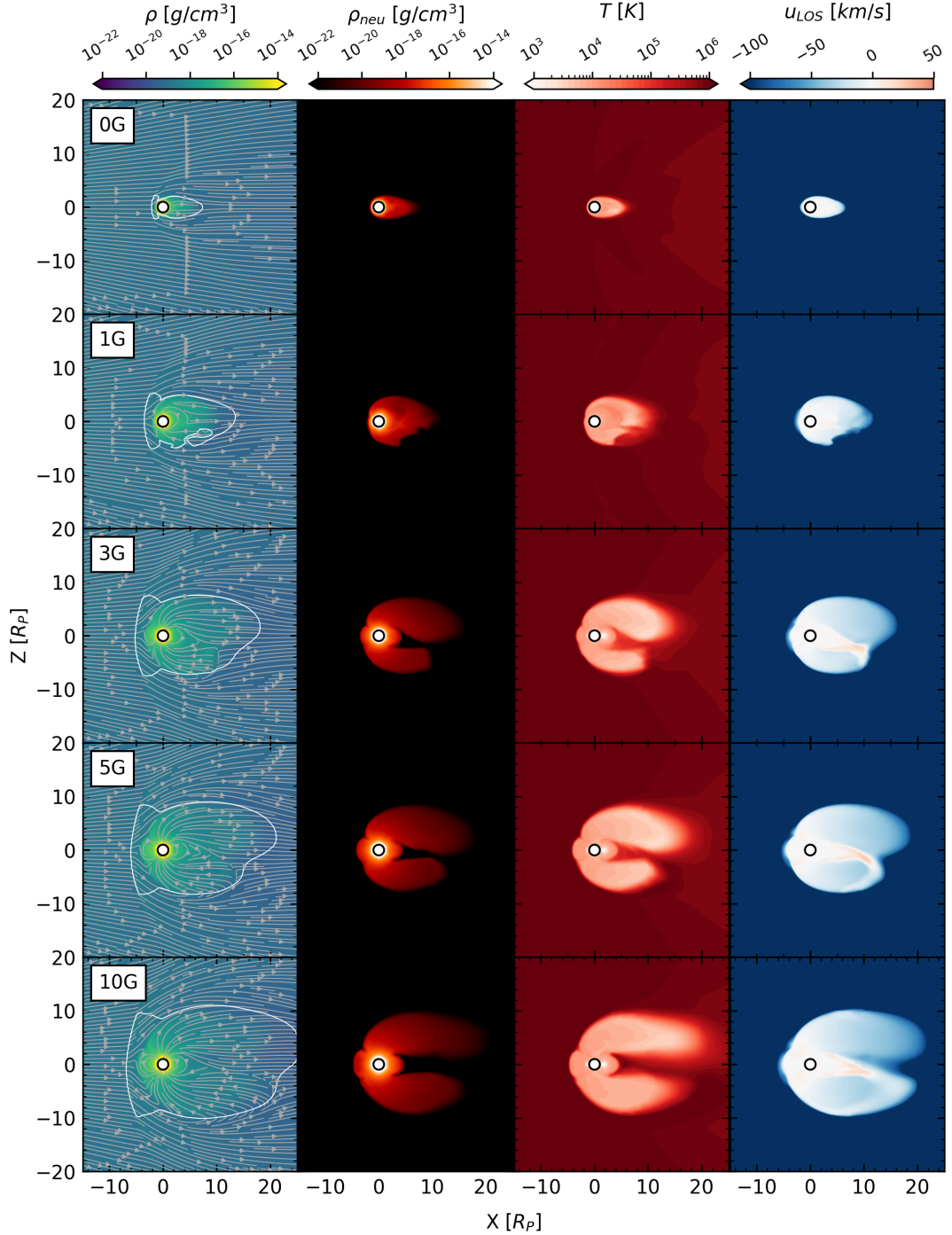


Figure 5.3: Cut at the polar plane in each of my models, similar to figure 5.2. The grey streamlines in the left column now trace the magnetic field lines in each model.

5. THE EFFECTS OF MAGNETIC FIELDS ON LY- α TRANSITS

Table 5.2: The size of the planet’s magnetosphere along the line shown in figure 5.2, chosen as the point where the stellar wind velocity is perpendicular to the shock. B_p is the planet’s magnetic field strength in Gauss, R_m and R_b are distance of the magnetopause and bow shock standoff distance relative to the radius of the planet. R_τ is the position of the $\tau = 1$ surface on the sub-stellar line.

B_p	R_m	R_b	R_τ
[G]	[R_p]	[R_p]	[R_p]
0	—	2.2	1.2
1	2.1	3.5	1.4
3	3.5	5.2	1.7
5	4.2	6.0	1.7
10	4.8	6.9	1.8

in the 0G model, along the sub-stellar line. The exact values for the position of the $\tau = 1$ surface in each of these models can be found in table 5.2. As previously discussed, when the magnetic field strength of the planet is increased, the size of the dead-zone grows. This larger, denser dead-zone is then able to absorb more of the incident stellar radiation before it gets lower into the planet’s atmosphere, and as a result the $\tau = 1$ surface is pushed to higher altitudes.

To quantify the change in the escaping atmosphere in my models, I examine the planetary mass-loss through planes parallel to the orbital plane above and below the planet at $z = \pm 2.5R_p$ vs that lost through the night-side between these planes at $x = 2.5R_p$ (figure 5.4). We can then compare these to the total mass-loss calculated through concentric spheres around the planet to investigate where the planet is losing most of its atmosphere. As expected from figures 5.2 and 5.3, the 0G model loses most of its mass through the night-side, as the stellar wind funnels the escaping atmosphere into a tight comet-like tail centred on the orbital plane. Once a planetary magnetic field is introduced, we begin to see much more mass-loss through polar outflows than through the night-side, with these polar flows contributing to the majority of atmospheric escape for $B_p \geq 3G$. For the 1G model (and the 3G model to a lesser extent) we can see significant difference between the north and south polar flows, which we attribute to the variation in this quasi-steady state solution (see appendix 5.7). I note also the increase in the total atmospheric escape rate (\dot{m}) seen from the 0 to 10G models (factor of 2). This is caused by the funnelling geometry of the magnetic field which assists in the driving of escape in the polar flows, compared to the predominantly night-side outflow in the 0G model. This is similar to what is seen in

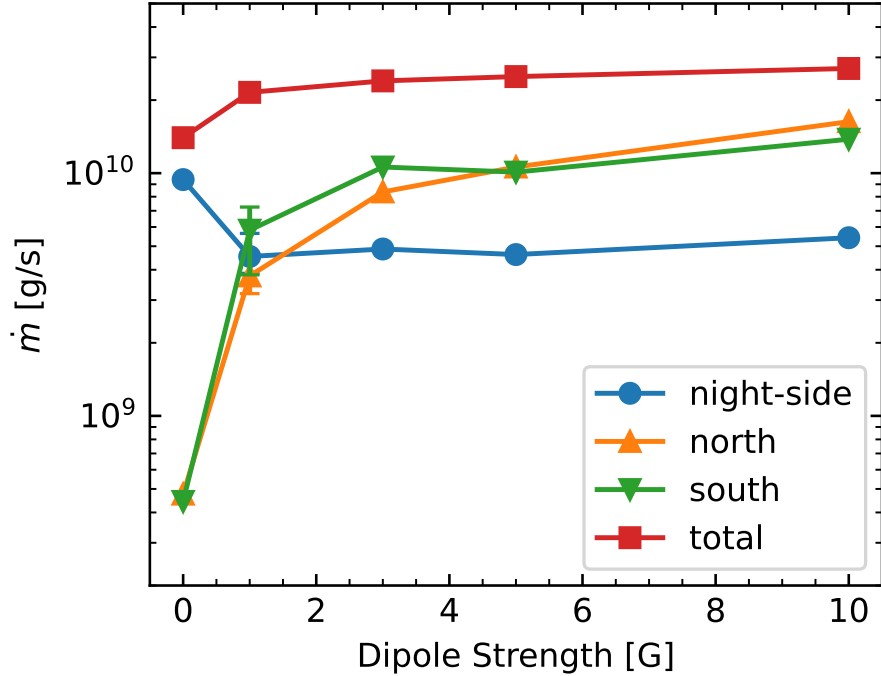


Figure 5.4: The mass-loss rates of each of my models. The blue circles mark the mass lost through a plane at $x = 2.5R_p$ representing the night-side mass-loss. The orange and green triangles mark the mass lost through planes at $z = 2.5R_p$ and $z = -2.5R_p$ respectively, representing the polar flows. The red squares mark the total mass lost, marking the average mass lost through concentric spheres around the planet. For the 1G model, I plot the mean and variation of the mass-loss rates during the quasi-steady state solution, discussed in appendix 5.7.

stellar wind models with magnetic fields (Vidotto et al., 2009, 2014; Réville et al., 2015; Ó Fionnagáin et al., 2019, 2021; Kavanagh et al., 2019, 2021). However for stronger field strengths ($>3\text{G}$) the magnetic field does not cause significant changes to the escape rate, though it does change the observational signatures of this escape, as discussed in section 5.4.

Figure 5.5 shows the ram, magnetic and thermal pressures in these models along the white line shown in figure 5.2. This is the line where the stellar wind velocity is perpendicular to the bow shock, where the size of the magnetosphere is quantified. As seen in figure 5.5 I find a similar pressure structure to the Earth models in chapter 2 (Carolan et al., 2019), and so I use a similar procedure to quantify the size of the magnetosphere in each of these models, given in table 5.2. I find that in the stellar wind, ram pressure

5. THE EFFECTS OF MAGNETIC FIELDS ON LY- α TRANSITS

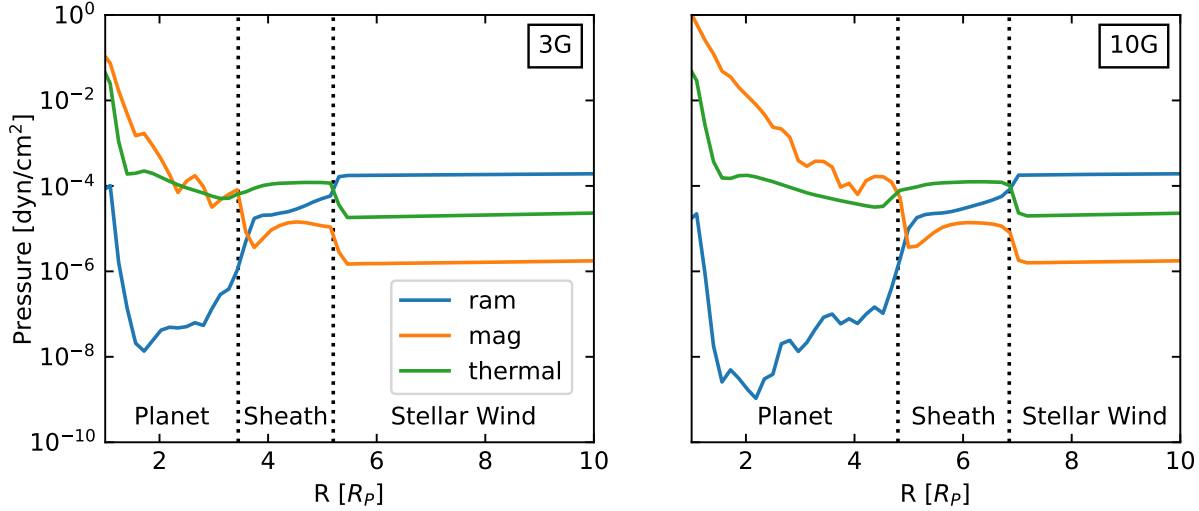


Figure 5.5: The ram, magnetic and thermal pressures in two of my models, along the lines marked in left middle and bottom panels of figure 5.2. This line was chosen where the stellar wind velocity is perpendicular to the shock. The black dotted lines mark the position of the magnetopause and bow shock standoff distances, which separate the planetary, magnetosheath, and stellar wind material respectively.

is the dominant pressure component, while the shocked material in the magnetosheath is dominated by thermal pressure. The bow shock standoff distance can then be found as the point where ram and thermal pressures are balanced. Inside the planetary magnetosphere the dominant pressure component is magnetic, and so the magnetopause is found by the balance of magnetic and thermal pressures. As expected, increasing the magnetic field strength of the planet’s dipole increases the size of the magnetosphere, as increasing the magnetic pressure will push the balance of magnetic and thermal pressures further from the planet. Note that due to the lack of intrinsic magnetic field in the 0G model, we cannot identify the magnetopause in this model. In reality it is likely that stellar wind interaction would generate a weak induced magnetic field, which would yield a magnetopause standoff distance $< 1.5R_p$. For all models, we observe a “weak” bow shock, similar to the $30\Omega_\odot$ model from chapter 2 (Carolan et al., 2019). This is due to a relatively low Mach number of the stellar wind $\mathcal{M} \approx 1.5$, which causes a jump in density and decrease in velocity by a factor of approx 2.6 (for a strong shock this factor is approximately 4, Spreiter et al., 1966; Gombosi, 2004; Balogh & Treumann, 2013). I also obtain a relatively thick magnetosheath in these simulations because of this, with the bow shock distance being greater than 1.4

times the magnetopause standoff distance in each model (1.275 in a strong shock).

5.4 Effect Of Magnetic Fields: Observational Signatures

To investigate how magnetic fields affect observational signatures of escape, I calculate transit absorption profile of each of these models in Ly- α , as described in section 1.7. The transit depth of each model at mid transit can be seen in figure 5.6.

Even though the variation in \dot{m} is small, varying the strength of the planet's magnetic field causes significant changes to absorption in Ly- α . As the comet-like tail in the 0G model is tightly funnelled down the line of sight by the stellar wind, we see significant blue wing absorption in this model. For small magnetic field strengths the tail begins to extend further above and below the orbital plane¹. The magnetic field now introduces a larger obstacle to the stellar wind. As a result the escaping atmosphere is less accelerated along the line of sight, and so we do not see as much blue-shifted absorption.

I find a significant increase in line centre absorption with increasing magnetic field strength. This is due to the growing dead-zones around the planet. As the planet's dipole strength increases, the size of the dead-zone increases as shown in figures 5.2 and 5.3. This region contains mostly low velocity, low temperature neutrals, and so as the size of the dead-zone grows, so does the line centre absorption.

In figure 5.3 we see asymmetry in the planetary material above and below the orbital plane. This is due to the interaction between the stellar wind and planetary magnetic fields. When the super-magnetosonic stellar wind reaches the planet, it is shocked and deflected around the planet. This deflection is what shapes the comet-like tail following the planet. As the stellar wind is shocked to sub-alfvénic velocities, reconnection of field lines can occur, which we see happen just inside the Alfvén surface. Due to the orientation of the planetary magnetic field and radial stellar field in these models, the stellar and planetary field lines reconnect at the south pole, below the orbital plane, while the northern planetary field lines are opened. I note that as the upstream stellar wind is super-alfvénic, this reconnection cannot accelerate particles that travel back to the star (this is believed

¹This is the case where the planet's dipole axis is perpendicular to the orbital plane. However if the dipole was tilted on the polar plane, the separation between the polar flows and the orbital axis would be reduced (see section 5.1).

5. THE EFFECTS OF MAGNETIC FIELDS ON LY- α TRANSITS

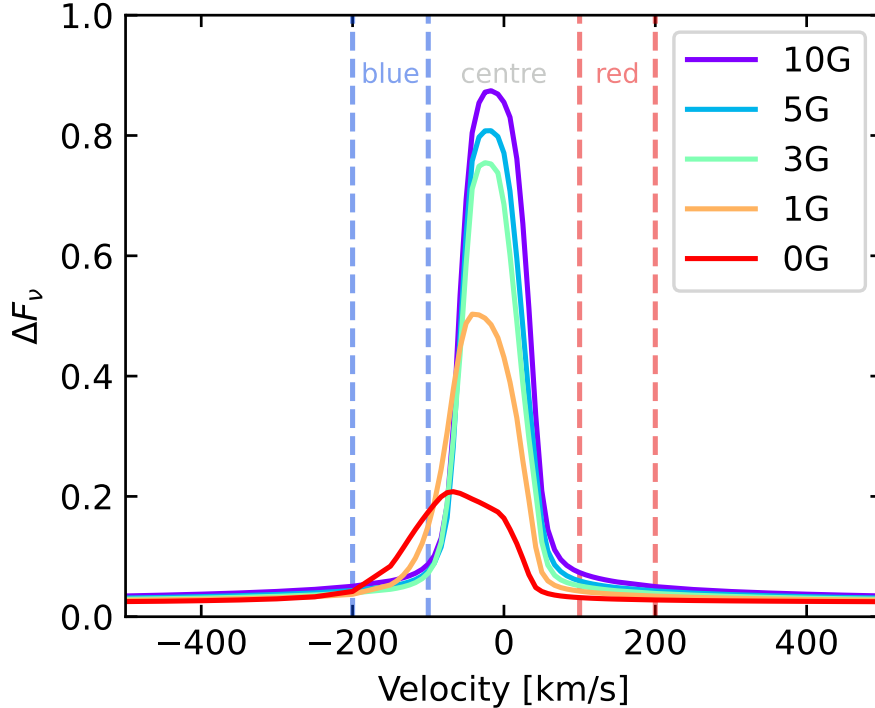


Figure 5.6: The mid-transit absorption profiles for each of my models, for an impact parameter $b = 0$. The blue and red dashed lines mark the bounds for the integrals of the blue, line centre and red wing absorptions in figure 5.7

to cause enhanced activity in the star Shkolnik & Llama 2018; Cauley et al. 2019; Folsom et al. 2020; Kavanagh et al. 2021, which could change the properties of the stellar wind). As a result of this reconnection the absorbing neutral material is less extended below the orbital plane, as the bending magnetic field lines at the interface between the stellar wind and escaping atmosphere act as a boundary (see figure 5.3). Above the orbital plane (north pole) there are now more open field lines allowing the neutral material to extend further compared below the plane.

Due to the asymmetry in the distribution of absorbing neutrals above and below the orbital plane we can expect this to affect the absorption profiles depending on the transit geometry of the planet. In figure 5.7 I show the percentage absorptions in the blue, line centre and red wings of the Ly- α line shown in figure 5.6, for a variety of impact parameters (b) in the northern and southern hemispheres of the stellar disc.

In the line centre, mid disc ($b = 0$) has the largest absorption, as it maximises the

5.4 Effect Of Magnetic Fields: Observational Signatures

volume of material within the stellar disc (green curves). In the blue wing we initially see a decrease in absorption for increasing magnetic field strength. As previously mentioned this is because the structure of the comet-like tail moves away from being funnelled fully along the line of sight on the orbital plane, as the polar outflows perpendicular to the orbital plane are introduced. The most asymmetry between positive and negative impact parameters (see top panel of figure 5.7) is seen in the 1G model. As previously mentioned this model reaches a quasi-steady state, showing some variation in the distribution of material. As we do not see this in other simulations with higher B_p , I believe this is due to the magnetic field not being able to fully break this single comet-like tail structure into the polar outflows and dead-zones we see in other models with higher B_p . During the quasi-steady state solution for this model, a positive impact parameter shows more blue wing absorption than the negative values, suggesting that more high velocity Ly- α absorption is caused by material under the orbital plane. This is caused by the disparity in the mass lost through the southern pole in this model (see figure 5.4), as the magnetic field begins to break the single comet-like tail structure. I note that depending on the stage during the quasi-steady state variation examined, the velocity of the material under the plane will vary significantly and so this asymmetry will not remain constant (see appendix 5.7).

For strong planetary fields, we see that blue wing absorption increases with magnetic field strength. As the magnetic field strength increases the size of the magnetosphere increases, allowing more room for absorbing material to accelerate along the polar outflows. As expected from figure 5.3 we see some asymmetry between the positive and negative impact parameters. The negative values yield higher absorption than the positive counterparts. For positive impact parameters the more extended northern flows will lie outside the stellar disc (while it will lie inside the disc for negative impact parameters), yielding less absorption in Ly- α . This is also the case for absorption in line centre. As there are more neutrals above the plane the negative impact parameters will allow more lower velocity absorbing material to cover the disc than positive values.

There is no asymmetry present in red-shifted material when comparing positive and negative impact parameters. From figures 5.2 and 5.3 we can see that most red-shifted material lies on the orbital plane between the polar outflows on the night-side of the planet, as a small amount of material falls from the polar outflows back towards the planet. As a result there is no significant difference between the positive and negative impact transits.

5. THE EFFECTS OF MAGNETIC FIELDS ON LY- α TRANSITS

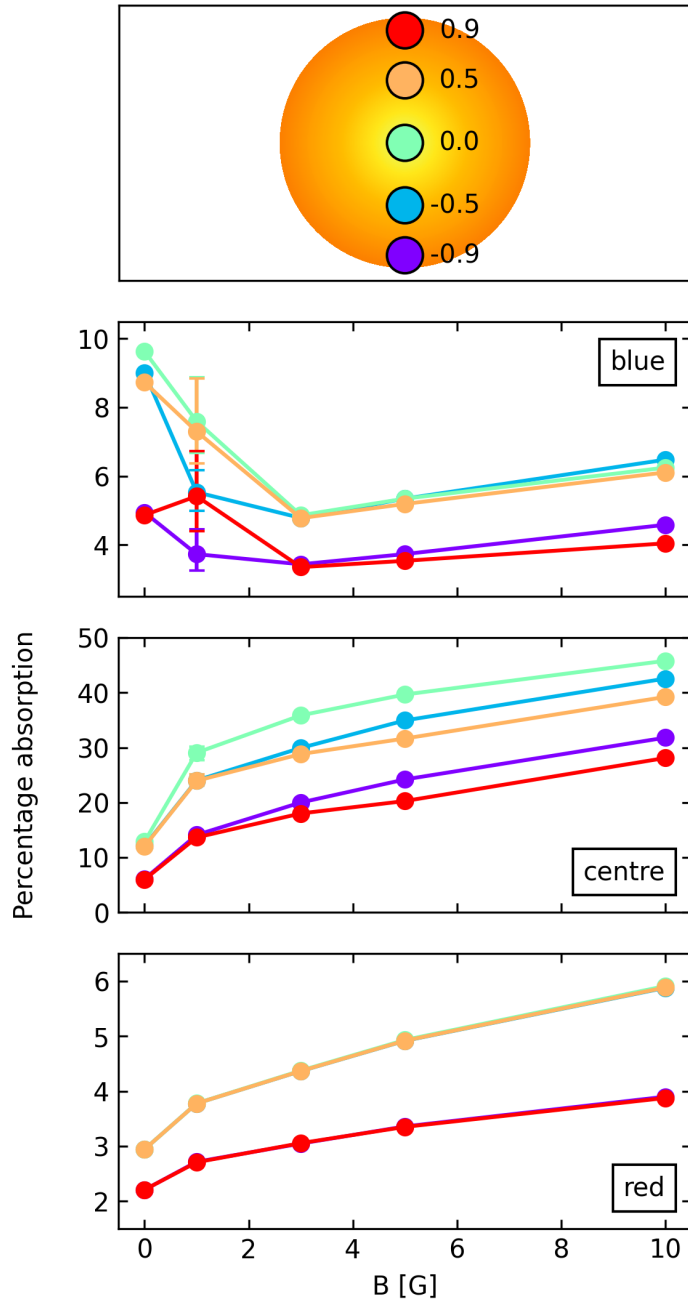


Figure 5.7: The blue, line centre and red wing absorptions (marked on figure 5.6) of each of these models for a variety of impact parameters. The top panel illustrates the position of the planet at mid transit as it transits horizontally across the stellar disc. In the second panel I plot the mean and variation in the blue wing absorption for the 1G model during its quasi-steady state solution (see appendix 5.7). Note that there is no such variation in the red wing, or at line centre.

5.5 Discussion

5.5.1 Magnetic Field Geometries

As the absorption is related on the geometry of the escaping atmosphere, which is dependent on a combination of B_* and B_p , my results are expected to change for different magnetic field topologies. For example, if B_* had the opposite polarity, then the results for positive and negative impact parameters would be inverted. In this scenario, the reconnection of stellar and planetary field lines now occurs above the orbital plane (as opposed to below, shown in figure 5.3). This would lead to more open field lines below than above the plane. As a result, the distribution of material we currently see in these models would be flipped through the orbital plane, leading to the opposite result for transits with positive and negative impact parameters. Similarly, if the planetary dipole was tilted, the position of reconnection would change. The topology used in this chapter, where the planetary dipole axis is perpendicular to both the sub-stellar line and direction of transit, yields the greatest difference between positive and negative impact parameter transits. Tilting the dipole towards / away from the star will reduce the vertical distance between the two polar outflows, as rotating the dipole brings the poles closer to the orbital plane. As a result of this reduced separation, the observed asymmetry between transit geometry would also be reduced. Similarly tilting the dipole towards/away from the transit direction (towards positive y) will reduce asymmetry. Transits close to the edge of the stellar disc now no longer fully remove one of the polar outflows, but rather parts of both, producing less asymmetry between transit geometries.

5.5.2 No Significant Change In Escape Rate

In this chapter I find that increasing the planet's magnetic field strength causes a minor increase in the planet's total mass-loss rate (increasing by a factor of 2). This result is contrary to what other works have found for hot Jupiters (eg. Owen & Adams, 2014; Khodachenko et al., 2015; Arakcheev et al., 2017, all found reductions by up to an order of magnitude), and likely caused by difference in the physics included in each model. Similar to other works, I find that the inclusion of magnetic fields creates dead-zones in these models around the equator, where planetary material is held inside the closed field lines.

5. THE EFFECTS OF MAGNETIC FIELDS ON LY- α TRANSITS

This reduces the mass-loss around the equator, while also causing an increase in the line centre absorption as these dead-zones hold a significant amount of low velocity neutrals. Despite this, all of the models with planetary magnetic fields lose more mass than the 0G model. As previously discussed, in these models more mass is funnelled through the polar flows, leading to two outflows above and below the equatorial dead-zones. Unlike Khodachenko et al. (2015), I do not find suppressed polar winds, where faster adiabatic cooling leads to reduced polar winds. This could be in part due to the inclusion of stellar wind in my model. While Khodachenko et al. (2015) found most mass is lost through the “wind zone” between the equatorial dead-zones and suppressed polar winds, the inclusion of the stellar wind in the model deflects material from the dayside “wind zone” towards the night-side comet-like tails. Through this deflection material lost through the dayside “wind zone” must flow through where the suppressed polar outflows would reside to reach the comet-like tail, leading to no apparent suppression of polar winds in my models. Instead I see an increase in polar outflows when compared to the 0G model. This increased polar flow accompanied by the decreased night-side mass-loss nets an increase in the total mass-loss rate by a factor of 2, though this is not significant enough to affect the timescale for atmospheric loss. This further emphasises the importance of considering the stellar wind when modelling atmospheric loss, as it can significantly alter the the geometry and rate of atmospheric escape.

5.5.3 Implications On Observations

The results I present in this chapter have important implications on interpreting transit observations. Despite the mass-loss rate only increasing by a factor of 2, increasing the magnetic field strength greatly alters the absorption line profile. At line centre, the total percentage absorption increases by a factor of 4 at mid transit, when comparing the 0 and 10G models. The presence of a magnetic field greatly alters the geometry and distribution of absorbing material in the planetary magnetosphere, and so is crucial to consider in order to correctly interpret transit observations. One issue with observing Ly- α transits is that this line is not observable at line centre, due to both interstellar absorption and geocoronal emission. Recent work has identified the infra-red 10830Å Helium I triplet as an atmospheric escape identifier (eg. Spake et al., 2018; Nortmann et al., 2018). A popular approach has been to calculate the population of the triplet in post processing, i.e., a

Parker-type wind is used to calculate the bulk properties of the escaping atmosphere and, afterwards, the population state is calculated (eg. Oklopčić & Hirata, 2018; Lampón et al., 2020; Dos Santos et al., 2022; MacLeod & Oklopčić, 2022). There have also been numerous detections of heavier elements in the transmission spectra of exoplanets (eg. Hoeijmakers et al., 2018, 2019; Gibson et al., 2020; Seidel et al., 2021), with a current popular theory to explain this suggesting that these heavier elements are dragged to these altitude by the escaping Hydrogen (Cubillos et al., 2020). There are still many open questions on what the effects of magnetic field would be in the dynamics of heavier particles. For example, given that increasing the dipole strength increases Ly- α absorption at line centre as more neutral Hydrogen is trapped in the dead-zones, we can infer that this will also increase the line centre absorption of other heavier elements if they are well mixed with Hydrogen in the escaping fluid. Likewise, the strong Hydrogen outflow emerging from the poles could bring heavier elements to high altitudes. If this is the case, we could also expect asymmetries in spectroscopic transits of heavier elements.

5.6 Conclusions

In this chapter, I have examined how magnetic fields affect the interaction between the stellar wind and escaping atmosphere. I use newly developed 3D self-consistent radiative MHD models. Using the same magnetised stellar wind in each model, I vary the planetary dipole strength to examine how the planetary magnetic field affects the interaction with the stellar wind, the mass lost by the planet, and the observational signatures of this escape. To the best of my knowledge this is the first 3D radiative model capable of simulating the inner most regions of the escaping atmosphere which includes: radiative heating & cooling; cooling from collisions; the planetary magnetic field; magnetised stellar wind; Coriolis & centrifugal forces; and the force due to tidal gravity.

I performed five simulations, varying the planetary dipole strength from 0 to 10G. I find that increasing the magnetic field strength of the planet greatly alters the structure of material in the magnetosphere. Just as was shown in other works (Trammell et al., 2014; Owen & Adams, 2014; Khodachenko et al., 2015; Arakcheev et al., 2017), I found that the planetary magnetic field creates dead-zones, where the closed magnetic field lines around the planet trap material, reducing escape around the equator. This dead-zone grows with magnetic field strength, and is able to absorb more of the incident stellar

5. THE EFFECTS OF MAGNETIC FIELDS ON LY- α TRANSITS

radiation before it gets lower into the planet's atmosphere. As a result the $\tau = 1$ surface is pushed to higher altitudes when the magnetic field strength is increased. I also presented the novel finding of a double comet-like tail structure, one below and above the orbital plane, caused by the polar outflows. I found that the mass-loss through the poles increases with magnetic field strength, causing an increase in the total atmospheric escape rate. This is due to the interaction with the stellar wind, which deflects dayside atmospheric escape through the poles into this double tail structure, placing further emphasis on the importance of considering the interaction of the escaping atmosphere with the stellar wind when investigating atmospheric escape.

Using the results of these 3D simulations I investigated how changing the planetary magnetic field strength affects the observational signatures of atmospheric escape. I found an increase in line centre absorption with magnetic field strength, as more absorbing material is trapped in the growing dead-zones around the planet. The blue wing absorption initially decreases upon the introduction of the planetary field, as planetary material begins to be launched above and below the orbital plane, instead of being fully funnelled onto the orbital plane by the stellar wind, as seen in the 0G model. As the field strength continues to increase I see the blue wing absorption also increases. Similarly to the line centre absorption, the red wing absorption increases with magnetic field strength. I found that most of the red-shifted material exists around the night-side orbital plane, as some material falls from the comet-like tails back towards the planet.

Finally I investigated the asymmetry between positive and negative impact parameters during transit (i.e. if the planet transits in the northern or southern hemisphere of the star). With the exception of the 1G model (see appendix 5.7), I find a growing asymmetry in the blue wing absorption with increasing magnetic field strength, with negative impact parameters leading to more absorption. This is caused by the interaction between the planetary dipole and radial stellar magnetic fields. Below the orbital plane, as the stellar wind is shocked back to sub-alfvénic velocities the stellar and planetary magnetic field lines reconnect (note that as the stellar wind is super-alfvénic before this interaction, this cannot affect the upstream stellar wind). Above the plane the opposite occurs, leading to more open planetary field lines. As a result I found that the planetary outflow is more extended above the plane than below for all magnetic field strengths. This causes asymmetry between positive and negative impact parameters, as depending on which comet-like tail is mostly covering the stellar disc during transit, different absorption profiles will be obtained. This

work places importance not only on knowledge of the planetary magnetic field, but also on the geometry of its interaction with the stellar wind's field when interpreting observational signatures of atmospheric escape.

5.7 Appendix: Quasi Steady-State Solutions

The 1G model (and the 3G model, to a lesser extent) presented in this chapter does not settle to a fully steady-state solution. Instead I find a quasi steady-state where the resulting solution varies periodically with iteration number. Similar quasi steady-state solutions were found by McCann et al. (2019); Carolan et al. (2021a), with Christie et al. (2016) demonstrating that the amplitude of the variation in the solution decreases with increasing resolution in the grid.

To illustrate the variation in this model, in figure 5.8 I show how the line of sight velocity varies at two points in the grid, one above and below the orbital plane. Above the plane, we can see a small variation in the line of sight velocity after iteration 25000, with a period of 3000-4000 iterations, covering a range of velocities from 0 to -20 km/s. However below the plane we see a much larger variation, with the velocity ranging from -10 to -125 km/s, with a period of approximately 5000 iterations. This variation is responsible for the differences in northern/southern escape and absorption ins figures 5.4 and 5.7.

The mass-loss rates shown in figure 5.4 for this model are calculated at the final iteration shown in figure 5.8. At this point, we can see that in the quasi steady-state solution, the magnitude of the velocity of material below the plane is much larger than that above the plane. As a result in this model we obtain a larger difference between mass lost through the north and south poles that what is found in other models.

Similarly, the effects of the quasi steady-state can be seen in the absorption of planetary material in figure 5.7. As the magnitude of the line of sight velocity below the plane it much larger at this stage in the solution, when the planet transits in the northern hemisphere of the star we see much more blue wing absorption than when it transits in the south. As we can see from figure 5.8 this difference in absorption will vary depending on the stage of the solution examined (eg. at iteration 32000 the velocities above and below are much more similar), and so is not indicative of the overall trend I find in these models: that the asymmetry between mid-transit absorption when transiting above and below the mid-disc will increase with the magnetic field strength of the planet.

5. THE EFFECTS OF MAGNETIC FIELDS ON LY- α TRANSITS

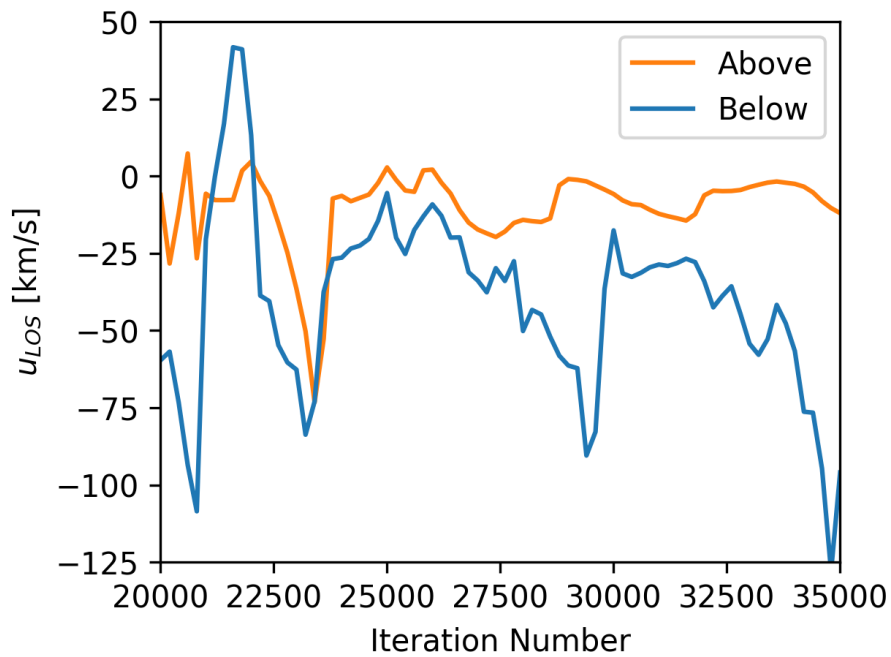


Figure 5.8: The quasi steady-state variation of the line of sight velocity in the 1G model. The two lines refer to points above and below the orbital plane, at X-Z coordinates [6, 3] and [6,-3] respectively. These points lie just within the magnetosonic surface in the left panel of the 1G model in figure 5.3.

6

Modelling Charge-Exchange & Radiation Pressure

In previous chapters (3 to 5) I discussed several instalments of my 3D code for atmospheric escape, each improving on the previous version adding new capabilities to the model. Here I discuss preliminary work to include two processes which have been neglected in previous versions, both of which are thought to produce observed high energy neutral atoms: charge exchange and radiation pressure. Both of these processes are thought to accelerate neutral Hydrogen atoms to large blue-shifted velocities. For Ly- α , this is particularly important as the line centre is not observable, and so neglecting processes which can create absorption at observable velocities could greatly alter one's prediction on the observability of atmospheric escape in a particular system. Here I discuss the preliminary work to implement these two processes and perform 3D self-consistent HD simulations (no magnetic fields), before investigating the impact they have on both the structure of the tail and observable characteristics of the escaping atmosphere in Ly- α .

This chapter is presented as follows. In section 6.1 I contextualise this preliminary work, before discussing the implementation and models including these processes in section 6.2. In section 6.3 I investigate how these processes are affecting the observational signatures in Ly- α in their current setup. In section 6.4 I discuss and compare my results to other works, as well as exploring avenues for improvement in section 6.5. Finally I summarize my conclusions in section 6.6.

6. MODELLING CHARGE-EXCHANGE & RADIATION PRESSURE

6.1 Context

Until this point, my simulations have neglected the effects of charge exchange and radiation pressure. Radiation pressure from Ly- α photons has been thought to accelerate neutral atoms to significantly blue-shifted velocities (Bourrier et al., 2015; Schneider et al., 2016). However Debrecht et al. (2020) found that radiation pressure alone may not cause significant changes, with Villarreal D'Angelo et al. (2021) finding that if the stellar wind already causes most of this acceleration, the contribution from radiation pressure will be minimal. Though radiation pressure may have a small impact on the blue wing absorption it is not thought to affect the atmospheric escape rate Debrecht et al. (2020); Villarreal D'Angelo et al. (2021).

Charge exchange occurs when a stellar wind proton and a planetary neutral Hydrogen atom exchange an electron at the boundary between the stellar wind and escaping atmosphere (eg. Shaikhislamov et al., 2016). Though the net charge remain the same, charge exchange will result in more high velocity neutral atoms thus increasing blue-shifted absorption (Holmström et al., 2008; Kislyakova et al., 2014; Bourrier et al., 2016; Tremblin & Chiang, 2013; Shaikhislamov et al., 2016). Though these two processes are unlikely to affect the dynamics of these models, the transit line profiles may change (Cherenkov et al., 2018), with Esquivel et al. (2019); Odert et al. (2020) finding a combination of the two being the best fit for observations of HD209458b.

6.2 Simulating Charge Exchange And Radiation Pressure

In order to compare the results of models with charge exchange and/or radiation pressure, I first need a model to compare to. For this I simulate a HJ in a $5 \dot{M}_{\odot}$ stellar wind (same planetary parameters as chapter 5, table 5.1). This stellar wind mass-loss rate is chosen as it is not strong enough to fully confine the escaping atmosphere as seen in chapter 3, but can confine the day-side escape yielding a significant interaction surface on which charge exchange can occur. The total and neutral densities, temperature and line-of-sight velocity on the orbital plane in this model can be seen in figure 6.1.

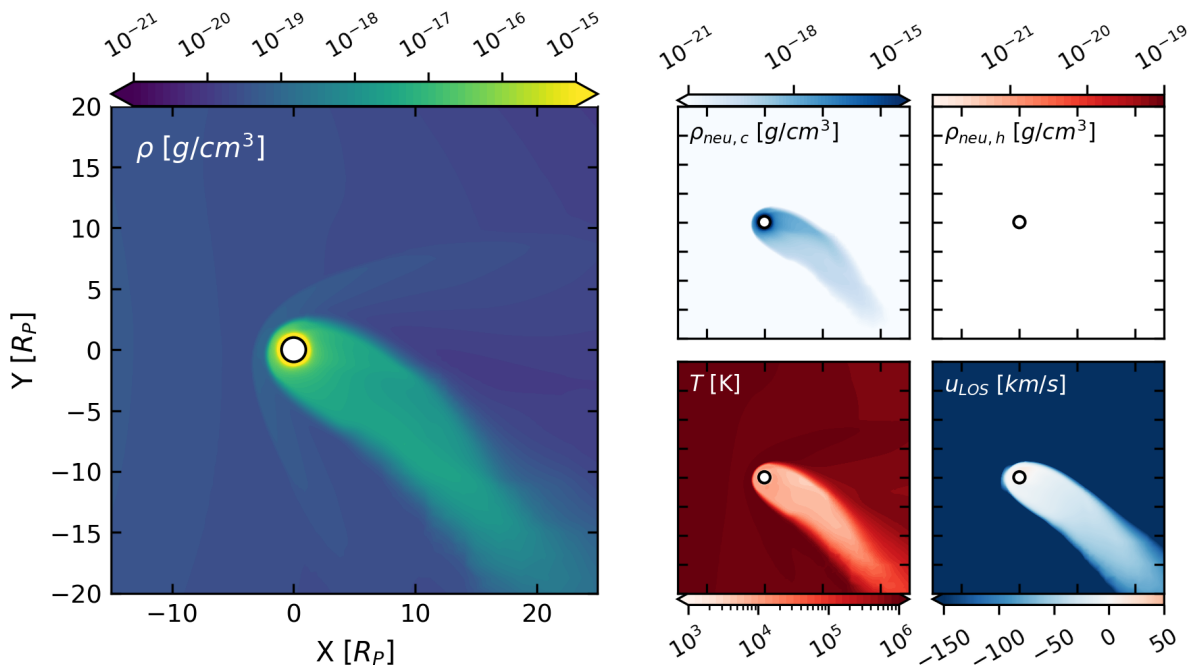


Figure 6.1: The base point for my models with charge exchange and radiation pressure. The large left panel shows the total density on the orbital plane. The four smaller panels show the cold neutrals, hot neutrals, temperature and line-of-sight velocity. Note that as there is no charge exchange in this model, no hot neutrals are created (top right panel).

6.2.1 Charge Exchange

Charge exchange is the process through which a stellar wind proton and a planetary neutral Hydrogen atom exchange an electron, yielding a neutral at the stellar wind velocity, and a lower velocity proton (Shaikhislamov et al., 2016). As this removes a lower velocity neutral, and creates a higher velocity one, we can expect this process to alter the transit line profile, as it acts to shift absorption to the blue wing (Holmström et al., 2008; Kislyakova et al., 2014; Bourrier et al., 2016; Tremblin & Chiang, 2013; Shaikhislamov et al., 2016).

In order to model this process we need a way to distinguish between stellar wind and planetary protons and neutrals. To do this I separate planetary and stellar wind material into four sets of species (henceforth referred to as cold and hot neutrals and cold and hot protons). This involves a new mass conservation equation for each new species:

$$\frac{\partial n_{c,n}}{\partial t} + \nabla \cdot n_{c,n} \mathbf{u} = \mathcal{R}_c - \mathcal{I}_c + \mathcal{C}, \quad (6.1)$$

6. MODELLING CHARGE-EXCHANGE & RADIATION PRESSURE

$$\frac{\partial n_{c,p}}{\partial t} + \nabla \cdot n_{c,p} \mathbf{u} = \mathcal{I}_c - \mathcal{R}_c - \mathcal{C}, \quad (6.2)$$

$$\frac{\partial n_{h,n}}{\partial t} + \nabla \cdot n_{h,n} \mathbf{u} = \mathcal{R}_h - \mathcal{I}_h - \mathcal{C}, \quad (6.3)$$

$$\frac{\partial n_{h,p}}{\partial t} + \nabla \cdot n_{h,p} \mathbf{u} = \mathcal{I}_h - \mathcal{R}_h + \mathcal{C}, \quad (6.4)$$

where the subscripts c and h refer to the cold and hot species. Note that when we sum the above equations for neutrals and ions respectively, we obtain equations 5.10 and 5.11 from the previous model, such that $\mathcal{I} = \mathcal{I}_c + \mathcal{I}_h$ and $\mathcal{R} = \mathcal{R}_c + \mathcal{R}_h$. \mathcal{C} is the rate of charge exchange given by:

$$\mathcal{C} = \alpha_{ce}(n_{h,n}n_{c,p} - n_{h,p}n_{c,n}). \quad (6.5)$$

α_{ce} is the rate coefficient of charge exchange:

$$\alpha_{ce} = 4\sigma_{ce} \sqrt{\frac{k_B T}{\pi m_p}}. \quad (6.6)$$

This is the energy dependent charge exchange cross section (σ_{ce}) times the average relative velocity from the Maxwell-Boltzmann distribution. σ_{ce} is given by

$$\sigma_{ce} = (4.15 - 0.531 \ln E)^2 (1 - e^{-67.3/E})^{4.5} 10^{-16} \text{cm}^2, \quad (6.7)$$

where E is the projectile energy (Lindsay & Stebbings, 2005).

Now that the hot and cold species have been separated, the boundary conditions of these simulations must be modified. The cold densities are set at the inner boundary, and are mostly neutrals, while the stellar wind is injected as purely hot protons. This setup allows for \mathcal{C} in the above equations to create Energetic Neutral Atoms (ENAs, or hot neutrals) when the two flows interact in the computational grid.

To properly model charge exchange one requires high resolution along the boundary between the hot and cold species, so that the boundary between the two fluids is well defined (eg. Tremblin & Chiang, 2013). Though this could be possible through adaptive mesh refinement dependent on the location of said interaction during runtime, it can be extremely computationally expensive. To get around this, I set a limit on where charge exchange can occur using the passive scalar. This is essentially another variable with

6.2 Simulating Charge Exchange And Radiation Pressure

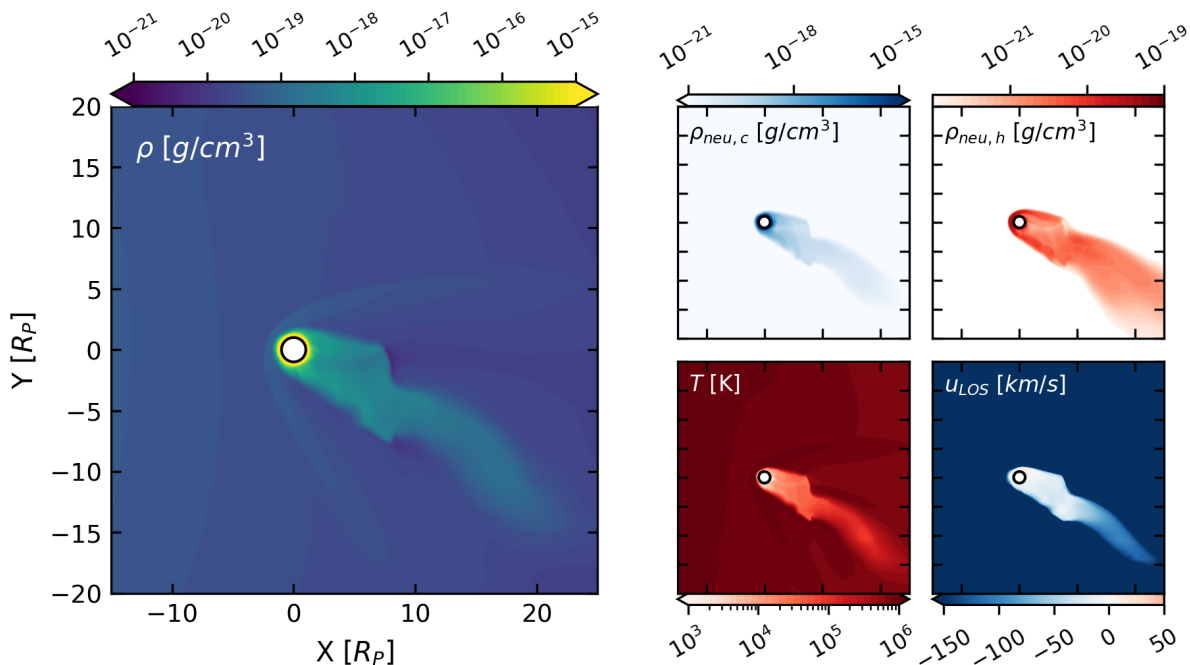


Figure 6.2: The charge exchange Model, in the same style as 6.1. This simulation reaches a QSS, of which I show a snapshot.

its own continuity equation, though it does not contribute to the total mass density. I set this value of the passive scalar to be negative in the stellar wind, and positive in the escaping atmosphere, such that when this equation is solved in the same way as the other hydrodynamic equations, the passive scalar will track whether a cell contains mostly stellar wind or planetary material. I can use this to confine the region in which charge exchange can occur. As we know that charge exchange requires both cold and hot species to be present and that it will occur in a shell around the bow shock, we can set an inner boundary with the passive scalar value (adapted for each simulation) such that this rate is not calculated deep in the escaping atmosphere, thus saving computational resources.

Starting from the base model in figure 6.1, I turn on the charge exchange process and allow the model to settle, yielding the model shown in figure 6.2. I note that this model reaches a QSS, and so a snapshot of this solution is shown here.

We can see that despite not changing the stellar wind, the introduction of charge exchange alters the structure of material around the planet. From the total density we can see that the shape of the tail has changed, due to the instability of the QSS solution

6. MODELLING CHARGE-EXCHANGE & RADIATION PRESSURE

(which is likely due to charge exchange generating an instability at the boundary between the tail and stellar wind). In the base model (Figure 6.1), the cold neutrals were largely contained around the planet, and in its shadow. When charge exchange is introduced we see a lower amount of cold neutrals as expected, with the hot neutrals concentrated on the day-side of the planet and along the bow shock (Figure 6.2, top right panel). With the variation of the QSS solution, we see changes in both the temperature and line-of-sight velocity when compared to the base model, both of which affect the transit line profile, which will be discussed later in this chapter. Though there are changes to the individual density structures, and changes in the velocity and temperature during the QSS solution, the overall structure of the tail is not greatly altered through the inclusion of the charge-exchange process.

6.2.2 Radiation Pressure

Radiation pressure is another process through which ENAs are thought to be created. This is a pressure exerted on the neutral Hydrogen atoms by the Ly- α radiation, which acts radially away from the star (Bourrier et al., 2015; Schneider et al., 2016). In a sense, radiation pressure acts to reduce stellar gravity (which as we have seen in chapter 3 contributes to the structure of the tail), and so can be modelled using an “effective” stellar gravity term in the HD equations:

$$\mathbf{g}_*^{\text{eff}} = \left(1 - \beta \frac{n_n}{n_{\text{total}}}\right) \mathbf{g}_*, \quad (6.8)$$

where β is the velocity dependent ratio of the force due to radiation pressure and stellar gravity (Lagrange et al., 1998; Esquivel et al., 2019). The general form of β is given by:

$$\beta \approx 0.506 f \left(\frac{d}{\text{pc}}\right)^2 \left(\frac{m}{\text{a.m.u.}}\right)^{-1} \left(\frac{M_*}{M_\odot}\right)^{-1} \left(\frac{\lambda}{2000\text{\AA}}\right)^2 \left(\frac{\phi_\lambda^d}{10^{-11} \text{erg cm}^{-2} \text{s}^{-1} \text{\AA}^{-1}}\right), \quad (6.9)$$

where f is the oscillator strength, m is the mass of the element, and ϕ_λ^d is the flux per unit wavelength λ at a distance d . One such profile, which I will use in this chapter, was produced by Bourrier & Lecavelier des Etangs (2013), shown in figure 6.3.

Note that though this method of implementing radiation pressure accounts for the

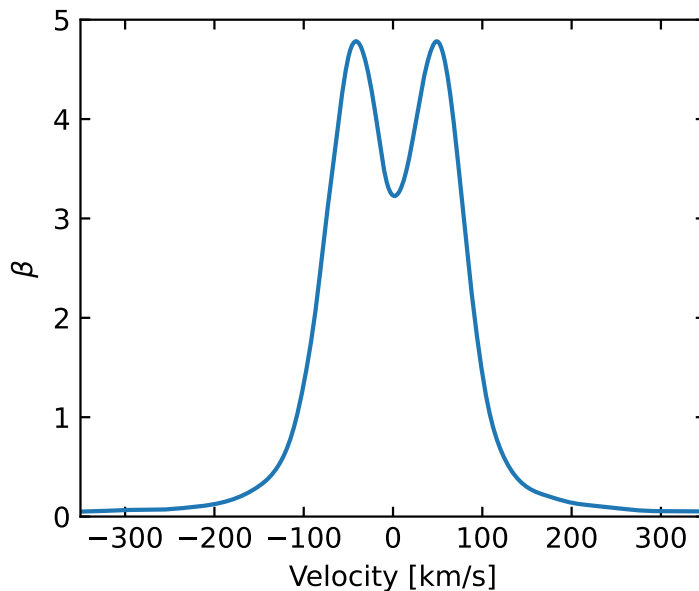


Figure 6.3: The β profile for HD209458, which I use in this chapter (See Figure 2 in Bourrier & Lecavelier des Etangs, 2013).

shadow of the planet (radiation pressure is not calculated in a cylinder of radius $1R_p$ on the nightside), this model does not consider “self-shielding”, in which case a neutral Hydrogen atom could be shielded from incident radiation by other material between it and the star. Should this be considered, the strength of the radiation pressure should decrease further into a volume of neutral Hydrogen (i.e. closer to the planet). To accurately model this, one could perform an optical depth calculation similar to that performed for the ionisation of Hydrogen, which would introduce an $e^{-\tau\alpha}$ term in equation 6.8. I will ignore self-shielding for now, but will discuss its implications on the results later in this chapter.

In figure 6.4 the effects of radiation pressure are clear. We can see that the additional pressure acts to shape the tail more radially away from the star, when compared to the base model in figure 6.1. As a result we obtain a thinner, denser tail which is more aligned with the line of sight. This suggests a significant change to the transit line profile. Also note that though this model does not contain charge exchange, we do obtain a small amount of the hot neutral species, which are generated by a small amount of stellar wind protons cooling and recombining in the bow shock.

6. MODELLING CHARGE-EXCHANGE & RADIATION PRESSURE

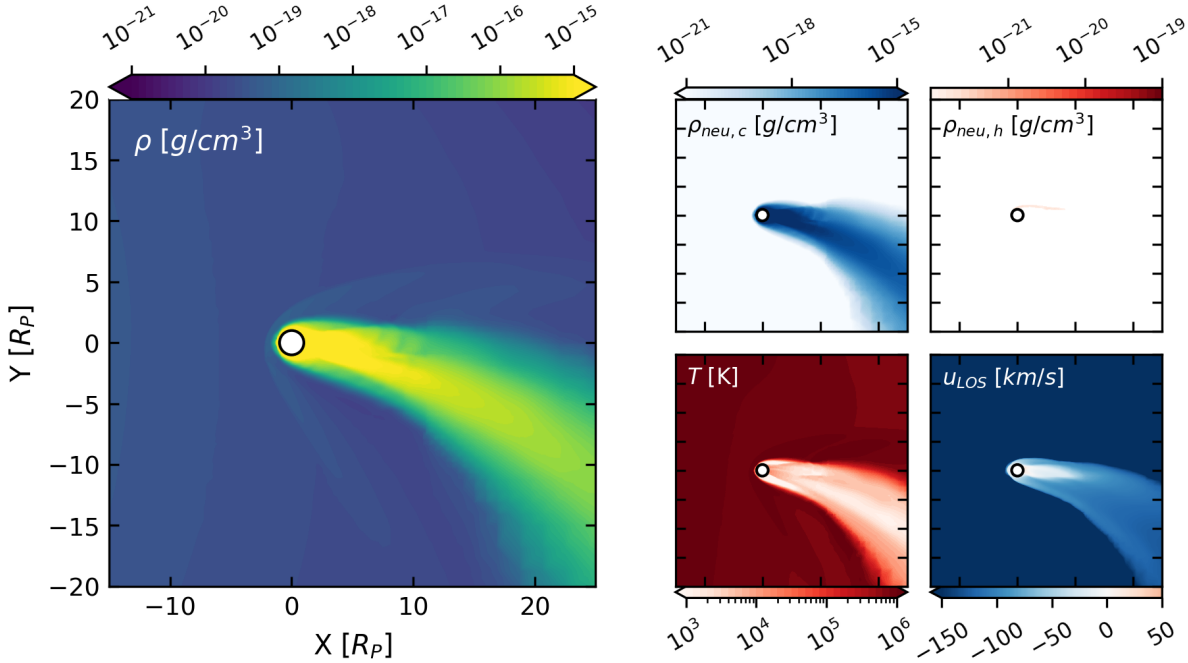


Figure 6.4: The Radiation Pressure Model, in the same style as figure 6.1.

6.2.3 Charge Exchange And Radiation Pressure

Starting from the steady-state solution of the radiation pressure model, I turn on the charge-exchange process. From figure 6.5 we can see that this model looks very similar to the radiation pressure model in figure 6.4. The only notable difference is in the hot neutral species, as expected. We again see high density regions along the bow shock, formed when the planetary neutrals interact with the stellar wind protons. Comparing this to what we see in the charge exchange model (figure 6.2), there is a higher density of hot neutrals along the edges of the tail, but fewer within the tail itself. This is related to the difference in the angle of the tail in the two models, which stems from the changes in the effective stellar gravity. In the case without radiation pressure (Figure 6.2), the tail is directed less radially away from the star and bent more towards the orbital motion, with the hot neutrals created on the stellar side of the tail being pushed into the tail by the stellar wind ram pressure. When including radiation pressure the tail is directed more radially away from the star, the stellar wind pushes the newly created hot neutrals along the border rather than into the tail itself, which creates the high density shells of hot neutrals we see

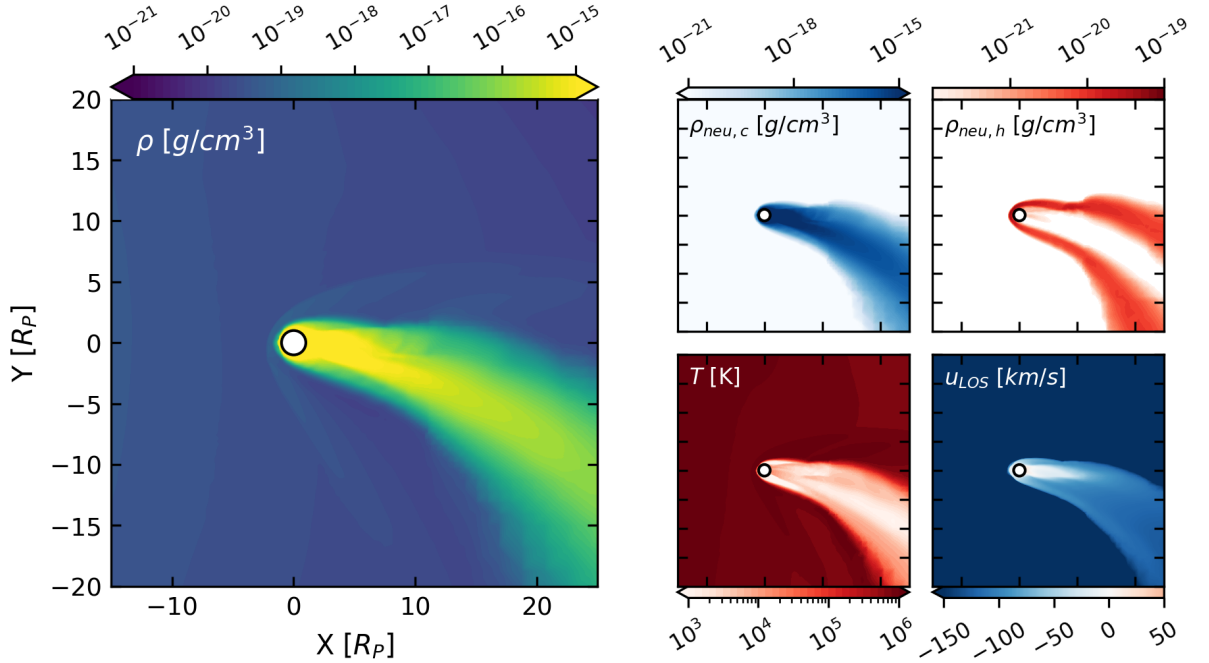


Figure 6.5: The Radiation Pressure and Charge exchange Model, in the same style as figure 6.1. As radiation pressure is strong in this model, and self shielding is ignored, the effect of charge exchange in this model is not as apparent.

in the top right panel of figure 6.5.

6.3 Effects On The Transit Line Profiles

Similarly to what was done in chapters 3, 4 and 5, I calculate the Ly- α transit line profile of each of the above models at mid-transit, the results of which can be seen in figure 6.6. We can see that the line profile of the base case (blue line) looks similar to the models which we have seen in previous chapters, where absorption is mostly at line centre, with small amounts of absorption at blue-shifted velocities. We do not see any significant red shifted absorption as the stellar wind confines day-side material close to the planet, where u_{LOS} is lower.

In the charge exchange model (orange line) we find lower line centre absorption, accompanied with greater absorption at blue-shifted velocities. This is what we expect as through charge exchange ENAs are created from low velocity neutrals, and so absorption

6. MODELLING CHARGE-EXCHANGE & RADIATION PRESSURE

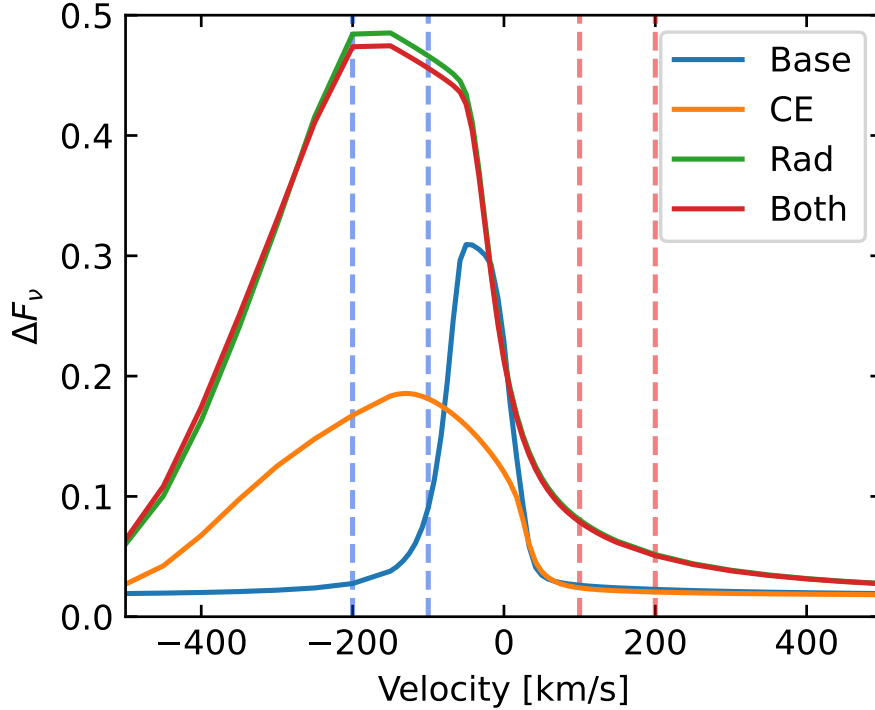


Figure 6.6: The Ly- α transit line profiles of each of my models at mid transit. The blue line is the absorption from the base model, while the orange line is for the model with charge exchange. The red line is the line profile for the model with radiation pressure, and the green is the absorption for the model with both charge exchange and radiation pressure. The blue and red wings are marked with blue and red dashed lines respectively.

at low velocities will be shifted to the blue wing. I find that neglecting this process could lead to underestimations of blue-shifted absorption, and therefore could introduce errors into predictions of detectable escape, given that the Ly- α line is not observable at line centre due to geocoronal emission and interstellar absorption.

In the radiation pressure model (green line) I find both an increase in the maximum absorption as well as more blue wing absorption. The increase in maximum absorption is caused by the changing tail angle. With a tail directed more radially away from the star, at mid transit the tail will be oriented more along the line of sight of the observer. As a result the column density will be higher along the line of sight, therefore increasing the maximum absorption in Ly- α at line centre. The reduced effective stellar gravity causes more acceleration of material along the line of sight when compared to the base model, increasing blue-shifted absorption. This, accompanied with a more radial tail results in

both more total absorption at line centre and in the blue wing.

The model of radiation pressure neglects self-shielding, and is therefore a theoretical limit for the maximum effect radiation pressure could have in these models. As a result, the obtained transit line profile also represents the maximum change from the base case that radiation pressure could cause. We can therefore infer that a model which includes self-shielding would predict an absorption profile bounded by the profile of the base case and that of the radiation pressure model.

Finally I find only a small change when charge exchange is introduced to the radiation pressure model (red line), when compared to its effect on the base case. We now see a small decrease in the maximum absorption compared to the radiation pressure model, with a slight increase at more blue-shifted velocities. This is again due to the change in the angle of the tail. For a larger tail angle like that in the base case, the interaction area on the bow shock will be much larger than that compared to the more radial tail in the radiation pressure model. Limiting the area on which charge exchange can occur consequently decreases the effect of charge exchange on the absorption line profile.

6.4 Discussion

The implementation of radiation pressure using an effective gravity causes the model to lose mass on the order of 10^{12} g/s, which is significantly higher than that of the base model (10^{10} g/s). This is contrary to what is found by Cherenkov et al. (2018); Debrecht et al. (2020); Villarreal D'Angelo et al. (2021), who found that the contribution of radiation pressure is minimal. This is likely due to the implementation of radiation pressure which neglects self shielding. Though Villarreal D'Angelo et al. (2021) also neglected self-shielding, their models did not simulate the inner regions of the escaping atmosphere, but rather started at the sonic surface. When self-shielding is neglected, the force due to radiation pressure is strongest in the inner regions of the escaping atmosphere, where the neutral density is at a maximum. As a result, the effective stellar gravity in these regions contributes to greater acceleration of the escaping material radially away from the star, therefore increasing the atmospheric escape rate. With self-shielding, the effects of radiation pressure in the inner regions of the atmosphere would be negligible, as material at higher altitudes would have absorbed incoming radiation, preventing the additional force we see in these regions. Similar to the models in chapter 3, if the inner regions of the

6. MODELLING CHARGE-EXCHANGE & RADIATION PRESSURE

escaping atmosphere are not affected, one would expect that the escape rate should not change significantly.

The charge exchange model behaves more as expected from other works, with no significant change to the dynamics of the simulation, though the transit line profile is shifted to the blue wing (Esquivel et al., 2019; Odert et al., 2020; Debrecht et al., 2022). Comparing the absorption of the base model to that of the charge exchange model, charge exchange alone could greatly increase the detectability of the escaping atmosphere, as it shifts absorption from the obscured line centre to the observable blue wing of the Ly- α line. However the results from the line profile we obtain are in contrast to that found by Debrecht et al. (2022), who also simulated a HD209458b analogue. While they only find approximately 1% absorption at 100 km/s, my model shows nearly 20%. The difference here is likely due to the different stellar wind conditions. The stellar wind mass-loss rate in my model is much stronger than Debrecht et al. (2022)'s strong and solar analogue cases, with the wind having a mass-loss rate of $5\dot{M}_{\odot}$ and a velocity of approximately 370 km/s, compared to a maximum of $1\dot{M}_{\odot}$ and a velocity of 200km/s in their models. With a denser and faster stellar wind it is to be expected that my simulations will create more hot neutrals at a high velocity, and therefore show more blue wing absorption.

In order to better compare with the work of Debrecht et al. (2022), I run an additional charge exchange model (no radiation pressure), reducing the stellar wind mass-loss rate from $5\dot{M}_{\odot}$ to $1\dot{M}_{\odot}$, without changing other parameters. This reduces the density of the stellar wind, with the velocity remaining unchanged at approximately 370 km/s at the planet. This results in the model shown in figure 6.7. When comparing with figure 6.2, the reduced stellar wind density can be seen in the left panel, however, despite this reduced stellar wind strength, atmospheric escape is still not strong enough to support an extended atmosphere on the day-side, and so it remains confined close to the planet. Comparing the top right panels of figures 6.2 and 6.7, we can see that the $1\dot{M}_{\odot}$ model is producing fewer hot neutrals compared to the $5\dot{M}_{\odot}$, which is to be expected with the reduced density of the stellar wind.

Figure 6.8 shows a comparison between the Ly- α line profiles resultant from synthetic transits of these systems. As seen in figure 6.7, reducing the density of the stellar wind, fewer hot neutrals are generated through charge exchange with the escaping atmosphere. As a result the $1\dot{M}_{\odot}$ stellar wind model (green line) shows reduced absorption in the blue wing when compared to the $5\dot{M}_{\odot}$ model, by approximately a factor of two. Though my

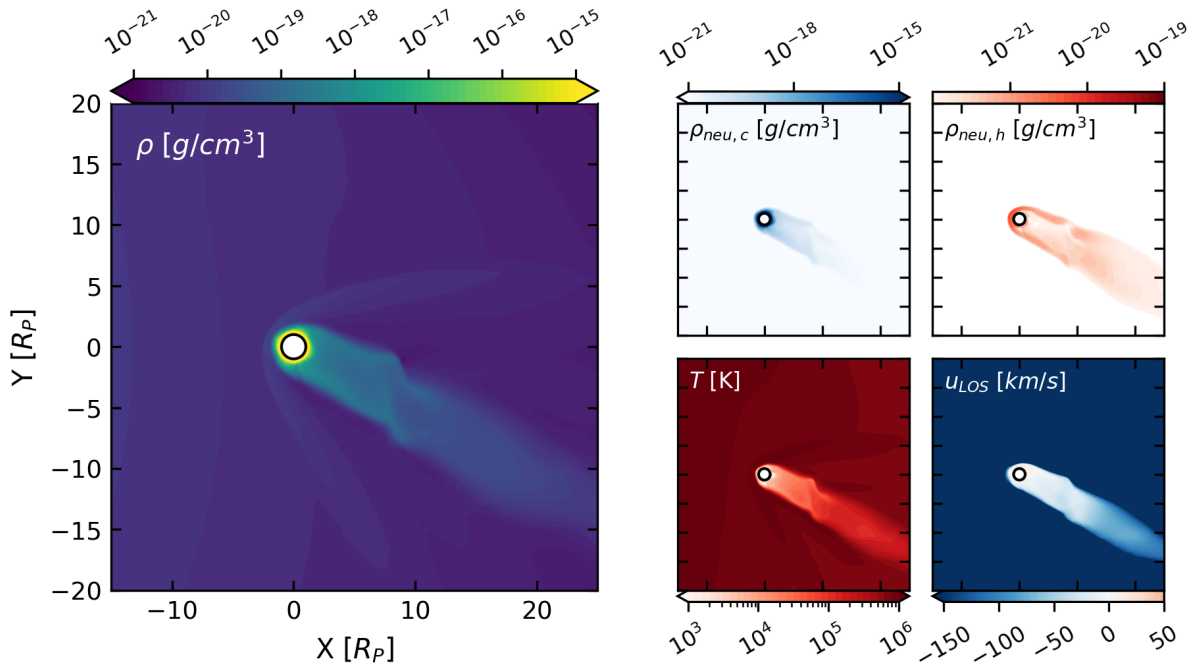


Figure 6.7: Charge Exchange Model for a $1\dot{M}_{\odot}$ stellar wind, in the same style as figure 6.1.

stellar wind velocities are higher I can compare the line profile of my $1\dot{M}_{\odot}$ model with Debrecht et al. (2022)’s solar analogue model. The stellar wind velocity in my $1\dot{M}_{\odot}$ model is approximately 50% faster than Debrecht et al. (2022)’s, and it produces 10 times more absorption at observable velocities (10% absorption compared to 1%). Though these are preliminary results and must be investigated further, it seems that the Ly- α absorption is extremely sensitive to the stellar wind conditions when charge exchange is considered, further emphasising the importance of considering fully the conditions of the stellar wind when investigating observational signatures of atmospheric escape.

6.5 Next Steps

Though significant progress has been made in the treatment of these processes in BATS-R-US, there are still a few improvements that could be made. As mentioned previously, I expect the inclusion of self-shielding in these models could greatly alter the results of the radiation pressure model. To implement this, a similar calculation to that which self-consistently launches the escaping atmosphere will be performed, calculating the optical

6. MODELLING CHARGE-EXCHANGE & RADIATION PRESSURE

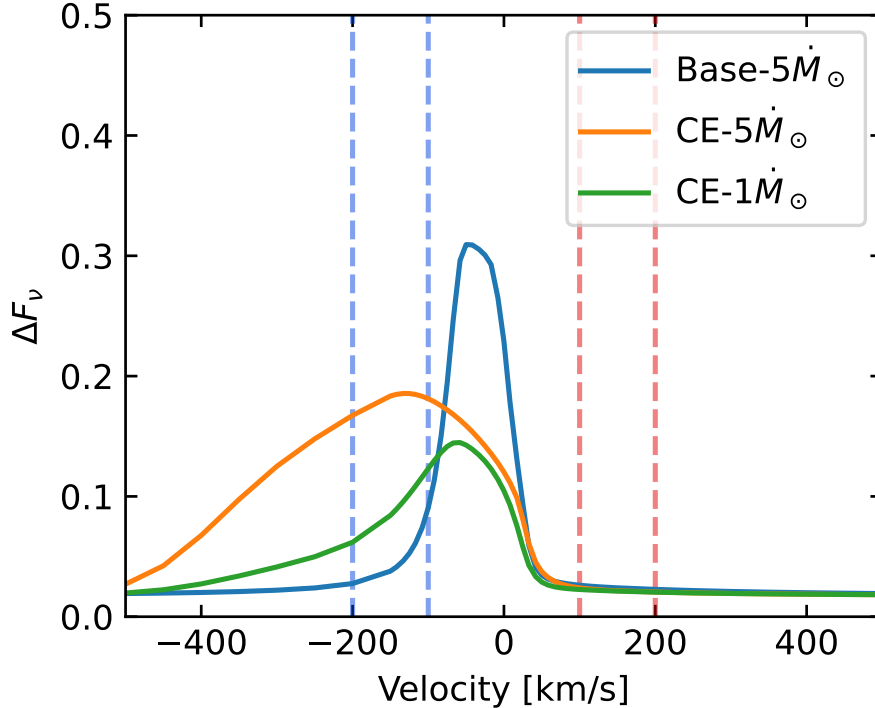


Figure 6.8: A comparison of the Ly- α transit line profiles for the different charge exchange model. The blue is the base case, the orange is the base case with charge exchange, and the green is the weaker ($1\dot{M}_\odot$) stellar wind with charge exchange.

depth of Ly- α photons through the escaping atmosphere during runtime. This will introduce a $e^{-\tau_\alpha}$ factor in equation 6.8, causing the strength of the force due to radiation pressure to drop further in the escaping atmosphere, where the effective gravity would return to just the stellar gravity term. This will not only produce fewer ENAs than the current implementation, it will no longer cause the tail to be oriented more radially away from the star. The combination of these two changes will reduce the differences between the line profiles we currently see between the base and radiation pressure models, which is more in line with literature.

Though the implementation of charge exchange performs well, there are also some small improvements that can be made. As previously mentioned, including the charge-exchange process requires high resolution around the bow shock, which can be computationally expensive. To get around this, I limit where charge exchange can occur to where there are significant numbers of both hot and cold species, using the passive scalar. This allows us to

obtain a QSS solution using a more achievable grid resolution. Additionally a more accurate implementation of charge exchange requires a multi-fluid model, as opposed to my current multi-species model. Similar to a multi-species model, a multi-fluid implementation would have separate mass conservation equations for each species, but would also have separate momentum equations for each fluid. This would remove the necessity for hot and cold species, replacing them with hot and cold fluids, representing the stellar wind and escaping atmosphere. This would allow for the boundary of the two fluids to more accurately be determined, when compared to the current passive scalar determination. As a result, charge exchange would be contained to the boundary of the fluids, which could remove some numerical issues faced during the implementation, where hot neutrals were created deep in the escaping atmosphere, removing the possibility of a stable solution.

6.6 Conclusions

In this chapter I presented preliminary work investigating the effects of charge exchange and radiation pressure on the dynamics and observational signatures of wind-planet interactions. For this I use newly developed 3D self-consistent HD models of a typical Hot Jupiter sized planet. Using the same base model, I introduce the processes of charge exchange and radiation pressure to the wind-atmosphere interaction, first individually, before considering the combination of these processes. To the best of my knowledge, this is the first implementation of radiation pressure and charge exchange for the escaping atmosphere-stellar wind interaction within the BATS-R-US framework.

In total I performed 5 simulations: A base model of the escaping atmosphere interacting with the stellar wind; The base model with charge exchange; with radiation pressure; with both charge exchange and radiation pressure; and finally an additional charge exchange model to compare with the work of Debrecht et al. (2022). I find that the models with charge exchange reached a QSS, with changes to the density structure as cold neutrals are removed and hot neutrals created. Though this model shows some variation the overall tail structure is not greatly altered through charge exchange. The model of radiation pressure shows a much greater difference to the base model, with the denser thinner tail now oriented more radially away from the star. This is likely caused by the current lack of self-shielding in the model. The inclusion of charge exchange in the radiation pressure model does not have as great an effect as in the base model. The hot neutrals created

6. MODELLING CHARGE-EXCHANGE & RADIATION PRESSURE

through charge exchange remain in shells close to the edges of the tail, while in the base model they were more uniformly distributed. This is caused by the difference in the tail angle, with the base model's larger tail angle allowing the stellar wind to push the newly created hot neutrals into the tail.

I calculate the Ly- α transit profile for each of these models at mid transit. I find that though charge exchange did not greatly alter the structure of the escaping atmosphere, the observational signatures are affected. Through the creation of hot neutrals at large velocities, the absorption in the charge exchange model is shifted more to the blue wing, with a decrease in the maximum percentage absorption. Comparing this to the absorption of the base model, the charge-exchange process has increased the detectability of the escaping atmosphere in this model, through increasing absorption at observable wavelengths in the blue wing. An additional charge exchange model was performed with a lower stellar wind density/mass-loss rate. This $1\dot{M}_{\odot}$ stellar wind (reduced from the original $5\dot{M}_{\odot}$) reduces the absorption in the blue wing to approximately 10%, which is still significant enough to be detectable. This is in contrast to Debrecht et al. (2022)'s solar analogue model, where they found the stellar wind in that model was not capable of creating the required absorption to match observational signatures, causing approximately 1% absorption in the blue wing. This is likely due to the difference in stellar wind velocity. Though my $1\dot{M}_{\odot}$ model has the same mass loss rate, it has a velocity which is approximately 150% of Debrecht et al. (2022)'s solar analogue, which shifts absorption to higher more observable velocities. This highlights the important role that the conditions of the stellar wind have on the obtained Ly- α absorption signatures.

The implementation of radiation pressure not only greatly alters the structure of the tail, but also changes the transit line profile. I obtained a Ly- α line profile which is skewed towards the blue wing, with a two thirds increase in maximum absorption compared to the base model. This is attributed to the change in the tail structure and increase in atmospheric escape-rate. As the tail is oriented more along the observer's line of sight, the column density has increased causing an increase in absorption. The reduction in the effective stellar gravity felt by the escaping atmosphere contributes to accelerating planetary material radially away from the star, which accompanied by the increase in column density produces a line profile showing more absorption at more blue-shifted velocities. Note that as this implementation neglects self-shielding, this line profiles provides a theoretical maximum effect that radiation pressure could have on the line profile, and so the absorption

obtained through a more realistic treatment of this process is expected to lie between those of the radiation pressure and base models. Finally I investigate how the inclusion of charge exchange changes this line profile. The effect of charge exchange on this model is not as noticeable, as due to the lower tail angle the interaction region between the stellar wind and tail will be smaller. As well as this the absorbing material in the tail is already at a higher blue-shifted velocity, and so charge exchange will not be as effective in altering the observed absorption.



Summary & Future Work

In this chapter I will first discuss several avenues for future work in this area, before summarising the main results presented in this thesis. Throughout this thesis I have presented novel work examining the various ways planets interact with the stellar wind, as well as investigating the observational signatures of these interactions. This was achieved through the extensive development to our model, which has yielded the first self-consistent 3D model of photoevaporation in close-in systems using the BATS-R-US framework, which includes magnetic fields, the tidal and Coriolis forces, charge exchange and radiation pressure.

7.1 Future Work

There are many interesting avenues for future work related to what I have presented in this thesis. In this section I will explore some of these options, discussing both why they are of interest as well as some of the challenges associated with them.

Self-Shielding

The immediate next step to follow on from this work is to include self-shielding with radiation pressure. This is when the incident Ly- α radiation which exerts a pressure on the escaping atmosphere is attenuated as it penetrates through the atmosphere. As I found in chapter 6, radiation pressure which neglects self-shielding can vastly change both the structure and line profiles in my model. Using self-shielding means the deeper regions of the atmosphere (closer to the planet) would receive less Ly- α flux and therefore be less affected by radiation pressure. When including self-shielding, one can therefore expect the

difference from the base model to be less substantial than what I have found, as neglecting self-shielding results in over-estimation of radiation pressure's affects (Carroll-Nellenback et al., 2017; Esquivel et al., 2019)

The additional calculation for self-shielding is similar to that performed to calculate the heating due to photoionisation. This will modify equation 6.8, including an $e^{-\tau_\alpha}$ term in the second term on the right-hand side. This involves a calculation similar to equation 5.7:

$$\tau_\alpha = \int_{x_{\text{boundary}}}^x n_n \sigma_\alpha dx. \quad (7.1)$$

where σ_α is now the absorption cross section of Ly- α photons. This can be performed in parallel to the calculation of photoionisation, where we would then perform two integrals calculating the two τ terms, one for EUV radiation and one for Ly- α . This calculation can be time consuming, though may be simplified if we assume that σ does not vary significantly from its value at line centre. This allows for σ_α to be taken outside the integral in equation 7.1, such that the integral calculating the column density can be performed once, and then multiplied by the relevant constant σ to obtain the desired optical depth term.

Multi-Fluid Simulations

In this work I presented several models; each model was single-fluid with the self-consistent model being multi-species. This means that in each cell of the computational grid there can be many densities (neutral and ionised Hydrogen), each with their own continuity equation, but there is only one velocity vector and temperature, and so one momentum and energy equation. In a multi-fluid simulation, there again can be multiple densities in each cell, but now there can be a velocity and temperature for each fluid. This increases the number of equations that the code must solve, now requiring one momentum and energy equation for each fluid, one continuity equation for the total density in each fluid as well as additional continuity equations for each species in each fluid.

Though this obviously increases the computational expense, it could be very applicable to exoplanetary study. An example of its application is to the computation of charge exchange. Currently in my simulations I do not consider the stellar wind and escaping atmosphere as separate fluids, but can distinguish between them using the passive scalar. This allows us to confine the region where charge exchange can occur to the region where

7. SUMMARY & FUTURE WORK

the stellar wind and escaping atmosphere meet. A multi-fluid simulation removes the necessity for the passive scalar, as the stellar wind and atmosphere can be modelled as separate fluids. In this setup charge exchange would occur between the planetary neutrals in the atmospheric fluid and the protons in the stellar wind fluid only at the boundary where the fluids meet. In this setup, one would no longer need to assume the relative velocity from the Maxwell-Boltzmann distribution in the calculation of α_{CE} (equation 6.6). Instead the relative velocity between the two fluids could be used.

Similarly this would make the calculations of the escape rate more exact. For example, when in chapter 5 I calculated the escape rate through planes above and below the magnetic poles of the planet, I required the passive scalar again to select only the planetary material flowing through these planes. In a multi-fluid simulation, we would be able to simply select the density and velocity from the planetary fluid, allowing for a more exact calculation.

Modelling Helium

In this work I presented a 3D model which I have steadily been developing to better simulate escaping Hydrogen from close-in exoplanets. This has allowed us to use this model to investigate the observation signatures of escaping Hydrogen, namely the Ly- α line at 1216Å. As previously discussed there are some difficulties observing Ly- α , given that the line centre is contaminated by interstellar absorption and geocoronal emission. Due to this, there have been significant efforts made exploring the use of other spectral lines in order to detect escaping atmospheres. As shown in chapter 1, a very promising line is the Helium I 10830Å triplet in the near infra-red, which has the advantage of being observable using ground-based telescopes.

As was discussed by Oklopčić & Hirata (2018), the neutral Helium atom can exist in different configurations depending on the spin of the electrons: the singlet state (electron spins are anti-parallel) and the triplet state (electron spins are parallel). The lowest triplet state (2^3S) is responsible for absorption in the 10830Å triplet. This state is meta-stable, as radiative transitions from this state to the singlet ground state are strongly suppressed, with a lifetime of approximately 2.2 hours (Drake, 1971). This state is populated by both recombination and collisional excitation from the ground state, with approximately 75% of recombinations of Helium resulting in the 2^3S configuration (Osterbrock & Ferland, 2006).

In order to model and interpret these observations we must include Helium in our

models. Recently there have been a number of works which include Helium, most of which are simulating in 1D (eg. Oklopčić & Hirata, 2018; Lampón et al., 2020; Dos Santos et al., 2022). These models simulate 1D isothermal Parker winds, solving for the neutral and ionised Hydrogen, as well as the various states of Helium in post-processing. The first assumption that these models make is that the contribution of Helium to the total density, with most choosing a 90-10 split between Hydrogen and Helium. While for Hydrogen one must solve an equation of ionisation balance to determine the fraction which is in the neutral and ionised states, for Helium one must solve for the fraction which is in the singlet, triplet and ionised states. This involves solving two additional equations, one for f_1 (the fraction of Helium in the singlet state) and one for f_3 (the fraction in the triplet), with the ionised fraction then inferred from the total Helium density (see equations 14 & 15 in Oklopčić & Hirata, 2018).

Note that in the isothermal Parker wind, the velocity and density profiles are independent (Parker, 1958). In these models the ionisation fraction of Hydrogen as well as the singlet and triplet fractions of Helium are found in post-processing, and are not calculated along with the total density during runtime. This post-processing calculation is not exclusive to 1D simulations, but can also be employed by 3D isothermal hydrodynamic simulations similar to my model in chapter 3. One such study has been performed by MacLeod & Oklopčić (2022), who demonstrated stellar wind confinement of the He 10830Å line using this method. Recall that in order to model photoevaporation self-consistently in 3D, we must calculate the heating/cooling of Hydrogen during runtime, which requires the calculation of ionised and neutral Hydrogen densities during runtime. If one assumes that the contribution to the total heating/cooling due to the photoionisation/recombination of Helium is small, then one could still populate the various Helium states in post-processing, which is an avenue future work in this area could explore (Dos Santos et al., 2022, have done this in 1D). Alternatively, one could include Helium self-consistently in the simulation, requiring additional continuity equations for each species of Helium, as well as their contributions to the heating and cooling rates of the fluid. The later is obviously much more computationally expensive, and so the necessity of including He self-consistently should be investigated in 1D first, in order to determine if it is worth the computational expense.

7. SUMMARY & FUTURE WORK

Modelling Heavier Elements

As can be done for Helium, the simulations could be extended to heavier elements. This is especially interesting, given the many detection of heavy elements in the upper atmospheres of close-in exoplanets (eg. Gibson et al., 2020; Hoeijmakers et al., 2018). Currently there are not many published models which account for heavier elements in the escaping atmosphere. One such model was presented by Koskinen et al. (2013a) which was used to explain the presence of heavier elements in the atmosphere of HD209458b (Koskinen et al., 2013b). This hydrodynamic model simulates species such as H, H⁺, He, He⁺, C, C⁺, O, O⁺, N, N⁺, Si, Si⁺, Si²⁺, with a continuity equation for each accounting for the source and sink terms, in 1D.

To include these heavier elements in the 3D code we again have two approaches. Similar to Koskinen et al. (2013a)'s model, we could include each species through additional continuity equations during runtime, though again we note that in 3D this greatly increases the computational expense for each additional species. Alternatively, if the presence of heavier elements is assumed to not contribute significantly to the total heating and cooling of the fluid (again the validity of this assumption should be checked thoroughly), their populations of the different elemental species could be calculated in post-processing, if the overall composition of the fluid is initially assumed. This would be the first avenue to pursue, given that the time consuming species calculations only have to be performed once during post-processing. This would allow for synthetic transits of a 3D model including heavier elements to be performed, in order to model observations of these elements.

Future Observations

Throughout this thesis, I have developed a numerical model capable of investigating the local environment of close-in exoplanets. I have used this model to to identify trends in observational characteristics associated with these systems, which provide important context for future observational efforts. With the launch of the JWST, and the ELT becoming operational in the not so distant future, an opportunity to investigate these trends presents itself.

In chapters 3, I showed that the stellar wind can decrease and even remove any detectable absorption in the blue wing of the Ly- α line. Strong stellar winds confine absorbing material close to the planet, limiting the area of the stellar disc covered by the gas, resulting

in lower absorption at all velocities, as shown in figure 3.9. In chapter 4, I discussed how this effect could be investigated in a test system: AU Mic b, where a non-detection of Ly- α absorption from such a young planet would suggest the presence of a strong stellar wind. Though in these chapters I focused on the escape of Hydrogen, and the corresponding signatures in Ly- α , stellar wind confinement will affect heavier elements. The stellar wind applies an opposing force to the bulk flow of the escaping atmosphere, and so is capable of confining the volume occupied by all absorbing species. This effect can therefore be investigated through observations at a variety of wavelengths, though the more abundant elements (Hydrogen: Ly- α & Helium: 10830Å) are likely to yield detections. As well as this, as discussed in chapter 4, young planets are good targets for these studies, given evaporation is strongest at young ages because of the high incident EUV flux from the host stars.

In chapter 5, I found that the planet's magnetic field can also suppress absorption in the blue wing of Ly- α , as the closed field lines trap escaping gas at low velocity in the dead-zones. However the suppression of blue wing absorption by magnetic fields is not degenerate with that of the stellar wind. The size of the dead-zones grows with magnetic field strength, with large magnetic fields yielding strong absorption at line centre (figure 5.6). As the main difference between these two effects occurs at line centre, it is challenging to disentangle these effects with Ly- α observations alone. In order to determine whether little to no absorption in the blue wings of Ly- α is due to the stellar wind or the planetary magnetic field, simultaneous observations in other spectral lines could be used. Should a set of observations find little to no absorption in the blue wing of Ly- α , while simultaneously finding low absorption from other elemental species at line centre, this would suggest that there is a strong stellar wind inhibiting absorption at all velocities in the system. However if absorption from other elements is found at line centre, this would suggest that the magnetic field is trapping material and reducing blue wing absorption, while supporting a dead-zone of low velocity material. This places importance on future observational missions probing different spectral lines during the same transit, given a set of these allows for the stellar wind strength and presence of a magnetic field to be inferred.

In chapter 6, I introduce charge-exchange and radiation pressure to the model, with both of these processes affecting observational characteristics. Charge exchange is thought to be a contributing factor to the large amount of blue shifted Ly- α absorption that past observations have found, where low velocity neutral Hydrogen atoms exchange an electron

7. SUMMARY & FUTURE WORK

with a stellar wind proton¹. Understanding charge exchange is particularly important, as it could give us a window into the stellar wind conditions. As I have shown in the preliminary work presented in chapter 6, charge exchange is sensitive to the stellar wind density, but also the stellar wind velocity, as the energetic neutrals are generated at the velocity of the stellar wind. It is therefore important that we continue to observe close-in systems with Ly- α observations, as well as with simultaneous observations in other spectral lines, so that we can capture a full picture of a particular system's conditions. Though Ly- α presents observational challenges, given that the line centre is contaminated by interstellar absorption and geocoronal emission, the launch of space based telescopes such as the Colorado Ultraviolet Transit Experiment (CUTE) provide ample opportunity to expand our Ly- α (and UV) observational catalogues.

7.2 Summary

Overview

In this thesis, I began by investigating how the Earth interacts with the solar wind in chapter 2, focusing on the evolution of this interaction with the changing solar wind conditions. I then moved to close-in systems in chapter 3, where I developed and presented models of atmospheric escape from a close-in Hot Jupiter and Warm Neptune. By varying the strength of the stellar wind I investigated how the stellar wind can confine these escaping atmospheres, and how this confinement affects the Ly- α transit line profile of the system. In chapter 4 I then applied my findings from this study to a test system: AU Mic b, where I was able to use stellar wind confinement to estimate the conditions of the local stellar wind depending on what future observations may find. I then continued the development of my model, reintroduced magnetic fields to the simulations in chapter 5, examining how varying the magnetic field strength of the planet can change the structure and signatures of atmospheric escape in close-in systems. Finally, in chapter 6 I presented preliminary work on the inclusion of two new processes in my simulations: charge exchange and radiation pressure, each of which is thought to contribute to the creation of the ENAs necessary to

¹Note that though not studied in this thesis, charge exchange is not exclusive to Hydrogen, but could happen with a stellar wind proton and a heavier atomic species from a planet's escaping atmosphere. In this scenario, absorption in Ly- α would be increased (at the stellar wind velocity), while absorption by the heavier species would decrease.

match observations of neutral Hydrogen at blue-shifted velocities.

The work presented in this thesis has resulted in four first authored works to date, having made significant developments to our 3D model of photoevaporation, in the pursuit of both the knowledge and technology needed to model observations of atmospheric escape. Additionally my models were incorporated in other works from our research group. These publications, which I co-authored, are listed in appendix A.

The Evolution Of Earth’s Magnetosphere

In chapter 2, I studied the evolution of Earth’s magnetosphere over the solar main sequence, published in Carolan et al. (2019). In this study I coupled two sets of simulations: 1.5D stellar wind models of solar-like stars with different rotation rates, with the conditions at 1 au in each of these winds used as inputs in the 3D simulations of Earth’s magnetosphere. Rotation rates here are used as a proxy for age, as stars are known to spin down over their main-sequence lifetime, though it is not certain whether the Sun was a fast, intermediate, or slow rotator (Gallet & Bouvier, 2013). As expected I see a split in the stellar wind conditions at 1au at a rotation rate of $1.4\Omega_{\odot}$, which is related to the broken power law relations adopted in the base properties of the winds (Ó Fionnagáin & Vidotto, 2018).

Using the balance of the thermal and magnetic pressures, I found the position of the magnetopause in each of the 3D simulations. Just like the stellar wind conditions, I found a broken power law best fits the magnetopause standoff distances: $r_M(< 1.4\Omega_{\odot}) \propto \Omega^{-2.04}$ and $r_M(\geq 1.4\Omega_{\odot}) \propto \Omega^{-0.27}$. This suggests that given the young Sun’s wind was much stronger, Earth’s magnetosphere was much smaller, but grew in size as the solar wind gradually relaxed with time as the Sun spun down. This also allows us to predict a larger magnetosphere for the Earth in the future. I showed that there is a linear relationship between the magnetopause and bow shock standoff distances, with the bow shock standoff distance therefore varying with the same broken power law. My numerical results agree with theoretical expectations.

My simulations of Earth’s evolving magnetosphere also allowed me to examine when stellar wind inflow and plasma collection pose a threat to Earth’s atmosphere, which was a topic of discussion at the time of my publication (Blackman & Tarduno, 2018). By finding the colatitude of the last open magnetic field line in each model, I found that the area on the Earth’s surface covered by open field lines decreases with the evolution

7. SUMMARY & FUTURE WORK

of Earth’s magnetosphere. This accompanied with the gradual increase in the size of the magnetosphere suggests that stellar wind inflow poses the greatest threat in the young system, while plasma collection becomes more and more important as the planet-wind interaction evolves.

The Effects Of The Stellar Wind On Ly- α Transits

In chapter 3, I moved to close-in systems, where I investigated how the stellar wind and escaping atmosphere interact. This was published in Carolan et al. (2021a). To do this I build upon the previous 3D model, developing its ability to launch an escaping atmosphere, and adding the necessary source terms to account for close-in orbital effects. I apply this code to two test systems: a typical Hot Jupiter similar to HD209458b; and a typical Warm Neptune similar to GJ 3470b, performing nearly 30 simulations in total.

Like the Earth simulations, the conditions of the stellar wind are taken as input, and injected from the outer boundary. I gradually increase the stellar wind mass-loss rate, while holding the velocity profile constant, to increase the ram pressure that the stellar wind exerts on the escaping atmosphere. This confines the escaping atmosphere closer to the planet, and once this confinement begins to affect the sonic surface, the rate of escape begins to change (Vidotto & Cleary, 2020). For the HJ planet, the escape rate is reduced from 5.8×10^{11} g/s to 2.1×10^{11} g/s when comparing a wind with $100\dot{M}_{\odot}$ to when no stellar wind was considered. Similarly for the WN planet, the escape rate was reduced from 6.5×10^{10} g/s to 3.9×10^{10} g/s. This demonstrates that in order to understand the escaping atmosphere one must also consider the conditions of the stellar wind, especially if the star can produce a strong stellar wind.

I found that this confinement does not only affect the escape rate of the planet, but also the observational signatures of this escape. Through synthetic observations in the Ly- α line, I demonstrated that for both planets stellar wind confinement can greatly reduce, and even remove any detectable excess absorption caused by the escaping atmosphere. This is due to the stellar wind reducing the volume within which the absorbing material can occupy, therefore also reducing the area on the stellar disc covered by absorbing material. Furthermore I found that the unaffected escape rate of the planet (before the sonic surface is disturbed by confinement) can produce a range of absorptions depending on the stellar wind strength considered, further emphasising the importance of considering the stellar

wind conditions when interpreting observations of atmospheric escape.

The Dichotomy Of Atmospheric Escape In AU Mic b

In chapter 4 I applied this newfound knowledge of how the stellar confinement can affect the escaping atmosphere and its observational characteristics to a test system: AU Mic b. This work was published in Carolan et al. (2020) as a letter. This newly discovered Warm Neptune provides an interesting laboratory to investigate this effect as the system has an interesting dichotomy. On one hand the planet orbits a young M-Dwarf type star, which are known to produce strong EUV radiation, and therefore should induce strong atmospheric escape from the planet. On the other hand young stars are also thought to produce strong stellar winds, which I have shown can confine the escaping atmosphere and mask its detection signatures.

Using a similar process to the previous chapter, I perform several models of the escaping atmosphere from AU Mic b, increasing the stellar wind mass-loss rate over the possible range proposed in literature, from $10\dot{M}_{\odot}$ up to $1000\dot{M}_{\odot}$. Similar to the previous planets, I found that the strongest stellar wind is capable of reducing the atmospheric escape rate by 50% as it confines the outflow. By performing synthetic transits of AU Mic b, I found that the strongest stellar winds erase any observational signatures in Ly- α , while the weaker winds yield approximately 10% absorption in the blue wing. This allows us to infer the conditions of the stellar wind of AU Mic depending on what future Ly- α observations detect. Should these observations find asymmetric absorption favouring the blue wing, my models would suggest that the stellar wind mass-loss rate is on the lower end of the proposed range, closer to $10\dot{M}_{\odot}$. However if future observations show a non-detection of the escaping atmosphere, this would suggest a very strong stellar wind, with a mass-loss rate closer to $1000\dot{M}_{\odot}$. This demonstrated that considering the stellar wind is not only important when investigating the conditions of the planet, but that these simulations can also be used to infer the characteristics of the stellar wind as well.

The Effects Of Magnetic Fields On Ly- α Transits

In chapter 5 I reintroduce magnetic fields to the newly developed self-consistent atmospheric escape model of Hazra et al. (2022). This work is published in Carolan et al. (2021b). This 3D MHD code now takes the EUV flux as input, and self-consistently cal-

7. SUMMARY & FUTURE WORK

culates the induced photoevaporation of the planet’s upper atmosphere in order to more accurately simulate photoevaporation and the asymmetry in this escape from day-side to night-side. While keeping the conditions of the stellar wind constant, I varied the planet’s dipole field strength up to 10G. Like other works I found that the inclusion of the planet’s magnetic field in these simulations creates both dead-zones, where material is trapped at low velocity within the closed magnetic field lines, and polar flows, where material escapes from the open field lines at the magnetic poles. I presented the novel finding that, as the magnetic field strength of the planet is increased, the comet-like tail structure which follows the planet begins to break, as the dead-zone grows and begins to funnel material above and below the orbital plane. For the larger magnetic field strengths this produces a “double-tail” structure, where the two polar flows produce two comet-like tails following the planet, one above and below the orbital plane (for a magnetic axis which is perpendicular to the orbital plane).

The change in magnetospheric structure yields changes in the observational signatures of the escaping atmosphere. I found an increase in absorption with magnetic field strength at the line centre, as the size of the dead-zone surrounding the equator grows. The blue wing absorption initially decreases, as the tail begins to be funnelled above and below the orbital plane instead of along the line of sight, before increasing again at larger field strengths. The red-shifted absorption was found to also increase with field strength, with most of the red-shifted material located between the two comet-like tails on the nightside of the planet, for larger magnetic field strengths.

Finally I investigated the asymmetry between the transits with positive and negative impact parameters. I found that planets which transit below mid-disc showed more absorption in the blue wing than those which transit above the mid disc. This is caused by the interaction between the planetary and stellar wind magnetic fields. Below the orbital plane, the stellar and planetary field lines reconnect. Above the orbital plane the opposite occurs, where the planetary and stellar field lines are aligned and more open field lines are found. As a result the outflow is more extended above the orbital plane than it is below, leading to more absorption when the upper tail covers the stellar disc than the lower. I find through this study that not only is it important to consider the magnetic field strength of the planet, but also its interaction with the stellar field when interpreting observational data.

Modelling Charge Exchange And Radiation Pressure

In chapter 6 I presented preliminary work on the inclusion of two new processes into my 3D simulations: charge exchange and radiation pressure. Both of these processes are thought to produce energetic neutral atoms, which cause the high velocity absorption necessary to match observational data. I performed in total 5 non-magnetic simulations: the base case, one with charge exchange, one with radiation pressure, one with both radiation pressure and charge exchange, as well as an additional charge exchange model to compare to the recent work of Debrecht et al. (2022). When charge exchange is considered, the model reaches a quasi-steady state solution, where the tail oscillates with iteration number, though the general structure of the tail remains the same. The radiation pressure model varies significantly from the base case, with a denser tail aligned more radially away from the star. I attribute this to the current lack of self-shielding in the model. Finally the model with both processes resembles the radiation pressure model closely, but now with the creation of hot neutrals along the boundaries of the more radial tail.

Though the general structure of the tail in the charge exchange model was unchanged, this was not true for its line profile. I obtained absorption between 10 and 20% in the blue wing, compared to only a few % in the base model. This is directly caused through the charge exchange process, where neutral Hydrogen atoms at the stellar wind velocity are generated. I found that the obtained line profile is sensitive to both the stellar wind density/mass-loss rate and the stellar wind velocity, highlighting again the importance of considering the characteristics of the stellar wind when interpreting observational data.

Contrary to what other works have found, I obtain significantly different line profiles in models with radiation pressure than those without. I see an increase in absorption at line centre and in the blue wing, caused by the denser tail which is aligned more along the line of sight. As there is already significant blue-shifted absorption in this model, the effects of charge exchange are not as noticeable when included here as opposed to when included in the base case. However due to the lack of self-shielding currently in the model, these line profiles represent the theoretical maximum absorption that can be generated through radiation pressure, and so should not be used to interpret observational data. Though this work is preliminary, my models provide promising results in the ability of charge exchange and radiation pressure to produce energetic neutral atoms that we observe in Ly- α .

Although I investigate a variety of different wind-planet interactions in this thesis,

7. SUMMARY & FUTURE WORK

my research consistently illustrates that considering the properties of the stellar wind is incredibly important in order to correctly interpret the structure of the planet's local environment, and how it affects the planet's atmosphere.

References

- Aarnio A. N., Stassun K. G., Hughes W. J., McGregor S. L., 2011, *Solar Physics*, 268, 195 (Cited on page 60.)
- Airapetian V. S., Glocer A., Gronoff G., Hébrard E., Danchi W., 2016, *Nature Geoscience*, 9, 452 (Cited on page 41.)
- Alfvén H., 1942, *Nature*, 150, 405 (Cited on page 33.)
- Allan A., Vidotto A. A., 2019, *Monthly Notices of the Royal Astronomical Society*, 490, 3760 (Cited on pages 15, 34, 76, 77, 78, 90, 104, 110, 116 and 117.)
- Allart R., et al., 2018, *Science*, 362, 1384 (Cited on page 8.)
- Alonso-Floriano F. J., et al., 2019, *Astronomy & Astrophysics*, 629, A110 (Cited on page 9.)
- Alvarado-Gómez J. D., Drake J. J., Cohen O., Moschou S. P., Garraffo C., 2018, *Astrophysical Journal*, 862, 93 (Cited on page 60.)
- Arakcheev A. S., Zhilkin A. G., Kaigorodov P. V., Bisikalo D. V., Kosovichev A. G., 2017, *Astronomy Reports*, 61, 932 (Cited on pages 113, 129 and 131.)
- Bagenal F., 2013, in Oswald T. D., French L. M., Kalas P., eds, , *Planets, Stars and Stellar Systems. Volume 3: Solar and Stellar Planetary Systems*. p. 251, doi:10.1007/978-94-007-5606-9_6 (Cited on pages 22 and 23.)
- Ballester G. E., Ben-Jaffel L., 2015, *Astrophysical Journal*, 804, 116 (Cited on page 8.)
- Balogh A., Treumann R. A., 2013, *Physics of Collisionless Shocks: Space Plasma Shock Waves*. ISSI Scientific Report Series, Springer, New York, <http://cds.cern.ch/record/1517899> (Cited on pages 57, 64 and 124.)
- Baraffe I., Selsis F., Chabrier G., Barman T. S., Allard F., Hauschildt P. H., Lammer H., 2004, *Astronomy & Astrophysics*, 419, L13 (Cited on pages 2 and 10.)
- Barnes S. A., 2003, *Astrophysical Journal*, 586, 464 (Cited on page 46.)
- Beck P. G., et al., 2017, *Astronomy & Astrophysics*, 602, A63 (Cited on page 43.)
- Bharati Das S., Basak A., Nandy D., Vaidya B., 2019, *Astrophysical Journal*, 877, 80 (Cited on pages 41 and 68.)

REFERENCES

- Bisikalo D., Kaygorodov P., Ionov D., Shematovich V., Lammer H., Fossati L., 2013, *Astrophysical Journal*, 764, 19 (Cited on pages 8, 26, 73 and 75.)
- Black J. H., 1981, *Monthly Notices of the Royal Astronomical Society*, 197, 553 (Cited on pages 13 and 116.)
- Blackman E. G., Tarduno J. A., 2018, *Monthly Notices of the Royal Astronomical Society*, 481, 5146 (Cited on pages 24, 39, 40, 56, 65, 68 and 159.)
- Booth R. S., Poppenhaeager K., Watson C. A., Silva Aguirre V., Wolk S. J., 2017, *Monthly Notices of the Royal Astronomical Society*, 471, 1012 (Cited on page 43.)
- Bourrier V., Lecavelier des Etangs A., 2013, *Astronomy & Astrophysics*, 557, A124 (Cited on pages 98, 140 and 141.)
- Bourrier V., Ehrenreich D., Lecavelier des Etangs A., 2015, *Astronomy & Astrophysics*, 582, A65 (Cited on pages 136 and 140.)
- Bourrier V., Lecavelier des Etangs A., Ehrenreich D., Tanaka Y. A., Vidotto A. A., 2016, *Astronomy & Astrophysics*, 591, A121 (Cited on pages 136 and 137.)
- Bourrier V., et al., 2018, *Astronomy & Astrophysics*, 620, A147 (Cited on page 78.)
- Brain D. A., Leblanc F., Luhmann J. G., Moore T. E., Tian F., 2013, Planetary Magnetic Fields and Climate Evolution. pp 487–503, doi:10.2458/azu_uapress_9780816530595-ch020 (Cited on page 40.)
- Carolan S., Vidotto A. A., Loesch C., Coogan P., 2019, *Monthly Notices of the Royal Astronomical Society*, 489, 5784 (Cited on pages 30, 37, 40, 64, 76, 98, 103, 118, 123, 124 and 159.)
- Carolan S., Vidotto A. A., Plavchan P., Villarreal D'Angelo C., Hazra G., 2020, *Monthly Notices of the Royal Astronomical Society*, 498, L53 (Cited on pages 26, 38, 101, 102, 114, 117, 118, 119 and 161.)
- Carolan S., Vidotto A. A., Villarreal D'Angelo C., Hazra G., 2021a, *Monthly Notices of the Royal Astronomical Society*, 500, 3382 (Cited on pages 15, 26, 37, 72, 99, 102, 103, 109, 111, 114, 117, 118, 119, 133 and 160.)
- Carolan S., Vidotto A. A., Hazra G., Villarreal D'Angelo C., Kubyskhina D., 2021b, *Monthly Notices of the Royal Astronomical Society*, 508, 6001 (Cited on pages 38, 98, 102, 112 and 161.)
- Carroll-Nellenback J., Frank A., Liu B., Quillen A. C., Blackman E. G., Dobbs-Dixon I., 2017, *Monthly Notices of the Royal Astronomical Society*, 466, 2458 (Cited on pages 26, 73, 75, 97, 98 and 153.)
- Cauley P. W., Shkolnik E. L., Llama J., Lanza A. F., 2019, *Nature Astronomy*, 3, 1128 (Cited on pages 119 and 126.)

REFERENCES

- Chadney J. M., Galand M., Unruh Y. C., Koskinen T. T., Sanz-Forcada J., 2015, *Icarus*, 250, 357 (Cited on pages 102, 104 and 110.)
- Chapman S., Ferraro V. C. A., 1931, Terrestrial Magnetism and Atmospheric Electricity (Journal of Geophysical Research), 36, 77 (Cited on page 22.)
- Cherenkov A. A., Bisikalo D. V., Kosovichev A. G., 2018, *Monthly Notices of the Royal Astronomical Society*, 475, 605 (Cited on pages 136 and 145.)
- Chiang E., Fung J., 2017, *Astrophysical Journal*, 848, 4 (Cited on page 103.)
- Christie D., Arras P., Li Z.-Y., 2016, *Astrophysical Journal*, 820, 3 (Cited on pages 25, 73, 87, 99, 103 and 133.)
- Cravens T. E., 2004, Physics of Solar System Plasmas (Cited on pages 53 and 68.)
- Crivellari L., Simón-Díaz S., Arévalo M. J., 2019, Radiative Transfer in Stellar and Planetary Atmospheres, doi:10.1017/9781108583572. (Cited on page 35.)
- Cubillos P. E., Fossati L., Koskinen T., Young M. E., Salz M., France K., Sreejith A. G., Haswell C. A., 2020, *Astronomical Journal*, 159, 111 (Cited on pages 8 and 131.)
- Cumming A., Butler R. P., Marcy G. W., Vogt S. S., Wright J. T., Fischer D. A., 2008, *Publications of the Astronomical Society of the Pacific*, 120, 531 (Cited on page 1.)
- Cuntz M., Saar S. H., Musielak Z. E., 2000, *Astrophysical Journal Letters*, 533, L151 (Cited on page 2.)
- De Zeeuw D. L., Sazykin S., Wolf R. A., Gombosi T. I., Ridley A. J., Tóth G., 2004, Journal of Geophysical Research: Space Physics, 109 (Cited on page 117.)
- Debrecht A., Carroll-Nellenback J., Frank A., McCann J., Murray-Clay R., Blackman E. G., 2019, *Monthly Notices of the Royal Astronomical Society*, 483, 1481 (Cited on page 98.)
- Debrecht A., Carroll-Nellenback J., Frank A., Blackman E. G., Fossati L., McCann J., Murray-Clay R., 2020, *Monthly Notices of the Royal Astronomical Society*, 493, 1292 (Cited on pages 26, 73, 98, 136 and 145.)
- Debrecht A., Carroll-Nellenback J., Frank A., Blackman E. G., Fossati L., Murray-Clay R., McCann J., 2022, *Monthly Notices of the Royal Astronomical Society*, (Cited on pages 146, 147, 149, 150 and 163.)
- Dong C., Jin M., Lingam M., Airapetian V. S., Ma Y., van der Holst B., 2018, Proceedings of the National Academy of Science, 115, 260 (Cited on pages 3 and 33.)
- Dos Santos L. A., et al., 2022, *Astronomy & Astrophysics*, 659, A62 (Cited on pages 131 and 155.)

REFERENCES

- Drake G. W., 1971, *Physical Review A*, 3, 908 (Cited on page 154.)
- Drake J. J., Cohen O., Yashiro S., Gopalswamy N., 2013, *Astrophysical Journal*, 764, 170 (Cited on page 60.)
- Dressing C. D., Charbonneau D., 2013, *Astrophysical Journal*, 767, 95 (Cited on page 1.)
- Edson A., Lee S., Bannon P., Kasting J. F., Pollard D., 2011, *Icarus*, 212, 1 (Cited on pages 15 and 80.)
- Ehrenreich D., et al., 2015, *Nature*, 522, 459 (Cited on pages 5 and 6.)
- Esquivel A., Schneider M., Villarreal D'Angelo C., Sgró M. A., Krapp L., 2019, *Monthly Notices of the Royal Astronomical Society*, 487, 5788 (Cited on pages 26, 73, 136, 140, 146 and 153.)
- Fichtinger B., Güdel M., Mutel R. L., Hallinan G., Gaidos E., Skinner S. L., Lynch C., Gayley K. G., 2017, *Astronomy & Astrophysics*, 599, A127 (Cited on page 99.)
- Folsom C. P., Ó Fionnagáin D., Fossati L., Vidotto A. A., Moutou C., Petit P., Dragomir D., Donati J. F., 2020, *Astronomy & Astrophysics*, 633, A48 (Cited on page 126.)
- Fossati L., et al., 2010, *Astrophysical Journal Letters*, 714, L222 (Cited on page 8.)
- Fossati L., Ayres T. R., Haswell C. A., Bohlender D., Kochukhov O., Flöer L., 2013, *Astrophysical Journal Letters*, 766, L20 (Cited on page 8.)
- Fressin F., et al., 2013, *Astrophysical Journal*, 766, 81 (Cited on page 1.)
- Fulton B. J., et al., 2017, *Astronomical Journal*, 154, 109 (Cited on page 4.)
- Gallet F., Bouvier J., 2013, *Astronomy & Astrophysics*, 556, A36 (Cited on pages 45, 46, 47, 62 and 159.)
- García Muñoz A., 2007, *Planetary and Space Science*, 55, 1426 (Cited on page 12.)
- García Muñoz A., Youngblood A., Fossati L., Gandolfi D., Cabrera J., Rauer H., 2020, *Astrophysical Journal Letters*, 888, L21 (Cited on page 95.)
- Gibson N. P., et al., 2020, *Monthly Notices of the Royal Astronomical Society*, 493, 2215 (Cited on pages 8, 131 and 156.)
- Ginzburg S., Schlichting H. E., Sari R., 2016, *Astrophysical Journal*, 825, 29 (Cited on page 10.)
- Ginzburg S., Schlichting H. E., Sari R., 2018, *Monthly Notices of the Royal Astronomical Society*, 476, 759 (Cited on page 10.)
- Goedbloed J. P. H., Poedts S., 2004, *Principles of Magnetohydrodynamics* (Cited on pages 15 and 20.)

REFERENCES

- Goldstein H., Poole C., Safko J., 2002, *Classical mechanics* (Cited on page 81.)
- Gombosi T. I., 2004, *Physics of the Space Environment* (Cited on pages 57, 60, 64 and 124.)
- Guilluy G., et al., 2020, *Astronomy & Astrophysics*, 639, A49 (Cited on page 8.)
- Gupta A., Schlichting H. E., 2019, *Monthly Notices of the Royal Astronomical Society*, 487, 24 (Cited on pages 4 and 10.)
- Gupta A., Schlichting H. E., 2020, *Monthly Notices of the Royal Astronomical Society*, 493, 792 (Cited on pages 4 and 10.)
- Harbach L. M., Moschou S. P., Garraffo C., Drake J. J., Alvarado-Gómez J. D., Cohen O., Frascchetti F., 2021, *Astrophysical Journal*, 913, 130 (Cited on page 113.)
- Haswell C. A., et al., 2012, *Astrophysical Journal*, 760, 79 (Cited on page 8.)
- Hazra G., Vidotto A. A., D'Angelo C. V., 2020, *Monthly Notices of the Royal Astronomical Society*, 496, 4017 (Cited on page 116.)
- Hazra G., Vidotto A. A., Carolan S., Villarreal D'Angelo C., Manchester W., 2022, *Monthly Notices of the Royal Astronomical Society*, 509, 5858 (Cited on pages 26, 98, 112, 113, 114, 116, 161 and 178.)
- Hoeijmakers H. J., et al., 2018, *Nature*, 560, 453 (Cited on pages 8, 131 and 156.)
- Hoeijmakers H. J., et al., 2019, *Astronomy & Astrophysics*, 627, A165 (Cited on pages 8 and 131.)
- Holmström M., Ekenbäck A., Selsis F., Penz T., Lammer H., Wurz P., 2008, *Nature*, 451, 970 (Cited on pages 136 and 137.)
- Holzwarth V., Jardine M., 2007, *Astronomy & Astrophysics*, 463, 11 (Cited on pages 42, 43 and 48.)
- Howard A. W., et al., 2010, *Science*, 330, 653 (Cited on page 1.)
- Howard A. W., et al., 2012, *Astrophysical Journal Supplemental Series*, 201, 15 (Cited on page 1.)
- Ivanova N., Taam R. E., 2003, *Astrophysical Journal*, 599, 516 (Cited on page 43.)
- Jardine M., Collier Cameron A., 2019, *Monthly Notices of the Royal Astronomical Society*, 482, 2853 (Cited on pages 48, 65 and 99.)
- Jia X., Kivelson M. G., 2016, *Journal of Geophysical Research (Space Physics)*, 121, 1413 (Cited on page 30.)
- Jia X., Slavin J. A., Gombosi T. I., Daldorff L. K. S., Toth G., Holst B., 2015, *Journal of Geophysical Research (Space Physics)*, 120, 4763 (Cited on page 30.)

REFERENCES

- Jin S., Mordasini C., 2018, *Astrophysical Journal*, 853, 163 (Cited on page 4.)
- Johnstone C. P., Güdel M., 2015, *Astronomy & Astrophysics*, 578, A129 (Cited on page 43.)
- Johnstone C. P., Güdel M., Lüftinger T., Toth G., Brott I., 2015a, *Astronomy & Astrophysics*, 577, A27 (Cited on pages 19, 20 and 118.)
- Johnstone C. P., Güdel M., Brott I., Lüftinger T., 2015b, *Astronomy & Astrophysics*, 577, A28 (Cited on pages 19 and 48.)
- Johnstone C. P., et al., 2015c, *Astrophysical Journal Letters*, 815, L12 (Cited on pages 15, 39 and 42.)
- Johnstone C. P., Khodachenko M. L., Lüftinger T., Kislyakova K. G., Lammer H., Güdel M., 2019, *Astronomy & Astrophysics*, 624, L10 (Cited on page 41.)
- Kasting J. F., Whitmire D. P., Reynolds R. T., 1993, *Icarus*, 101, 108 (Cited on pages 15 and 80.)
- Kavanagh R. D., et al., 2019, *Monthly Notices of the Royal Astronomical Society*, 485, 4529 (Cited on pages 31 and 123.)
- Kavanagh R. D., Vidotto A. A., Klein B., Jardine M. M., Donati J.-F., Ó Fionnagáin D., 2021, *Monthly Notices of the Royal Astronomical Society*, 504, 1511 (Cited on pages 123 and 126.)
- Keppens R., Goedbloed J. P., 1999, in Wilson A., et al. eds, ESA Special Publication Vol. 448, Magnetic Fields and Solar Processes. p. 1177 (Cited on page 18.)
- Khodachenko M. L., Shaikhislamov I. F., Lammer H., Prokopov P. A., 2015, *Astrophysical Journal*, 813, 50 (Cited on pages 98, 113, 119, 129, 130 and 131.)
- Khodachenko M. L., Shaikhislamov I. F., Lammer H., Berezutsky A. G., Miroshnichenko I. B., Rumenskikh M. S., Kislyakova K. G., Dwivedi N. K., 2019, *Astrophysical Journal*, 885, 67 (Cited on pages 26 and 73.)
- Kipping D. M., Sandford E., 2016, *Monthly Notices of the Royal Astronomical Society*, 463, 1323 (Cited on page 1.)
- Kislyakova K. G., et al., 2014, *Astronomy & Astrophysics*, 562, A116 (Cited on pages 136 and 137.)
- Koskinen T. T., Harris M. J., Yelle R. V., Lavvas P., 2013a, *Icarus*, 226, 1678 (Cited on pages 12 and 156.)
- Koskinen T. T., Yelle R. V., Harris M. J., Lavvas P., 2013b, *Icarus*, 226, 1695 (Cited on page 156.)
- Kubyshkina D., Lendl M., Fossati L., Cubillos P. E., Lammer H., Erkaev N. V., Johnstone C. P., 2018, *Astronomy & Astrophysics*, 612, A25 (Cited on pages 15 and 109.)

REFERENCES

- Kubyshkina D., Vidotto A. A., Villarreal D'Angelo C., Carolan S., Hazra G., Carleo I., 2022a, *Monthly Notices of the Royal Astronomical Society*, 510, 2111 (Cited on pages 26, 98 and 178.)
- Kubyshkina D., Vidotto A. A., Villarreal D'Angelo C., Carolan S., Hazra G., Carleo I., 2022b, *Monthly Notices of the Royal Astronomical Society*, 510, 3039 (Cited on page 178.)
- Kulikov Y. N., Lammer H., Lichtenegger H. I. M., Penz T., Breuer D., Spohn T., Lundin R., Biernat H. K., 2007, *Space Science Reviews*, 129, 207 (Cited on page 39.)
- Lagrange A. M., et al., 1998, *Astronomy & Astrophysics*, 330, 1091 (Cited on page 140.)
- Lai D., Helling C., van den Heuvel E. P. J., 2010, *Astrophysical Journal*, 721, 923 (Cited on page 8.)
- Lamers H. J. G. L. M., Cassinelli J. P., 1999, Introduction to Stellar Winds (Cited on page 16.)
- Lammer H., Selsis F., Ribas I., Guinan E. F., Bauer S. J., Weiss W. W., 2003, *Astrophysical Journal Letters*, 598, L121 (Cited on pages 2, 10 and 98.)
- Lammer H., et al., 2011, Origins of Life and Evolution of the Biosphere, 41, 503 (Cited on page 39.)
- Lammer H., et al., 2012, Earth, Planets, and Space, 64, 179 (Cited on page 39.)
- Lampón M., et al., 2020, *Astronomy & Astrophysics*, 636, A13 (Cited on pages 90, 131 and 155.)
- Lavie B., et al., 2017, *Astronomy & Astrophysics*, 605, L7 (Cited on pages 26 and 27.)
- Lhotka C., Narita Y., 2019, *Annales Geophysicae*, 37, 299 (Cited on page 21.)
- Linde T. J., 1998, PhD thesis, University of Michigan (Cited on page 30.)
- Linde T. J., Gombosi T. I., Roe P. L., Powell K. G., Dezeew D. L., 1998, *Journal of Geophysical Research*, 103, 1889 (Cited on page 30.)
- Lindsay B. G., Stebbings R. F., 2005, *Journal of Geophysical Research (Space Physics)*, 110, A12213 (Cited on page 138.)
- Lingam M., Loeb A., 2018, *International Journal of Astrobiology*, 17, 116 (Cited on pages 3 and 33.)
- Linsky J. L., Yang H., France K., Froning C. S., Green J. C., Stocke J. T., Osterman S. N., 2010, *Astrophysical Journal*, 717, 1291 (Cited on page 8.)
- Llama J., Shkolnik E. L., 2015, *Astrophysical Journal*, 802, 41 (Cited on page 8.)
- Llama J., Shkolnik E. L., 2016, *Astrophysical Journal*, 817, 81 (Cited on page 8.)
- Ma Y., Russell C. T., Nagy A. F., Toth G., Dong C., Bougher S. W., 2013, AGU Fall Meeting Abstracts, pp P13C-05 (Cited on pages 30 and 39.)

REFERENCES

- Ma Y. J., et al., 2015, *Geophysical Research Letters*, 42, 9113 (Cited on page 39.)
- MacLeod M., Oklopčić A., 2022, *Astrophysical Journal*, 926, 226 (Cited on pages 26, 73, 131 and 155.)
- Manchester W. B., Gombosi T. I., Roussev I., Ridley A., De Zeeuw D. L., Sokolov I. V., Powell K. G., Tóth G., 2004, *Journal of Geophysical Research* (Space Physics), 109, 2107 (Cited on page 30.)
- Mansfield M., et al., 2018, *Astrophysical Journal Letters*, 868, L34 (Cited on page 8.)
- Matsakos T., Uribe A., Königl A., 2015, *Astronomy & Astrophysics*, 578, A6 (Cited on pages 24, 25, 85, 91, 99 and 113.)
- Matt S. P., MacGregor K. B., Pinsonneault M. H., Greene T. P., 2012, *Astrophysical Journal Letters*, 754, L26 (Cited on page 42.)
- Matt S. P., Brun A. S., Baraffe I., Bouvier J., Chabrier G., 2015, *Astrophysical Journal Letters*, 799, L23 (Cited on pages 48 and 49.)
- Mayor M., Queloz D., 1995, *Nature*, 378, 355 (Cited on page 1.)
- McCann J., Murray-Clay R. A., Kratter K., Krumholz M. R., 2019, *Astrophysical Journal*, 873, 89 (Cited on pages 26, 73, 85, 91, 99, 102, 117 and 133.)
- Moore T. E., Horwitz J. L., 2007, *Reviews of Geophysics*, 45, RG3002 (Cited on page 40.)
- Murray-Clay R. A., Chiang E. I., Murray N., 2009, *Astrophysical Journal*, 693, 23 (Cited on pages 12, 13, 14, 15, 78, 98, 102, 116 and 117.)
- Ngwira C. M., Pulkkinen A. A., 2014, AGU Fall Meeting Abstracts, pp SM31A–4166 (Cited on page 41.)
- Nichols J. D., et al., 2015, *Astrophysical Journal*, 803, 9 (Cited on page 8.)
- Nortmann L., et al., 2018, *Science*, 362, 1388 (Cited on pages 8 and 130.)
- Odert P., et al., 2020, *Astronomy & Astrophysics*, 638, A49 (Cited on pages 136 and 146.)
- Oklopčić A., 2019, *Astrophysical Journal*, 881, 133 (Cited on page 9.)
- Oklopčić A., Hirata C. M., 2018, *Astrophysical Journal Letters*, 855, L11 (Cited on pages 8, 90, 131, 154 and 155.)
- Osterbrock D. E., 1989, *Astrophysics of gaseous nebulae and active galactic nuclei* (Cited on page 116.)
- Osterbrock D. E., Ferland G. J., 2006, *Astrophysics of gaseous nebulae and active galactic nuclei* (Cited on page 154.)

REFERENCES

- Owen J. E., Adams F. C., 2014, *Monthly Notices of the Royal Astronomical Society*, 444, 3761 (Cited on pages 98, 113, 129 and 131.)
- Owen J. E., Jackson A. P., 2012, *Monthly Notices of the Royal Astronomical Society*, 425, 2931 (Cited on page 15.)
- Owen J. E., Lai D., 2018, *Monthly Notices of the Royal Astronomical Society*, 479, 5012 (Cited on page 3.)
- Owen J. E., Wu Y., 2017, *Astrophysical Journal*, 847, 29 (Cited on page 4.)
- Owen J. E., et al., 2021, arXiv e-prints, p. arXiv:2111.06094 (Cited on pages 6 and 7.)
- Parker E. N., 1958, *Astrophysical Journal*, 128, 664 (Cited on pages 12, 15, 18, 20, 73, 76 and 155.)
- Pillitteri I., Maggio A., Micela G., Sciortino S., Wolk S. J., Matsakos T., 2015, *Astrophysical Journal*, 805, 52 (Cited on page 25.)
- Pizzolato N., Maggio A., Micela G., Sciortino S., Ventura P., 2003, *Astronomy & Astrophysics*, 397, 147 (Cited on page 42.)
- Plavchan P., Werner M. W., Chen C. H., Stapelfeldt K. R., Su K. Y. L., Stauffer J. R., Song I., 2009, *Astrophysical Journal*, 698, 1068 (Cited on pages 103 and 109.)
- Plavchan P., et al., 2020, *Nature*, 582, 497 (Cited on pages 101 and 104.)
- Pneuman G. W., Kopp R. A., 1971, *Solar Physics*, 18, 258 (Cited on page 42.)
- Pognan Q., Garraffo C., Cohen O., Drake J. J., 2018, *Astrophysical Journal*, 856, 53 (Cited on page 41.)
- Réville V., Brun A. S., Strugarek A., Matt S. P., Bouvier J., Folsom C. P., Petit P., 2015, *Astrophysical Journal*, 814, 99 (Cited on page 123.)
- Réville V., Folsom C. P., Strugarek A., Brun A. S., 2016, *Astrophysical Journal*, 832, 145 (Cited on pages 42 and 43.)
- Ribas I., Guinan E. F., Güdel M., Audard M., 2005, *Astrophysical Journal*, 622, 680 (Cited on page 41.)
- Ridley A. J., De Zeeuw D. L., Gombosi T. I., Powell K. G., 2001, *Journal of Geophysical Research*, 106, 30067 (Cited on page 39.)
- Rogers J. G., Gupta A., Owen J. E., Schlichting H. E., 2021, *Monthly Notices of the Royal Astronomical Society*, 508, 5886 (Cited on page 10.)
- Rybicki G. B., Lightman A. P., 1986, *Radiative Processes in Astrophysics* (Cited on page 35.)

REFERENCES

- Sakai S., Seki K., Terada N., Shinagawa H., Tanaka T., Ebihara Y., 2018, *Geophysical Research Letters*, 45, 9336 (Cited on page 39.)
- Salz M., et al., 2018, *Astronomy & Astrophysics*, 620, A97 (Cited on page 8.)
- Saxena P., Killen R. M., Airapetian V., Petro N. E., Curran N. M., Mandell A. M., 2019, *Astrophysical Journal*, 876, L16 (Cited on page 60.)
- Schneider E. M., Esquivel A., Villarreal D'Angelo C. S., Velázquez P. F., Raga A. C., Costa A., 2016, *Monthly Notices of the Royal Astronomical Society*, 457, 1666 (Cited on pages 26, 73, 136 and 140.)
- See V., Jardine M., Vidotto A. A., Petit P., Marsden S. C., Jeffers S. V., do Nascimento J. D., 2014, *Astronomy & Astrophysics*, 570, A99 (Cited on page 48.)
- See V., et al., 2018, *Monthly Notices of the Royal Astronomical Society*, 474, 536 (Cited on page 49.)
- Seidel J. V., et al., 2021, *Astronomy & Astrophysics*, 653, A73 (Cited on page 131.)
- Seki K., Elphic R. C., Hirahara M., Terasawa T., Mukai T., 2001, AGU Spring Meeting Abstracts, pp SM51A-05 (Cited on page 40.)
- Shaikhislamov I. F., et al., 2016, *Astrophysical Journal*, 832, 173 (Cited on pages 25, 26, 73, 99, 136 and 137.)
- Shaikhislamov I. F., Fossati L., Khodachenko M. L., Lammer H., García Muñoz A., Youngblood A., Dwivedi N. K., Rumenskikh M. S., 2020, *Astronomy & Astrophysics*, 639, A109 (Cited on pages 96, 102 and 110.)
- Shkolnik E. L., Llama J., 2018, in Deeg H. J., Belmonte J. A., eds, , *Handbook of Exoplanets*. p. 20, doi:10.1007/978-3-319-55333-7_20 (Cited on pages 25 and 126.)
- Sing D. K., et al., 2019, *Astronomical Journal*, 158, 91 (Cited on page 8.)
- Skumanich A., 1972, *Astrophysical Journal*, 171, 565 (Cited on pages 41 and 51.)
- Spake J. J., et al., 2018, *Nature*, 557, 68 (Cited on pages 8, 9 and 130.)
- Spreiter J. R., Summers A. L., Alksne A. Y., 1966, *Planetary and Space Science*, 14, 223 (Cited on pages 57 and 124.)
- Sterenborg M. G., Cohen O., Drake J. J., Gombosi T. I., 2011, *Journal of Geophysical Research (Space Physics)*, 116, A01217 (Cited on pages 30, 39 and 41.)
- Storey P. J., Hummer D. G., 1995, *Monthly Notices of the Royal Astronomical Society*, 272, 41 (Cited on page 13.)

REFERENCES

- Strangeway R. J., Russell C. T., Luhmann J. G., Moore T. E., Foster J. C., Barabash S. V., Nilsson H., 2010, AGU Fall Meeting Abstracts, (Cited on page 40.)
- Strubbe L. E., Chiang E. I., 2006, *Astrophysical Journal*, 648, 652 (Cited on pages 103 and 109.)
- Tarduno J. A., et al., 2010, *Science*, 327, 1238 (Cited on pages 49 and 55.)
- Tarduno J. A., Blackman E. G., Mamajek E. E., 2014, *Physics of the Earth and Planetary Interiors*, 233, 68 (Cited on page 40.)
- Terada N., Kulikov Y. N., Lammer H., Lichtenegger H. I. M., Tanaka T., Shinagawa H., Zhang T., 2009a, *Astrobiology*, 9, 55 (Cited on page 39.)
- Terada N., Shinagawa H., Tanaka T., Murawski K., Terada K., 2009b, *Journal of Geophysical Research (Space Physics)*, 114, A09208 (Cited on page 39.)
- Toro E. F., 2013, *Riemann solvers and numerical methods for fluid dynamics: a practical introduction*. Springer Science & Business Media (Cited on page 29.)
- Tóth G., 1996, *Astrophysical Letters and Communications*, 34, 245 (Cited on pages 20, 39, 42 and 118.)
- Tóth G., et al., 2005, *JGR (Space Physics)*, 110, A12226 (Cited on pages 30, 113 and 117.)
- Trammell G. B., Li Z.-Y., Arras P., 2014, *Astrophysical Journal*, 788, 161 (Cited on pages 113 and 131.)
- Tremblin P., Chiang E., 2013, *Monthly Notices of the Royal Astronomical Society*, 428, 2565 (Cited on pages 136, 137 and 138.)
- Treumann R. A., 2006, *Astronomy & Astrophysics Review*, 13, 229 (Cited on page 2.)
- Turner J., et al., 2021, in *European Planetary Science Congress*. pp EPSC2021–430, doi:10.5194/epsc2021-430 (Cited on page 2.)
- Vidal-Madjar A., Lecavelier des Etangs A., Désert J.-M., Ballester G., Ferlet R., Hébrard G., Mayor M., 2003, *Nature*, 422, 143 (Cited on pages 2, 5 and 102.)
- Vidal-Madjar A., et al., 2004, *Astrophysical Journal Letters*, 604, L69 (Cited on page 8.)
- Vidotto A., 2013, *Astronomy and Geophysics*, 54, 1.25 (Cited on page 40.)
- Vidotto A. A., 2018, in Deeg H. J., Belmonte J. A., eds, *Handbook of Exoplanets*. p. 26, doi:10.1007/978-3-319-55333-7_26 (Cited on page 42.)
- Vidotto A. A., 2021, *Living Reviews in Solar Physics*, 18, 3 (Cited on pages 20 and 42.)

REFERENCES

- Vidotto A. A., Cleary A., 2020, *Monthly Notices of the Royal Astronomical Society*, 494, 2417 (Cited on pages 25, 73, 87, 94, 95, 96, 99, 103, 109 and 160.)
- Vidotto A. A., Donati J. F., 2017, *Astronomy & Astrophysics*, 602, A39 (Cited on pages 48, 99 and 103.)
- Vidotto A. A., Opher M., Jatenco-Pereira V., Gombosi T. I., 2009, *Astrophysical Journal*, 703, 1734 (Cited on page 123.)
- Vidotto A. A., Jardine M., Helling C., 2010, *Astrophysical Journal Letters*, 722, L168 (Cited on pages 8 and 25.)
- Vidotto A. A., Jardine M., Morin J., Donati J. F., Lang P., Russell A. J. B., 2013, *Astronomy & Astrophysics*, 557, A67 (Cited on page 56.)
- Vidotto A. A., et al., 2014, *Monthly Notices of the Royal Astronomical Society*, 441, 2361 (Cited on pages 41, 43 and 123.)
- Vidotto A. A., Fares R., Jardine M., Moutou C., Donati J. F., 2015, *Monthly Notices of the Royal Astronomical Society*, 449, 4117 (Cited on pages 2, 102 and 111.)
- Vidotto A. A., et al., 2016, *Monthly Notices of the Royal Astronomical Society*, 455, L52 (Cited on page 48.)
- Vidotto A. A., et al., 2018, *Monthly Notices of the Royal Astronomical Society*, 481, 5296 (Cited on pages 31 and 34.)
- Villarreal D'Angelo C., Esquivel A., Schneider M., Sgró M. A., 2018, *Monthly Notices of the Royal Astronomical Society*, 479, 3115 (Cited on pages 26, 73, 75, 98, 99, 113 and 119.)
- Villarreal D'Angelo C., Vidotto A. A., Esquivel A., Hazra G., Youngblood A., 2021, *Monthly Notices of the Royal Astronomical Society*, 501, 4383 (Cited on pages 26, 27, 28, 73, 86, 136 and 145.)
- Vogt J., Zieger B., Stadelmann A., Glassmeier K. H., Gombosi T. I., Hansen K. C., Ridley A. J., 2004, *Journal of Geophysical Research (Space Physics)*, 109, A12221 (Cited on page 39.)
- Weber E. J., Davis Jr. L., 1967, *Astrophysical Journal*, 148, 217 (Cited on pages 15, 20, 42 and 73.)
- Wood B. E., Müller H.-R., Zank G. P., Linsky J. L., 2002, *Astrophysical Journal*, 574, 412 (Cited on page 48.)
- Wood B. E., Müller H. R., Zank G. P., Linsky J. L., Redfield S., 2005, *Astrophysical Journal*, 628, L143 (Cited on pages 47 and 99.)
- Wood B. E., Müller H.-R., Redfield S., Edelman E., 2014, *Astrophysical Journal*, 781, L33 (Cited on pages 47 and 48.)

REFERENCES

- Wood B. E., et al., 2021, *Astrophysical Journal*, 915, 37 (Cited on page 48.)
- Yelle R. V., 2004, *Icarus*, 170, 167 (Cited on pages 2, 10 and 12.)
- Zank G. P., Müller H. R., 2003, *Journal of Geophysical Research (Space Physics)*, 108, 1240 (Cited on page 85.)
- Zuluaga J. I., Bustamante S., Cuartas P. A., Hoyos J. H., 2013a, *Astrophysical Journal*, 770, 23 (Cited on page 39.)
- Zuluaga J. I., Bustamante S., Cuartas P. A., Hoyos J. H., 2013b, *Astrophysical Journal*, 770, 23 (Cited on page 55.)
- van Saders J. L., Ceillier T., Metcalfe T. S., Silva Aguirre V., Pinsonneault M. H., García R. A., Mathur S., Davies G. R., 2016, *Nature*, 529, 181 (Cited on page 43.)
- van der Holst B., et al., 2011, *Astrophysical Journal Supplemental Series*, 194, 23 (Cited on page 30.)
- Ó Fionnagáin D., Vidotto A. A., 2018, *Monthly Notices of the Royal Astronomical Society*, 476, 2465 (Cited on pages 41, 42, 43, 55 and 159.)
- Ó Fionnagáin D., et al., 2019, *Monthly Notices of the Royal Astronomical Society*, 483, 873 (Cited on pages 41 and 123.)
- Ó Fionnagáin D., Vidotto A. A., Petit P., Neiner C., Manchester W. I., Folsom C. P., Hallinan G., 2021, *Monthly Notices of the Royal Astronomical Society*, 500, 3438 (Cited on page 123.)

Published Works

Below are the manuscripts of the first-authored papers resultant from the work presented in this thesis.

In addition to these I participated as a co-author in Hazra et al. (2022), and Kubyshkina et al. (2022a,b). My main additions to these studies were contributions to the testing and implementation of self-consistent photoevaporation in the 3D model. During this development process I mainly focused on debugging MPI issues in the optical depth calculation and investigating the performance of the stellar wind boundary. I also reviewed and gave comments on these manuscripts prior to submission.



The evolution of Earth’s magnetosphere during the solar main sequence

S. Carolan¹,¹★ A. A. Vidotto¹,¹ C. Loesch² and P. Coogan¹

¹*School of Physics, Trinity College Dublin, College Green, Dublin 2, Ireland*

²*Instituto de Educação Superior de Brasília – IESB Centro Universitário Brasília, Brasília - DF, 70200-730, Brazil*

Accepted 2019 August 3. Received 2019 July 26; in original form 2019 May 10

ABSTRACT

As a star spins-down during the main sequence, its wind properties are affected. In this work, we investigate how Earth’s magnetosphere has responded to the change in the solar wind. Earth’s magnetosphere is simulated using 3D magnetohydrodynamic models that incorporate the evolving local properties of the solar wind. The solar wind, on the other hand, is modelled in 1.5D for a range of rotation rates Ω from 50 to 0.8 times the present-day solar rotation (Ω_{\odot}). Our solar wind model uses empirical values for magnetic field strengths, base temperature, and density, which are derived from observations of solar-like stars. We find that for rotation rates $\simeq 10 \Omega_{\odot}$, Earth’s magnetosphere was substantially smaller than it is today, exhibiting a strong bow shock. As the Sun spins-down, the magnetopause standoff distance varies with $\Omega^{-0.27}$ for higher rotation rates (early ages, $\geq 1.4 \Omega_{\odot}$) and with $\Omega^{-2.04}$ for lower rotation rates (older ages, $< 1.4 \Omega_{\odot}$). This break is a result of the empirical properties adopted for the solar wind evolution. We also see a linear relationship between the magnetopause distance and the thickness of the shock on the subsolar line for the majority of the evolution ($\leq 10 \Omega_{\odot}$). It is possible that a young fast rotating Sun would have had rotation rates as high as 30–50 Ω_{\odot} . In these speculative scenarios, at 30 Ω_{\odot} , a weak shock would have been formed, but for 50 Ω_{\odot} , we find that no bow shock could be present around Earth’s magnetosphere. This implies that with the Sun continuing to spin-down, a strong shock would have developed around our planet and remained for most of the duration of the solar main sequence.

Key words: MHD – planets and satellites: magnetic fields – planets and satellites: physical evolution – stars: winds, outflows.

1 INTRODUCTION

In the Solar system, all the giant planets and the Earth have intrinsic magnetic fields. These magnetic fields are largely dipolar and create cavities, preventing the solar wind from reaching the surface directly (e.g. Bagenal 2013). Recently, there have been discussions on whether smaller or larger magnetospheres can protect the atmospheres of planets (Strangeway et al. 2010; Brain et al. 2013; Vidotto 2013; Tarduno, Blackman & Mamajek 2014; Blackman & Tarduno 2018). Some say that a large magnetosphere would act as a shield from stellar wind particles directly impacting the planet; and the larger the shield, the more protected the atmosphere is against erosion. On the other hand, others say that a larger magnetosphere would have a greater collecting area for stellar wind plasma, which would be channelled towards polar regions. This inflow would generate local heating, which could induce atmospheric escape through polar flows (e.g. Moore & Horwitz 2007). It is also possible that both effects coexist, but they have

different contributions depending on the physical characteristics of the system, such as the planetary magnetic field strength and the energy of stellar winds. Blackman & Tarduno (2018) suggested that it is the competition between low inflow speeds (from stellar winds) and large collecting areas (from magnetospheres) that define whether planetary magnetospheres can have protective effects in a planet’s atmosphere. They found that for the Earth, even though the total amount of solar wind material captured in our magnetosphere is larger than that of a fictitious non-magnetic Earth, our magnetic field still has had a protective effect in protecting our atmosphere. This scenario however could be different in Earth’s future due to different solar wind characteristics.

For close-in exoplanets, it has been suggested that, as well as protecting from the stellar wind, magnetic fields can act to hinder planetary outflows (e.g. Adams 2011; Trammell, Arras & Li 2011; Khodachenko et al. 2015). Closed magnetic field lines can trap gas close to the planet, creating ‘dead zones’ from which mass is not lost (Khodachenko et al. 2015). Planetary atmospheres would then escape through open field lines, similar to stellar wind theory (Vidotto et al. 2009). For example, in the numerical study of Owen & Adams (2014), it was found that magnetized exoplanets lose a factor

* E-mail: carolast@tcd.ie

of 4–8 less mass than unmagnetized exoplanets as only a fraction of magnetic field lines remain open and night-side loss is suppressed. The amount of material captured in the dead zones is controlled by the geometry of the magnetic field lines (Khodachenko et al. 2015), giving the structure of the magnetosphere importance in understanding atmospheric escape in close-in exoplanets. The shape and size of the magnetosphere is controlled by the stellar wind, so an understanding of the evolving wind–planet interaction is key before implications can be made to evolving atmospheric escape (Egan, Jarvinen & Brain 2019).

Short-term effects can impact the shape and size of the magnetosphere. Impulsive events, such as coronal mass ejections, may briefly increase the strength of the solar wind impacting the planet, causing a short-term variation in the magnetosphere, its surrounding bow shock, and atmosphere of the planet (Ngwira & Pulkkinen 2014; Airapetian et al. 2016), which could alter atmospheric escape (Johnstone et al. 2019).

For these short-term events as well, the Sun is known to flip polarity on an 11-yr cycle. As was seen by Bharati Das et al. (2019), the direction of the stellar wind's magnetic field can have large implications on the structure of the magnetosphere. The most extreme cases caused by this cyclical polarity flip are the open and closed magnetospheres. These occur when the magnetic field of the wind and the field lines on the dayside of the planet are aligned and anti-aligned, respectively. (These cases are discussed further in Appendix B.) In the case where they are parallel on the dayside (no reconnection), the magnetic field of the wind forces the planet's field lines to remain closed. Conversely, when they are antiparallel (with reconnection), there is a much greater number of open field lines on the nightside and at the poles of the planets. This could lead to the inflow/outflow of material at the polar regions, which has implications on the sustainability of a planet's atmosphere as previously mentioned.

Though these relatively short-term cyclical variations are important, the long-term evolution of the solar wind will have a larger effect on Earth's magnetosphere. As discussed later on, the magnetosphere is influenced by the conditions of the stellar wind, which depends on the magnetic activity of the star. Since stellar activity declines with both age and rotation (Skumanich 1972; Ribas et al. 2005; Vidotto et al. 2014), the wind of the young Sun is believed to have been stronger, which then declined with age (or rotation rate) (O'Fionnagáin & Vidotto 2018; Pognan et al. 2018; Ó Fionnagáin et al. 2019). In a numerical study of the interaction between the paleo-Earth (~3.5 Gyr ago) and the young Sun, Stenborg et al. (2011) concluded that the young Sun's wind would have had easier access to Earth's surface at that age.

In this paper, we examine the evolution of Earth's magnetosphere over the solar main-sequence lifetime. The novelty of our work is that we couple two sets of simulations: one set of simulations characterizes the evolving stellar wind and the other characterizes the evolution of Earth's magnetosphere, using as input the results of the former. Our work on the interaction between the evolving solar wind and Earth is relevant for contextualizing atmospheric protection in own planet and in other exoplanets, which is likely linked to the evolution of life (Lammer et al. 2011, 2012; Zuluaga et al. 2013; Blackman & Tarduno 2018). This paper is organized as follows. We first simulate the evolution of the solar wind with time using empirical relations for base temperature, density, and magnetic field strength (Section 2). We use rotation as a proxy for age, in which case the rotation of the young Sun is faster than the

current rotation rate. Although our models reproduce observations of mass-loss rates derived for fast rotators, they do not consider wind saturation at very fast rotation. This limitation is further discussed in Section 2. We then simulate the interaction between the solar wind and Earth's magnetosphere at different ages (rotations) using 3D numerical simulations (Section 3). We examine the variations of the dayside of Earth's magnetosphere and bow shock with rotation (Section 4). At a very early age, it is still unknown whether the Sun was a fast, moderate, or slow rotator. We explore the extreme environment around the young Earth in Section 5 and present our conclusions in Section 6.

2 STELLAR WIND MODELLING

For our stellar wind modelling, we use a 1.5D Weber–Davis model (Weber & Davis 1967). For that, we use the Versatile Advection Code (VAC; Tóth 1996), based on the version of the code from Johnstone et al. (2015a). Our wind model is polytropic, such that the pressure and density are related by $p^{sw} \propto (\rho^{sw})^\alpha$. This relation is enforced in the model and there is no need for an energy equation to be solved (Keppens & Goedbloed 1999). Here, we adopt a constant polytropic index of $\alpha = 1.05$ in our simulations, which implies that the stellar wind temperature profile, for each model, is nearly isothermal. Additionally, we consider the stars to be magnetized and rotating. The rotation rate Ω is varied from 0.8 to $50\Omega_\odot$, to mimic the solar wind evolution through the main-sequence phase. The wind temperature, density, and magnetic field depend on rotation in our models. We describe next how we chose these wind parameters.

2.1 Choice of stellar wind parameters

Polytropic wind models have two important free parameters, namely the temperature and density at the base of the wind. The values of these parameters are typically assumed to be coronal values, which generate hotter and rarefied winds, similar to what is adopted for the present-day Sun (e.g. Pneuman & Kopp 1971). However, these parameters are not easy to measure in stars other than the Sun. To derive the wind temperatures of low-mass stars, theoretical works have either assumed a relationship between temperature and X-ray fluxes (e.g. Holzwarth & Jardine 2007; Johnstone et al. 2015a; Réville et al. 2016; O'Fionnagáin & Vidotto 2018) or being proportional to the square root of the escape velocity (e.g. Matt et al. 2012). These two families of models have been discussed in depth by Johnstone et al. (2015a). They are, by definition, equivalent for the present-day Sun, but for other stars, they can lead to much different wind models (see also Vidotto 2018). In the latter approach, for example, the escape velocity does not vary significantly in the main sequence, during which the stars spin-down and become less active. This implies that wind temperatures in these models would be approximately constant throughout the main-sequence evolution. In our models, we use the former approach – given that X-ray emission is seen to vary by several orders of magnitude for stars at different rotation rates (e.g. Pizzolato et al. 2003), we naively would expect that a high-temperature corona would lead to a high-temperature wind and, hence, we adopt in our models a correlation between the two. More specifically, we follow the approach by O'Fionnagáin & Vidotto (2018), who modelled the wind base temperature (T_0) by scaling the average coronal temperatures of Sun-like stars to current solar wind values following the X-ray flux–temperature relations of

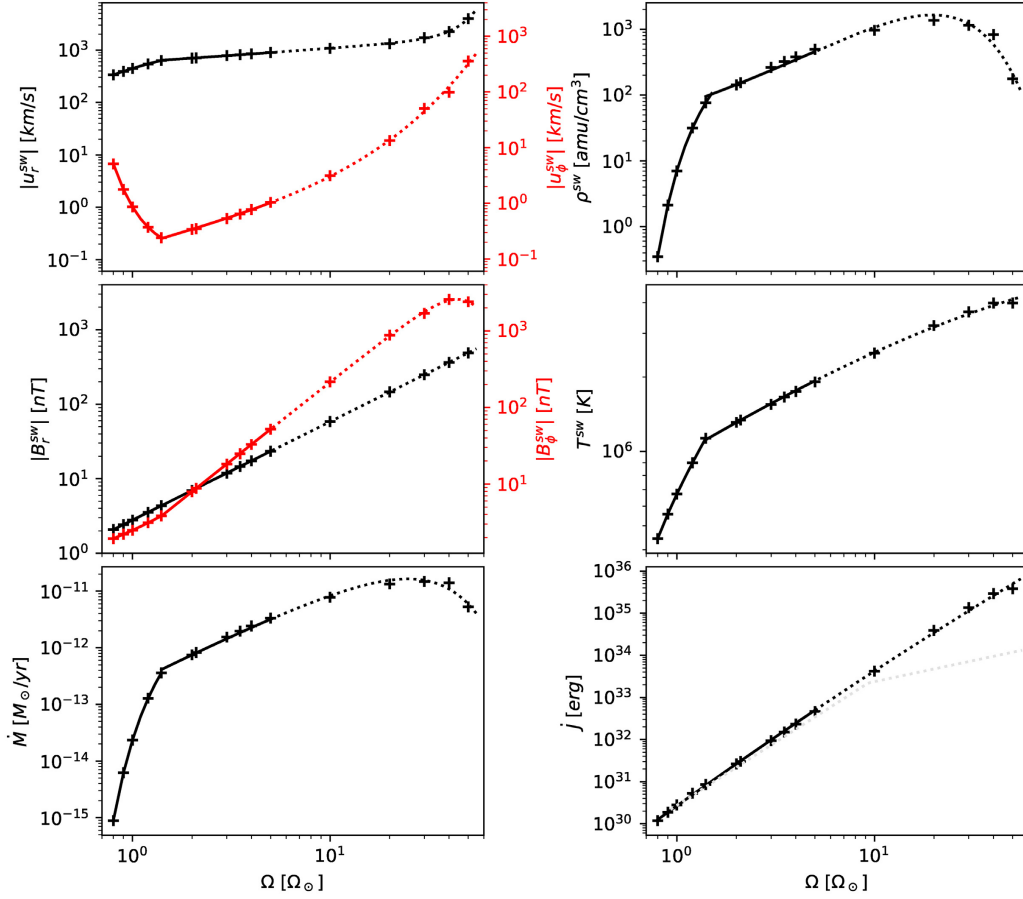


Figure 1. Stellar wind local velocity, density, magnetic field, and temperature at 1 au, and mass- and angular-momentum-loss rate profiles for stellar rotation rates from 0.8 to $50\Omega_{\odot}$. Fits are shown in black and red (when an azimuthal component is shown in the same panel). The fitting parameters are in Tables A1 and A2. The crosses mark the results of a particular model and are also listed in Table 1. To represent the uncertainty of whether the Sun would have rotated faster than $\sim 5\Omega_{\odot}$, part of the fits are shown as dotted lines. The grey dotted line in the last panel shows the break in angular-momentum-loss rates one would expect if our models adopted saturation of the wind (see text for a discussion).

Johnstone & Güdel (2015). Our base temperature is dependent on the stellar rotation rate Ω according to

$$T_0 \text{ (K)} = \begin{cases} 1.5 \times 10^6 \left(\frac{\Omega}{\Omega_{\odot}}\right)^{1.2} & \text{for } \Omega < 1.4\Omega_{\odot}, \\ 1.98 \times 10^6 \left(\frac{\Omega}{\Omega_{\odot}}\right)^{0.37} & \text{for } \Omega \geq 1.4\Omega_{\odot}. \end{cases} \quad (1)$$

O’Fionnagáin & Vidotto (2018) fitted a broken power law to the X-ray data in light of other works suggesting a break in other activity quantities – rotation rates, lithium abundances, and X-ray luminosity (van Saders et al. 2016; Beck et al. 2017; Booth et al. 2017).

For the base number density (n_0) we use a rotation-dependent density relation, derived by Ivanova & Taam (2003) from X-ray observations, and employed in other wind studies of solar-like stars

(Holzwarth & Jardine 2007; Réville et al. 2016; O’Fionnagáin & Vidotto 2018):

$$n_0 \text{ (g cm}^{-3}\text{)} = 10^8 \left(\frac{\Omega}{\Omega_{\odot}}\right)^{0.6}. \quad (2)$$

In a Weber–Davis model, the magnetic field lines are assumed to be approximately radial at the wind base. In the initial condition of our simulations, we assume that the field is purely radial and decays with distance squared. As the simulation evolves, in addition to the radial magnetic field component B_r^{sw} , an azimuthal component B_{ϕ}^{sw} is created due to stellar rotation. The spiral angle that characterizes the tightness of the Parker spiral is $\Psi = \arctan(B_{\phi}^{\text{sw}}/B_r^{\text{sw}})$. The magnetic field strength at the wind base $B_{r,0}^{\text{sw}}$ is derived from the empirical relation from Vidotto et al. (2014), based in observationally derived

Table 1. The absolute magnitude of wind parameters for different stellar rotation rates Ω . The columns are: estimated age based on the rotation tracks from Gallet & Bouvier (2013), the mass- (\dot{M}) and angular-momentum-loss rates (J), the local radial and azimuthal components of the velocity ($u_r^{\text{sw}}, u_\phi^{\text{sw}}$), magnetic field ($B_r^{\text{sw}}, B_\phi^{\text{sw}}$), temperature (T^{sw}), proton number density (n_p^{sw}). \mathcal{M} is the local magnetosonic Mach number and Ψ is the spiral angle of the wind. All the local quantities were computed at 1 au and are used as input in the 3D simulations of Earth's magnetosphere.

Ω (Ω_\odot)	Age (Myr)	\dot{M} ($M_\odot \text{ yr}^{-1}$)	J (erg)	u_r^{sw} (km s^{-1})	u_ϕ^{sw} (km s^{-1})	B_r^{sw} (G)	B_ϕ^{sw} (G)	T^{sw} ($\times 10^5 \text{ K}$)	n_p^{sw} (cm^{-3})	\mathcal{M}	Ψ ($^\circ$)
0.8	7700	8.9×10^{-16}	1.2×10^{30}	337	5.1	2.1×10^{-5}	1.9×10^{-5}	4.4	0.35	2.5	47
0.9	6500	6.2×10^{-15}	1.9×10^{30}	393	1.8	2.4×10^{-5}	2.2×10^{-5}	5.6	2.1	3.6	48
1.0	5000	2.3×10^{-14}	2.8×10^{30}	446	0.86	2.8×10^{-5}	2.5×10^{-5}	6.7	7.0	4.0	48
1.2	3100	1.3×10^{-13}	5.3×10^{30}	545	0.37	3.5×10^{-5}	3.1×10^{-5}	9.0	32	4.3	49
1.4	2100	3.6×10^{-13}	8.5×10^{30}	634	0.24	4.4×10^{-5}	3.8×10^{-5}	11	76	4.5	49
2.0	1100	7.5×10^{-13}	2.6×10^{31}	702	0.34	7.0×10^{-5}	7.9×10^{-5}	13	143	4.6	41
5.0	40–440	3.3×10^{-12}	4.6×10^{32}	900	1.0	2.3×10^{-4}	5.2×10^{-4}	19	497	4.7	24
10	≤ 280	7.8×10^{-12}	4.2×10^{33}	1078	3.1	5.8×10^{-4}	0.0022	25	968	4.1	15
30	≤ 140	1.5×10^{-11}	1.4×10^{35}	1723	50.5	0.0025	0.017	37	1154	1.5	8
50	≤ 100	5.3×10^{-12}	3.8×10^{35}	3994	360	0.0049	0.024	40	177	0.99	11

magnetic maps,

$$B_{r,0}^{\text{sw}} \text{ (G)} = 1.29 \left(\frac{\Omega}{\Omega_\odot} \right)^{1.32}. \quad (3)$$

Note that the values from Vidotto et al. (2014) represent an average field strength of the large-scale magnetic field over the stellar surface and, here, is used as the radial component of the field strength.

Our wind simulations extend to 1 au (equivalent to $215 R_\odot$). For each one of them, we compute the density, temperature, the radial (r) component of velocity u_r^{sw} , and magnetic field, as well as the azimuthal (ϕ) component of velocity u_ϕ^{sw} and magnetic field with distance. The values of these quantities at 1 au, for each assumed rotation rate, are shown in Fig. 1 and listed in Table 1.

These wind parameters at 1 au are the inputs of our magnetosphere simulations (cf. Section 3). The magnetosonic velocity at the interaction, together with the stellar wind velocity, determine the magnetosonic Mach number

$$\mathcal{M} = \frac{u_r^{\text{sw}}}{\sqrt{v_A^2 + c_s^2}}, \quad (4)$$

where v_A is the Alfvén velocity and c_s is the sound speed. \mathcal{M} determines the strength of the shock. Given that a shock is only present around the Earth if $\mathcal{M} > 1$, we note a surprising result that, at rotation rate of $50 \Omega_\odot$, our models do not predict the presence of a shock around the Earth. As we will see next, it is uncertain whether the Sun rotated that fast – if that indeed occurred, it happened only for a short amount of time, relative to the Sun's lifetime, and at an age $\lesssim 100$ Myr. We discuss age determination and rotation–age relation next.

2.2 The rotation rate of the young Sun

To mimic the ageing of the Sun, we use rotation as a proxy for age, and compute stellar wind models at different rotation rates from 0.8 to $50 \Omega_\odot$. However, here, we are very careful in assigning an age to our models as the age–rotation relationship is only well constrained for stars older than ~ 800 Myr. Fig. 2 shows the rotation evolution tracks for a $1-M_\odot$ star during the main-sequence phase, extracted from the work of Gallet & Bouvier (2013). These tracks are the upper/lower envelopes of the observed rotation distributions from open clusters and they indicate the evolution of a slowly rotating (red dashed line) and a fast-rotating (solid blue) star. The convergence of the slow and fast rotator tracks happens at around ~ 800 Myr,

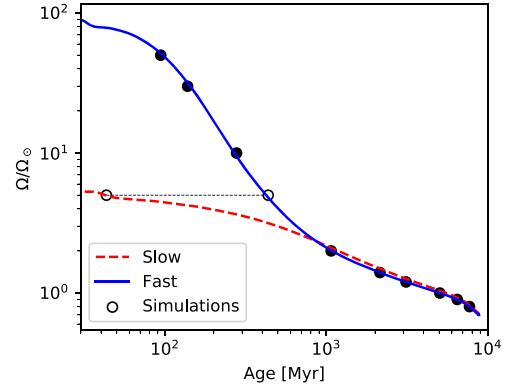


Figure 2. The evolution of stellar rotation rate (Ω) from Gallet & Bouvier (2013), for a $1-M_\odot$ star. The blue solid line tracks the evolution of a fast rotating solar-like star, while the dashed red line tracks the slow rotator. The black points mark the values of Ω adopted in our simulations. The fast and slow models give a well constrained age for the $\lesssim 2.0 \Omega_\odot$ models. For higher rotation rates, ages are more uncertain. For example, the Sun could have rotated at $5 \Omega_\odot$ at any age between 40 and 440 Myr, depending whether it was a slow to fast rotator (connected by a dashed black line). Note that the Sun would only have rotated faster than $\sim 5 \Omega_\odot$, if it were not born as a slow rotator.

after which, we can assign an age to a star from observed rotation rates – this forms the basis of the gyrochronology method (Barnes 2003).

The symbols in Fig. 2 represent the selected rotation rates to which we perform our simulations. As can be seen, for $\Omega \lesssim 2 \Omega_\odot$, there is a unique function between age and rotation and thus we can assign an age to our solar wind models. However, for $\Omega \gtrsim 2 \Omega_\odot$, there are ambiguities in age determination. For example, for the model with rotation rate of $5 \Omega_\odot$ (open symbols, connected by a dotted line), possible ages range from 40 to 440 Myr, depending whether the Sun used to be a slow or a fast rotator, respectively. Note that the Sun would only have rotated faster than $\sim 5 \Omega_\odot$, if it were not born as a slow rotator. Because of this, it is only possible to assign an upper limit on the age for the models with a given

rotation rate $\gtrsim 2\Omega_{\odot}$ – for that, we assume that the Sun was in the fast rotator track. These age estimates and upper limits are listed in Table 1 for each of our simulated rotation rates.

Given that we are unsure whether the Sun indeed rotated faster than $\sim 5\Omega_{\odot}$, the computed quantities associated with these rotation rates are represented as dotted lines in Fig. 1. The very fast rotating young Sun (30 and $50\Omega_{\odot}$) will be discussed in Section 5.

2.3 Global properties of the young solar wind

In addition to the local conditions (at 1 au) of the solar wind in time, we also present in the bottom panels of Fig. 1 and Table 1 two global quantities of stellar winds – the mass-loss rate

$$\dot{M} = 4\pi(1 \text{ au})^2(m_p n_p^{\text{sw}})u_r^{\text{sw}} \quad (5)$$

and the angular-momentum-loss rate

$$\dot{J} = \frac{2}{3}\dot{M}r_A^2\Omega. \quad (6)$$

Here, m_p is the mass of the proton and r_A is the distance where the wind radial velocity reaches the Alfvén velocity, and is known as the Alfvén point (or Alfvén surface in a multidimension wind model). We discuss the evolution of \dot{M} and \dot{J} next.

Mass-loss rates of solar-type stars are challenging to derive from observations. The most successful technique to date has been the astrophysical Lyman- α absorption (Wood et al. 2005; 2014), which has derived mass-loss rates for about a dozen stars. This technique has shown that mass-loss rates increase with X-ray fluxes (F_x), which also increase with Ω . For ages $\gtrsim 1000$ Myr, the mass-loss rate in our models are very similar to those predicted by Wood et al. (2014) – this covers the majority of our models ($\leq 10\Omega_{\odot}$). For example, our models predict that the Sun had a mass-loss rate of $7.5 \times 10^{-13} M_{\odot} \text{ yr}^{-1}$, or about 40 times the present-day solar mass-loss rate, at a rotation rate of $2\Omega_{\odot}$. At a similar rotation rate, Wood et al. (2002) found that the star ϵ Eri shows a mass-loss rate of $\sim 6 \times 10^{-13} M_{\odot} \text{ yr}^{-1}$, similar to the value we find in our models.

For $F_x \gtrsim 10^6 \text{ erg cm}^{-2} \text{ s}^{-1}$, i.e. above approximately $15\Omega_{\odot}$, Wood et al. (2014) predicted a break in the \dot{M} - F_x relation, arguing that mass-loss rates of a very young Sun (high F_x) could actually have been very low ($\sim 10^{-14} M_{\odot} \text{ yr}^{-1}$). This break, however, has been difficult to explain with other observations (e.g. Vidotto et al. 2016), and theoretically (e.g. Holzwarth & Jardine 2007; See et al. 2014). It has been suggested that the low mass-loss rates of the ‘outlier’ stars in Wood’s sample (π^1 UMa, ξ Boo A) do not follow the \dot{M} - F_x relation due to scattering, and that the relation between mass-loss rates and activity could extend to higher X-ray fluxes without a break (Jardine & Collier Cameron 2019), albeit with some scatter.

Jardine & Collier Cameron (2019) estimated that AB Dor, a widely used proxy for the young Sun, has mass-loss rate $7 \times 10^{-12} M_{\odot} \text{ yr}^{-1}$. With a rotation period of ~ 0.5 d, or $54\Omega_{\odot}$, their derived mass-loss rate is surprisingly similar to our $50\Omega_{\odot}$ model ($5.3 \times 10^{-12} M_{\odot} \text{ yr}^{-1}$). Another clue that fast-rotating stars might actually have stronger stellar winds is that when we go to even younger stars (not studied in this work), mass-loss rates are observed to be $\sim 10^{-10}$ to $10^{-12} M_{\odot} \text{ yr}^{-1}$ in the weak T Tauri phase, after disc clearing (Vidotto & Donati 2017). Naively, one would expect that the wind of a young Sun would have mass-loss rates that are intermediate between those of weak T Tauri stars and the current solar one. Altogether, these facts give support to the relatively high mass-loss rates, reaching $10^{-11} M_{\odot} \text{ yr}^{-1}$, we obtain for very fast rotating Suns.

Our model, however, does not include saturation on the mass-loss rate nor on magnetic field at high rotation rates.¹ Saturation is required to explain the spin-down of the very fast rotators (e.g. Matt et al. 2015; Johnstone et al. 2015b). When considering saturation, the wind angular-momentum-loss rate presents a break with Ω , which is illustrated by the grey dotted line in the bottom right panel of Fig. 1. This curve is from See et al (submitted), which is based on the torque formalism of Matt et al. (2015, we divided their curve by 2.9 to match our solar value). We note that for $\Omega \lesssim 10\Omega_{\odot}$, their trend is similar to ours, roughly obeying a cubic dependence with Ω . However, for $\Omega \gtrsim 10\Omega_{\odot}$, saturation requires an approximately linear dependence between \dot{J} and Ω , which is not seen in our model.

3 MAGNETOSPHERE MODELLING

There have been numerical studies investigating present-day and past interactions between the solar wind and Solar system planets, such as with Mars (Terada et al. 2009a; Ma et al. 2013, 2015; Sakai et al. 2018), Venus (Kulikov et al. 2007; Terada et al. 2009b), and Earth (Ridley et al. 2001; Vogt et al. 2004; Sterenborg et al. 2011). However, to the best of our knowledge, the magnetospheric evolution of the Earth over the solar main-sequence lifetime has not yet been examined. We investigate this evolution through 3D magnetohydrodynamic (MHD) modelling of Earth’s magnetosphere. We use the Space Weather Modelling Framework’s (SWMF) Global Magnetosphere module (Tóth et al. 2005). SWMF has been used to study planets in the Solar system (e.g. Sterenborg et al. 2011; Ma et al. 2013; Jia et al. 2015; Jia & Kivelson 2016).

To simulate Earth’s magnetosphere and its surrounding bow shock in a given stellar wind condition, our magnetosphere simulations take the stellar wind parameters as inputs. The wind is injected into our computation domain at a distance of 20 planetary radii (R_p) on the dayside of the planet, as shown in Fig. 3. For the planetary parameters, we use current day values for magnetic dipole strength ($B_0 = -0.3$ G); radius ($R_p = 6.3 \times 10^8$ cm); and mass (5.976×10^{27} g) in our models. We assume that Earth’s geodynamo has not changed during this evolution, although some works suggest that Earth’s dipolar field strength might have been 50 per cent smaller ~ 3.5 Gyr ago (Tarduno et al. 2010). We discuss the effects of our hypothesis of constant dipolar field strength has on our simulations in Section 4.

Our simulation is Cartesian and solves for eight parameters: mass density (ρ), velocity (u_x, u_y, u_z), magnetic field (B_x, B_y, B_z), and thermal pressure (P_T). These are found through iteratively solving a set of ideal MHD equations: the mass conservation, momentum conservation, magnetic induction, and energy conservation equations, respectively:

$$\frac{\partial \rho}{\partial t} + \nabla \cdot (\rho \vec{u}) = 0, \quad (7)$$

¹Although we do not impose a saturation in mass-loss rate, our models show a ‘levelling off’ of mass-loss rate for $\Omega \gtrsim 20\Omega_{\odot}$ (cf. the bottom left panel of Fig. 1). This inflection is more clearly seen in the local densities (top right panel of Fig. 1). Although the base densities are larger for larger rotation rates, the decrease in wind density with distance is steeper for $\gtrsim 20\Omega_{\odot}$. In the limit where the wind reaches terminal velocity, the density should fall with r^{-2} . The steeper decrease is thus an indication that the wind is still being accelerated for $\Omega \gtrsim 20\Omega_{\odot}$ at 1 au. In fact, we note that in these cases, the local magnetocentrifugal force (at 1 au) is comparable or greater than the thermal pressure gradient in the wind radial momentum equation. Beyond $\gtrsim 20\Omega_{\odot}$, the thermal pressure gradient ceases to be the dominant force in our models.

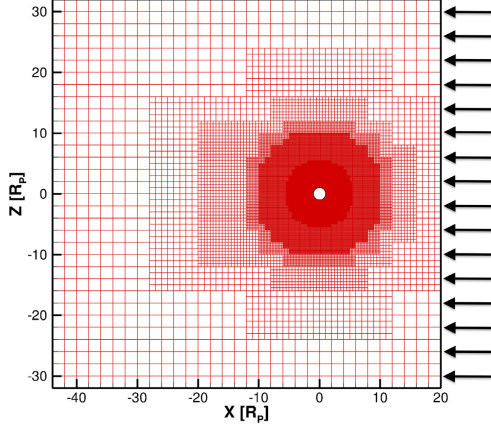


Figure 3. The refinement grid used in our models. A maximum resolution of $1/32 R_p$ is used within a radius of $5 R_p$, which slowly decreases outwards by a factor of 2 at each step as seen above. The arrows visualize the injection of the stellar wind into this domain.

$$\frac{\partial(\rho\vec{u})}{\partial t} + \nabla \cdot \left[\rho\vec{u}\vec{u} + (P_T + \frac{B^2}{8\pi})\mathbf{I} - \frac{\vec{B}\vec{B}}{4\pi} \right] = \rho\vec{g}, \quad (8)$$

$$\frac{\partial\vec{B}}{\partial t} + \nabla \cdot (\vec{u}\vec{B} - \vec{B}\vec{u}) = 0, \quad (9)$$

$$\frac{\partial\epsilon}{\partial t} + \nabla \cdot \left[\vec{u} \left(\epsilon + P_T + \frac{B^2}{8\pi} \right) - \frac{(\vec{u} \cdot \vec{B})\vec{B}}{4\pi} \right] = \rho\vec{g} \cdot \vec{u}, \quad (10)$$

where \mathbf{I} denotes the identity matrix and \vec{g} the acceleration due to gravity. The total energy density ϵ is

$$\epsilon = \frac{\rho u^2}{2} + \frac{P_T}{\gamma - 1} + \frac{B^2}{8\pi}, \quad (11)$$

with $\gamma = 5/3$.

We place the centre of the planet at the origin, within a rectangular box. Since we are considering the dayside of the planet in this paper, we choose a cubic grid of length $32 R_p$ ($x = [-44, 20] R_p$; $y = z = [-32, 32] R_p$) as seen in Fig. 3. The X -axis points towards the star and the Z -axis is oriented perpendicular to the ecliptic plane. The Y -axis constructs the right-handed system. Our simulations have a maximum resolution of $1/32 R_p$ within a radius of $5 R_p$, which gradually decreases to a minimum resolution of $2 R_p$ at the edges of the grid. We can achieve this high resolution by sacrificing grid space on the nightside of the planet. We tested the effects of numerical resolution, by changing the highest resolution from $1/32$ to $1/64$ and $1/128 R_p$ at the inner regions of our simulations. We found no significant change in the position of pressure balances (used to identify the magnetopause, further discussed in Section 4) and so in this work, we present the results for the case of $1/32 R_p$. With this resolution, our simulations contain 22.6 million cells.

The inner boundary is set at $1R_p$ in our simulations. We chose values for base density (10 amu cm^{-3}), temperature (25000 K), and thermal pressure ($3.45 \times 10^{-11} \text{ dyn cm}^{-2}$) that are appropriate

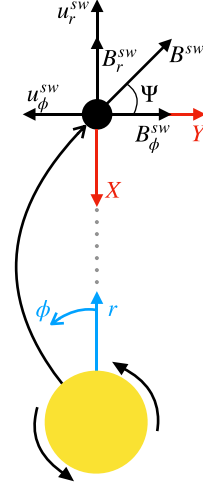


Figure 4. Illustration of how the stellar winds are oriented in our grid. The black circle represents the Earth, while the yellow represents the Sun. The magnetic and velocity vectors are drawn in the inertial frame of the star. The blue vectors show the stellar coordinate system, while the red ones show the orientation of the planetary coordinate system. Z constructs the right handed system, with the origin placed at the centre of the planet.

for the current ionosphere and keep them the same for all our simulations. Note that the ionospheric structure is not computed in our models. Since we are interested in the interaction region of the magnetosphere with the stellar wind, which happens significantly above the planet, the values of pressure and density have no effects on the dynamics of the interaction (for example, for different values of density, we see no change in the position of thermal-magnetic and thermal-ram pressure balances). The boundary assumes that the density at $1R_p$ is fixed, and the magnetic field and thermal pressure have outflow conditions. The velocity vector is reflected upon reaching this boundary in the frame corotating with the planet. The outer boundary assumes an outflow of all parameters. Earth's rotation is kept at 1 d for all the simulations.

In our simulations we align the magnetic axis of the Earth with the rotational axis, which is 23.5° inclined with respect to the orbital plane. All the simulations are thus at summer solstice. Presently, Earth's magnetic axis is misaligned by $\sim 11^\circ$ to the rotational axis. However, as the magnetic tilt can vary on a relatively short time-scale compared to the evolutionary times considered here, and given that we do not know precisely how this variation would have happened in the distant past, we chose to neglect the misalignment between magnetic and rotation axes in this work. The radial velocity u_r^{sw} of the solar wind is injected along the negative X direction in this coordinate system. u_ϕ^{sw} is aligned with the negative Y direction such that the simulated 1.5D winds act in the X - Y plane. Note that we assume $B_r^{\text{sw}} > 0$. Hence $B_\phi^{\text{sw}} < 0$ in the stellar reference frame due to the trailing nature of the Parker spiral. This is illustrated in Fig. 4.

As $u_r^{\text{sw}} \gg u_\phi^{\text{sw}}$ the wind is mainly radial at 1 au. This orientation yields a solar wind which enters our domain through the dayside of the box seen in Fig. 3 where it interacts with the planet's magnetic field. Once the wind reaches the magnetic field from the planet, it is

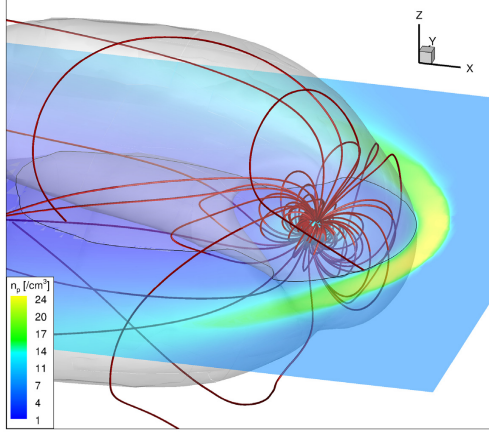


Figure 5. A 3D image of the planet considering the star is rotating at $1.0 \Omega_{\odot}$. Red lines represent the magnetic field lines connected to the planet. The slice shows the density around the planet in the X – Y plane. The surface marks a constant pressure value, which is where the thermal pressure equals the magnetic pressure. We use this surface to mark the magnetopause boundary on the dayside of the planet in our models.

shocked which is visualized in Fig. 5 by the density slice in the X – Y plane. The magnetic field from the planet deflects most incoming material.

4 EARTH IN TIME

As stellar rotation is a proxy for age (Skumanich 1972), here we choose to sample 10 stages in the solar wind’s evolution spanning a range of stellar rotation rates from 0.8 to $50 \Omega_{\odot}$ as seen in Table 1. The magnetosphere and bow shock formed from the interaction between these winds and Earth’s magnetic field can be seen in Fig. 6.

Here we examine how the dayside of Earth’s magnetosphere varies in time, mainly focusing our analysis along the X -axis in each of our 3D models (towards the star).

4.1 The magnetopause

The size of the magnetosphere, the region where the dominant magnetic field is due to the planet, is marked by the magnetopause standoff distance (r_M), which analytically can be described as the point at which the magnetic pressure in the plasma due to the planet’s magnetic field balances the ram pressure of the stellar wind (Chapman & Ferraro 1931):

$$r_M^{\text{analyt}} = \left(\frac{B_0^2}{8\pi\rho^{\text{sw}}(u^{\text{sw}})^2} \right)^{\frac{1}{6}} R_p, \quad (12)$$

where B_0 is the planet’s magnetic dipole strength and ρ^{sw} is stellar wind mass density. This equation neglects the presence of the bow shock and magnetosheath, so we will use an alternate method to locate the magnetopause.

There are three main contributors to the total pressure in our models: thermal ($P_T = n_p k_B T$); magnetic ($P_B = B^2/8\pi$); and ram pressure ($P_{\text{ram}} = \rho u^2$). k_B is Boltzmann’s constant. To examine

which contributor dominates at a certain distance from the planet, these have been separated and plotted alongside the normalized density in Fig. 7, for two representative cases: low- ($1.2 \Omega_{\odot}$) and high- ($10 \Omega_{\odot}$) stellar rotation.

For both high- and low-stellar rotation rates, we see similar trends in the thermal, magnetic, and ram pressures. Inside the magnetosphere, magnetic pressure dominates due to the strong magnetic field of the planet. In the stellar wind, we see the dominant component is the ram pressure due to the high density, much higher velocity, and relatively low magnetic field and thermal components in the wind.

When the stellar wind is shocked, the majority of ram pressure is converted to thermal pressure (Cravens 2004). In our models, this fraction is 75 per cent. In the shock the velocity of the wind drops by a factor of 4 and the density increases by a factor of 4, for models with stellar rotation $< 10 \Omega_{\odot}$, which exhibit strong shocks.

The Chapman–Ferraro equation (equation 12) neglects the extent of the shock. It balances the magnetic pressure on the left side (inside magnetosphere) with the ram pressure on the right side (in the stellar wind). In our simulations we can see that this transition is mediated by the presence of a finite shock (the magnetosheath), dominated by thermal pressure. The magnetopause standoff distance is marked by the point on the X -axis where the magnetic and thermal pressures are balanced. Similarly, to identify the bow shock standoff distance we use the balance of thermal and ram pressures. These distances for the $1.2 \Omega_{\odot}$ model are marked in Figs 7 and 8. We can see that the magnetopause corresponds to a local minimum in the velocity magnitude, with a density cavity just inside this. This cavity is carved by the large closed magnetic field lines in this region, which lead shocked material away.

As faster rotating stars are more active, they have stronger stellar winds. Therefore we expect a faster rotator to induce a smaller magnetosphere around the Earth, as the stronger stellar wind leads to a larger ram pressure. This is seen in Fig. 9, as we see a gradual decrease in standoff distance with increasing Ω (Table 2). There is a break in the trend of standoff distance with stellar rotation at approximately $1.4 \Omega_{\odot}$. This is due to how the base temperature of the winds is specified in Section 2, which is given by a piece-wise function about $1.4 \Omega_{\odot}$. To find a relation in terms of Ω we fit our data using a piece-wise function. We find the standoff distance varies with Ω according to the following relation:

$$r_M \propto \begin{cases} \Omega^{-2.04} & \Omega < 1.4\Omega_{\odot} \\ \Omega^{-0.27} & \Omega \geq 1.4\Omega_{\odot} \end{cases}. \quad (13)$$

In our models, we adopted a dipolar field strength of the Earth that is constant in time (the same value across all our simulations). However, Tarduno et al. (2010) found that when the Earth was approximately 1 Gyr old, its magnetic dipole strength was lower than it is today, within the range from 0.5 to 0.7 times the present-day value. Zuluaga et al. (2013) modelled the change in planetary dipole moment with time, suggesting that the magnetic field strength of the Earth averaged over its evolution is approximately 90 per cent of its current value (i.e. during most of its evolution, the magnetic moment of the Earth has not changed). Given that r_M depends very weakly on the field strength ($r_M \propto B_0^{1/3}$), the evolving dipole moment would contribute a mean change of 3 per cent to r_M over the magnetosphere’s evolution, when compared to models using present-day values at all ages. Additionally, as can be seen in our piece-wise function (equation 13), which has the same break seen in the assumption of stellar wind temperature, the variation in magnetospheric size is much more sensitive to the changing stellar

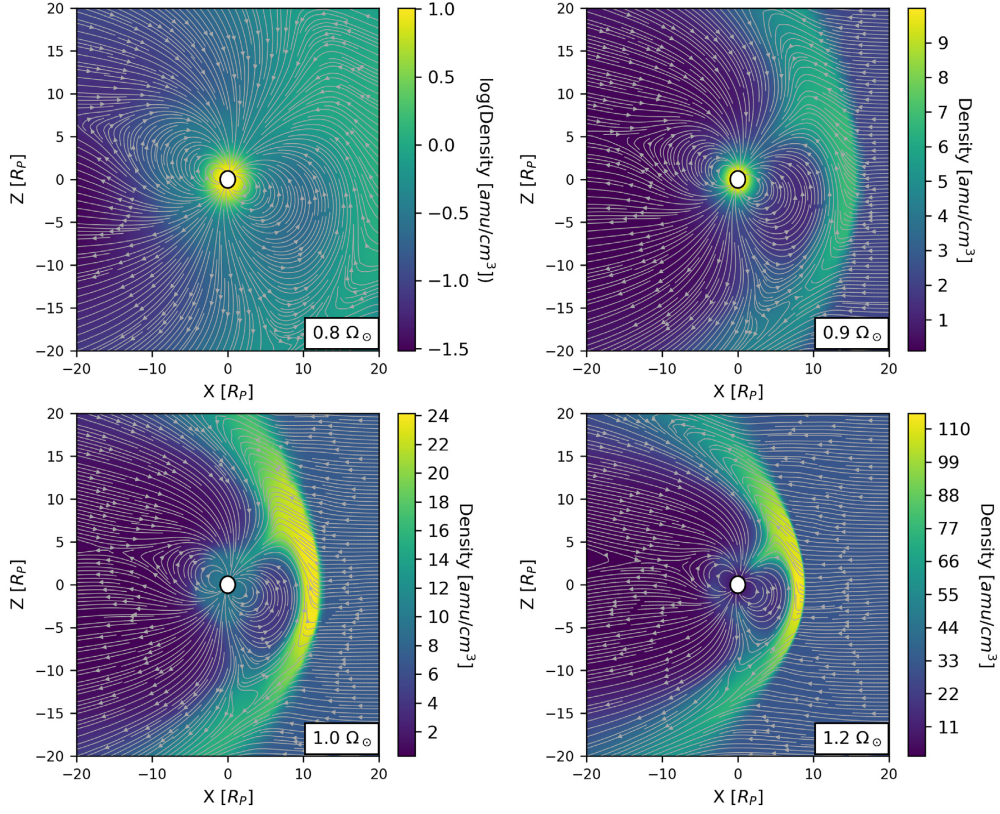


Figure 6. Earth's magnetosphere for different values of stellar rotation from 0.8 to $10 \Omega_{\odot}$. For each model the density distribution in the X - Z plane is shown as a contour. The streamtracers show the magnetic field lines, illustrating the magnetospheres in our models.

wind than what would be expected due to an evolving planetary dipole (see also O'Fionnagáin & Vidotto 2018).

As was discussed in Section 1, the shape and size of the magnetosphere has important implications on atmospheric loss. The area on the planet connected to open magnetic field lines determines the extent to which stellar wind material can reach the planet (We call this scenario 'impact' from now on). If this area is large, a greater amount of stellar wind will impact the atmosphere, which could induce atmospheric loss. If this area is small, there are a greater number of closed field lines, which can collect stellar wind plasma and focus it on to the atmosphere (hereon referred to as 'collection'), which also could cause the same effect of enhancing atmospheric loss (Blackman & Tarduno 2018).

Which of these two competing mechanisms (impact versus collection) causes more harm to the planet over its lifetime is currently still in debate. We do not model atmospheric loss here. However from our models we can examine the area on the planet connected to open field lines, which is quantified by the colatitude Φ of the last open field line on the dayside of the North pole in the X - Z plane. These are given in Table 2.

In the young system, the area covered by open field lines is much larger than for lower stellar rotation rates. This increased area could lead to a higher rate of stellar wind impact than in an old system. With the stellar wind gradually relaxing, the difference between young and old systems is further enhanced. As the magnetosphere is small in the earlier stages of Earth's evolution and the area of open field lines is large, we expect that stellar wind impact will dominate over plasma collection in the young systems.

As the Sun spun-down, this area gradually decreased, with a colatitude of open field lines of approximately 10.3° obtained for present day. Analytically, the colatitude of open field lines can be found from the magnetopause standoff distance through the following expression (Vidotto et al. 2013):

$$\Phi^{\text{analyt}} = \arcsin \left(\sqrt{\frac{R_p}{r_M}} \right). \quad (14)$$

Using this expression, we find $\Phi = 18.8^\circ$ for the present day, using r_M from our models. This value is significantly higher than what we obtain from our simulation. We attribute this difference to the

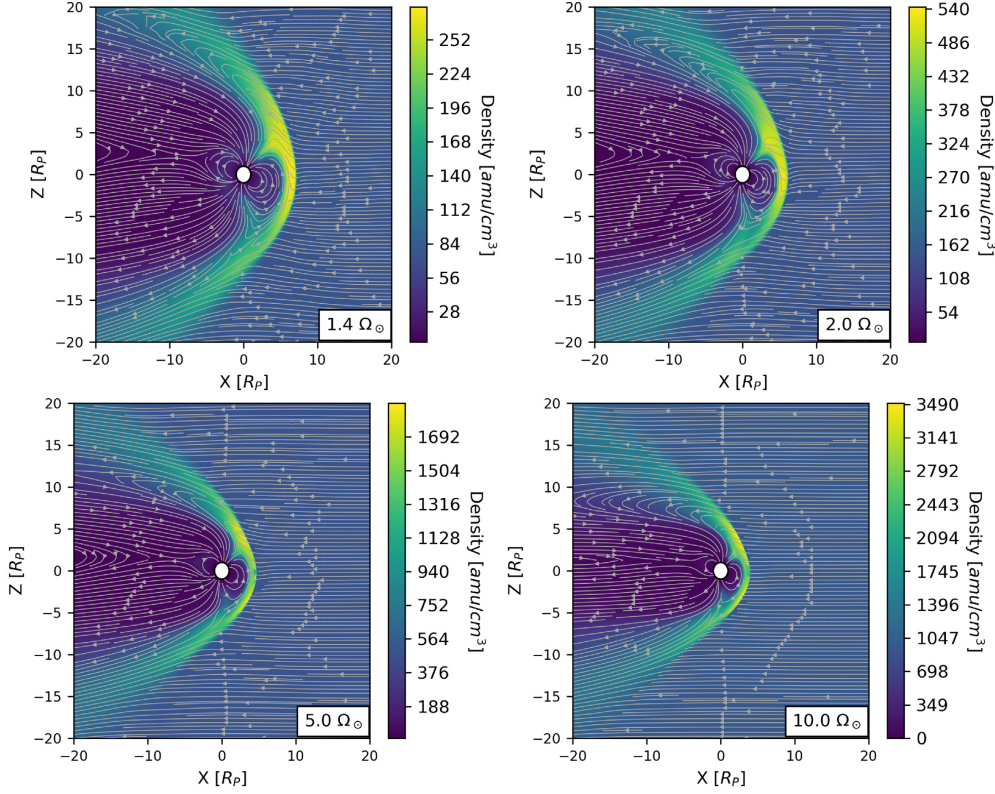


Figure 6 – continued

orientation of the magnetic fields in the system. For example, in the case of magnetic fields are antiparallel on the dayside, which we examine in Appendix B, the numerical and analytical values agree with each other.

With the magnetosphere gradually growing in size, the stellar wind gradually relaxing, and the area of open field lines decreasing, it is clear that the amount of stellar wind inflow will decrease with time. Contrary to this, the collecting area for stellar wind plasma will increase through Earth's evolution, as the magnetospheric size and area covered by closed field lines increases. It is clear that of the two competing effects, stellar wind inflow will dominate in the young system, whilst plasma collection will dominate at old ages.

4.2 The bow shock and magnetosheath

The bow shock standoff distance is the distance from the centre of the planet towards the star where the shock wave is formed. In line with how we define the magnetosphere standoff distance, we use the balance of thermal and ram pressures to establish the bow shock standoff distance. At this point a shock wave is formed as the supermagnetosonic stellar wind encounters the magnetic field of the planet. The region between this point and the magnetosphere

standoff distance contains the shocked material and is known as the magnetosheath. As outlined by Balogh & Treumann (2013), Gombosi (2004), and Spreiter, Summers & Alksne (1966), the bow shock distance (r_{BS}) is related to the magnetopause standoff distance according to the following relation:

$$r_{BS} - r_M = \Delta r \approx 1.1 \frac{N_2}{N_1} r_M, \quad (15)$$

where the density compression factor $\frac{N_2}{N_1}$ (ratio of the density in front of the shock, and that in the shock) is given by the inverse of the equation below

$$\frac{N_1}{N_2} \approx \frac{\gamma + 1}{\gamma - 1} - 2 \frac{\gamma + 1}{\mathcal{M}^2(\gamma - 1)^2}, \quad (16)$$

where $\gamma = 5/3$ is the adiabatic index. In a strong shock this ratio is approximately 4, as the Mach number is large and the second term may be neglected.

The strength of the shock is determined by the Mach number of the stellar wind (see Table 1). If this is much greater than 1, a strong shock is formed and so the obtained magnetosheath thickness should be $0.275 r_M$ (Gombosi 2004) in the strong shock models ($\leq 10 \Omega_\odot$). Using the above relation we can predict the expected bow shock distance and compare this to what we obtain in our simulations.

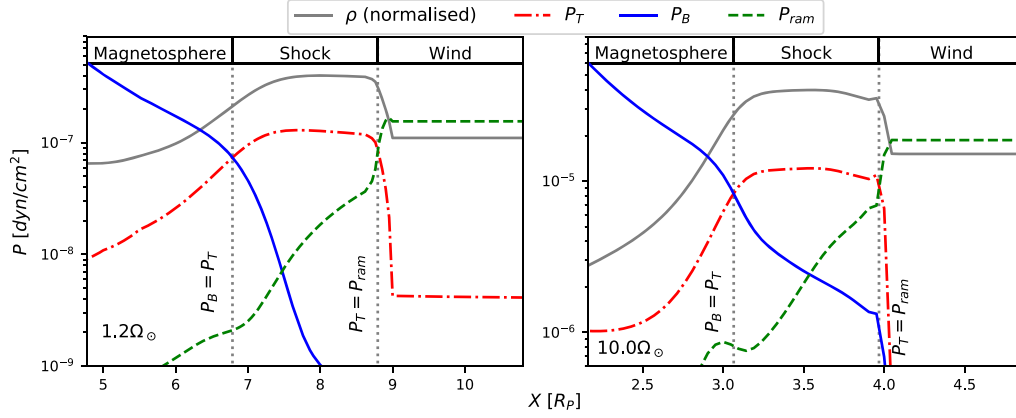


Figure 7. The variation of thermal, magnetic, and ram pressures on the dayside of the planet towards the star for the 1.2 and 10 Ω_{\odot} models. The grey vertical dotted lines mark the points where thermal-magnetic and thermal-ram pressure balances occur, which represent the magnetopause and bow shock standoff distances. This allows for the size of the magnetosphere and magnetosheath to be established. The solid blue lines are the magnetic pressure, the dot-dashed red are the thermal pressures, and the dashed green are the ram pressures.

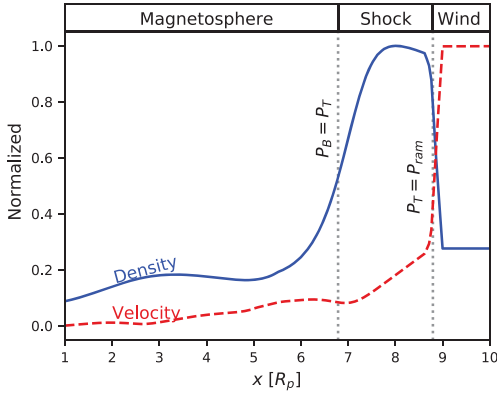


Figure 8. The variation of velocity magnitude and density towards the star in the 1.2 Ω_{\odot} model. These are normalized for comparison. This verifies the pressure balance method for establishing the standoff distance and magnetosheath thickness from our models, as we see the ram-thermal pressure balance correctly identifies the shock location, while the magnetic-thermal balance marks a minimum in velocity. We confirm that these models show adiabatic shocks following the Rankine–Hugoniot conditions, with the density increasing by a factor of 4 and the velocity decreasing by a factor of 4 compared to the stellar wind values.

The relationship between bow shock distance and standoff distance can be rationalized by considering the pressures and forces on the shocked material. On the planet side of the planet–star line, the magnetic field of the planet is exerting a force on the shocked material directed away from the planet. On the star side, the wind is exerting a force directed in the opposite direction, as wind particles impacting shocked materials are themselves shocked. For a smaller standoff distance, the stellar wind must be relatively stronger. As a result, both the ram pressure and the magnetic pressure will be

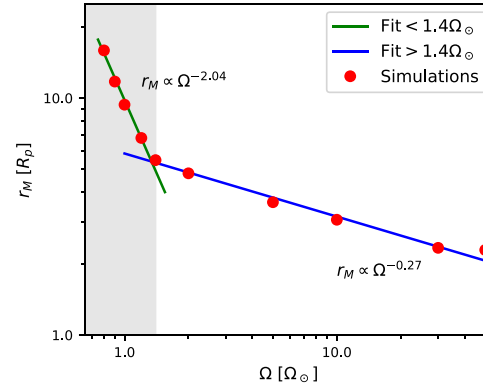


Figure 9. The variation in standoff distance with Ω for all magnetosphere models. As was seen in the stellar wind models, we see a different trend in r_M with Ω around 1.4 Ω_{\odot} . Our fits are shown with the green line ($< 1.4 \Omega_{\odot}$) and blue line ($\geq 1.4 \Omega_{\odot}$), with the grey region marking the lower Ω domain.

Table 2. Properties of the magnetopause extracted from our simulations: the size of the magnetopause (r_M), calculated along the X -axis, and the colatitude Φ of the last open field line on the dayside, which is calculated from the rotational axis of the planet (23.5° from the ecliptic).

Ω (Ω_{\odot})	r_M (R_p)	Φ ($^\circ$)
0.8	15.9	11.1
0.9	11.7	10.2
1.0	9.4	10.3
1.2	6.8	10.5
1.4	5.5	11.3
2	4.8	12.1
5	3.6	13.4
10	3.1	17.1
30	2.4	26.2
50	2.3	31.8

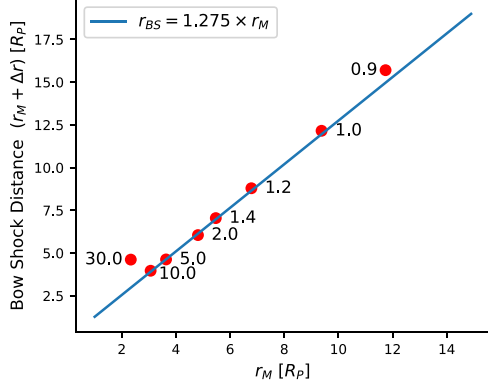


Figure 10. The obtained bow shock distance (standoff distance + magnetosheath thickness) versus each magnetosphere standoff distance. We see the results from our models follow closely equation (15) for a strong shock $\mathcal{M} \gg 1$.

stronger as the shock is closer to the planet. Therefore the net force acting on the bow shock will act to reduce the thickness of the shock for a lower standoff distance. For a weaker wind the opposite effect is achieved.

In our models, a strong correlation exists between the bow shock distance and the prescribed relation in equation (15) for the strong shock ($\mathcal{M} \gg 1$) in the $<10 \Omega_{\odot}$ models. This confirms that as the host star spins-down during the main sequence the magnetosphere and magnetosheath both increase in size proportional to the piecewise function in equation (13) for the majority of its evolution. The $30 \Omega_{\odot}$ model deviates from this trend. This is due to the weaker shock exhibited in this model, which is discussed in Section 5.

Figs 6 and 9 show that the magnetosphere standoff distance moves closer to the planet for higher stellar rotation (stronger winds). We also see a general decrease in the thickness of the bow shock for higher values of Ω as shown in Fig. 10, and an increase in the peak density up to $30 \Omega_{\odot}$ as shown in Fig. 11. In this figure, we see the density distribution is constant at large X for different stellar rotation rates. This indicates the extent to which the stellar wind penetrates into our computational grid. There is a jump in density closer to the planet, signifying the formation of a bow shock. For most of our models these shocks follow the Rankine–Hugoniot jump conditions, which predict for an adiabatic shock a factor of 4 increase in density. The exceptions to this are the 30 and $50 \Omega_{\odot}$ models, showing a weaker and no shock, respectively. This is discussed in Section 5.

In the case of large magnetospheres (lower stellar rotation) we see a low-density cavity within the magnetosphere. To understand why this occurs we compare the density and velocity magnitude in the model, as seen in Fig. 8. This minimum in density occurs at the point where the velocity magnitude is at a local maximum. This region corresponds to where some of the largest closed magnetic field lines from the planet exist, seen in Fig. 6. The top panels of Fig. 12 shows the dominant components of velocity in this region are positive u_r and negative u_{θ} . (In the higher Ω models, u_{ϕ} begins to become significant). On the boundary of the magnetopause, the u_{θ} component is at a maximum magnitude. Along the X -axis this corresponds to the Z direction, which is perpendicular to the orbital

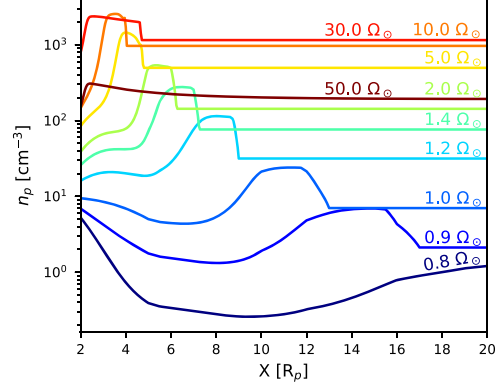


Figure 11. Variation of density on the dayside of the planet, towards the star (X -axis) for different values of stellar rotation Ω . This shows the relative change of density through each of our models, as well as illustrating the Rankine–Hugoniot shock conditions followed in our models (increase by factor of 4 in density).

plane of the planet in this instance. The high u_{θ} velocity here shows that the magnetic field lines lead a significant amount of material away. Just inside this region, the positive u_r component is moving material away from the planet and towards the sweeping θ component. As a result there is an underdensity in this region. Fig. 12 shows that the u_{ϕ} component is relatively negligible along the subsolar line. Finally outside the bow shock we can see u_r is at a maximum, which is to be expected as the stellar wind is mostly radial.

Across the shock, we see little variation in the radial component of the magnetic field (Fig. 12, bottom panel). In the B_{ϕ} component however we see a small shock like behaviour in both low- and high-stellar rotation models, with an overall increase of a factor of 4 (adiabatic shock).

The largest variation in the magnetic field is observed in B_{θ} . Just inside the magnetosphere, this component is strong and positive, corresponding to a northward (positive Z) direction of the dipolar field. This corresponds to the largest closed field lines in the X – Z plane, which at this point on the X -axis will be oriented in the positive Z direction. This is true for all models. Through the bow shock, there is a steep decrease in this B_{θ} component for both high and low rotation models. This illustrates how the magnetic field lines across the magnetopause transition from closed to open field lines in the X – Y plane.

The middle panel in Fig. 12 shows two notable trends in current, which are similar in both low and high Ω models. The j_{ϕ} component shows the ‘Chapman–Ferraro’ current, also known as the magnetopause current. This current separates the shocked magnetosheath from the relatively empty magnetopause. This prevents the terrestrial dipole field from penetrating into the solar wind (Gombosi 2004). At the boundary between the magnetopause and bow shock, there is a strong negative j_{θ} component. At the boundary between the stellar wind and bow shock, the j_{θ} component is strong and positive. This can be explained by the variation in B_{ϕ} . This tangential component to the shock surface itself shows shock-like behaviour, transitioning from low values in the magnetosphere, to shocked values in the magnetosheath before returning to low

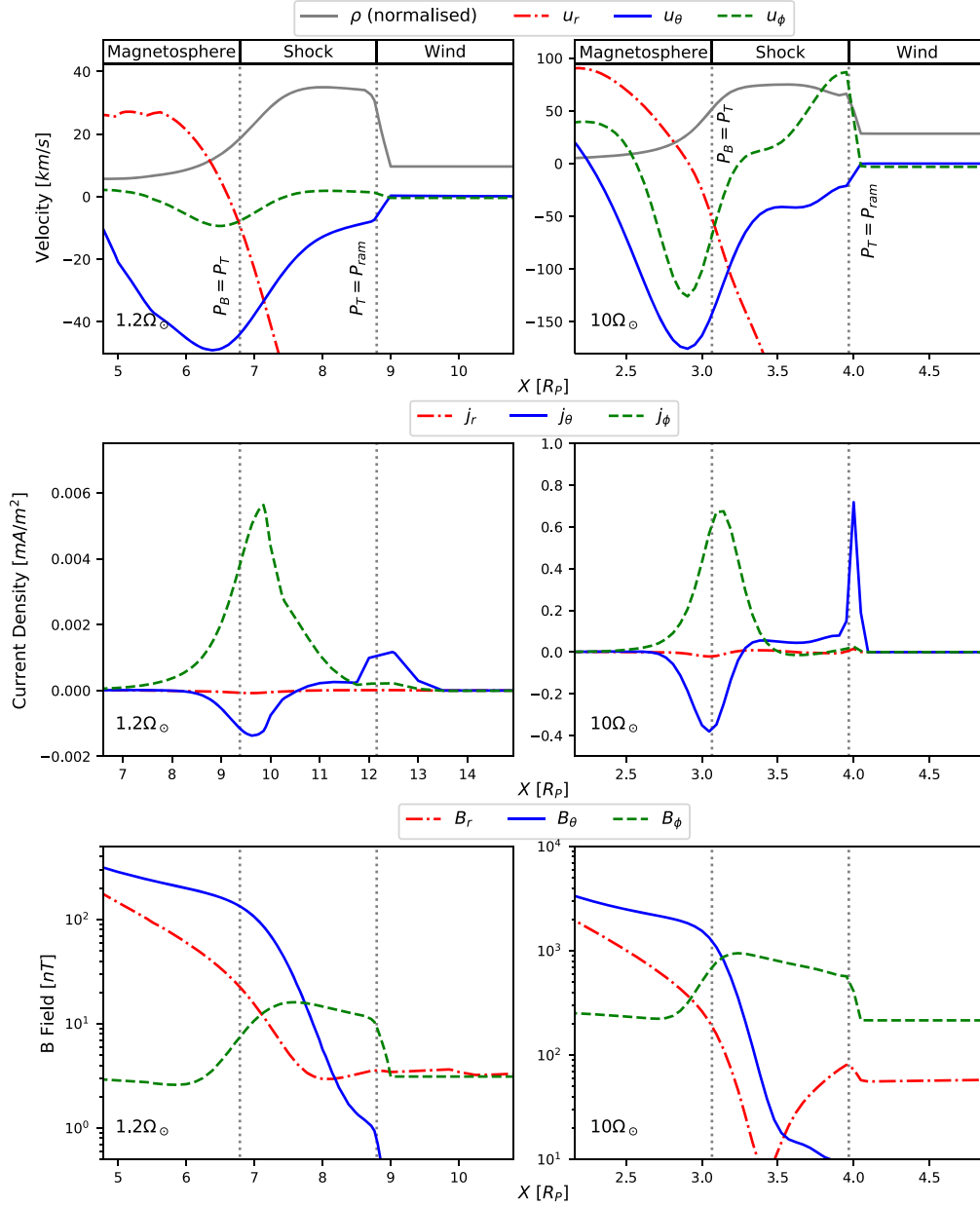


Figure 12. The variation velocity, current, and B-field components along the x -axis towards the star, for the 1.2 and $10.0\Omega_{\odot}$ model. The grey vertical lines again mark the point where magnetic-thermal (left) and ram-thermal (right) pressures are balanced. The red dot-dashed lines are the radial components, the solid blue are the θ components, and the dashed green are the ϕ components.

in the stellar wind. This variation in B_ϕ generates a perpendicular current component, with a negative j_θ generated by the difference the magnetic field orientation and strength on opposite side of the magnetopause (B_θ dominated inside, B_ϕ dominated outside), and a positive j_θ when it decreases across the shock.

5 VERY FAST ROTATING YOUNG SUN?

It is not currently known the rotation rate of the Sun at early ages. Recently, a neat study based on the composition of volatile elements in lunar samples from Saxena et al. (2019) suggested that the Sun would have been a slow rotator – these authors argue that slow rotators are expected to generate lesser amount of energetic particles through coronal mass ejections (CME) and thus would not completely deplete the sodium and potassium still seen in the moon regolith. To reach such a conclusion, the authors rely on a correlation between solar flares and CMEs (e.g. Aarnio et al. 2011), and extend it to younger Sun-like stars using observed flare frequencies from solar analogues. As a consequence, a slowly rotating (less active) young Sun would present less frequent CMEs than a fast rotating young Sun. However, there has been some suggestions in the literature that the solar CME–flare relation might actually overpredict the number of CMEs in younger and more active stars (Drake et al. 2013). In this case, a fast rotating Sun could actually have had a lower frequency of CMEs (or more ‘failed CMEs’, see Alvarado-Gómez et al. 2018) for its predicted flare rate at young ages. This could have an impact in the calculated sputtering of volatile elements recorded in lunar data sample. Here, we speculate what would have happened to Earth’s magnetosphere in the case that the young Sun was a fast rotator.

In the fast rotating regime it is possible for the young Sun to have a rotation rate as high as $100 \Omega_\odot$, while models of slow rotators suggest a maximum of approximately $5 \Omega_\odot$ (Gallet & Bouvier 2013, see also our Fig. 2). To understand the magnetosphere in the fast young system, we perform two additional simulations for stellar rotation rates of 30 and $50 \Omega_\odot$. The results of these models can be seen in Fig. 13.

In both of these models, the thermal pressure does not become large enough within the magnetosheath to balance either the magnetic or ram pressures, due to a weak shock for $30 \Omega_\odot$, and lack of shock for $50 \Omega_\odot$. We therefore cannot use the points of pressure balance to identify the magnetopause and bow shock standoff distances. Instead we use the j_ϕ current density as seen in Fig. 14. In all our models, there is a positive j_ϕ component around the magnetopause. This is the Chapman–Ferraro or magnetopause current mentioned previously in this section. We use this current density to identify the position of the magnetopause in these fast rotating models. To identify the position of the bow shock in the $30 \Omega_\odot$ model, we use the point where ram pressure begins to dominate all other components.

Due to the lower magnetosonic Mach numbers (1.5 and 0.99, respectively), both these models exhibit some differences to those in Fig. 6. In the $30 \Omega_\odot$ model there is a much weaker shock than for lower rotation rates. As a result the density jumps by only a factor of ≈ 2 in the bow shock, whereas in the stronger shocks this factor was 4. Due to the larger N_1/N_2 compression ratio, resultant from the lower Mach number, the magnetosheath in this model is thicker than expected for a strong shock. This model therefore deviates from the expected Equation for bow shock standoff distance shown in Fig. 10.

In the $50 \Omega_\odot$ model, the wind is submagnetosonic so no bow shock is formed. However the magnetosphere still exists in this

model, marked by the magnetopause current, and is not completely crushed. With the absence of a bow shock in this system, the magnetosheath thickness can no longer be quantified. These models suggest that if the Sun was a fast rotator, the young Earth would first have no bow shock. As the Sun spun-down a weak shock would then form, followed by a strong shock for the remainder of the main sequence. The magnetopause would have had a minimum value of approximately $2.3 R_p$ in this system. For an intermediate or slow rotating system, the Earth would have been surrounded by a strong shock for the entirety of its evolution.

6 CONCLUSIONS

In this work, we study the evolution of Earth’s magnetosphere over the main-sequence lifetime of our Sun. The novelty of our work is that we coupled two sets of simulations: one to model the evolution of our solar wind and the other to model the evolution of Earth’s magnetosphere. The results obtained in the former set of simulations were used as external boundary condition for the second set of simulations. We simulated the evolution of the solar wind using 1.5D stellar wind models of Sun-like stars with different stellar rotation rates. We simulated these winds out to 1 au. We see a split in stellar wind properties at 1 au around $1.4 \Omega_\odot$, in line with how we specify relations for base temperature. The resulting temperature, density, velocity, and magnetic field vectors at 1au were then employed in our 3D magnetosphere models.

Using the balance of thermal and magnetic pressures, we found that the magnetopause standoff distance varies according to the following piece-wise function due to the break in stellar wind properties: $r_M (< 1.4 \Omega_\odot) \propto \Omega^{-2.04}$ and $r_M (\geq 1.4 \Omega_\odot) \propto \Omega^{-0.27}$. This suggests that given the early solar wind strength, the young Earth’s magnetosphere was much smaller than it is today. As the Sun spun-down, this size gradually increased, before experiencing greater an increase once the Sun’s rotation rate dropped to $1.4 \Omega_\odot$. Furthermore we can predict a much larger magnetosphere size in the future, according to the steep increase with magnetopause distance with decreasing Ω for $< 1.4 \Omega_\odot$. Our models yield a standoff distance of $9.4 R_p$ for the present-day magnetosphere, which is within the bounds of observed values.

We found a linear relationship between magnetopause standoff distance and the thickness of the magnetosheath for stellar rotations $\leq 10 \Omega_\odot$. This is in line with the relation prescribed by Gombosi (2004) and Balogh & Treumann (2013), for example, for a strong shock ($\mathcal{M} \gg 1$). These stellar wind models all have a $\mathcal{M} \gg 1$, allowing us to use equation (15) to predict that this thickness will be approximately $0.275 r_M$ for a given magnetopause distance (Fig. 10). Therefore, we can say that the magnetosheath thickness is proportional to stellar rotation rate in the same way as the magnetopause distance for the majority of its evolution, according to the following piece-wise function: $\Delta r (< 1.4 \Omega_\odot) \propto \Omega^{-2.04}$ and $\Delta r (\geq 1.4 \Omega_\odot) \propto \Omega^{-0.27}$.

We examined the variation of parameters along the subsolar line (line from the centre of the planet towards the star). We see that in our models the magnetosheath is dominated by thermal pressure, while ram pressure dominates in the stellar wind and magnetic pressure dominates in the magnetosphere. We use the balance of magnetic and thermal pressures to define the magnetopause standoff distance, and the balance of thermal and ram pressures to define the boundary between the magnetosheath and the stellar wind. In our models, current densities also mark both of these positions well. We see strong ϕ and θ currents at the magnetopause boundary, corresponding to the ‘Chapman–Ferraro’ current, with

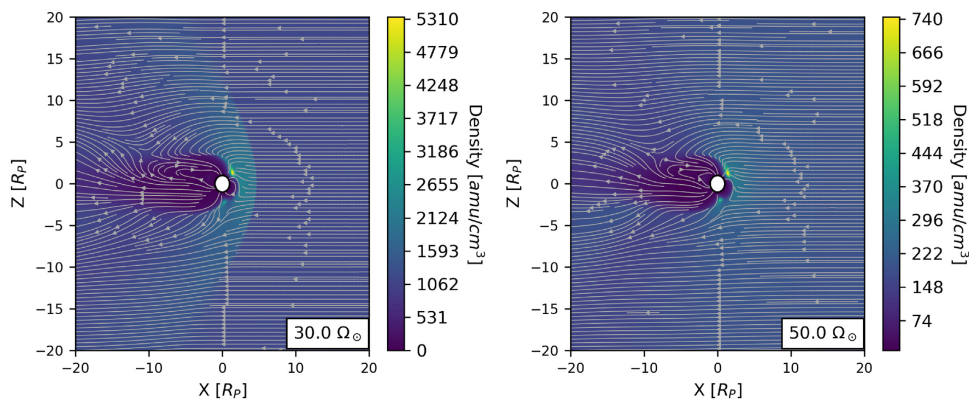


Figure 13. Earth's magnetosphere in the wind of a very fast rotating young Sun. In the $30\Omega_{\odot}$ model (left) we see a weaker shock than those in Fig. 6, with a comparably inflated magnetosheath. In the $50\Omega_{\odot}$ model (right) there is no shock present, as the wind is submagnetosonic. Despite this, the magnetosphere is not completely crushed, though is reduced to a magnetopause standoff distance of $\approx 2.3 R_p$.

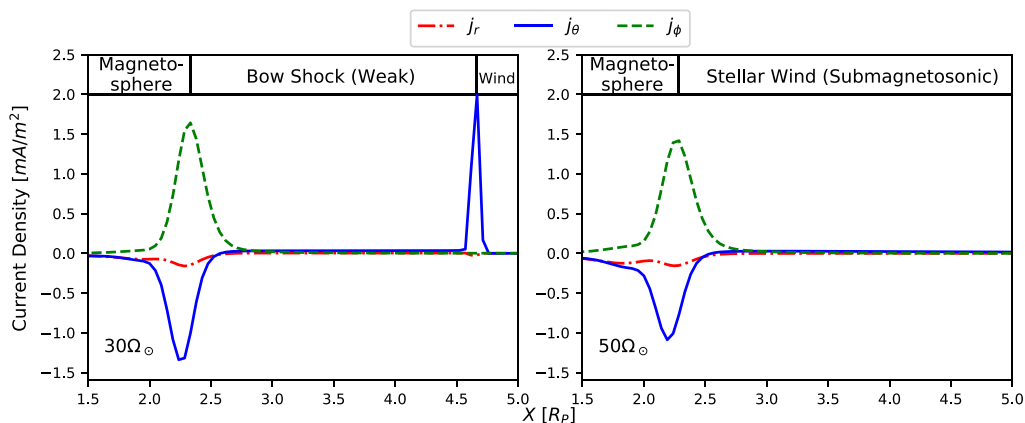


Figure 14. The current components along the subsolar line in the $30\Omega_{\odot}$ (left) and $50\Omega_{\odot}$ (right) models. The positive j_{ϕ} component is the magnetopause current, which is a current system flowing around the magnetosphere. The positive j_{θ} marks the position of the bow shock, and is generated from the change in magnetic field in the shock. As there is no shock in the $50.0\Omega_{\odot}$, this current density is not seen here.

the θ component being strong and positive at the boundary of the stellar wind, due to the varying ϕ magnetic field at this boundary.

We examined the colatitude if the last open magnetic field line, to discuss whether stellar wind inflow or plasma collection poses a greater threat to Earth's atmosphere at a certain stage of its evolution, which is currently in debate (Blackman & Tarduno 2018). We found that this colatitude decreases through the evolution of Earth's magnetosphere. This accompanied by the gradual increase in the size of the magnetosphere suggests that stellar wind inflow would pose the greatest threat in the young system before decreasing slowly with Ω , with the threat posed by plasma collection increasing with Ω .

It is possible that a young fast rotating Sun could have had a rotation rate as high as $50\Omega_{\odot}$. It is uncertain whether the Sun rotated that fast – if that indeed occurred, it happened only for a

short amount of time, relative to the Sun's lifetime, and at an age $\lesssim 100$ Myr. We simulated Earth's magnetosphere in this extreme young system, modelling the wind of the Sun at speculative rotation rates of 30 and $50\Omega_{\odot}$. For a fast-rotating Sun, our stellar wind models predict mass-loss rates of up to $10^{-11} M_{\odot} \text{ yr}^{-1}$, which agrees with observations of mass-loss rates derived for fast rotators, like AB Dor (Jardine & Collier Cameron 2019). However, our models do not consider wind saturation at very fast rotation. As a result, our wind models overpredict angular-momentum loss at high rotation ($>10\Omega_{\odot}$). Given our choice of parameters, at rotation rates 30 and $50\Omega_{\odot}$, our wind models have Mach numbers of 1.5 and 0.99 , respectively. As a result, we expect Earth's surroundings to exhibit differences between the young system and the majority of its evolution. As the wind is submagnetosonic in the $50\Omega_{\odot}$ model, in our speculative scenario, there would have been no bow

shock surrounding the Earth in this fast young system. Once the rotation rate dropped to $30 \Omega_{\odot}$, a weak shock would then be formed, accompanied by a relatively inflated magnetosheath when compared to other models. With the Sun continuing to spin-down, a strong shock would then surround our planet, and would remain for most of the duration of the solar main sequence.

ACKNOWLEDGEMENTS

SC and AAV acknowledge funding received from the Irish Research Council Laureate Awards 2017/2018. This work was carried out using the BATSUS tools developed at The University of Michigan Center for Space Environment Modeling (CSEM) and made available through the NASA Community Coordinated Modeling Center (CCMC). The authors also wish to acknowledge the Science Foundation Ireland (SFI)/Higher Education Authority (HEA) Irish Centre for High-End Computing (ICHEC) for the provision of computational facilities and support. AAV thanks Dr. Brian Wood for bringing to our attention the recent work on the moon regolith and its association to break in flare–CME relation for active stars, during the meeting ‘The Solar and Stellar Wind Connection: Heating Processes and Angular Momentum Loss’ at the International Space Science Institute (ISSI). We thank the anonymous reviewer for their constructive criticism, which helped improve the clarity of our paper.

REFERENCES

- Aarnio A. N., Stassun K. G., Hughes W. J., McGregor S. L., 2011, *Sol. Phys.*, 268, 195
- Adams F. C., 2011, *ApJ*, 730, 27
- Airapetian V. S., Gloer A., Gronoff G., Hébrard E., Danchi W., 2016, *Nat. Geosci.*, 9, 452
- Alvarado-Gómez J. D., Drake J. J., Cohen O., Moschou S. P., Garraffo C., 2018, *ApJ*, 862, 93
- Bagenal F., 2013, in Oswald T. D., French L. M., Kalas P., eds, *Planetary Magnetospheres, Planets, Stars and Stellar Systems.*, Springer, Dordrecht, p. 487
- Balogh A., Treumann R. A., 2013, *Physics of Collisionless Shocks: Space Plasma Shock Waves.* ISSI Scientific Report Series, Springer, New York
- Barnes S. A., 2003, *ApJ*, 586, 464
- Beck P. G. et al., 2017, *A&A*, 602, A63
- Bharati Das S., Basak A., Nandy D., Vaidya B., 2019, *ApJ*, 877, 80
- Blackman E. G., Tarduno J. A., 2018, *MNRAS*, 481, 5146
- Booth R. S., Poppenhaeger K., Watson C. A., Silva Aguirre V., Wolk S. J., 2017, *MNRAS*, 471, 1012
- Brain D. A., Leblanc F., Luhmann J. G., Moore T. E., Tian F., 2013, in Mackwell S. J., Simon-Miller A. A., Harder J. W., Bullock M. A., eds, *Planetary Magnetic Fields and Climate Evolution, Comparative Climatology of Terrestrial Planets*, Univ. Arizona Press, Tucson, AZ, p. 487
- Chapman S., Ferraro V. C. A., 1931, *Terr. Magn. Atmos. Electr.*, 36, 77
- Cravens T. E., 2004, *Physics of Solar System Plasmas*, Cambridge Univ. Press, Cambridge
- Drake J. J., Cohen O., Yashiro S., Gopalswamy N., 2013, *ApJ*, 764, 170
- Egan H., Jarvinen R., Brain D., 2019, *MNRAS*, 486, 1283
- Gallet F., Bouvier J., 2013, *A&A*, 556, A36
- Gombosi T. I., 2004, *Physics of the Space Environment*, Cambridge Univ. Press, Cambridge
- Holzwarth V., Jardine M., 2007, *A&A*, 463, 11
- Ivanova N., Taam R. E., 2003, *ApJ*, 599, 516
- Jardine M., Collier Cameron A., 2019, *MNRAS*, 482, 2853
- Jia X., Kivelson M. G., 2016, *J. Geophys. Res.: Space Phys.*, 121, 1413
- Jia X., Slavin J. A., Gombosi T. I., Daldorff L. K. S., Toth G., Holst B., 2015, *J. Geophys. Res.: Space Phys.*, 120, 4763
- Johnstone C. P., Güdel M., 2015, *A&A*, 578, A129
- Johnstone C. P., Güdel M., Lüftinger T., Toth G., Brott I., 2015a, *A&A*, 577, A27
- Johnstone C. P., Güdel M., Brott I., Lüftinger T., 2015b, *A&A*, 577, A28
- Johnstone C. P., Khodachenko M. L., Lüftinger T., Kislyakova K. G., Lammer H., Güdel M., 2019, *A&A*, 624, L10
- Keppens R., Goedbloed J. P., 1999, *A&A*, 343, 251
- Khodachenko M. L., Shaikhislamov I. F., Lammer H., Prokopov P. A., 2015, *ApJ*, 813, 50
- Kulikov Y. N., Lammer H., Lichtenegger H. I. M., Penz T., Breuer D., Spohn T., Lundin R., Biernat H. K., 2007, *Space Sci. Rev.*, 129, 207
- Lammer H. et al., 2011, *Orig. Life Evol. Biosph.*, 41, 503
- Lammer H. et al., 2012, *Earth Planets Space*, 64, 179
- Matt S. P., MacGregor K. B., Pinsonneault M. H., Greene T. P., 2012, *ApJ*, 754, L26
- Matt S. P., Brun A. S., Baraffe I., Bouvier J., Chabrier G., 2015, *ApJ*, 799, L23
- Ma Y., Russell C. T., Nagy A. F., Toth G., Dong C., Bougher S. W., 2013, AGU Fall Meeting Abstracts, #P13C-05
- Ma Y. J. et al., 2015, *Geophys. Res. Lett.*, 42, 9113
- Moore T. E., Horwitz J. L., 2007, *Rev. Geophys.*, 45, RG3002
- Ngwira C. M., Pulkkinen A. A., 2014, AGU Fall Meeting Abstracts, #SM31A-4166
- O’Fionnagáin D., Vidotto A. A., 2018, *MNRAS*, 476, 2465
- Ó Fionnagáin D. et al., 2019, *MNRAS*, 483, 873
- Owen J. E., Adams F. C., 2014, *MNRAS*, 444, 3761
- Pizzolato N., Maggio A., Micela G., Sciortino S., Ventura P., 2003, *A&A*, 397, 147
- Pneuman G. W., Kopp R. A., 1971, *Sol. Phys.*, 18, 258
- Pognan Q., Garraffo C., Cohen O., Drake J. J., 2018, *ApJ*, 856, 53
- Réville V., Folsom C. P., Strugarek A., Brun A. S., 2016, *ApJ*, 832, 145
- Ribas I., Guinan E. F., Güdel M., Audard M., 2005, *ApJ*, 622, 680
- Ridley A. J., De Zeeuw D. L., Gombosi T. I., Powell K. G., 2001, *J. Geophys. Res.*, 106, 30067
- Sakai S., Seki K., Terada N., Shinagawa H., Tanaka T., Ebihara Y., 2018, *Geophys. Res. Lett.*, 45, 9336
- Saxena P., Killen R. M., Airapetian V., Petro N. E., Curran N. M., Mandell A. M., 2019, *ApJ*, 876, L16
- See V., Jardine M., Vidotto A. A., Petit P., Marsden S. C., Jeffers S. V., do Nascimento J. D., 2014, *A&A*, 570, A99
- Skumanich A., 1972, *ApJ*, 171, 565
- Spreiter J. R., Summers A. L., Alksne A. Y., 1966, *Planet. Space Sci.*, 14, 223
- Sterenberg M. G., Cohen O., Drake J. J., Gombosi T. I., 2011, *J. Geophys. Res.*, 116, A01217
- Strangeway R. J., Russell C. T., Luhmann J. G., Moore T. E., Foster J. C., Barabash S. V., Nilsson H., 2010, AGU Fall Meeting Abstracts, #SM31A-4166
- Tarduno J. A. et al., 2010, *Science*, 327, 1238
- Tarduno J. A., Blackman E. G., Mamajek E. E., 2014, *Phys. Earth Planet. Inter.*, 233, 68
- Terada N., Kulikov Y. N., Lammer H., Lichtenegger H. I. M., Tanaka T., Shinagawa H., Zhang T., 2009a, *Astrobiology*, 9, 55
- Terada N., Shinagawa H., Tanaka T., Murawski K., Terada K., 2009b, *J. Geophys. Res.: Space Phys.*, 114, A09208
- Tóth G., 1996, *Astrophys. Lett. Commun.*, 34, 245
- Tóth G. et al., 2005, *J. Geophys. Res.: Space Phys.*, 110, A12226
- Trammell G. B., Arras P., Li Z.-Y., 2011, *ApJ*, 728, 152
- van Saders J. L., Ceillier T., Metcalfe T. S., Silva Aguirre V., Pinsonneault M. H., García R. A., Mathur S., Davies G. R., 2016, *Nature*, 529, 181
- Vidotto A., 2013, *Astron. Geophys.*, 54, 1.25
- Vidotto A. A., 2018, in Deeg H., Belmonte J., eds, *Stellar Coronal and Wind Models: Impact on Exoplanets*, Handbook of Exoplanets, Springer, Cham, p. 26
- Vidotto A. A., Donati J. F., 2017, *A&A*, 602, A39
- Vidotto A. A., Opher M., Jatenco-Pereira V., Gombosi T. I., 2009, *ApJ*, 703, 1734
- Vidotto A. A., Jardine M., Morin J., Donati J. F., Lang P., Russell A. J. B., 2013, *A&A*, 557, A67

- Vidotto A. A. et al., 2014, *MNRAS*, 441, 2361
 Vidotto A. A. et al., 2016, *MNRAS*, 455, L52
 Vogt J., Zieger B., Stadelmann A., Glassmeier K. H., Gombosi T. I., Hansen K. C., Ridley A. J., 2004, *J. Geophys. Res.: Space Phys.*, 109, A12221
 Weber E. J., Davis Jr. L., 1967, *ApJ*, 148, 217
 Wood B. E., Müller H.-R., Zank G. P., Linsky J. L., 2002, *ApJ*, 574, 412
 Wood B. E., Müller H. R., Zank G. P., Linsky J. L., Redfield S., 2005, *ApJ*, 628, L143
 Wood B. E., Müller H.-R., Redfield S., Edelman E., 2014, *ApJ*, 781, L33
 Zuluaga J. I., Bustamante S., Cuartas P. A., Hoyos J. H., 2013, *ApJ*, 770, 23

APPENDIX A: STELLAR WIND FITS

For ease of use in future works, here we provide the fit parameters obtained for some physical quantities of the solar wind at 1 au, as a function of rotation rate. The fits are shown as solid/dashed lines in Fig. 1 and take the form:

$$\log_{10}(F(\Omega)) = a \left(\frac{\Omega}{\Omega_{\odot}} \right)^b + c \left(\frac{\Omega}{\Omega_{\odot}} \right)^d + e \left(\frac{\Omega}{\Omega_{\odot}} \right)^f \quad (\text{A1})$$

The functions $F(\Omega)$ are computed at 1 au, and are the following: The stellar wind radial and azimuthal velocities in km s^{-1} ; stellar wind radial and azimuthal magnetic field strengths in G; stellar wind mass density in g cm^{-3} ; temperature in MK; mass-loss rate in $M_{\odot} \text{ yr}^{-1}$ and angular-momentum-loss rate in erg. The parameters a – f for each of these functions are shown in Table A1 for $\Omega < 1.4 \Omega_{\odot}$ and A2 for $\Omega \geq 1.4 \Omega_{\odot}$.

To find the solar wind conditions at other orbital distances x , we use the values obtained at Earth's orbit x_E (i.e. from Tables A1 and A2), with the following power laws with distance

$$B_r^{\text{sw}}(x) = B_r^{\text{sw}}(x_E) \left(\frac{x_E}{x} \right)^2, \quad (\text{A2})$$

$$B_{\phi}^{\text{sw}}(x) = B_{\phi}^{\text{sw}}(x_E) \left(\frac{x_E}{x} \right), \quad (\text{A3})$$

$$u_r^{\text{sw}}(x) = u_r^{\text{sw}}(x_E), \quad (\text{A4})$$

$$u_{\phi}^{\text{sw}}(x) = u_{\phi}^{\text{sw}}(x_E) \left(\frac{x_E}{x} \right), \quad (\text{A5})$$

Table A1. The fitting parameters to derive the stellar wind properties at 1au for $\Omega < 1.4 \Omega_{\odot}$. Parameters a – f should be implemented in equation (A1) to derive the solar wind conditions.

Parameter	u_r^{sw}	u_{ϕ}^{sw}	B_r^{sw}	B_{ϕ}^{sw}	ρ^{sw}	T^{sw}	\dot{M}	\dot{J}
a	-8.50×10^1	-2.60×10^0	-1.32×10^2	1.09×10^2	-1.25×10^0	-7.17×10^{-2}	-1.21×10^0	-5.71×10^2
b	5.84×10^{-1}	-7.93×10^{-1}	-2.32×10^{-3}	2.80×10^{-1}	-2.93×10^0	-2.80×10^0	-2.95×10^0	-1.85×10^{-2}
c	8.77×10^1	2.54×10^0	1.32×10^2	-1.09×10^2	2.10×10^0	5.90×10^0	-1.24×10^1	6.01×10^2
d	5.72×10^{-1}	-1.82×10^0	2.02×10^{-3}	2.76×10^{-1}	3.37×10^{-1}	9.04×10^{-2}	-1.03×10^{-1}	-1.51×10^{-2}

Table A2. The same as in Table A1, but for $\Omega \geq 1.4 \Omega_{\odot}$.

Parameter	u_r^{sw}	u_{ϕ}^{sw}	B_r^{sw}	B_{ϕ}^{sw}	ρ^{sw}	T^{sw}	\dot{M}	\dot{J}
a	8.21×10^{-8}	2.01×10^{-1}	-1.32×10^2	-9.56×10^1	1.83×10^0	1.22×10^2	-1.26×10^1	-5.71×10^2
b	3.91×10^0	6.71×10^{-1}	-2.32×10^{-3}	-6.97×10^{-3}	2.56×10^{-1}	9.22×10^{-2}	-5.98×10^{-2}	-1.85×10^{-2}
c	2.77×10^0	-9.90×10^{-1}	1.32×10^2	-1.33×10^{-7}	-1.02×10^{-2}	-1.16×10^2	-1.24×10^{-3}	6.01×10^2
d	3.99×10^{-2}	-3.32×10^{-1}	2.02×10^{-3}	3.79×10^0	1.42×10^0	9.52×10^{-2}	1.76×10^0	-1.51×10^{-2}
e	–	–	–	9.59×10^1	–	–	–	–
f	–	–	–	2.39×10^{-3}	–	–	–	–

$$T^{\text{sw}}(x) = T^{\text{sw}}(x_E) \left(\frac{\rho(x)}{\rho(x_E)} \right)^{\alpha-1} = T^{\text{sw}}(x_E) \left(\frac{x_E}{x} \right)^{2(\alpha-1)}, \quad (\text{A6})$$

$$\rho^{\text{sw}}(x) = \rho^{\text{sw}}(x_E) \left(\frac{x_E}{x} \right)^2, \quad (\text{A7})$$

where $\alpha = 1.05$ is the polytropic index. Note that in these relations, we assume that u_r^{sw} does not depend on x , which implies that the wind has reached terminal velocity. This is valid for orbital distances approximately larger than Mercury's orbit.

APPENDIX B: OPEN AND CLOSED MAGNETOSPHERES

In Section 4, we discussed the various trends observed in Earth's magnetosphere with time, from 1.5D stellar wind simulations. It is also likely that the polarity of either the star's or planet's magnetic field will flip cyclically. This may lead to both 'open' and 'closed' magnetospheres (Cravens 2004; Bharati Das et al. 2019). To examine this difference we perform two simulations, both with the same parameters as the 1.2 Ω_{\odot} wind (see Table 1), but now with a northward and southward magnetic field (positive and negative Z). Instead of using a total magnetic field strength of 4.7×10^{-5} G as in Table 1, we use a strength of 1×10^{-3} G so that the nightside magnetosphere is entirely contained in our numerical grid. These can be seen in Fig. B1.

For the positive case, the magnetic field is anti-aligned with the magnetic field of the planet. This creates a closed magnetosphere. For the negative case, the magnetic field in the wind is aligned with that of the planet. This creates an open magnetosphere. When the magnetic field lines of the wind and the magnetic field of the planet are anti-aligned, the planet's field lines remain closed on both the dayside and nightside of the planet, unlike what occurs in the models examined in Section 4. This results in a reduced inflow of material from the stellar wind, due to the lack of open field lines around the poles. Magnetic reconnection no longer occurs on the nightside of the planet, which can drive material towards the atmosphere (Bharati Das et al. 2018). However due to an increase in closed field lines surrounding the planet, there is a larger amount of material held within these loops, compared to models in Section 4.

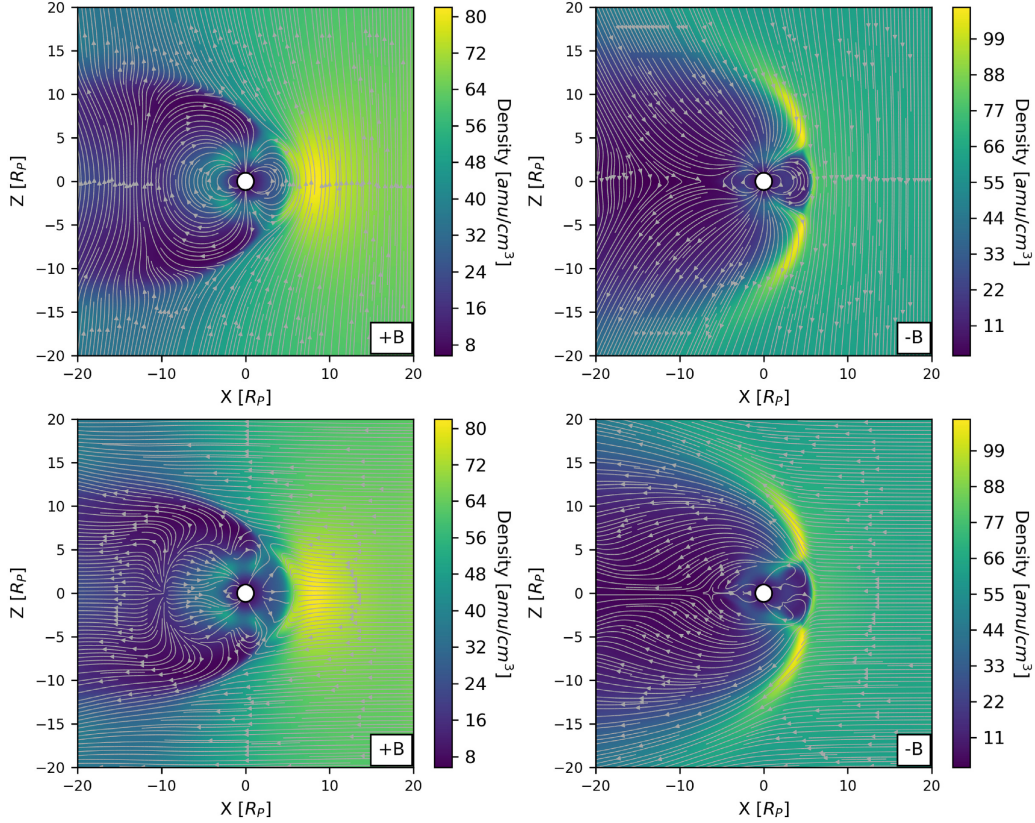


Figure B1. Closed (Left, northward stellar wind) and open (Right, southward stellar wind) magnetosphere. Top: The contour shows the density distribution in the models, while the streamtracers are magnetic field lines. Bottom: The contour shows the density distributions while the stream lines now show the velocity vectors. All parameters were kept constant between these models, except for the orientation of the stellar wind's magnetic field.

When the fields are aligned an open magnetosphere is observed. There is now a much lower number of closed magnetic field lines, which are mostly on the dayside of the planet. Open field lines now exist at much lower latitudes than seen in other models – this simulation gives a $\Phi = 23.3^\circ$, similar to the analytical value of 24.4° . As a result, there is now a much larger inflow of material, and a lower amount held by closed field lines. These two scenarios correspond to the two competing effects discussed by Blackman & Tarduno (2018). In one case we have a much larger region covered by closed field lines and so a larger collecting area for plasma. While in the other we see a greater potential for inflow of material directly from the stellar wind.

As is clear in Fig. B1, there are significant differences in the dayside of open and closed magnetospheres. To examine these differences, we look at the subsolar line, in a similar way to Section 4. The density and thermal pressure distributions along this line can be seen in Fig. B2.

In the open magnetosphere (Negative Z magnetic field) model, reconnection occurs on the dayside at a distance of $\sim 5 R_p$ from the planet. This corresponds to both an under and overdensity

seen in this model along the X-axis. On the planet side of this reconnection, material is driven away from this point with the closed field lines trapping a portion of this material. On the wind side of the reconnection, material is driven away from the planet but the stellar wind acts as a resisting force creating the overdensity seen in this model at $\sim 6 R_p$. As a result there is an increase in thermal pressure at $\sim 6 R_p$ as the forces from both reconnection and the stellar wind compress the material at this point.

In the closed magnetosphere there is a much smoother density profile on the dayside of the planet, as there is no reconnection on this side in the model. As a result the over and underdensities observed in the open case are not seen here. We no longer see a bow shock with high density that extends northward and southward, but instead the closed planetary magnetic field lines focus material towards the subsolar line. This can be seen in Fig. B2, in the velocity streamlines. This forms a high-density ‘bubble’ on the dayside instead of an extended shock. In the open model, this is not the case. The open planetary field lines from the planet lead to the opposite effect, where we observe more inflow of material, but also a more extended shock northwards and southwards.

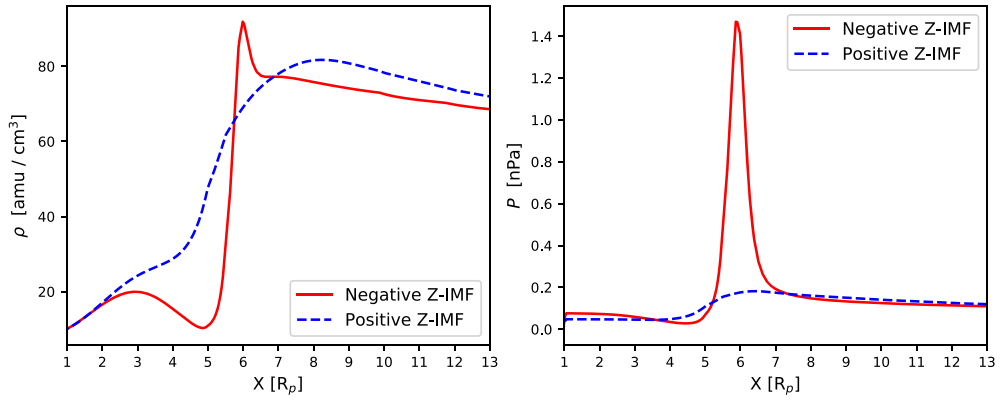


Figure B2. Left: The density distributions along the x -axis for both a negative Z stellar wind (open) and a positive Z stellar wind (closed) case. Right: Variation in thermal pressure for both open and closed cases. We can see that the overdensity caused by magnetic reconnection on the dayside of the planet leads to a peak in thermal pressure.

This paper has been typeset from a \LaTeX file prepared by the author.



Effects of the stellar wind on the Ly α transit of close-in planets

S. Carolan¹,^{*} A. A. Vidotto¹, C. Villarreal D'Angelo^{1,2} and G. Hazra¹¹*School of Physics, Trinity College Dublin, College Green, Dublin 2, Ireland*²*Observatorio Astronómico de Córdoba – Universidad Nacional de Córdoba. Laprida 854, X5000BGR Córdoba, Argentina*

Accepted 2020 November 2. Received 2020 October 28; in original form 2020 June 16

ABSTRACT

We use 3D hydrodynamics simulations followed by synthetic line profile calculations to examine the effect increasing the strength of the stellar wind has on observed Ly α transits of a hot Jupiter (HJ) and a warm Neptune (WN). We find that increasing the stellar wind mass-loss rate from 0 (no wind) to 100 times the solar mass-loss rate value causes reduced atmospheric escape in both planets (a reduction of 65 per cent and 40 per cent for the HJ and WN, respectively, compared to the ‘no wind’ case). For weaker stellar winds (lower ram pressure), the reduction in planetary escape rate is very small. However, as the stellar wind becomes stronger, the interaction happens deeper in the planetary atmosphere, and, once this interaction occurs below the sonic surface of the planetary outflow, further reduction in evaporation rates is seen. We classify these regimes in terms of the geometry of the planetary sonic surface. ‘Closed’ refers to scenarios where the sonic surface is undisturbed, while ‘open’ refers to those where the surface is disrupted. We find that the change in stellar wind strength affects the Ly α transit in a non-linear way (note that here we do not include charge-exchange processes). Although little change is seen in planetary escape rates ($\approx 5.5 \times 10^{11} \text{ g s}^{-1}$) in the closed to partially open regimes, the Ly α absorption (sum of the blue $[-300, -40 \text{ km s}^{-1}]$ and red $[40, 300 \text{ km s}^{-1}]$ wings) changes from 21 to 6 per cent as the stellar wind mass-loss rate is increased in the HJ set of simulations. For the WN simulations, escape rates of $\approx 6.5 \times 10^{10} \text{ g s}^{-1}$ can cause transit absorptions that vary from 8.8 to 3.7 per cent, depending on the stellar wind strength. We conclude that the same atmospheric escape rate can produce a range of absorptions depending on the stellar wind and that neglecting this in the interpretation of Ly α transits can lead to underestimation of planetary escape rates.

Key words: hydrodynamics – planets and satellites: atmospheres – planet–star interactions – stars: winds, outflows.

1 INTRODUCTION

Close-in exoplanets experience high levels of irradiation from their host stars, causing a substantial amount of photoevaporation of their atmospheres (Lammer et al. 2003; Baraffe et al. 2004; Yelle 2004). The amount of atmospheric escape determines the lifespan of a planet’s atmosphere (e.g. Johnstone et al. 2015; Kubyskhina et al. 2020), which is a key contributor to planetary habitability (Dong et al. 2018; Lingam & Loeb 2018), and is thought to shape the observed mass–radius distribution of close-in exoplanets (Kurokawa & Nakamoto 2014; Owen & Lai 2018; Berger et al. 2020). Additionally, atmospheric escape is believed to shape the period–radius distribution of close-in exoplanets, giving rise to the ‘evaporation desert’ and the ‘radius valley’. The evaporation desert, also known as the Neptunian desert, affects gas giants in short orbit (Mazeh, Holczer & Faigler 2016). The radius valley is an underpopulation of exoplanets with radius between 1.5 and 2.0 Earth radii and orbital periods lower than about 100 d (Beaugé & Nesvorný 2013; Fulton et al. 2017). More direct observational signatures of atmospheric escape have been found in transmission spectroscopic transits of a few planets, such as HD209458b (Vidal-Madjar et al. 2003), HD189733b (Lecavelier Des Etangs et al. 2010, 2012; Jensen et al. 2012; Ben-Jaffel & Ballester 2013), GJ436b (Kulow et al. 2014;

Ehrenreich et al. 2015), GJ3470b (Bourrier et al. 2018), and some others. These observations are often done in Ly α line, where absorption is a consequence of neutral hydrogen leaving the planet due to the outflow generated by high-energy radiation from the host star.

Once the planetary atmosphere expands and escapes, it interacts with the stellar wind, which shapes the geometry of the escaping atmosphere. This interaction can create different structures in the escaping atmosphere, such as a comet-like tail, trailing behind the planet, and a stream of material oriented ahead of the planet’s orbit and towards the star. The size and presence of these structures depend on a few key properties in the system, such as the orbital velocity, the ram pressure of the stellar wind, and tidal forces exerted by the star (Matsakos, Uribe & Königl 2015; Pillitteri et al. 2015; Shaikhislamov et al. 2016). For example, if the stellar wind is weak and the tidal forces are strong, a stream of planetary material can be created towards the star. If the stellar wind is strong, the orientation of the comet-like tail can become more aligned with the star–planet line. These different structures can be detected in Ly α , as they can contain a significant portion of neutral hydrogen. Because these structures are not spherically symmetric, they cause asymmetries in the transit light curve (e.g. an early ingress or late egress), and also affect the line profile (larger absorption in the blue and/or red wings of the line) (Vidal-Madjar et al. 2003; Lecavelier des Etangs et al. 2012; Kulow et al. 2014; Ehrenreich et al. 2015; Bourrier et al. 2018).

Using simulations, we can model the interactions between the stellar and planetary outflows, gaining key insights into the char-

* E-mail: carolast@tcd.ie

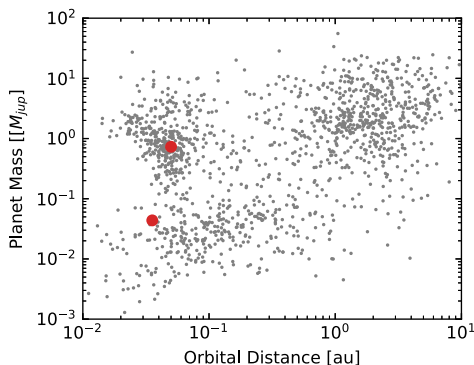


Figure 1. The masses versus orbital semimajor axis of all confirmed exoplanets are marked in grey (exoplanetarchive.ipac.caltech.edu). The red points mark the positions of the two planets examined in this work; they were chosen to have characteristics similar to GJ3470b, and HD209458b but orbiting a more active star.

acteristics of the system. In this work, we focus more specifically on the role of the stellar wind on the interaction with the escaping atmosphere and in particular whether the stellar wind can affect the amount of planetary escape. One crucial point in the theory of astrophysical flows, such as stellar winds and accretion discs, is the presence of ‘critical points’ (e.g. Parker 1958; Weber & Davis 1967). In the case of hydrodynamic outflows, such as the escaping atmospheres of close-in giants, one important critical point is the sonic point, which represents the location beyond which the planetary outflow becomes supersonic. Planetary atmospheric escape models have suggested that the position of the sonic point (or surface, in the case of 3D geometries) in relation to the position where the interaction with the stellar wind happens, can act to reduce planetary escape rate (Christie, Arras & Li 2016; Vidotto & Cleary 2020). It has been suggested that if the stellar wind interacts with the supersonic escaping atmosphere, the information cannot propagate upstream and it does not affect the inner regions of the planetary outflow. However, if this interaction occurs where the escaping atmosphere is subsonic, the inner outflow can be altered and therefore the escape rate can be affected (Vidotto & Cleary 2020). In the latter scenario, the stellar wind would act to confine the planetary outflow and reduce/prevent their escape (Christie et al. 2016).

Although an increase body of work on the 3D interaction between planetary atmospheres and stellar winds has become available recently (Bisikalo et al. 2013; Schneider et al. 2016; Shaikhislamov et al. 2016; Carroll-Nellenback et al. 2017; Villarreal D’Angelo et al. 2018; Esquivel et al. 2019; Khodachenko et al. 2019; McCann et al. 2019; Debrecht et al. 2020, Villarreal D’Angelo et al., submitted), the effect of stellar wind ‘confinement’ of planetary atmospheres has not yet been studied in 3D. For that, the interaction must occur within the sonic surface of the planetary outflow, and to the best of our knowledge, the aforementioned 3D studies have focused on the interaction that happens when the planetary outflow has already reached supersonic speeds. To best model the confinement, the planetary outflow must be launched from the surface of the planet, as the inner regions of the planetary outflow must be examined in order to accurately quantify changes in the escape rate. This requires high resolution close to the planet, in which case a planet-centric single-body model is therefore preferred (‘local’ simulations), as opposed

to ‘global’ models that incorporate both the star and the planet in the numerical grid.

In this work, we perform 3D local hydrodynamic simulations of atmospheric escape in close-in exoplanets, including the interaction with the stellar wind. We vary the strength of the stellar wind to investigate the effects it has on confining the outflowing atmosphere and on the atmospheric escape rate. We chose two exoplanetary systems (shown in Fig. 1, similar to HD209458b but orbiting a more active star and GJ3470b) to represent typical close-in gas giants. The details of our 3D model are discussed in Section 2.2, with the results of these models presented in Section 3. We compute the synthetic observations in Ly α transits in Section 4, and we show that properly accounting for the presence of the stellar wind can affect the interpretation of spectroscopic transits. In particular, not including the stellar wind interaction can lead to an underestimation of atmospheric escape rates detected. A discussion of our results is shown in Section 5 and we present our conclusions in Section 6.

2 3D MODELLING OF THE INTERACTION BETWEEN THE STELLAR WIND AND PLANETARY ATMOSPHERIC ESCAPE

To model the interaction between the stellar wind and the escaping atmosphere, we use two numerical setups. First, we run 1D radiation hydrodynamic simulations to simulate the photoevaporation of the planetary atmosphere. This yields an escape rate and velocity structure for a given atmosphere. These are then used to inform our 3D isothermal simulations, constraining the two free parameters: the base density and temperature of the outflowing atmosphere. Below, we detail our 1D radiation hydrodynamic model and 3D hydrodynamic model.

2.1 1D model

Here, we briefly present the main characteristics of our 1D radiation hydrodynamics calculation, and refer the reader to Allan & Vidotto (2019) or Murray-Clay, Chiang & Murray (2009) for further details. This model treats the escaping atmosphere as a fluid. As well as the standard conservation of mass and momentum equations (discussed in Section 2.2), this model solves an energy equation that contains additional heating/cooling terms to consider heating from photoionization and Ly α cooling (in the 1D model, we do not include the Coriolis effect, and set $\gamma = 5/3$). This model also solves an equation of ionization balance:

$$\frac{n_n F_{\text{EUV}} e^{-\tau} \sigma_{\text{v}_0}}{e_{\text{in}}} = n_p^2 \alpha_{\text{rec}} + \frac{1}{r^2} \frac{d}{dr} (r^2 n_p u), \quad (1)$$

where n_n and n_p are the number densities of neutral and ionized hydrogen, F_{EUV} is the EUV flux received by the planet, τ is the optical depth to ionizing photons, σ_{v_0} is the cross-section for the ionization of hydrogen, and α_{rec} is the radiative recombination coefficient of hydrogen ions. This model assumes that the incoming EUV flux is concentrated at an energy of $e_{\text{in}} = 20$ eV (Murray-Clay et al. 2009).

This model takes the planetary parameters (Table 1) as input, as well as the EUV flux from the host star: For the hot Jupiter (HJ), we used $L_{\text{EUV, HJ}} = 2.06 \times 10^{-5} L_{\odot}$, (chosen to be 25 times larger than that assumed in Murray-Clay et al. 2009) and for the warm Neptune (WN), we used $L_{\text{EUV, WN}} = 3.73 \times 10^{-6} L_{\odot}$ (Bourrier et al. 2018). As a result, this yields an escape rate, as well as the velocity and ionization fraction ($f_{\text{ion}} = n_p/(n_p + n_n)$) as a function of distance. With this information, we can constrain the two free parameters of the 3D isothermal model: the base density and temperature at the

Table 1. The planet and stellar properties in each set of models.

Planet	M_p (M_{Jup})	r_p (R_{Jup})	a (AU)	\dot{m}_0 (10^{10} g s^{-1})	u_{kep} (km s^{-1})	T_p (10^4 K)	$n_{0,p}$ (10^9 cm^{-3})	M_* (M_{\odot})	R_* (R_{\odot})	T_* (10^6 K)	u_{local} (km s^{-1})	$F_{\text{EUV}}(a)$ ($\text{erg cm}^{-2} \text{ s}^{-1}$)
HJ	0.7	1.4	0.050	58	147	1	3.86	1.00	1.00	2	400	1.12×10^4
WN	0.04	0.41	0.036	6.5	116	0.5	3.03	0.54	0.55	1	240	3.92×10^3

Notes. M_p and r_p describe the planet's mass and radius; a is the orbital distance; \dot{m}_0 is the planetary atmospheric escape rate (with no stellar wind); u_{kep} is the Keplerian velocity of the system; T_p and $n_{0,p}$ are the temperature and base density of the planet's outflowing atmosphere in the 3D model that were found to best match the results of the 1D model; M_* , R_* , and T_* describe the stellar mass, radius, and stellar wind temperature, respectively, while the stellar wind radial velocity at each planet's orbital distance is given as u_{local} . Finally, $F_{\text{EUV}}(a)$ is the EUV flux at the planet's orbital distance.

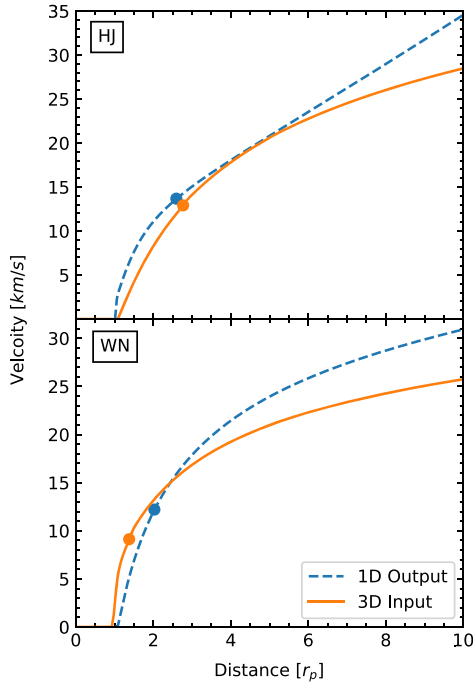


Figure 2. Velocity versus distance for the escaping atmosphere of both of our models. The dashed blue line shows the output of the 1D model, while the solid orange line shows the initial condition we implement in our isothermal 3D model. The base density in the 3D model is then adjusted so that the same escape rate is obtained in both the 1D and 3D models. The circles mark the position of the sonic point in each model.

planetary radius (inner boundary). A unique temperature is chosen such that the velocity structure in 3D best matches the velocity structure from the 1D model, seen in Fig. 2. Similarly, the base density in the 3D simulations is adjusted, so that it and the matched velocity structure reproduce the escape rates resultant from the 1D model (\dot{m}_0 in Table 1). By matching the velocity structure and escape rate, we ensure that the ram pressure of the escaping atmospheres in our 3D simulations without a stellar wind is close to that of the 1D model. We can then inject a stellar wind to examine the interaction between the stellar and planetary outflows, having vastly saved computational time by informing our 3D model with the 1D model.

2.2 Setup of our 3D models

To investigate the effects of the stellar wind on the reduction of atmospheric escape rates, we simulate the environments around close-in exoplanets using the Space Weather Modelling Framework (SWMF; Tóth et al. 2005). SWMF has previously been used to study, e.g. various Solar system objects (Sternberg et al. 2011; Ma et al. 2013; Jia et al. 2015; Jia & Kivelson 2016; Carolan et al. 2019), the solar wind (e.g. Manchester et al. 2004; van der Holst et al. 2011), and stellar winds (e.g. Vidotto et al. 2018; Kavanagh et al. 2019). For our investigation, we create a new user implementation to SWMF. This involves the design of new inner and outer boundary conditions, and additional source terms in the hydrodynamic equations, all of which are outlined below.

We model the stellar wind and escaping atmosphere as isothermal winds (Parker 1958), we do not include the effects of magnetic fields (this will be the topic of a future study), and consider only hydrogen in our simulations. There are two unknowns in the Parker wind model, the base density and temperature. To guide the selection of temperature and density of the planetary outflow, we use information from our 1D model (Allan & Vidotto 2019, see Section 2.1). For the stellar winds, we chose temperatures appropriate for stars hosting close-in exoplanets (see Table 1), and vary the base density to control the stellar mass-loss rate.

Our 3D simulations are Cartesian and solve for five parameters in the corotating frame: the mass density (ρ), velocity (u_x , u_y , u_z), and thermal pressure (P_T). These are found through iteratively solving a set of ideal hydrodynamic equations that includes the mass conservation equation

$$\frac{\partial \rho}{\partial t} + \nabla \cdot (\rho \vec{u}) = 0, \quad (2)$$

the momentum conservation equation

$$\frac{\partial(\rho \vec{u})}{\partial t} + \nabla \cdot [\rho \vec{u} \vec{u} + P_T I] = \rho \left(\vec{g} - \frac{GM_*}{(r-a)^2} \hat{R} - \vec{\Omega} \times (\vec{\Omega} \times \vec{R}) - 2(\vec{\Omega} \times \vec{u}) \right), \quad (3)$$

and energy conservation equation

$$\frac{\partial \epsilon}{\partial t} + \nabla \cdot [\vec{u}(\epsilon + P_T)] = \rho \left(\vec{g} - \frac{GM_*}{(r-a)^2} \hat{R} - \vec{\Omega} \times (\vec{\Omega} \times \vec{R}) \right) \cdot \vec{u}, \quad (4)$$

where I is the identity matrix, \vec{g} the acceleration due to the planet's gravity, G the gravitational constant, and M_* is the mass of the star. \vec{r} is the position vector relative to the planet, \vec{a} the position of the star relative to the planet, $\vec{\Omega}$ the orbital rotation rate, and \vec{R} is the position vector relative to the star, as shown in Fig. 3. The total energy density ϵ is given by

$$\epsilon = \frac{\rho u^2}{2} + \frac{P_T}{\gamma - 1}. \quad (5)$$

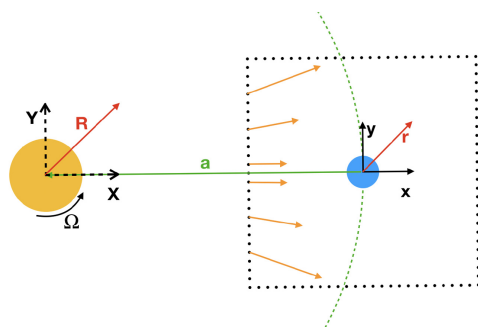


Figure 3. The coordinate system used in our simulations (not to scale). The orange circle represents the star, while the blue shows the planet. The uppercase letters show the direction of vectors in the stellar system, while the lowercase letters show the axes in the planetary system. The black dotted square represents our computational grid, while the green dashed line shows the path of the planet’s orbit. The orange arrows represent the changing direction and magnitude of the stellar wind velocity as it enters the simulation grid. Note that, because of the close distance to the star, we can not assume that the stellar wind has a plane-parallel injection, as is usually assumed in simulations of planets that orbit far from their host stars (e.g. Carolan et al. 2019).

where the thermal pressure is $P_T = \rho k_B T / (\mu m_p)$, where k_B is the Boltzmann constant, μ is the mean mass per particle, and m_p is the mass of the proton. Given that our calculations are done in the non-inertial frame, where the planet is fixed at the origin, we include the non-inertial forces in the hydrodynamic equations as source terms. These terms are shown in the right-hand side of equations (3) and (4), and they are the Coriolis force ($-2\rho(\vec{\Omega} \times \vec{u})$), the centrifugal force, and stellar gravity that combined give rise to the ‘tidal force’ ($-\rho(GM_*/(r-a)^2)\hat{R} - \rho\vec{\Omega} \times (\vec{\Omega} \times \vec{R})$).

Our simulations model the isothermal flow of ionized hydrogen around the planet, similar to the work of Bisikalo et al. (2013) and Carroll-Nellenback et al. (2017). To achieve this, we set the mean mass per particle $\mu = 0.5m_p$ and the polytropic index $\gamma \simeq 1$, which ensures a constant temperature in the outflow. The exoplanet is placed at the origin of a rectangular grid ($x, y = [-50, 50r_p]$, $z = [-32, 32r_p]$), where r_p is the radius of the planet) as seen in Figs 3 and 4. For simplicity, we chose the planet to be tidally locked to the star, such that the star is always located at negative x , while the planet orbits in the positive y -direction. z constructs the right-handed system. This approach is justified, given that many close-in exoplanets are thought to be tidally locked to their host star (Kasting, Whitmire & Reynolds 1993; Edson et al. 2011). Our simulations contain 16 million cells and have a minimum cell size of $1/16r_p$ within a radius of $5r_p$, which gradually decreases towards the edge of the grid. We found increasing the maximum resolution of these simulations showed no significant change in the results.

The inner boundary is placed at the surface of the planet ($r = 1r_p$), where we keep the base density $n_{0,p}$ and temperature T_p of the escaping atmosphere fixed throughout the simulations. The base values adopted for each of the modelled planets are shown in Table 1. These values give rise to an escape rate \dot{m}_0 , which matches that found in the 1D model. Finally, we assume the velocity of the outflow to be reflective in the non-inertial frame, effectively setting the inner velocity to $\simeq 0$.

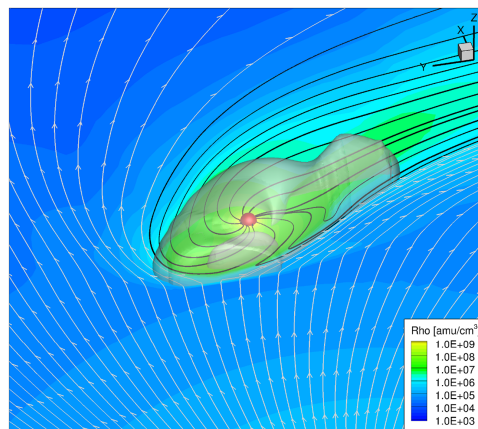


Figure 4. A 3D view of the HJ model for a stellar mass-loss rate of $10 \dot{M}_\odot$. The colour shows the density in the orbital plane. The grey surface marks the sonic surface around the planet. The grey streamlines show the flow of the stellar wind in the grid, while the black lines trace the escaping atmosphere of the planet.

The simulation box has six outer boundaries, one for each face of the rectangular grid. The stellar wind is injected to the grid at the negative x boundary. The physical properties of the stellar wind are found by modelling an isothermal 1D stellar wind model at a given temperature T_* (Parker 1958). The mass-loss rate (\dot{M}) is a free parameter of the stellar wind model, that we vary in our study to change the strength of the incoming stellar wind. For a given \dot{M} and T_* , the 1D solution provides the velocity and density of the stellar wind at every point on the face of the negative x boundary. We orient the stellar wind to flow radially away from the star, but as it is injected in the simulation domain, we account for the Coriolis velocity ($-\vec{\Omega} \times \vec{R}$) to convert into the planet’s reference frame. On all remaining faces of our rectangular grid, we use an inflow limiting boundary condition, similar to McCann et al. (2019). This means that the outer boundary applies normal floating boundary conditions to cells where the velocity is directed outward, but set the momenta to 0 if the velocity component is directed inward. This is necessary as the Coriolis force can bend the flow of material close to the outer boundaries, such that uncontrolled inflows are generated when normal floating outflow conditions are applied. This can cause numerical issues such that no steady-state solution is attainable, especially in smaller computational grids. The inflow limiting condition prevent this, ensuring that only the stellar wind is being injected into our grid.

3 SIMULATIONS OF REDUCED ATMOSPHERIC ESCAPE IN CLOSE-IN PLANETS

Using this computational setup, we model two exoplanets for a range of stellar wind conditions: an HJ similar to HD209458b but orbiting a more active solar-like star (labelled ‘HJ’); and a WN similar to GJ3470b (labelled ‘WN’) that orbits an M dwarf. The relevant parameters used in the HJ and WN models are also provided in Table 1.

For each planet, we compute 13 and 14 models, respectively, increasing the stellar wind mass-loss rate from 0 to 100 times the

solar mass-loss rate ($\dot{M}_\odot = 2 \times 10^{-14} M_\odot \text{ yr}^{-1}$). Given that it is difficult to measure the winds of cool dwarf stars, we chose this large range of stellar mass-loss rates to establish if and when neglecting the presence of the stellar wind as a contributing factor to signatures of atmospheric escape is appropriate. We note that this can only be achieved in multidimensional studies, as 1D models cannot account for the presence of a stellar wind. We chose to keep the temperatures of the isothermal stellar wind constant in each set ($T_{*,\text{HJ}} = 2 \times 10^6 \text{ K}$, $T_{*,\text{WN}} = 1 \times 10^6 \text{ K}$), retaining the same stellar wind velocity structure within each set of models. Varying the mass-loss rate, therefore, solely changes the stellar wind density. This setup allows us to investigate the effect that gradually increasing the stellar wind ram pressure ($\propto \dot{M} u_{\text{local}}$, where \dot{M} is the stellar wind mass-loss rate, and u_{local} is the velocity of the stellar wind at the planet's orbit) has on the planet's escaping atmosphere. The density structure and velocity flow in the orbital plane of three models from each set are shown in Fig. 5. As we increase the stellar wind mass-loss rate, we see the transition from type 2/'weak' to the type 1/'strong' scenarios shown by Matsakos et al. (2015) and McCann et al. (2019), respectively.

In the left-hand panels of Fig. 5, we can see a large sonic surface created when the supersonic stellar wind is shocked as it meets the supersonic planetary outflow. As the ram pressure of the stellar wind increases, this interaction happens closer to the planet. This confinement eventually affects the sonic surface of the escaping atmosphere, as seen in the changing white contour close to the planet from the left- to right-hand panels in Fig. 5. The inner circular sonic surfaces in the left-hand panels are unaffected (labelled 'closed'). In the right-hand panels, the stellar wind has confined the outflow such that the sonic surface has been altered on all sides of the planet (labelled 'open'). The middle panels show the transition between these two states, where the dayside sonic surface has changed, while the nightside surface remains largely unaffected.¹ Note that the inner sonic surface of the WN planet is at $1.1r_p$. Published models (e.g. Villarreal D'Angelo, submitted) of GJ436b, also a WN, have shown that the $M = 1$ transition occurs farther out, where M is the mach number. The low position of the sonic point in our 3D models is due to our choice of temperature (see Fig. 2). We will come back to how a larger sonic surface would change our results when we further discuss the limitations of our model in Section 5.2.

Previous models have shown that stellar wind confinement can affect the escape rate of the planets atmosphere (Christie et al. 2016; Vidotto & Cleary 2020). To investigate the difference in escape rate between our closed and open 3D models, we integrate the mass flux through concentric spheres around the planet, obtaining the atmospheric escape rate:

$$\dot{m} = \oint_A \rho \vec{u} \cdot d\vec{A}. \quad (6)$$

Table 2 shows a summary of the results of our simulations. The escape rate from each model is plotted in Fig. 6. Due to resolution, the escape rate can show small variations with distance from the planet, especially at the point where the stellar wind and escaping atmosphere meet. This small variation is quantified by the blue error bars in Fig. 6, which show 1 standard deviation from the mean

¹The additional $M = 1$ transition in fig. 5 is due to the fact that both the stellar and planetary winds are supersonic. As a result, there are two shocks, one outer 'bow shock' where the stellar wind is shocked, and an inner 'termination shock' where the supersonic escaping atmosphere is shocked. This is similar to what is shown in models of the interaction between the heliosphere and the ISM (eg. Zank & Müller 2003), where, instead, it is the inner stellar wind and outer ISM forming two shockwaves.

escape rate in each model. Some models only reach a quasi-steady-state solution, showing small periodic variability with increasing time-step. For these models, the maximum deviation is shown as a red error bar, while the average deviation over one period of the quasi-steady-state variability is shown in blue. In both model sets, increasing the stellar wind mass-loss rate has reduced the atmospheric escape rate. For the HJ models, the escape rate has been reduced by 65 per cent (from 5.8×10^{11} to $2.1 \times 10^{11} \text{ g s}^{-1}$, see Table 2). The WN models show a more gradual change, with a maximum reduction of 40 per cent (from 6.5×10^{10} to $3.9 \times 10^{10} \text{ g s}^{-1}$) over the range of stellar winds examined.

As the stellar wind mass-loss rate increases, the escaping atmosphere is confined to a reduced volume around the planet, which is clearly visible from the velocity streamlines in Fig. 5 (left to right). This decelerates material on the dayside of the planet, redirecting it towards the planetary tail as seen in Fig. 5. As the flow of the escaping atmosphere is further confined, this deceleration occurs closer to the planet, where it eventually inhibits the dayside flow from reaching supersonic speeds. As a result, the atmospheric escape rate is gradually reduced as the flow's sonic surface is further disrupted.

This change in escape rate occurs more suddenly in the HJ models than in the WN models as \dot{M} is increased. We propose this is related to the distance of the sonic point. In the closed HJ and WN models, these are approximately $2.5r_p$ and $1.1r_p$, respectively. As a result, the outflow in the WN models must be confined relatively closer to the planet in order for the sonic surface to be affected. This results in a more gradual reduction of atmospheric escape in the WN models, as a stronger stellar wind is required to further confine this outflow and open the sonic surface. In the HJ models, this is not the case. The change from closed to open geometries happens over a much shorter range of \dot{M} , as the sonic surface is relatively further from the planet, and so can be more easily accessed by the stellar wind.

4 SYNTHETIC OBSERVATIONS: REDUCED $\text{Ly } \alpha$ TRANSIT DEPTH BY STELLAR WIND CONFINEMENT

We use a ray-tracing model to simulate the $\text{Ly } \alpha$ line profile of each planet at mid transit. A full description of this model is outlined in Vidotto et al. (2018) and Allan & Vidotto (2019). We further adapt this model to take our 3D grids as input. Given that the ray tracing model is constructed for an equally spaced grid and calculations are done in the inertial reference frame, we interpolate our non-uniform 3D grid to contain 201 points equally spaced in each dimension, describing the density, temperature, and line-of-sight velocity of the planetary material in the (observer's) inertial frame. Given that the stellar wind and the planetary outflow have very different temperatures, we separate planetary from stellar wind material by means of a temperature cutoff. To ensure we capture all the material escaping the planet, we use a temperature cutoff that is slightly higher than the temperature of the planetary outflow, ensuring that all the planetary material capable of absorbing in $\text{Ly } \alpha$ is considered when producing the synthetic observations. Our current 3D model does not treat both the neutral and ionized portions of the planetary outflow; it simulates purely the ionized part ($\mu = 0.5$). Therefore, we estimate the neutral hydrogen density (n_n) from the ionization balance equation solved self-consistently in the 1D escape model from Allan & Vidotto (2019), which tracks both the neutral and ionized density, as outlined in Section 2.1. Our 3D model yields the density of ionized hydrogen (n_p), which can be used with the ionization fraction from the 1D model (f_{ion}) to find the neutral density

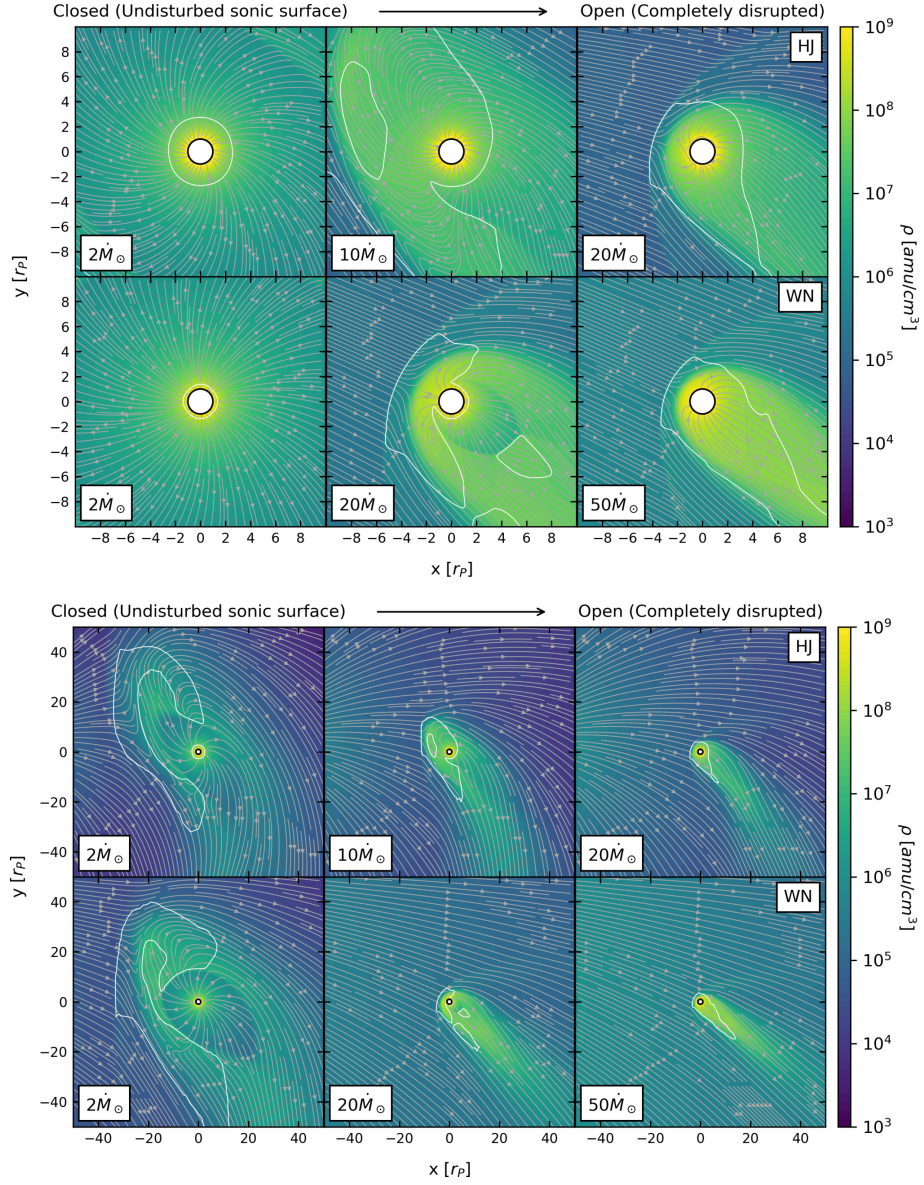


Figure 5. Top panels: the orbital slice of three HJ (HJ, top panels) and three WN (WN, bottom panels) models, chosen to illustrate transition from ‘closed’ to ‘open’ sonic surfaces for each planet. ‘Closed’ refers to the scenarios where the inner (circular) sonic surface around the planet is not disturbed by the stellar wind. Contrary to that, ‘open’ refers to the scenarios where this surface is disrupted. The planet is orbiting in the positive y-direction, with the star at negative x. The colour shows the distribution of density around the planets, while the white contour marks a Mach number of 1, which shows the sonic surface around each planet. The streamlines trace the velocity of material in each model, in the planet’s reference frame. Bottom panels: a zoomed-out version of this figure, showing the orbital plane from our grids. Here we can more clearly see the injection of the stellar wind from the negative x side of our grid, as well as the extension of material both ahead and behind the planet’s orbit.

Table 2. Summary of our simulation results.

\dot{M} (HJ) (\dot{M}_\odot)	\dot{m}^{HJ} (10^{10} g s^{-1})	ΔF^{HJ} (per cent)	\dot{M} (WN) ($\dot{M}_\odot \text{ yr}^{-1}$)	\dot{m}^{WN} (10^{10} g s^{-1})	ΔF^{WN} (per cent)
0	58	20.7	0	6.5	8.8
2	56	12.0	1	6.6	7.3
4	55	8.6	2	6.4	5.3
6	55	6.9	4	6.5	4.0
8	57	6.4	10	6.4	3.7
10	51	6.0	15	6.4	3.7
12	40	5.9	20	6.5	3.7
14	37	5.8	25	6.4	3.7
16	35	5.8	30	6.2	3.6
20	30	5.5	35	6.0	3.5
30	27	5.1	40	5.8	3.4
60	22	4.2	50	5.4	3.2
100	21	3.9	75	4.6	2.8
–	–	–	100	3.9	2.4

Notes. The stellar wind mass-loss rate (\dot{M}) is varied in each simulation, affecting the planetary atmospheric escape rate \dot{m} and Ly α absorption at mid-transit computed in the blue [–300 to –40 km s^{–1}] plus red [40 to 300 km s^{–1}] wings (including the broad-band absorption due to the planetary disc). Here, the superscripts HJ and WN refer to the hot Jupiter and warm Neptune cases, respectively.

as follows:

$$n_n = n_p \frac{1 - f_{\text{ion}}}{f_{\text{ion}}}. \quad (7)$$

Although this is not the most precise approach to calculate the neutral hydrogen density, this post-processing technique is a work-around adopted when the ionization balance equation is not solved self-consistently with the hydrodynamics equations (similar approach has been used by Oklopčić & Hirata (2018) when calculating the population levels of helium, and by Lampón et al. (2020) when modelling helium in HD209458b’s atmosphere). One limitation of this approach is that the 1D model computes the ionization fraction along the star–planet line. Therefore, when we incorporate the ionization fraction predicted in the 1D models in our 3D grid, the density of neutral material in the night side, or planetary tail, is not properly calculated. However, given that the inner regions of our 3D simulations are approximately spherically symmetric and contain most of the absorbing material, using the resultant ion fraction from the 1D model is an acceptable approximation for computing the synthetic observations.

Once the neutral density is estimated, the frequency ν -dependent optical depth along the line of sight is given by

$$\tau_\nu = \int n_n \sigma \phi_\nu dx, \quad (8)$$

where the observer is placed at positive x , and ϕ_ν is the Voigt line profile function. The absorption cross-section at line centre is $\sigma = \pi e^2 f / (m_e c)$, where $f = 0.416410$ is the oscillator strength for Ly α , m_e is the mass of the electron, e is the electron charge, and c is the speed of light. Using these, the fraction of transmitted intensity is given by

$$\frac{I_\nu}{I_*} = e^{-\tau_\nu}. \quad (9)$$

Therefore, $1 - I_\nu/I_*$ represents the fraction of intensity that is absorbed by the planet’s disc and atmosphere. We shoot 201×201 stellar rays through the grid. Integrating over all rays, and dividing by the flux of the star allows for the frequency-dependent transit depth

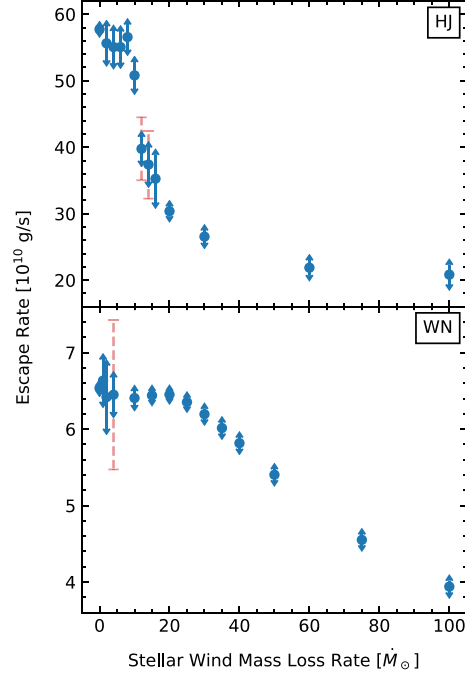


Figure 6. The variation of atmospheric escape rate with stellar mass-loss rate for each of our models. The points mark the mean escape rate, while the blue error bars illustrate 1 standard deviation from the mean. As some models reach a quasi-steady-state solution, the average over several time-steps is taken, and plotted in blue. For these models, the standard deviation at a single time-step is shown in red.

(ΔF_ν) to be calculated:

$$\Delta F_\nu = \frac{\int \int (1 - e^{-\tau_\nu}) dy dz}{\pi R_*^2}. \quad (10)$$

For each of the models in the HJ and WN set, the transit depth as a function of velocity is shown in Fig. 7, and the integrated percentage absorption is given in Table 2. As the Ly α line centre is dominated by interstellar absorption and geocoronal emission, we omit the line centre [–40, 40] km s^{–1} from these plots. In both model sets, the maximum transit depth decreases as the planetary outflow is further confined. This is due to the volume of absorbing planetary material around the planet decreasing as the escaping atmosphere is confined.

For most models, there is an obvious asymmetry in the line profile, with the blue wing showing more absorption than the red. In the low \dot{M} models, there is significant dayside (redshifted) outflow towards the star, similar to that seen by Matsakos et al. (2015) in their type 2 interaction, and in the ‘weak’ stellar wind scenarios of McCann et al. (2019). As \dot{M} increases, this dayside stream is suppressed completely, as seen in Fig. 5. What remains is the planetary tail, containing mostly blueshifted material (type 1 in Matsakos et al. 2015; ‘strong’ stellar wind in McCann et al. 2019), leading to the line profile asymmetry we see in Fig. 7.

We quantify this asymmetry by integrating the modelled transit line profiles in Fig. 7 over velocity in the blue [–300, –40 km s^{–1}]

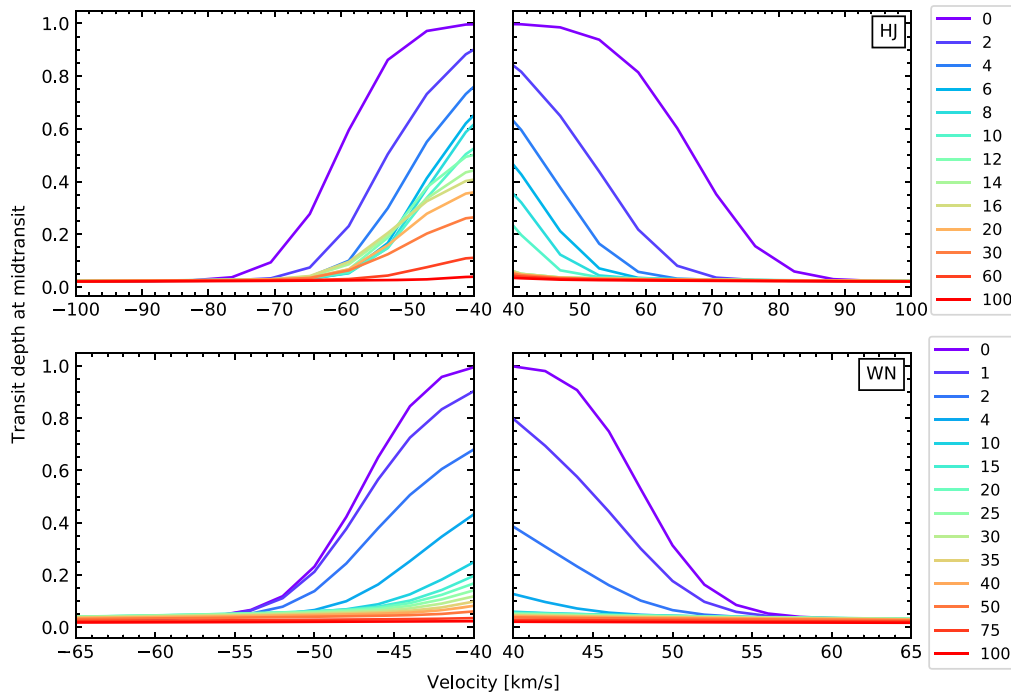


Figure 7. The blue (left-hand panels) and red (right-hand panels) wings of the in-transit Ly α line profile (equation 10) for each of our HJ (top panels) and WN (bottom panels) models. The colour shows the variation of stellar mass-loss rate from 0 to 100 M_{\odot} . As the line centre is contaminated by interstellar absorption and geocoronal emission, we ignore the velocity range of -40 to 40 km s^{-1} . Note how the transit absorption is larger in the red wing for low stellar \dot{M} and larger in the blue wing for high stellar \dot{M} .

and red [$40, 300$ km s^{-1}] wings. Note that our 3D model does not consider energetic neutral atoms (ENAs), and so the effect of these in the transit line profiles are not reflected in these calculations. For more discussion on this see Section 5.2. The results of this are shown in Fig. 8. Note that even in the case with no stellar wind the line shows asymmetry due to the orbital motion and tidal forces. We can clearly see that in both models, at low stellar mass-loss rates, the absorption in the red wing dominates due to the significant dayside stream as mentioned above. As the stellar mass-loss rate is increased, the absorption in the blue wing begins to dominate as this dayside flow is further confined. This is a more sudden change in the WN model than with the HJ planet, as the HJ planet has a stronger outflow/higher escape rate. For both models, the level of asymmetry is approximately constant within a certain range of stellar mass-loss rates. For the HJ models, the blue wing absorbs 1–2 per cent more than the red from models between 10 and 30 M_{\odot} . The WN models absorb roughly 0.25 per cent more in the blue between 10 and 40 M_{\odot} . Above these ranges, the difference in absorption between the blue and red wing gradually decreases as the outflow becomes significantly more confined. For stellar wind mass-loss rates $< 10 M_{\odot}$, despite the percentage absorption of each wing changing significantly (approximately 10 per cent in the HJ, 3 per cent in WN), the atmospheric escape rate has not been affected as seen by the values on Figs 8 and 9. As mentioned in Section 3, the stellar wind further confines the escaping planetary material, which,

in turn, shapes the absorbing material around the planet. However, for low stellar mass-loss rates, the sonic surface of the atmospheric outflow is not yet affected, thus the escape rate remains unchanged.

We further investigate the total absorption (blue + red) relationship with the atmospheric escape rate in Fig. 9. The filled and open circles represent the results for the HJ and WN models, respectively. The stellar wind mass-loss rate is increased from the right to left points, with the right-most point in each set being the one without the presence of a stellar wind (marked with an x). For each set of models, we see a region of our parameter space where, although the planetary escape rate is constant (marked with dotted lines), the transit absorption is not. As mentioned previously, this is due to stellar wind confinement, whereby the increasing ram pressure of the stellar wind confines absorbing material closer to the planet, therefore covering a decreased region on the stellar disc (Vidotto & Cleary 2020). In the HJ model set, a constant planetary escape rate of approximately $\dot{m}_{\text{HJ}} \simeq 5.5 \times 10^{11}$ g s^{-1} produces 6–21 per cent absorption, depending on the stellar wind condition. For the WN planet, a constant planetary escape rate of $\dot{m}_{\text{WN}} \simeq 6.5 \times 10^{10}$ g s^{-1} produces 4–9 per cent absorption. This reflects what is seen in Fig. 8, where the absorption of each wing has changed significantly, but the escape rate has not. As previously discussed in Section 3, in the models showing absorption within the quoted ranges, the sonic surface remains intact (our ‘closed’ scenario), so the escape rate is unaffected by the changing stellar wind. Above a mass-loss rate of

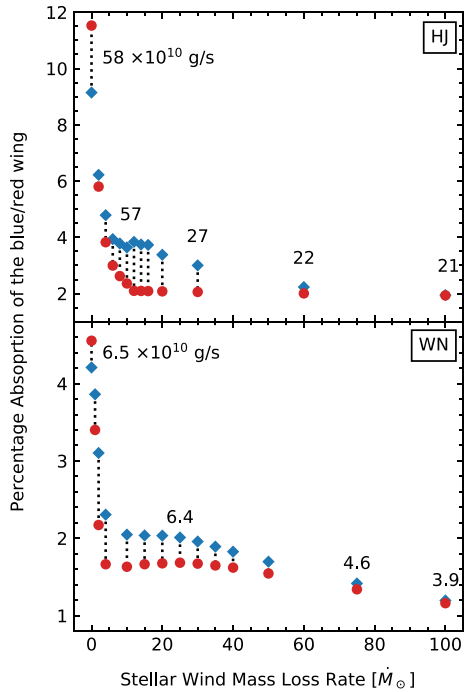


Figure 8. The percentage absorption in the blue (blue diamonds, -300 to -40 km s^{-1}) and red (red circles, 40 to 300 km s^{-1}) wings of $\text{Ly}\alpha$ line as the stellar wind mass-loss rate is increased. The dotted line links points from the same model. The top panel shows the results for the HJ model, while the bottom panel shows the WN models. At various points, the atmospheric escape rate of the planet is marked in units of 10^{10} g s^{-1} .

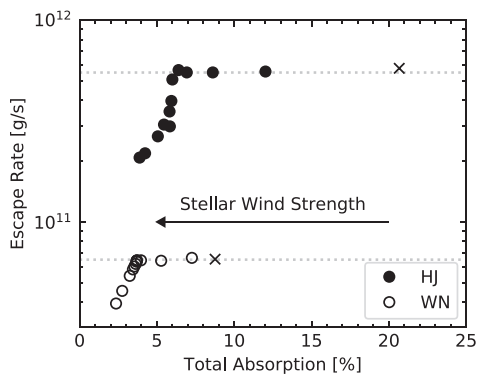


Figure 9. Atmospheric escape rate as a function of the percentage absorption of the blue+red wings of the $\text{Ly}\alpha$ line at mid-transit. The filled and open circles represent the HJ and WN models, respectively. For each set of models, we see a region where, although the escape rate is constant (marked with dotted lines), the transit absorption is not. The points marked with x are the models of each planet with no stellar wind, and from the right- to left-hand side, the stellar wind strength is increases (marked with an arrow).

$10 \dot{M}_\odot$ (or $20 \dot{M}_\odot$ for the WN model), i.e. below an absorption of approximately 6 per cent for the HJ models (or 4 per cent for the WN models), the stellar wind begins to open the sonic surface, causing reduced atmospheric escape. In the range of WN models examined, the escape rate is reduced by approximately 40 per cent, from 6.5×10^{10} to 4×10^{10} g s^{-1} , changing the total absorption by about 7 per cent. For comparison, a similar 40 per cent reduction in the HJ set, say, from 5.8×10^{11} to 3.3×10^{11} g s^{-1} , in escape rate occurs over a 15 per cent range in total absorption.

5 DISCUSSION

5.1 Implications for interpreting $\text{Ly}\alpha$ signatures

The results presented in Section 4 emphasize the importance of considering the stellar wind when interpreting transit observations. For example, suppose that a planet similar to our HJ model is observed with 5.5 per cent of absorption in the $\text{Ly}\alpha$ line. In the presence of a stellar wind, we would interpret this observational result as being caused by a planetary outflow that has an intrinsic escape rate of $\sim 3 \times 10^{11}$ g s^{-1} (see Fig. 9). However, had we not considered the presence of a stellar wind, we would have predicted a lower planetary escape rate to be able to reproduce this 5.5 per cent observed transit absorption. This is because, without stellar wind confinement, the absorbing material can now occupy a greater volume around the planet, yielding the same percentage absorption for a lower escape rate. Therefore, given the degeneracy between planetary escape rates and stellar wind strengths for a same percentage absorption, we suggest that, in order to make a more accurate estimate of a planet's atmospheric escape rate, one should also consider the presence of a stellar wind.

Another consequence found in our study is that the stellar wind confinement can act to mask observational signatures of atmospheric escape in $\text{Ly}\alpha$. One instance of this could be with the sub-Neptune π Men c. The surprising lack of detection of $\text{Ly}\alpha$ absorption led García Muñoz et al. (2020) to suggest a lack of hydrogen in the atmosphere of π Men c. If this is indeed the case, they proposed that further observations of heavier elements, such as O I and C II lines, could still reveal high atmospheric evaporation rate. An alternate explanation was proposed by Vidotto & Cleary (2020), who suggested that the atmosphere of π Men c could be hydrogen-rich, but would remain undetected if a significant reduction in escape was being caused by the stellar wind. They proposed that this could take place in π Men c as they found that the stellar wind interaction happened in the subsonic part of the planetary outflow.

As we showed here, the position where the interaction happens depends on the strength of the stellar wind and on the properties of the escaping atmosphere. One important parameter in atmospheric modeling is the stellar high-energy flux that is deposited on the planet's atmosphere. In Vidotto & Cleary (2020), they assumed a flux of $1340 \text{ erg cm}^{-2} \text{ s}^{-1}$ and a stellar wind mass-loss rate of $1 \dot{M}_\odot$ for π Men c. To investigate this further, Shaikhislamov et al. (2020) performed 3D simulations of the stellar wind of π Men c and, using a similar stellar wind condition and high-energy flux than those assumed in Vidotto & Cleary (2020), confirmed that the interaction was taking place in the subsonic regime, but did not obtain a significant reduction in the escape rate of the planet (only a factor of 2.5 per cent of the value obtained in their other simulations). We believe such a simulation performed by Shaikhislamov et al. (2020) falls in our partially-open scenario (middle panels in Fig. 5).

Although we did not model the π Men system, in this work, we also found that the stellar wind might not necessarily lead to a significant reduction in escape rate, agreeing with Shaikhislamov et al. (2020). Nevertheless, when looking at the whole parameter space covered in our simulations, we found reduction in evaporation rates of up to 65 per cent for the HJ simulations and 40 per cent for the WN simulations. However, more importantly, we also found that this reduction is not linearly related to the depth of Ly α transits – even when the escape rate is not substantially reduced, the absorption signature of escaping atmosphere can be significantly affected. This is because the stellar wind confinement can change the volume of the absorbing material, without affecting too much the planetary escape rate.

5.2 Model limitations

The aim of this work was to study in a systematic way how the stellar wind could affect atmospheric escape rates and how this would be observed in synthetic transits. Our model is relatively fast to run – roughly, a simulation takes about 8 h to compute in 40 processors, although it could take longer in some cases. This enabled us to model nearly 30 different physical setups. However, our model can still be improved. For example, our 3D simulations model the flow of ionized hydrogen. They are isothermal and ignore the effects of magnetic fields, radiation pressure and charge exchange.

A caveat of the 3D isothermal model is that we cannot match both the ram pressure and sonic point found in the 1D model.² In this work, we chose to match the ram pressure of the escaping atmospheres, and as a result obtain sonic surfaces that are much closer to the planet than that predicted in the 1D model. To investigate how matching the sonic point would affect our results, we run one additional model of the WN planet in a 100- M_{\odot} stellar wind, ensuring that the sonic point remains at the same position as the 1D model, i.e. at $1.9r_p$. This was done by reducing the temperature of the outflow from 5000 to 3100 K, resulting in a sonic point that is further out, and a lower velocity outflow. We chose a base density such that escape rate for this model with no stellar wind matches that of the previous version, $6.5 \times 10^{10} \text{ g s}^{-1}$. When the 100- M_{\odot} stellar wind is injected into this model, we find that the atmospheric escape rate is reduced further than in the original, to $2.2 \times 10^{10} \text{ g s}^{-1}$ (previously $3.9 \times 10^{10} \text{ g s}^{-1}$). This confirms that the larger the sonic point distance, the easier a stellar wind can disrupt this surface, and a greater reduction in escape rate will be found. However, it also places importance on advancing our 3D model, as although we have now matched the sonic point, the ram pressure of the outflow is lower than found in the 1D model. This lower ram pressure provides less resistance against the incoming stellar wind, which when accompanied by the higher sonic point means the stellar wind can more easily disrupt the inner regions of the escaping atmosphere and affect the escape rate.

Carroll-Nellenback et al. (2017) showed using 3D hydrodynamics simulations that the sonic surface of the escaping atmosphere is significantly different when assuming an isotropic versus an anisotropic temperature distribution at the planetary boundary (their anisotropic model mimics a nightside of the planet). This obviously has implications on the atmospheric escape rate, with the anisotropic models of Carroll-Nellenback et al. (2017) showing an escape rate that was approximately 50 per cent lower compared to the isotropic models. Temperature differences arise naturally in 3D models that

solve for the radiative transfer of stellar photons through the planetary atmosphere (e.g. Debrecht et al. 2019). Although the day–night temperature differences are important to model, as they affect the planetary escape rate, we nevertheless expect that the hydrodynamic effects of the stellar wind on atmospheric escape is overall consistent to what we modeled here.

The presence of planetary magnetic fields, not included here, should also affect atmospheric escape. Owen & Adams (2014) demonstrated that magnetized exoplanets lose a factor of 4–8 less mass than unmagnetized planets. This is because only a fraction of magnetic field lines around the planet remains open, along which ionized flows can escape. Khodachenko et al. (2015) found that a dipolar magnetic field of 1G around a HD209458b-analogue planet was capable of reducing mass-loss by up to an order of magnitude. Additionally, in the case of a magnetized planet, the planetary magnetic field can deflect the stellar wind (e.g. Carolan et al. 2019), which might no longer directly access the upper atmosphere of the planet. There has been recent debate in the literature discussing whether a planet’s magnetic field can prevent atmospheric erosion or could increase atmospheric losses (Blackman & Tarduno 2018). On one hand, the stellar wind is believed to erode atmospheres of unmagnetized planets, as is believed was the case of the young Mars, which was embedded in a much stronger young solar wind (Kulikov et al. 2007). On the other hand, the similar present-day ion escape rates of Mars, Venus, and Earth have been used as counter-examples of planets that have very different magnetic field structures and yet present similar escape rates (Strangeway et al. 2010). There are still several unanswered questions on how the magnetic field of a close-in exoplanet could affect atmospheric escape and transit signatures.

Finally, our model neglects two physical processes, namely radiation pressure and charge exchange, both of which have been suggested to produce the population of neutral atoms that absorbs in the wing of Ly α at high blueshifted velocities ($\sim 100 \text{ km s}^{-1}$). Radiation pressure has been proposed to cause the acceleration of neutral hydrogen to speeds required to reproduce what is seen in Ly α transits (Bourrier, Ehrenreich & Lecavelier des Etangs 2015; Schneider et al. 2016). However, radiation pressure alone might not be as significant (Debrecht et al. 2020). Another alternative is that charge exchange processes could produce high-velocity neutral hydrogen (Holmström et al. 2008; Tremblin & Chiang 2013; Kislyakova et al. 2014; Bourrier et al. 2016; Shaikhislamov et al. 2016), with a combination of charge exchange and radiation pressure processes best explaining observations of HD209468b (Esquivel et al. 2019). Though both of these effects can yield more high-velocity hydrogen and thus affect the observational characteristics of the system, they are not thought to affect the inner regions of the escaping atmosphere. Charge exchange happens mostly around the shock, as one needs stellar wind protons interacting with neutrals from the planet’s atmosphere (Shaikhislamov et al. 2016). Radiation pressure could affect the outer layers of the planetary atmosphere, but gets absorbed as they penetrate the atmosphere (self-shielding). Due to this, they are unlikely to significantly change the hydrodynamics of the planetary outflow though may contribute to the obtained transit line profile (Cheremkov, Bisikalo & Kosovichev 2018). For these reasons, we do not expect them to contribute to the disruption of the sonic surface that we study with our models.

6 CONCLUSIONS

We have seen significant progress in modeling atmospheric escape in close-in planets over the past two decades (Lammer et al. 2003; Murray-Clay et al. 2009; Bourrier & Lecavelier des Etangs 2013;

²It is a coincidence that the sonic point in the HJ simulation is at a similar distance in the 1D and 3D models

Villarreal D'Angelo et al. 2018; Debrecht et al. 2020). However, many current models still neglect the interaction of the planet's upper atmosphere with the wind of the host stars. In particular, 1D hydrodynamic escape models are unable to treat the presence of the stellar wind – for that, multidimensional simulations are required. It has been demonstrated that the wind of the host star can affect atmospheric escape in exoplanets (Matsakos et al. 2015; Shaikhislamov et al. 2016; Villarreal D'Angelo et al. 2018; McCann et al. 2019; Vidotto & Cleary 2020). However, one of the open questions is currently for which systems the stellar wind would mostly affect atmospheric escape. One particular issue is that we do not have a full picture of how winds of cool dwarf stars vary from star to star. Cool dwarf stars are the most commonly known planet hosts, but their winds are difficult to probe, with only a few techniques currently providing stellar wind measurements (e.g. Wood et al. 2005; Fichtinger et al. 2017; Vidotto & Donati 2017; Jardine & Collier Cameron 2019).

In this work, we systematically examined the effects of stellar winds on planetary atmospheric escape to determine whether and when neglecting the presence of the stellar wind is justified. We used 3D hydrodynamic simulations to model the planetary outflowing atmosphere interacting with the stellar wind, which was injected in the simulation domain by means of an outer boundary condition. We performed this study on two different gas giant planets, an HJ similar to HD209458b but orbiting a more active star (HJ) and a WN similar to GJ3470b (WN), and varied the stellar wind mass-loss rate from 0 to $100 \dot{M}_{\odot}$, where $\dot{M}_{\odot} = 2 \times 10^{-14} M_{\odot} \text{ yr}^{-1}$ is the present-day solar mass-loss rate. In total, we performed nearly 30 3D hydrodynamics simulations of these systems.

For both planets, we found that as the stellar wind mass-loss rate was increased the planetary outflow was confined closer to the planet. As this confinement moved closer to the planet, planetary material could not properly accelerate, which eventually inhibited the dayside outflow from reaching supersonic speeds. The inner regions of the escaping atmosphere were then affected, causing a reduced escape rate. For the HJ planet, the escape rate was reduced from $5.8 \times 10^{11} \text{ g s}^{-1}$, when no stellar wind was considered, to $2.1 \times 10^{11} \text{ g s}^{-1}$, when a wind with $100 \dot{M}_{\odot}$ was considered. For the WN model, the planetary escape rates varied from 6.5×10^{10} (no stellar wind) to $3.9 \times 10^{10} \text{ g s}^{-1}$ (strongest wind).

This reduction happened more suddenly in the HJ models than in the WN models, which we proposed is related to the distance of the sonic point. As the stellar wind strength increases, the escaping atmosphere is confined closer to the planet. This eventually disturbs the sonic surface of the outflowing atmosphere, transitioning from a 'closed' to an 'open' sonic surface configuration as seen in Fig. 5. This is ultimately what reduces the escape rate of the planet's atmosphere, as the stellar wind now interacts with a subsonic planetary outflow and prevents an outflow from fully developing (Christie et al. 2016; Vidotto & Cleary 2020). As the sonic point in the HJ models is further from the planet, the stellar wind can more easily affect it, so we see the escape rate of the HJ planet change over a short range in \dot{M} . In the WN planet, the sonic surface is very close to the planet. The stellar wind must now confine the escaping atmosphere much closer to the planet for the sonic surface to be affected, which results in a much more gradually transition from 'closed' to 'open' sonic surfaces in these models.

Using a ray-tracing technique, we investigated the possible observational signatures of this escape rate reduction in Ly α transits. We found significant asymmetry towards the blue wing at mid-transit, which is to be expected when the dayside (redshifted) material is suppressed, and more material is funneled towards the planetary

comet-like tail. This happens in the cases with larger stellar wind mass-loss rates. In the scenarios where only a weak wind (or no wind) were considered, the absorption in the red wing of the Ly α line was larger, as some planetary material flows towards the star.

We also found that the changes caused in the atmospheric escape rate by the stellar wind affects Ly α transits in a non-linear way. Across our set of models, the escape rate of the HJ planet was reduced from by 65 per cent with the Ly α absorption changing from 20.7 to 3.9 per cent. For the WN planet, the escape rate was reduced by 40 per cent, with a corresponding change in Ly α absorption from 8.8 to 2.4 per cent. However above 14 per cent absorption in the HJ set (5 per cent in the WN set) despite the percentage absorption changing significantly the atmospheric escape rate does not. These models represent the 'closed' sonic surface models, where despite the volume of absorbing material changing, the sonic surface remains unaffected and so the escape rate does not vary. We concluded that the same atmospheric escape rate can therefore produce a range of absorptions depending on the strength of the stellar wind.

Neglecting the stellar wind when interpreting Ly α observations can also lead to underestimations of the planet's atmospheric escape rate. An unconfined escaping atmosphere can occupy a larger volume around the planet, and so a lower escape rate is required to produce significant absorption. Contrary to this, if the escaping atmosphere is confined by a strong stellar wind, a higher escape rate can produce the same absorption as the unconfined scenario, as the density of absorbing material increases. These degeneracies emphasize the importance of considering the stellar wind when interpreting transmission spectroscopic transits, in order to accurately estimate the atmospheric escape rate.

ACKNOWLEDGEMENTS

We thank the referee for their constructive review of this paper. This project has received funding from the European Research Council (ERC) under the European Union's Horizon 2020 research and innovation programme (grant agreement No. 817540, ASTROFLOW). The authors wish to acknowledge the SFI/HEA Irish Centre for High-End Computing (ICHEC) for the provision of computational facilities and support. This work used the BATS-R-US tools developed at the University of Michigan Center for Space Environment Modeling and made available through the NASA Community Coordinated Modeling Center. CVD acknowledge the funding from the Irish Research Council through the postdoctoral fellowship (Project ID: GOIPD/2018/659). Figure 1 has made use of the NASA Exoplanet Archive, which is operated by the California Institute of Technology, under contract with the National Aeronautics and Space Administration under the Exoplanet Exploration Program.

DATA AVAILABILITY

The data described in this paper will be shared on reasonable request to the corresponding author.

REFERENCES

- Allan A., Vidotto A. A., 2019, *MNRAS*, 490, 3760
 Baraffe I., Selsis F., Chabrier G., Barman T. S., Aillard F., Hauschildt P. H., Lammer H., 2004, *A&A*, 419, L13
 Beaugé C., Nesvorný D., 2013, *ApJ*, 763, 12
 Ben-Jaffel L., Ballester G. E., 2013, *A&A*, 553, A52
 Berger T. A., Huber D., Gaidos E., van Saders J. L., Weiss L. M., 2020, *AJ*, 160, 108

- Bisikalo D., Kaygorodov P., Ionov D., Shematovich V., Lammer H., Fossati L., 2013, *ApJ*, 764, 19
- Blackman E. G., Tarduno J. A., 2018, *MNRAS*, 481, 5146
- Bourrier V. et al., 2018, *A&A*, 620, A147
- Bourrier V., Lecavelier des Etangs A., 2013, *A&A*, 557, A124
- Bourrier V., Ehrenreich D., Lecavelier des Etangs A., 2015, *A&A*, 582, A65
- Bourrier V., Lecavelier des Etangs A., Ehrenreich D., Tanaka Y. A., Vidotto A. A., 2016, *A&A*, 591, A121
- Carolan S., Vidotto A. A., Loesch C., Coogan P., 2019, *MNRAS*, 489, 5784
- Carroll-Nellenback J., Frank A., Liu B., Quillen A. C., Blackman E. G., Dobbs-Dixon I., 2017, *MNRAS*, 466, 2458
- Cherenkov A. A., Bisikalo D. V., Kosovichev A. G., 2018, *MNRAS*, 475, 605
- Christie D., Arras P., Li Z.-Y., 2016, *ApJ*, 820, 3
- Debrecht A., Carroll-Nellenback J., Frank A., McCann J., Murray-Clay R., Blackman E. G., 2019, *MNRAS*, 483, 1481
- Debrecht A., Carroll-Nellenback J., Frank A., Blackman E. G., Fossati L., McCann J., Murray-Clay R., 2020, *MNRAS*, 493, 1292
- Dong C., Jin M., Lingam M., Airapetian V. S., Ma Y., van der Holst B., 2018, *Proc. Natl. Acad. Sci.*, 115, 260
- Edson A., Lee S., Bannon P., Kasting J. F., Pollard D., 2011, *Icarus*, 212, 1
- Ehrenreich D. et al., 2015, *Nature*, 522, 459
- Esquivel A., Schneider M., Villarreal D'Angelo C., Sgró M. A., Krapp L., 2019, *MNRAS*, 487, 5788
- Fichtinger B., Güdel M., Mutel R. L., Hallinan G., Gaidos E., Skinner S. L., Lynch C., Gayley K. G., 2017, *A&A*, 599, A127
- Fulton B. J. et al., 2017, *AJ*, 154, 109
- García Muñoz A., Youngblood A., Fossati L., Gandolfi D., Cabrera J., Rauer H., 2020, *ApJ*, 888, L21
- Holmström M., Ekenbäck A., Selsis F., Penz T., Lammer H., Wurz P., 2008, *Nature*, 451, 970
- Jardine M., Collier Cameron A., 2019, *MNRAS*, 482, 2853
- Jensen A. G., Redfield S., Endl M., Cochran W. D., Koesterke L., Barman T., 2012, *ApJ*, 751, 86
- Jia X., Kivelson M. G., 2016, *J. Geophys. Res.*, 121, 1413
- Jia X., Slavin J. A., Gombosi T. I., Daldorff L. K. S., Toth G., Holst B., 2015, *J. Geophys. Res.*, 120, 4763
- Johnstone C. P. et al., 2015, *ApJ*, 815, L12
- Kasting J. F., Whitmire D. P., Reynolds R. T., 1993, *Icarus*, 101, 108
- Kavanagh R. D. et al., 2019, *MNRAS*, 485, 4529
- Khodachenko M. L., Shaikhislamov I. F., Lammer H., Prokopov P. A., 2015, *ApJ*, 813, 50
- Khodachenko M. L., Shaikhislamov I. F., Lammer H., Berezutsky A. G., Miroshnichenko I. B., Rumenskikh M. S., Kislyakova K. G., Dwivedi N. K., 2019, *ApJ*, 885, 67
- Kislyakova K. G. et al., 2014, *A&A*, 562, A116
- Kubyskhina D., Vidotto A. A., Fossati L., Farrell E., 2020, *MNRAS*, 499, 77
- Kulikov Y. N., Lammer H., Lichtenegger H. I. M., Penz T., Breuer D., Spohn T., Lundin R., Biernat H. K., 2007, *Space Sci. Rev.*, 129, 207
- Kulow J. R., France K., Linsky J., Loyd R. O. P., 2014, *ApJ*, 786, 132
- Kurokawa H., Nakamoto T., 2014, *ApJ*, 783, 54
- Lammer H., Selsis F., Ribas I., Guinan E. F., Bauer S. J., Weiss W. W., 2003, *ApJ*, 598, L121
- Lampón M. et al., 2020, *A&A*, 636, A13
- Lecavelier Des Etangs A. et al., 2010, *A&A*, 514, A72
- Lecavelier des Etangs A. et al., 2012, *A&A*, 543, L4
- Lingam M., Loeb A., 2018, *Int. J. Astrobiol.*, 17, 116
- McCann J., Murray-Clay R. A., Kratter K., Krumholz M. R., 2019, *ApJ*, 873, 89
- Ma Y., Russell C. T., Nagy A. F., Toth G., Dong C., Bougher S. W., 2013, AGU Fall Meeting Abstracts, p. P13C-05
- Manchester W. B., Gombosi T. I., Roussev I., Ridley A., De Zeeuw D. L., Sokolov I. V., Powell K. G., Tóth G., 2004, *J. Geophys. Res.*, 109, 2107
- Matsakos T., Uribe A., Königl A., 2015, *A&A*, 578, A6
- Mazeh T., Holczer T., Faigler S., 2016, *A&A*, 589, A75
- Murray-Clay R. A., Chiang E. I., Murray N., 2009, *ApJ*, 693, 23
- Oklopčić A., Hirata C. M., 2018, *ApJ*, 855, L11
- Owen J. E., Adams F. C., 2014, *MNRAS*, 444, 3761
- Owen J. E., Lai D., 2018, *MNRAS*, 479, 5012
- Parker E. N., 1958, *ApJ*, 128, 664
- Pillitteri I., Maggio A., Micela G., Sciortino S., Wolk S. J., Matsakos T., 2015, *ApJ*, 805, 52
- Schneider E. M., Esquivel A., Villarreal D'Angelo C. S., Velázquez P. F., Raga A. C., Costa A., 2016, *MNRAS*, 457, 1666
- Shaikhislamov I. F. et al., 2016, *ApJ*, 832, 173
- Shaikhislamov I. F., Fossati L., Khodachenko M. L., Lammer H., García Muñoz A., Youngblood A., Dwivedi N. K., Rumenskikh M. S., 2020, *A&A*, 639, 7
- Sterenberg M. G., Cohen O., Drake J. J., Gombosi T. I., 2011, *J. Geophys. Res.*, 116, A01217
- Strangeway R. J., Russell C. T., Luhmann J. G., Moore T. E., Foster J. C., Barabash S. V., Nilsson H., 2010, AGU Fall Meeting Abstracts, SM33B
- Tóth G. et al., 2005, *J. Geophys. Res.*, 110, A12226
- Tremblin P., Chiang E., 2013, *MNRAS*, 428, 2565
- van der Holst B. et al., 2011, *ApJS*, 194, 23
- Vidal-Madjar A., Lecavelier des Etangs A., Désert J. M., Ballester G. E., Ferlet R., Hébrard G., Mayor M., 2003, *Nature*, 422, 143
- Vidotto A. A. et al., 2018, *MNRAS*, 481, 5296
- Vidotto A. A., Cleary A., 2020, *MNRAS*, 494, 2417
- Vidotto A. A., Donati J. F., 2017, *A&A*, 602, A39
- Villarreal D'Angelo C., Esquivel A., Schneider M., Sgró M. A., 2018, *MNRAS*, 479, 3115
- Weber E. J., Davis L., Jr., 1967, *ApJ*, 148, 217
- Wood B. E., Müller H. R., Zank G. P., Linsky J. L., Redfield S., 2005, *ApJ*, 628, L143
- Yelle R. V., 2004, *Icarus*, 170, 167
- Zank G. P., Müller H. R., 2003, *J. Geophys. Res.*, 108, 1240

This paper has been typeset from a \LaTeX file prepared by the author.



The dichotomy of atmospheric escape in AU Mic b

S. Carolan¹,^{*} A. A. Vidotto¹, P. Plavchan², C. Villarreal D'Angelo^{1,3} and G. Hazra¹

¹*School of Physics, Trinity College Dublin, The University of Dublin, Dublin 2, Ireland*

²*Department of Physics and Astronomy, George Mason University, Fairfax, VA 22030, USA*

³*Observatorio Astronómico de Córdoba, Universidad Nacional de Córdoba, Laprida 854, X5000BGR Córdoba, Argentina*

Accepted 2020 July 10. Received 2020 July 10; in original form 2020 June 23

ABSTRACT

Here, we study the dichotomy of the escaping atmosphere of the newly discovered close-in exoplanet AU Microscopii (AU Mic) b. On one hand, the high extreme-ultraviolet stellar flux is expected to cause a strong atmospheric escape in AU Mic b. On the other hand, the wind of this young star is believed to be very strong, which could reduce or even inhibit the planet's atmospheric escape. AU Mic is thought to have a wind mass-loss rate that is up to 1000 times larger than the solar wind mass-loss rate (\dot{M}_{\odot}). To investigate this dichotomy, we perform 3D hydrodynamics simulations of the stellar wind–planetary atmosphere interactions in the AU Mic system and predict the synthetic Ly α transits of AU Mic b. We systematically vary the stellar wind mass-loss rate from a 'no wind' scenario to up to a stellar wind with a mass-loss rate of 1000 \dot{M}_{\odot} . We find that, as the stellar wind becomes stronger, the planetary evaporation rate decreases from $6.5 \times 10^{10} \text{ g s}^{-1}$ to half this value. With a stronger stellar wind, the atmosphere is forced to occupy a smaller volume, affecting transit signatures. Our predicted Ly α absorption drops from ~ 20 per cent in the case of 'no wind' to barely any Ly α absorption in the extreme stellar wind scenario. Future Ly α transits could therefore place constraints not only on the evaporation rate of AU Mic b, but also on the mass-loss rate of its host star.

Key words: planet–star interactions – stars: planetary systems.

1 INTRODUCTION

AU Microscopii (AU Mic) is the second closest pre-main-sequence star to the Solar system (9.79 pc). With an age of approximately 22 Myr, it is orbited by an edge-on debris disc, within which lies the recently discovered warm Neptune AU Mic b (Plavchan et al. 2020). Detections of such young exoplanets are still rare, given that young stars like AU Mic pose many observational challenges for planet detection, such as the presence of spots and frequent flares. AU Mic b can therefore provide unique insights into newly formed planets and their atmospheres.

Due to its youth and activity, AU Mic emits a large flux of high-energy photons in the extreme ultraviolet (EUV). Combined with the small orbital distance (0.066 au), the estimated EUV flux impinging on AU Mic b is $4.7 \times 10^3 \text{ erg cm}^{-2} \text{ s}^{-1}$, and can be as high as $2.2 \times 10^4 \text{ erg cm}^{-2} \text{ s}^{-1}$ when the star is in a flaring state (stellar fluxes from Chadney et al. 2015). These values are 10–50 times larger than the estimated flux received in HD 209458b of $450 \text{ erg cm}^{-2} \text{ s}^{-1}$ (Murray-Clay, Chiang & Murray 2009), a hot Jupiter that shows strong atmospheric evaporation (Vidal-Madjar et al. 2003). By analogy, one would expect that AU Mic b would be strongly evaporating. Additionally, due to the youth of the system, the planet likely still has its primordial atmosphere, which would be mainly composed of hydrogen. A strong evaporation of a hydrogen-rich atmosphere, such as the one AU Mic b could host, is better probed in hydrogen lines, such as in Ly α or the Balmer series, through spectroscopic transits.

As the high-energy flux is deposited in the thermosphere, the atmosphere is heated and expands. As a consequence, the atmosphere escapes the planet in the form of a photoevaporative outflow (e.g. Murray-Clay et al. 2009). On its journey up, the evaporating atmosphere is accelerated from a subsonic to a supersonic flow that eventually crosses the Roche lobe and escapes from the planet.

One important point to consider when studying planetary evaporation is that the escaping atmospheres do not expand into an empty space, but rather the atmosphere pushes its way into the stellar wind. The stellar wind of cool dwarfs consists of a hot, ionized plasma that is embedded in the stellar magnetic field (Vidotto et al. 2015). Stellar winds can affect atmospheric evaporation of close-in exoplanets (e.g. McCann et al. 2019; Carolan et al. 2020; Shaikhislamov et al. 2020). In particular, the stronger the stellar wind, the larger the pressure it exerts in the planetary atmosphere. In a simplified way, we can think of this as the interaction of two fluids. The point where the two fluids meet is determined by pressure balance. Therefore, for a stronger stellar wind, the point where balance is achieved will be deeper in the evaporating atmosphere, which, as a consequence, is forced to occupy a smaller volume.

If the interaction happens so deep in the planetary atmosphere, where the planetary outflow is still subsonic, the stellar wind could substantially reduce the evaporation (Christie, Arras & Li 2016; Vidotto & Cleary 2020). Using 3D hydrodynamics simulation, Carolan et al. (2020) performed a systematic study of the effects of the stellar wind on the evaporation rate of a typical hot Jupiter. They showed that for weaker stellar winds, the reduction in planetary escape rate was very small. Nevertheless, because the atmosphere was forced to occupy a smaller volume, spectroscopic transit sig-

* E-mail: carolast@tcd.ie

natures were substantially affected. The atmospheric escape rates remained approximately constant ($\simeq 5.5 \times 10^{11} \text{ g s}^{-1}$), while its Ly α transit absorption changed from 24 to 14 per cent as the stellar wind mass-loss rate was only moderately increased from ‘no wind’ to a wind with a mass-loss rate that is 10 times the solar value of $\dot{M}_\odot = 2 \times 10^{-14} M_\odot \text{ yr}^{-1}$. However, as the stellar wind became stronger than that, a more substantial reduction in evaporation rates was seen, in particular after this interaction started to occur below the sonic surface of the planetary outflow. For a stellar wind mass-loss rate of $100 \dot{M}_\odot$, the evaporation rate had reduced 65 per cent and the absorption in the Ly α line went down to less than 5 per cent.

This leads to a dichotomy for the AU Mic system. While, due to the large EUV flux impinged on the atmosphere, the evaporation rate of a close-in planet is expected to be very strong during its youth, the stellar wind is also stronger at young ages (Vidotto & Donati 2017; Carolan et al. 2019). AU Mic in particular is thought to have a wind mass-loss rate that is larger than solar. Theoretical estimates range from $10 \dot{M}_\odot$ (Plavchan et al. 2009) to $1000 \dot{M}_\odot$ (Strubbe & Chiang 2006; Chiang & Fung 2017).

To investigate what could be possibly happening in the AU Mic system and to guide whether strong evaporation could be detected in Ly α transits, we study how the wind of AU Mic could affect the evaporation rate of AU Mic b and its predicted transit. For that, we use 3D hydrodynamics simulations followed by synthetic line profile calculations that investigate the effect increasing the strength of the stellar wind has on Ly α transits of AU Mic b.

2 ATMOSPHERIC ESCAPE AND SYNTHETIC LY α TRANSIT MODELS

We use the model presented in Carolan et al. (2020) to study the effects of the stellar winds on AU Mic b. Here, we briefly introduce the model and point the reader to Carolan et al. (2020) for further details. Our model uses the Space Weather Modelling Framework (Tóth et al. 2005) to perform the 3D hydrodynamics simulation of the interaction between the stellar wind and the planetary atmosphere. The planet is centred in the 3D grid and the stellar wind is injected through an outer boundary. We assume these two flows are isothermal, with the stellar wind having a temperature of 2 MK and the planetary outflow having a temperature of 5300 K (our choice of temperature is discussed below). We use a rectangular grid that extends from $[-50, 50]r_p$ in the x and y directions and $[-32, 32]r_p$ in the z direction, where r_p is the radius of the planet. The orbital plane is in the xy plane and the orbital spin axis is along positive z . AU Mic b is in a prograde orbit nearly perpendicular to the stellar spin axis (Martoli et al. 2020). Our grid contains ~ 16 million cells and has a non-uniform resolution, with the highest resolution of $(1/16)r_p$ within a radius of $5r_p$, and gradually coarser towards the edge of the grid. We solve for the mass density ρ , velocity $\vec{u} = [u_x, u_y, u_z]$, and thermal pressure P in the frame corotating with the planet, which is assumed to have the same rotational angular velocity as the orbital angular velocity, for simplicity. We solve a set of coupled hydrodynamic equations. The momentum equation is

$$\frac{\partial(\rho\vec{u})}{\partial t} + \nabla \times [\rho\vec{u}\vec{u} + P\mathbf{I}] = \rho\vec{g} - \frac{\rho GM_*}{(r-a)^2} \hat{R} - \rho\vec{\Omega} \times (\vec{\Omega} \times \vec{R}) - 2\rho(\vec{\Omega} \times \vec{u}), \quad (1)$$

where \mathbf{I} is the identity matrix, \vec{g} is the acceleration due to the planet’s gravity, G is the gravitational constant, and M_* is the mass of the star. \vec{R} is the position vector relative to the planet, \vec{a} is the position of the star relative to the planet, $\vec{\Omega}$ is the orbital rotation rate, and \hat{R}

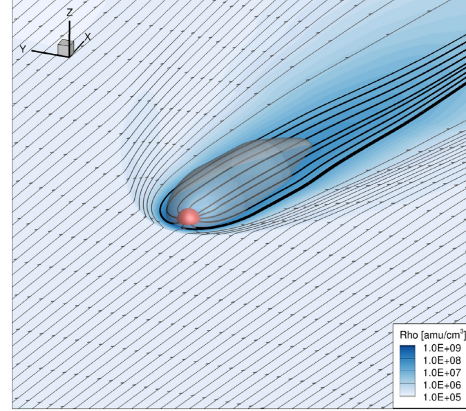


Figure 1. Atmospheric escape of AU Mic b, when it interacts with a stellar wind with $\dot{M} = 100 \dot{M}_\odot$. The stellar wind is injected in the negative x . Its streamlines are shown in grey, while the black streamlines represent the velocity field of the planetary outflowing atmosphere. The density is shown in the equatorial plane and the grey surface around the planet shows the region used in the synthetic transits (with temperature $\lesssim 1.1T_p$, Section 2).

is the position vector relative to the star. On the right-hand side of equation (1), we have the planetary gravitational force, stellar gravity, and the centrifugal and Coriolis forces. The energy conservation equation is

$$\frac{\partial\epsilon}{\partial t} + \nabla \times [\vec{u}(\epsilon + P)] = \rho \left(\vec{g} - \frac{GM_*}{(r-a)^2} \hat{R} - \vec{\Omega} \times (\vec{\Omega} \times \vec{R}) \right) \times \vec{u}, \quad (2)$$

where $\epsilon = \rho u^2/2 + P/(\gamma - 1)$. We take $\gamma = 1.001$, which implies that the flows are nearly isothermal. We assume an ideal gas, where the thermal pressure is $P = \rho k_B T / (\mu m_p)$, where k_B is the Boltzmann constant, and μ is the mean mass per particle, and m_p is the mass of the proton. Our 3D simulations assume fully ionized hydrogen flows; thus, $\mu = 0.5$. The set of equations is closed with the mass conservation equation

$$\frac{\partial\rho}{\partial t} + \nabla \times (\rho\vec{u}) = 0. \quad (3)$$

We assume a planetary mass of $0.69M_{\text{Nep}}$ and radius of $1.08R_{\text{Nep}}$. The stellar mass and radius are $M_* = 0.5 M_\odot$ and $R_* = 0.75 R_\odot$. The orbital distance is $a = 0.066 \text{ au}$, transit duration is 3.5 h, and the impact parameter is $0.16R_*$. All these values are from Plavchan et al. (2020), with the exception of the planetary mass that is from Plavchan et al. (in preparation), and was obtained from additional radial velocity measurements. Fig. 1 shows the output of one of our simulations, after reaching a steady state.

To calculate the Ly α transit profiles, we use the ray-tracing technique detailed in Allan & Vidotto (2019). Stellar rays are shot through the planetary material, which is represented by the volume entailed by the grey surface in Fig. 1. We calculate the velocity-dependent optical depth τ_v of this material along the line of sight and integrate over all rays that are transmitted through the atmosphere to obtain the velocity-dependent transit depth

$$\Delta F_v = \int \int (1 - e^{-\tau_v}) dy dz / (\pi R_*^2). \quad (4)$$

The optical depth of the Ly α transit requires the density of neutrals n_n , such that $\tau_v = \int n_n \sigma_v \phi_v dx$, where ϕ_v is the Voigt line profile, and $\sigma = 0.01103 \text{ cm}^2 \text{ Hz}$ is the Ly α absorption cross-section at line centre. Because our 3D model does not treat the neutral material of the planetary outflow, we use a post-processing technique to estimate its ionization fraction f_i . This is done using the 1D atmospheric escape model of Allan & Vidotto (2019), where we assume an EUV luminosity of $1.5 \times 10^{-5} L_\odot$ appropriate for the quiescent state of AU Mic (Chadney et al. 2015). With this, we derive the density of neutrals as $n_n = n_p(1 - f_i)/f_i$, where n_p is the proton density from our 3D simulations.

The results of our 1D model are also used to constrain the free parameters in the 3D simulations, namely the atmospheric base temperature and density. The 1D model solves the energy equation of the planetary outflow assuming photoionization by stellar EUV photons and Ly α cooling (Allan & Vidotto 2019). As a result, the atmospheric temperature varies from 1000 K at $1r_p$ to nearly 8000 K at $\sim 2r_p$, and cools beyond that. We pick an intermediate temperature of 5300 K for our 3D model. We also chose the base density of our 3D simulations such that it matches the predicted escape rate of $6.5 \times 10^{10} \text{ g s}^{-1}$ from the 1D model.

3 RESULTS: SYSTEMATIC VARIATION OF THE STELLAR WIND STRENGTH

We perform five simulations where we systematically vary the stellar wind mass-loss rate: $\dot{M} = 0$ (no wind), 1, 10, 100, and 1000 \dot{M}_\odot . We use a temperature of 2 MK for the stellar wind, so that the stellar wind is always injected with the same velocity (about 540 km s^{-1}). As this is a thermally driven wind, the wind velocity is independent of the density, so changing \dot{M} while the velocity structure is constant solely changes the density profile of the injected stellar wind.

Fig. 2 shows the orbital slice of each of these simulations. We see that as the stellar wind mass-loss rate (and thus its ram pressure) is increased, the escaping atmosphere is confined closer to the planet, and forced to occupy a smaller volume. The position where the interaction happens eventually disrupts the sonic surface (originally at $1.3r_p$) of the escaping atmosphere, such that parts of the planetary outflow, especially in the dayside, can no longer accelerate to supersonic speeds. When this happens, we see a stronger decrease in the escape rate of the planetary atmosphere.

We calculate the escape rate by integrating the mass flux through concentric spheres (with areas A) around the planet: $\dot{m} = \oint_A \rho \bar{u} \cdot dA$. These values are given in Table 1, where we see that the escape rate is unaffected in the 1 and 10 \dot{M}_\odot models, and they are very similar to the values we obtain in the ‘no wind’ model. In the 100 \dot{M}_\odot model, the escape rate has decreased slightly from 6.5×10^{10} to $5.9 \times 10^{10} \text{ g s}^{-1}$. This is the first of our computed models where the wind is capable of sufficiently confining the escaping atmosphere such that the dayside sonic surface is disrupted. The dayside flow is no longer able to reach supersonic speeds. Material continues to outflow from the planet but it is funnelled back towards the comet-like tail (better seen in Fig. 1). The nightside sonic surface remains unaffected, so only a small decrease in escape rate is found in this model. This is not the case in the 1000 \dot{M}_\odot model, where the stellar wind confines the escaping atmosphere such that the sonic surface on all sides of the planet is affected. This results in a 50 per cent lower escape rate, when compared to other models.

We investigate the effect this confinement has on the Ly α transit by performing synthetic transit calculations. To ensure that the material we use in the ray-tracing computation is planetary, we use a temperature cut-off that is 10 per cent higher than the planetary

outflow and follow the description presented in Section 2. The contours of this temperature cut-off are seen in the last panel of Fig. 2 for the orbital plane, further illustrating how the confinement of the planetary atmosphere varies in each model.

In none of our models, the line centre is saturated (i.e. 100 per cent absorption), but models with 0 and 1 \dot{M}_\odot reach more than 95 per cent absorption at line centre. However, given the line centre of the Ly α line is contaminated by geocoronal emission and interstellar absorption (assuming the stellar and ISM radial velocities are $\simeq 0$), we do not consider the line centre ($[-36, 36] \text{ km s}^{-1}$) in our results presented next. The blue ($[-100, -36] \text{ km s}^{-1}$) and red ($[36, 100] \text{ km s}^{-1}$) wings of the Ly α line are shown in Fig. 3(a) and (b), respectively. The absorptions computed in these velocity intervals $\int_{v_i}^{v_f} \Delta F_\lambda dv / (v_f - v_i)$ are shown in Table 1 and Fig. 3(c), where v_i and v_f , respectively, are initial and final velocities in the ranges quoted above.

The no-wind model is the only case where the line profile is nearly symmetric in both wings. Line asymmetry is already seen in model 1 \dot{M}_\odot . Despite the escape rate of the planet remaining unchanged for models 0, 1, and 10 \dot{M}_\odot , the Ly α absorption has changed significantly when compared to the no-wind model. For the 10 \dot{M}_\odot model, we see a greater reduction in the red wing absorption, as the planetary flow towards the star is suppressed by the stellar wind. Though we still see blue wing absorption in the 10 \dot{M}_\odot model, it has been significantly reduced compared to the 0 and 1 \dot{M}_\odot models. This is because the stronger stellar wind reduces the volume of the comet-like tail, which contains most of the blueshifted absorbing material. The volume of absorbing material is further reduced in the 100 \dot{M}_\odot model such that very little blue wing absorption is found, and essentially no detectable red wing absorption. The 1000 \dot{M}_\odot stellar wind confinement has not only reduced the escape rate of the planet by 50 per cent but also completely masked the observational signatures of this escape in Ly α , as we find no red or blue wing absorption.

4 DISCUSSION AND CONCLUSION

We investigated here the dichotomy of atmospheric escape in the newly discovered exoplanet AU Mic b. On one hand, the high EUV flux of young host stars is expected to cause strong atmospheric escape (Kubyschkina et al. 2018). On the other hand, the star is expected to have a strong stellar wind ($10\text{--}10^3 \dot{M}_\odot$) (Strubbe & Chiang 2006; Plavchan et al. 2009), which can reduce evaporation in the planet (Carolan et al. 2020; Vidotto & Cleary 2020). To investigate this dichotomy, we modelled the interaction between the wind of AU Mic and the escaping atmosphere of AU Mic b, by performing 3D hydrodynamics simulations of the system. We considered a number of stellar wind mass-loss rates from $\dot{M} = 0$ to $10^3 \dot{M}_\odot$. We found that increasing \dot{M} confines the escaping planetary atmosphere, which occupies a smaller volume. When this confinement disrupts the sonic surface of the planetary outflow, we see a more substantial reduction in the escape rate. For the models with 0, 1, and 10 \dot{M}_\odot , the escape rate is unaffected and remains $6.5 \times 10^{10} \text{ g s}^{-1}$. In the 100 \dot{M}_\odot model, the escape rate decreases slightly from 6.5×10^{10} to $5.9 \times 10^{10} \text{ g s}^{-1}$. However, for the 1000 \dot{M}_\odot model, escape rate is reduced by 50 per cent, with a value of $3.2 \times 10^{10} \text{ g s}^{-1}$. From an evolutionary point of view, a factor of 2 in the escape rate is negligible. The reduction is likely to be more important at young ages, when the stellar wind is stronger, but it is worth recalling that the evaporation of the planet is also stronger at younger ages, so investigating which process ‘wins’ (wind versus

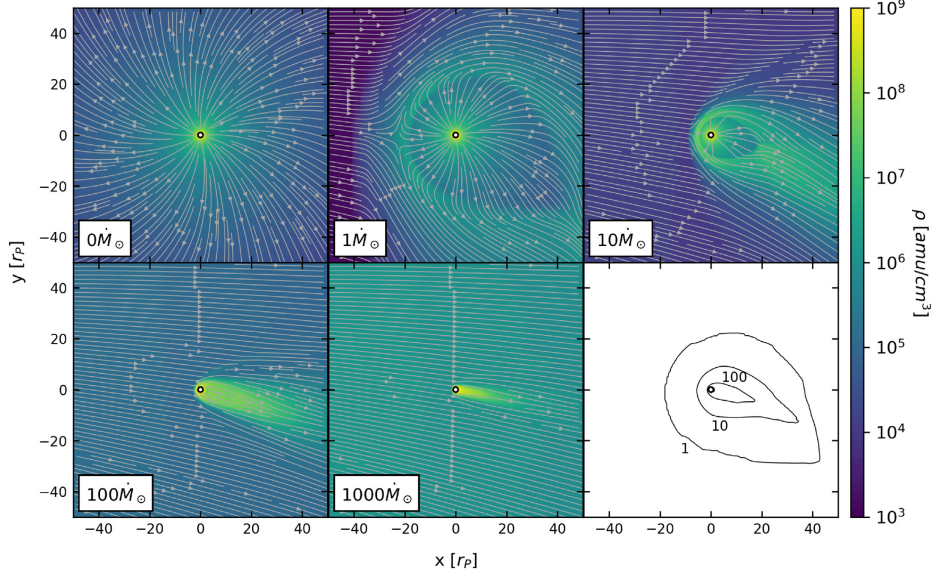


Figure 2. Density structure and velocity streamlines in the planet’s reference frame for the five simulations we run for varying stellar wind \dot{M} , quoted in the first five panels. The planet is shown at the centre of the grid on the orbital plane. As the stellar wind that is injected in the negative x boundary has a larger \dot{M} , the escaping atmosphere of AU Mic b is forced into smaller volumes. The last panel shows the isocontours of temperature at approximately the temperature we adopt for the planetary atmosphere. Material within these contours belongs to the planet and is used in the synthetic calculations of the Ly α transit profiles. The numbers shown next to each isocontour represent the stellar wind mass-loss rate in M_{\odot} . The inner-most contour is for the case with $1000 M_{\odot}$ (label not shown).

Table 1. Simulation results showing the stellar wind mass-loss rate (\dot{M}), planetary atmosphere escape rate (\dot{m}), absorption in the blue ($[-100, -36]$ km s $^{-1}$) and red ($[36, 100]$ km s $^{-1}$) wings of the Ly α line, and the sum of these absorptions.

\dot{M} (M_{\odot})	\dot{m} ($\times 10^{10}$ g s $^{-1}$)	ΔF_{blue} (%)	ΔF_{red} (%)	ΔF_{tot} (%)
0 (no wind)	6.5	9.9	10	20
1	6.5	9.8	5.8	16
10	6.3	4.1	1.4	5.5
100	5.9	1.4	1.1	2.5
1000	3.2	0.25	0.25	0.5

EUV flux) is an important point to consider in future studies of planetary evolution.

The reduction in evaporation affects differently Ly α transit absorption. We calculated synthetic Ly α line profiles at mid-transit and found that, although we still see blue wing absorption in the $10 M_{\odot}$ model, it is significantly smaller than the 0 and $1 M_{\odot}$ models. This happens even though no appreciable reduction is seen in the escape rate of these three models. This is because the stronger stellar wind reduces the volume of the comet-like tail, which contains most of the blueshifted absorbing material. For the $10^3 M_{\odot}$ model, we found almost no Ly α absorption, as most of the absorbing material is confined to a small volume around the planet. Our models do not consider the charge-exchange process, which converts a low-velocity planetary neutral atom into an ion and a high-velocity stellar wind ion into an energetic neutral atom (Shaikhislamov et al. 2020). The net effect of this process is to shift absorption in the Ly α centre

to the blue wing. Given the already low absorption around line centre in the $> 100 M_{\odot}$ models (low volume occupied by absorbing material), shifting this to higher velocities by charge exchange will not greatly alter absorption at line wings. Charge exchange can be more important for models with lower \dot{M} , given the volume containing neutrals is much larger than the higher \dot{M} models.

A few years ago, Chadney et al. (2015) predicted escape rates of a fictitious planet orbiting AU Mic. They assumed a hot-Jupiter planet similar to HD 209458b at 0.2 au, and obtained a strong evaporation rate of 1.2×10^{10} g s $^{-1}$. Due to differences in the planet parameters, a comparison between our results and theirs is not straightforward. If we were to ‘move’ their fictitious planet to the orbit of AU Mic b, we estimate a factor of $(0.2/0.066)^2 \simeq 9$ (i.e. linear with EUV flux) increase in their escape rates, bringing their estimates to 10^{11} g s $^{-1}$. This evaporation rate is about a factor of 2 larger than our ‘no wind’ model, but is of the same order of magnitude. Note though that we are comparing two different planets here – a fictitious hot Jupiter and AU Mic b, which is a warm Neptune, and that the differences in planetary gravity will affect escape rates (Allan & Vidotto 2019).

The numbers we quoted in this paper should be used with care, as they are dependent on assumptions we made for the system, such as the planetary escape rate in the no-wind model, which we set from an assumed EUV flux, and the stellar wind temperature, which we assumed is a typical coronal-like temperature of 2 MK. For example, the evaporation rate of a planet that has a sonic surface at a larger distance is more easily affected by the stellar wind. Likewise, a stellar wind that has a larger ram pressure more easily disrupts the planet’s sonic surface, affecting more the evaporation. Carolan et al. (2020) further discuss how different system characteristics affect

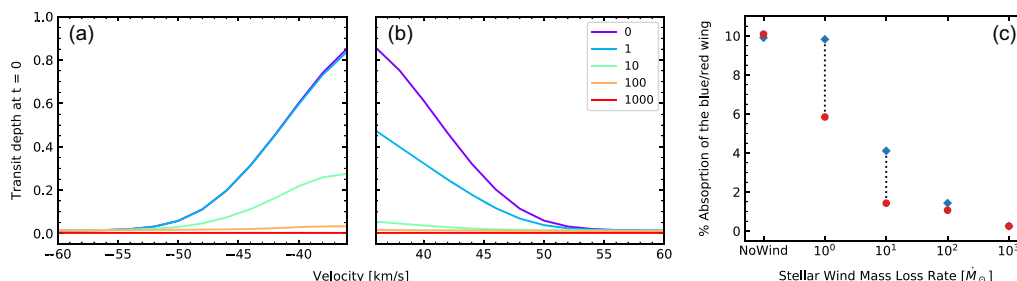


Figure 3. (a, b) Transit depth of the Ly α line computed at mid-transit for the blue (≤ -36 km s $^{-1}$) and red (≥ 36 km s $^{-1}$) wings, respectively, as a function of Doppler velocity. (c) Integrated absorption in the blue (blue diamonds) and red (red circles) wings of the Ly α line calculated at mid-transit, as a function of the stellar wind mass-loss rate. Table 1 shows these values and the total absorption.

the reduction of escape rate and absorption. Another assumption we made is that the stellar wind is spherically symmetric (purely radial velocity and isotropic mass flux). If the star has a complex magnetic field topology, the stellar wind will not be isotropic, as the field geometry leads to a non-homogeneous stellar wind along the planetary orbital path (Vidotto et al. 2015). Even if we were to adopt slightly different values for the planet escape rate or stellar wind properties, the general conclusions we found here should remain valid. Namely, we concluded that should future Ly α observations detect solely blue wing absorption during the transit of AU Mic b (i.e. little or no redshifted absorption), the stellar wind mass-loss rate of AU Mic can be estimated to be $\sim 10 \dot{M}_\odot$. A redshifted absorption would imply mass-loss rates $\lesssim 10 \dot{M}_\odot$. Should future observations find a non-detection in Ly α transits, we propose that this could be due to stellar wind confinement of the escaping atmosphere. In this case, our models would allow us to place a lower limit on the mass-loss rate of AU Mic of $\gtrsim 100 \dot{M}_\odot$. This would help clarify whether AU Mic has a moderately strong wind ($10 \dot{M}_\odot$) or substantially stronger ($10^3 \dot{M}_\odot$).

ACKNOWLEDGEMENTS

We acknowledge funding from the ERC grant 817540, AS-TROFLOW and computational facilities, and support from SFI/HEA ICHEC. This work used BATS-R-US developed at the University of Michigan CSEM and made available through the NASA CCMC. We thank the referee, Dr Fossati, for constructive comments.

DATA AVAILABILITY

The data described in this article will be shared on reasonable request to the corresponding author.

REFERENCES

- Allan A., Vidotto A. A., 2019, *MNRAS*, 490, 3760
 Carolan S., Vidotto A. A., Loesch C., Coogan P., 2019, *MNRAS*, 489, 5784
 Carolan S., Vidotto A. A., Villarreal D'Angelo C., Hazra G., 2020, *MNRAS*, submitted
 Chadney J. M., Galand M., Unruh Y. C., Koskinen T. T., Sanz-Forcada J., 2015, *Icarus*, 250, 357
 Chiang E., Fung J., 2017, *ApJ*, 848, 4
 Christie D., Arras P., Li Z. Y., 2016, *ApJ*, 820, 3
 Kubyskhina D., Lendl M., Fossati L., Cubillos P. E., Lammer H., Erkaev N. V., Johnstone C. P., 2018, *A&A*, 612, A25
 McCann J., Murray-Clay R. A., Kratter K., Krumholz M. R., 2019, *ApJ*, 873, 89
 Martioli E. et al., 2020, preprint (arXiv:2006.13269)
 Murray-Clay R. A., Chiang E. I., Murray N., 2009, *ApJ*, 693, 23
 Plavchan P., Werner M. W., Chen C. H., Stapelfeldt K. R., Su K. Y. L., Stauffer J. R., Song I., 2009, *ApJ*, 698, 1068
 Plavchan P. et al., 2020, *Nature*, 582, 497
 Shaikhislamov I. F., Fossati L., Khodachenko M. L., Lammer H., García M. A., Youngblood A., Dwivedi N. K., Rumenskikh M. S., 2020, *A&A*, preprint (arXiv:2006.06959)
 Strubbe L. E., Chiang E. I., 2006, *ApJ*, 648, 652
 Tóth G. et al., 2005, *J. Geophys. Res. (Space Phys.)*, 110, A12226
 Vidal-Madjar A., Lecavelier des Etangs A., Désert J. M., Ballester G., Ferlet R., Hébrard G., Mayor M., 2003, *Nature*, 422, 143
 Vidotto A. A., Cleary A., 2020, *MNRAS*, 494, 2417
 Vidotto A. A., Donati J. F., 2017, *A&A*, 602, A39
 Vidotto A. A., Fares R., Jardine M., Moutou C., Donati J. F., 2015, *MNRAS*, 449, 4117

This paper has been typeset from a \LaTeX file prepared by the author.



The effects of magnetic fields on observational signatures of atmospheric escape in exoplanets: Double tail structures

S. Carolan¹,¹★ A. A. Vidotto^{1,2}, G. Hazra^{1,2}, C. Villarreal D'Angelo³ and D. Kubyskhina¹

¹*School of Physics, Trinity College Dublin, College Green, D02 PN40 Dublin 2, Ireland*

²*Leiden Observatory, Leiden University, PO Box 9513, NL-2300 RA Leiden, the Netherlands*

³*Instituto de Astronomía Teórica y Experimental (CONICET-UNC), Laprida 854, X5000BGR Córdoba, Argentina*

Accepted 2021 October 11. Received 2021 October 6; in original form 2021 September 7

ABSTRACT

Using 3D radiative MHD simulations and Lyman- α transit calculations, we investigate the effect of magnetic fields on the observational signatures of atmospheric escape in exoplanets. Using the same stellar wind, we vary the planet's dipole field strength (B_p) from 0 to 10G. For $B_p < 3G$, the structure of the escaping atmosphere begins to break away from a comet-like tail following the planet ($B_p = 0$), as we see more absorbing material above and below the orbital plane. For $B_p \geq 3G$, we find a 'dead-zone' around the equator, where low velocity material is trapped in the closed magnetic field lines. The dead-zone separates two polar outflows where absorbing material escapes along open field lines, leading to a double tail structure, above and below the orbital plane. We demonstrate that atmospheric escape in magnetized planets occurs through polar outflows, as opposed to the predominantly night-side escape in non-magnetized models. We find a small increase in escape rate with B_p , though this should not affect the time-scale of atmospheric loss. As the size of the dead-zone increases with B_p , so does the line centre absorption in Lyman- α , as more low-velocity neutral hydrogen covers the stellar disc during transit. For $B_p < 3G$ the absorption in the blue wing decreases, as the escaping atmosphere is less funnelled along the line of sight by the stellar wind. In the red wing (and for $B_p > 3G$ in the blue wing) the absorption increases caused by the growing volume of the magnetosphere. Finally we show that transits below and above the mid-disc differ caused by the asymmetry of the double tail structure.

Key words: MHD – planets and satellites: atmospheres – planets and satellites: magnetic fields – planet–star interactions.

1 INTRODUCTION

Exoplanets that orbit close to their host stars can lose their atmospheres through photoevaporation, as they receive large amounts of high-energy flux at these orbits (Lammer et al. 2003; Baraffe et al. 2004; Yelle 2004). The lifetime of the planet's atmosphere depends strongly on the rate of this escape (e.g. Johnstone et al. 2015b; Kubyskhina et al. 2020). This has a number of interesting implications for the exoplanet community. While of course being crucial for understanding planetary habitability (Dong et al. 2018; Lingam & Loeb 2018), atmospheric escape is also thought to shape the distribution of observed exoplanets (Kurokawa & Nakamoto 2014; Owen & Lai 2018; Berger et al. 2020). The so-called 'radius gap', an underpopulation of short period exoplanets with radii between 1.5 and 2 Earth radii (Beaugé & Nesvorný 2013; Fulton et al. 2017), has been attributed to atmospheric loss. The mechanism of this loss is not certain, with photoevaporation and core-powered mass-loss both being likely candidates, with both probably contributing over the planet's evolution (Rogers et al. 2021). Direct observations of atmospheric escape have also been found. During transit the escaping atmosphere causes excess absorption, as absorbing elements and molecules cover a larger area on the stellar disc. The ever growing list of these observations contains hot Jupiters

such as HD209458b (Vidal-Madjar et al. 2003) and HD189733b (Lecavelier Des Etangs et al. 2010, 2012; Jensen et al. 2012; Ben-Jaffel & Ballester 2013), as well as warm Neptunes like GJ436b (Kulow et al. 2014; Ehrenreich et al. 2015) and GJ3470b (Bourrier et al. 2018).

To fully understand these observations, we need 3D simulations capable of modelling the escaping atmosphere. One very important factor that must be considered is the stellar wind (McCann et al. 2019; Carolan et al. 2021; Villarreal D'Angelo et al. 2021). As the escaping atmosphere leaves the planet it is soon met by the stellar wind, which shapes this outflow into structures like a comet-like tail following the planet in its orbit. The geometry and extent of these structures around the planet is sensitive to several external parameters such as the ram pressure of the stellar wind, as well as the orbital velocity and tidal forces from the star, which arise due to these close-in orbits (Matsakos, Uribe & Königl 2015; Pillitteri et al. 2015; Shaikhislamov et al. 2016). The stellar wind can also affect the atmospheric escape rate, whereby a strong stellar wind can prevent the day-side escaping atmosphere from reaching supersonic velocities (Vidotto & Cleary 2020). As a result the inner most regions of the escaping atmosphere can be affected, and the escape rate reduced due to a lack of day-side acceleration (Christie, Arras & Li 2016; Carolan et al. 2020, 2021; Vidotto & Cleary 2020). As this interaction is largely asymmetric, 3D models are required to fully accurately model atmospheric escape. Recently there has been an increasing number of 3D works which include the stellar wind (Bisikalo et al. 2013; Schneider et al. 2016;

* E-mail: carolast@tcd.ie

Shaikhislamov et al. 2016; Carroll-Nellenback et al. 2017; Villarreal D’Angelo et al. 2018; Esquivel et al. 2019; Khodachenko et al. 2019; McCann et al. 2019; Carolan et al. 2020, 2021; Debrecht et al. 2020; Villarreal D’Angelo et al. 2021; MacLeod & Oklopčić 2021; Hazra et al., submitted; Kubyskhina et al., submitted), however the effect of magnetic fields on this interaction, the escape rate, and observational signatures of this escape is not yet fully understood.

There have been a number of works that investigate different aspects of how the planet’s magnetic field affects escape and its observational signatures. Using 2D models, Trammell, Li & Arras (2014) showed that the transit depth increases strongly with magnetic field strength when the hydrogen ionization layer is magnetically dominated, while in the same year Owen & Adams (2014) demonstrated that the strength and geometry of the stellar magnetic field is crucial to determine the fraction of open field lines around the planet. Khodachenko et al. (2015) found that the atmospheric escape rate is weakly affected by field strengths $<0.3G$, but reduced by an order of magnitude for a 1G field, which could potentially have huge implications on the lifetime of the planet’s atmosphere. Though these have all used 2D models, Matsakos et al. (2015) performed 3D simulations of close-in magnetic star–planet interactions, identifying four classifications: bowshock, colliding winds, strong planetary wind causing accretion, and Roche lobe overflow. Arakcheev et al. (2017) found a 70 per cent reduction in WASP-12’s escape rate with a model containing the planet’s magnetic field and stellar wind, though not the magnetic field of the stellar wind / star. Using 3D global simulations of HD 209458b, Villarreal D’Angelo et al. (2018) showed that the shape of the Lyman- α line depends on both the stellar and planetary fields, as they control the geometry of the magnetosphere and the amount of neutrals inside it. Finally Harbach et al. (2021) used MHD models to demonstrate the dependence of the magnetosphere and Lyman- α absorption on the stellar wind, though their model did not self-consistently calculate the heating and photoionization due to stellar UV irradiation, and ignored close-in orbital forces. To the best of our knowledge, to date there has not been a 3D self-consistent radiative magnetohydrodynamic model capable of resolving the inner most regions of the escaping atmosphere, which contains both the stellar and planetary magnetic fields.

In this work we present such a model, and use it to investigate the effect of magnetic fields on the escaping atmosphere and their observational signatures. While keeping all other parameters constant (see Table 1) we vary the dipole strength of the planet’s magnetic field from 0 to 10 G, examining the change in the magnetosphere and mid-transit absorption in Lyman- α . The details of our 3D model are given in Section 2. In Section 3, we discuss the effects of the planetary magnetic field on the geometry of the escaping atmosphere, while in Section 4 we discuss the implications of this on the observational signatures present in Lyman- α . A discussion of the impact of our results can be found in Section 5, while we sum up our conclusions in Section 6.

2 3D SELF-CONSISTENT RADIATIVE MAGNETOHYDRODYNAMIC SIMULATIONS

To model the escaping atmosphere in the presence of a magnetic field, we build upon the non-magnetized code presented in Hazra et al (submitted), which uses the BATS-R-US framework (Tóth et al. 2005). This model is an extensive update to Carolan et al. (2020), Carolan et al. (2021)’s model, including new physics: the heating, cooling, ionization and recombination of neutral and ionized hydrogen, calculated during runtime. While the simulations of Hazra et al. (submitted) were hydrodynamic, we adapt this model to

investigate how magnetic fields affect atmospheric escape and its observational signatures. This is the first 3D self-consistent radiative magnetohydrodynamic model of photoevaporation of an exoplanet using the BATS-R-US framework. The output of one such model is shown in Fig. 1.

We simulate the escaping atmosphere in a 3D Cartesian grid $[-30:50, -40:40, -30:30]$ planetary radii (R_p) with a maximum resolution of $1/16 R_p$ inside $5 R_p$. For simplicity we assume that the exoplanet is centred on the origin of the coordinate system, is tidally locked to its host star located outside our numerical domain at negative x , and the simulation is performed in the co-rotating, co-orbiting reference frame. The model solves the ideal magnetohydrodynamic equations: the mass conservation; momentum conservation; energy conservation and induction equations, respectively:

$$\frac{\partial \rho}{\partial t} + \nabla \cdot \rho \vec{u} = 0, \quad (1)$$

$$\begin{aligned} \frac{\partial(\rho \vec{u})}{\partial t} + \nabla \cdot \left[\rho \vec{u} \vec{u} + \left(P_T + \frac{B^2}{8\pi} \right) I - \frac{\vec{B} \vec{B}}{4\pi} \right] \\ = \rho \left(\vec{g} - \frac{GM_*}{|\vec{R}|^2} \hat{R} - \vec{\Omega} \times (\vec{\Omega} \times \vec{R}) - 2(\vec{\Omega} \times \vec{u}) \right), \end{aligned} \quad (2)$$

$$\begin{aligned} \frac{\partial \epsilon}{\partial t} + \nabla \cdot \left[\vec{u} \left(\epsilon + P_T + \frac{B^2}{8\pi} \right) - \frac{(\vec{u} \cdot \vec{B}) \vec{B}}{4\pi} \right] \\ = \rho \left(\vec{g} - \frac{GM_*}{|\vec{R}|^2} \hat{R} - \vec{\Omega} \times (\vec{\Omega} \times \vec{R}) \right) \cdot \vec{u} + \mathcal{H} - \mathcal{C}, \end{aligned} \quad (3)$$

$$\frac{\partial \vec{B}}{\partial t} + \nabla \cdot (\vec{u} \vec{B} - \vec{B} \vec{u}) = 0. \quad (4)$$

ρ , \vec{u} , P_T , \vec{B} , and I are the mass density, velocity, thermal pressure, magnetic field, and identity matrix, respectively. \vec{R} is the position vector relative to the centre of the star, given by $\vec{R} = \vec{r} + \vec{a}$, where \vec{r} is the position vector relative to the centre of the planet, and \vec{a} is the orbital distance. The total energy density ϵ is

$$\epsilon = \frac{\rho u^2}{2} + \frac{P_T}{\gamma - 1} + \frac{B^2}{8\pi}. \quad (5)$$

γ is the adiabatic index, which we set to $5/3$. In the momentum equation (2), the source terms in order are the planet’s gravity, the stellar gravity, the centrifugal, and Coriolis forces. The energy conservation equation (3) contains \mathcal{H} and \mathcal{C} terms, denoting the volumetric heating and cooling rates. The volumetric heating rate due to stellar radiation is given by:

$$\mathcal{H} = \eta \sigma n_n F_{\text{XUV}} e^{-\tau}, \quad (6)$$

here η is the excess energy released when a hydrogen atom is ionized, n_n is the number density of neutrals, F_{XUV} is the incident XUV flux, and τ is the optical depth. We assume that the incident XUV radiation is plane-parallel, and that the entire XUV spectrum is concentrated at 20 eV. This yields $\sigma = 1.89 \times 10^{-18} \text{ cm}^{-2}$ and $\eta = 0.32$ (Murray-Clay, Chiang & Murray 2009; Allan & Vidotto 2019; Hazra, Vidotto & D’Angelo 2020) Hazra et al. (submitted). The XUV flux is injected into the grid from the negative x boundary, such that the optical depth is calculated by:

$$\tau = \int_{x_{\text{boundary}}}^x n_n \sigma dx. \quad (7)$$

For the total volumetric cooling rate \mathcal{C} , our model contains the cooling due to Lyman- α emission (Osterbrock 1989):

$$\mathcal{C}_{\text{Ly}\alpha} = 7.5 \times 10^{-19} n_p n_n \exp(-1.183 \times 10^5 / T), \quad (8)$$

Table 1. The parameters of our models. M_p and R_p are the mass and radius of the planet, while B_{0p} is the range of polar dipole field strength of the planet examined. a is the orbital distance from the star. F_{xuv} is the X-ray flux received by the planet. M_* and R_* are the mass and radius of the star. R_A is the alfvén point of the stellar wind while \dot{M}_* is the stellar wind mass-loss rate. u_{r*} is the range of stellar wind velocities along the negative x boundary, with the minimum at the centre and increasing towards the edge of the grid-face. Finally B_{0*} is the stellar dipole strength.

M_p	R_p	B_{0p}	a	F_{xuv}	M_*	R_*	R_A	\dot{M}_*	u_{r*}	B_{0*}
(M_J)	(R_J)	(G)	(au)	(erg cm ⁻² s ⁻¹)	(M_\odot)	(R_\odot)	(R_*)	(M_\odot yr ⁻¹)	(km s ⁻¹)	(G)
0.7	1.4	0–10	0.05	850	1	1	5.56	3.6×10^{-13}	327–368	2G

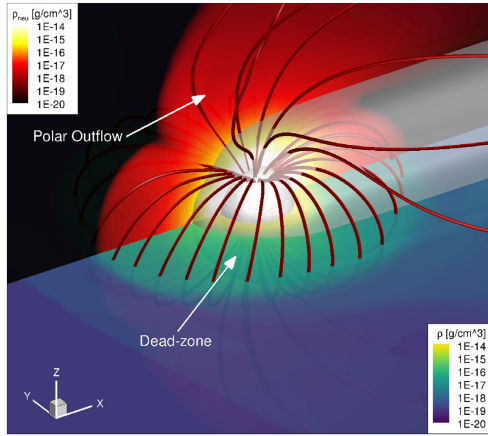


Figure 1. A 3D view of the 10G model. The white sphere is the planet, while the grey surface mark where the optical depth $\tau = 1$ of Lyman- α photons. The black-red contour shows the density of neutrals on the polar plane, while the blue-green contour shows the total mass density on the orbital plane. The red lines trace the planetary magnetic field lines. Here we can clearly see a dead-zone of material trapped by the closed field lines, as well as a polar outflow where the field lines are open.

and the cooling due to collisions (Black 1981):

$$C_{\text{col}} = 5.83 \times 10^{-11} n_e n_n \sqrt{T} \exp(-1.578 \times 10^5 / T) \chi_H, \quad (9)$$

where T is the temperature, $\chi_H = 2.18 \times 10^{-11}$ erg is the ionization potential of hydrogen, and n_p and n_e are the number density of protons and electrons in cm⁻³. This yields volumetric heating and cooling rates in units of erg cm⁻³ s⁻¹.

In addition to these, our model solves two additional mass conservation equations, tracking the density of neutrals and ions:

$$\frac{\partial n_n}{\partial t} + \nabla \cdot n_n \vec{u} = \mathcal{R} - \mathcal{I}, \quad (10)$$

$$\frac{\partial n_p}{\partial t} + \nabla \cdot n_p \vec{u} = \mathcal{I} - \mathcal{R}, \quad (11)$$

where \mathcal{R} and \mathcal{I} are the recombination rate and ionization rate due to photoionization and collisional ionization (Osterbrock 1989) given by:

$$\mathcal{R} = 2.7 \times 10^{-13} (10^4 / T)^{0.9} n_e n_p, \quad (12)$$

$$\mathcal{I} = \frac{\sigma n_n F_{xuv} e^{-\tau}}{h\nu} + 5.83 \times 10^{-11} n_e n_n \sqrt{T} \exp(-1.578 \times 10^5 / T), \quad (13)$$

where \mathcal{R} and \mathcal{I} are in cm⁻³ s⁻¹.

We impose an inner boundary at $1R_p$. Here we fix the base temperature and density to 1000 K and 2.4×10^{11} cm⁻³, respectively. Similar to the 1D models of Murray-Clay et al. (2009) we find that changing these values has no significant effect on the escape rate. For velocity, we use a reflective boundary (the velocity in the true and ghost cells have the same magnitude but the opposite sign), such that the velocity of material starts at ≈ 0 km s⁻¹ at $1R_p$. In spite of the very small initial velocity, the planetary atmosphere is accelerated above the boundary according to the forces in our momentum equation. For the magnetic field we use BATS-R-US' Global Magnetosphere module's default boundary (e.g. De Zeeuw et al. 2004; Tóth et al. 2005). This fixes the field strengths at $R = 0.5R_p$ such that the desired dipole strength is obtained at $R = 1R_p$, where a floating boundary condition is applied (the gradient of magnetic field is kept constant between true and ghost cells, such that the field lines can respond to changes in the outflow). For the outer boundaries (with the exception of the negative x boundary for the stellar wind) we use inflow limiting boundary conditions (McCann et al. 2019; Carolan et al. 2020, 2021). These are required when simulating in the co-rotating frame to remove any unwanted and uncontrolled inflows associated with the Coriolis force bending material near a boundary.

We initialize our computational domain with a 1D β profile of the escaping atmosphere, which is fit to a 1D model from Allan & Vidotto (2019). In the case studied here, this profile takes the form $u_r = u_\infty (1 - 1/r)^\beta$ where $u_\infty = 38$ km s⁻¹ is the terminal velocity of the outflow, and $\beta = 2.97$ is found as the best fit to the 1D model. From mass conservation, we then initialize the density in the whole grid as $n(r) = n_0 u_0 / u_r$, where n_0 is the density at the boundary (see previous paragraph) and u_0 is derived from our 1D model. Initially, we assume a constant ionization fraction throughout the grid (0.001 per cent), but as the solution advances, the ionization fraction is self-consistently obtained through equations (10) and (11). This setup ensures that there is absorbing material (i.e. neutral hydrogen) in the grid to absorb the ionizing radiation from the star when the simulation begins. We note that the exact setup of the β profile does not affect the resulting steady-state solution. We begin our simulations with just planetary material, and once the escaping atmosphere has reached steady-state, we then turn on the orbital forces and inject the stellar wind, yielding the resulting steady-state solutions seen in Figs 2 and 3, respectively.

We inject the stellar wind at the negative x boundary. Here we use similar boundary conditions to Carolan et al. (2020, 2021), now adapted to also handle the stellar wind's magnetic field. The boundary assumes a stellar wind velocity and magnetic field which is radial away from the star. We provide values of the stellar wind velocity, temperature, density, and magnetic field which are derived from an external model, which describes the stellar wind using a 1D polytropic model. We use a similar model to that of Carolan et al. (2019), which is based on Johnstone et al. (2015a)'s version of VAC (Tóth 1996). In polytropic wind models the density and pressure are related by the polytropic index (α) according to $P_{sw} \propto \rho_{sw}^\alpha$. We adopt a polytropic index of $\alpha = 1.05$, which implies that the temperature

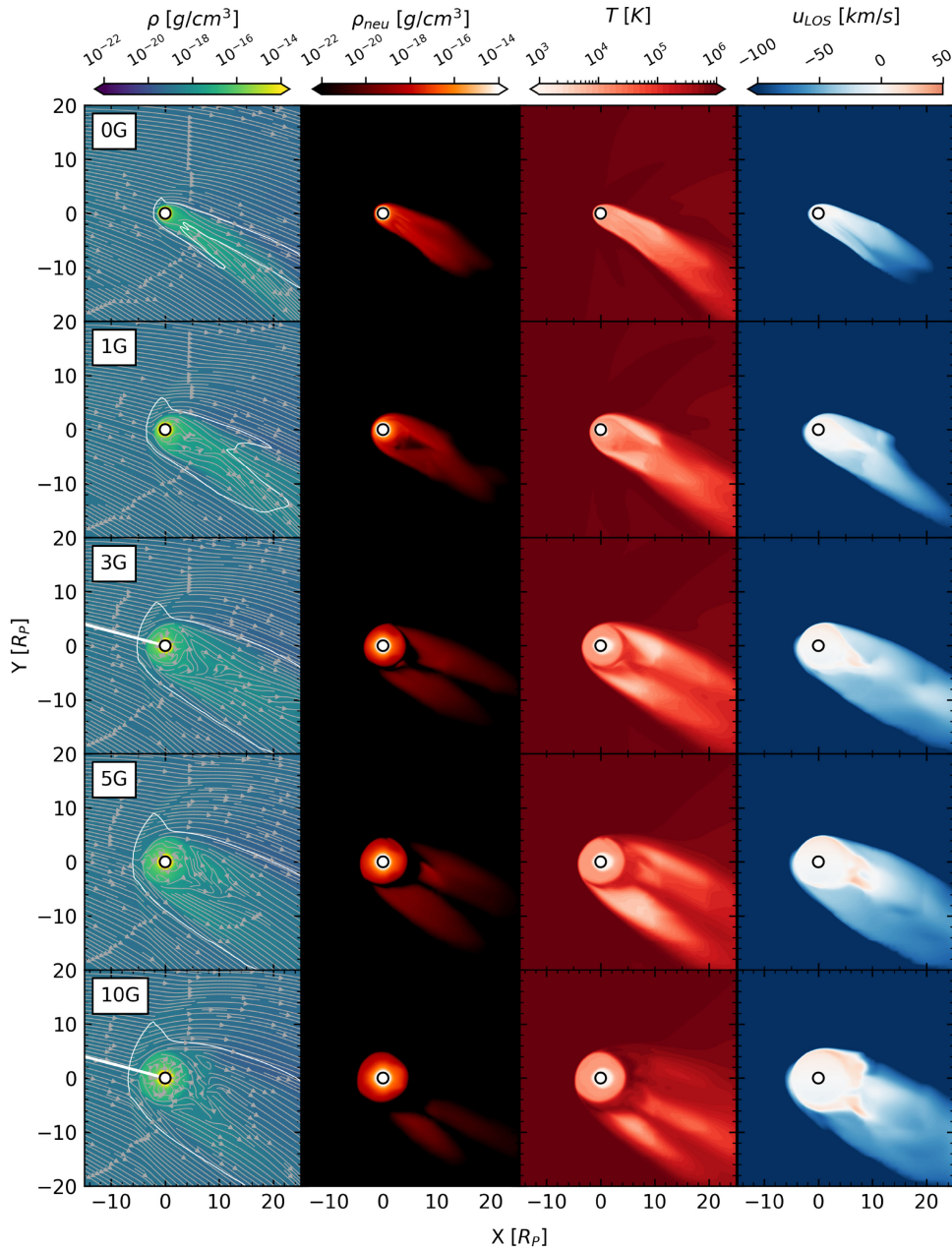


Figure 2. Cut at orbital plane of each of our models. Each row shows a different magnetic field strength of the planet, while each column shows the total density, neutral density, temperature, and line of sight velocity, respectively. The star is located at negative x, while the planet is marked by a circle centred on the origin. The grey streamlines in the left-hand column trace the flow of material in each model (see Fig. 3 for stream-tracers of magnetic field). The white contour in the left-hand middle panel shows the position of the magnetosonic surface. The white line in the left-hand middle panel is the line on which we examine different pressures in Fig. 5.

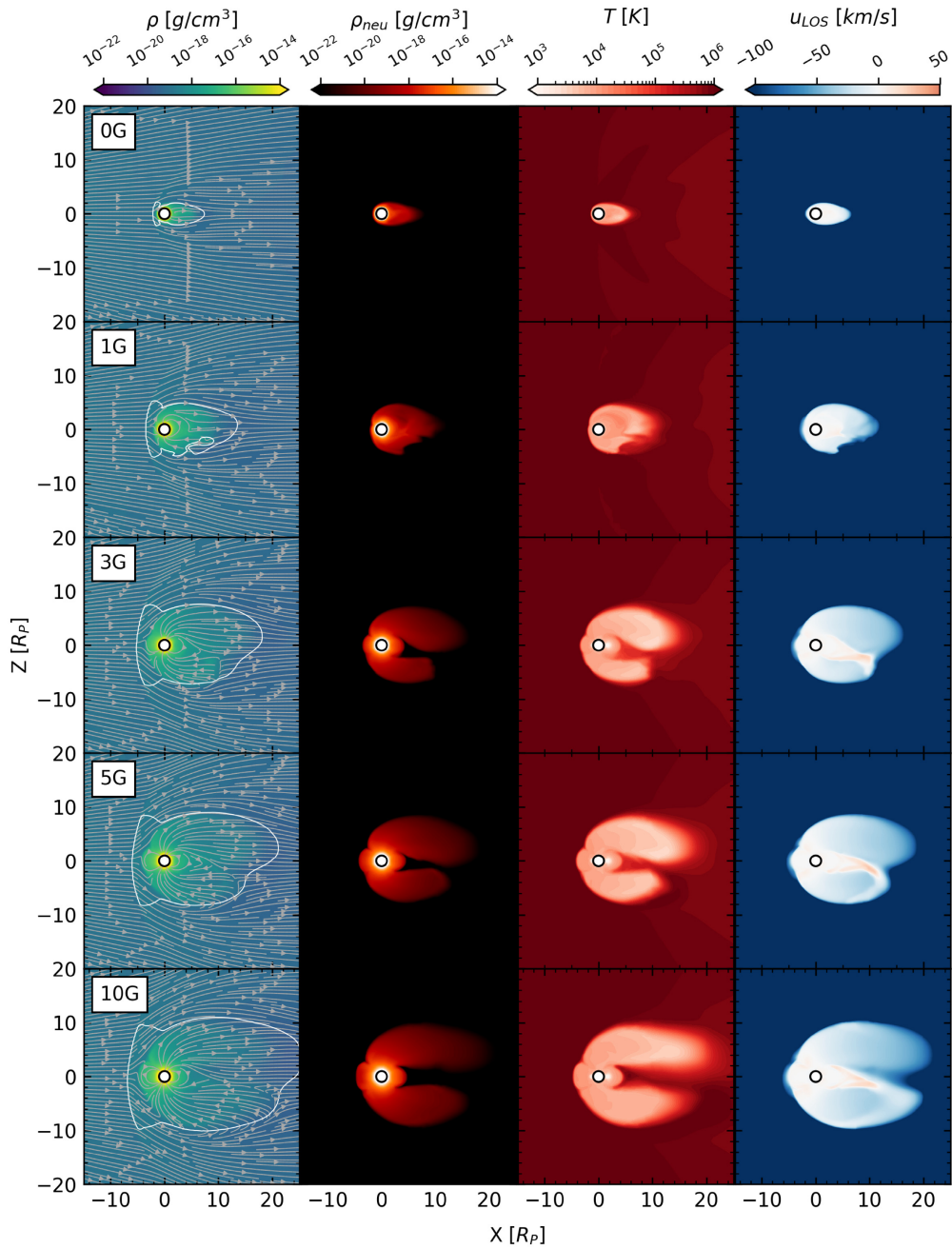


Figure 3. Cut at the polar plane in each of our models, similar to Fig. 2. The grey streamlines in the left-hand column now trace the magnetic field lines in each model.

of the stellar wind is nearly isothermal. We fix the stellar wind temperature and mass-loss rate at the boundary of our 3D simulations, the latter of which is used with the velocity solution from the 1D model to set the density along the boundary ($\rho_{SW} = \dot{M}/4\pi R^2 u_{SW}$). Note that the stellar wind model is separate to our 3D simulations, and is not updated during runtime. For the purpose of this work, we use the same stellar wind in each simulation (see Table 1 for details). The stellar wind is chosen as it is super-alfvénic at the planet’s orbit, so that the interaction with the escaping atmosphere cannot travel upstream in the stellar wind and affect the boundary condition. This will allow us to more consistently examine the effect of magnetic fields on the planetary outflow, as varying the planet’s magnetic field cannot affect the injected stellar wind, ensuring the stellar wind is identical in all models. The model parameters for the planet and stellar wind can be found in Table 1.

3 EFFECT OF MAGNETIC FIELDS: ATMOSPHERIC ESCAPE

We run five models in total using the parameters in Table 1, varying the magnetic field strength of the planet’s dipole from 0 to 10G, while keeping the stellar wind constant.

Figs 2 and 3 show the orbital and polar planes in each of our models, at steady-state (snapshot of quasi-steady state 1G model, see Appendix A). The 0G model resembles closely the strong stellar wind models from Carolan et al. (2020, 2021), where the stellar wind funnels material into a tight comet-like tail centred on the orbital plane. We can see that this tail contains all of the low temperature neutral material, most of which has an line of sight velocity that will contribute to blue shifted absorption in Lyman- α (see Section 4).

The presence of a planetary magnetic field leads to a different tail structure. Similar to other works (e.g. Khodachenko et al. 2015), as the planetary magnetic field strength is increased, the structure moves away from an tail centred on the orbital plane. Where the magnetic field lines are open, we obtain two polar outflows, one above and below the orbital plane (as seen in the lower panels of Fig. 3). These are separated by a ‘dead-zone’ around the planet where the field lines are closed, filled with mostly low velocity neutral material as seen in Fig. 1. In Fig. 3 we see that the size of the dead-zone increases with magnetic field strength, as a growing circle of low temperature and low velocity material is held around the planet on the orbital plane. In Figs 2 and 3 we can see that as the size of the dead-zone increases the separation between the polar outflows also increases, until no singular comet-like tail is seen in the orbital plane of the 10G model. Instead we see two tail-like structures following the planet, one above and one below the orbital plane. Note that these two flows are asymmetric which will be discussed in Section 4.1.

For lower magnetic field strengths ($<3G$), most of the absorbing material is at low to blue-shifted velocities. For stronger magnetic fields ($\geq 3G$), we see a small amount of red-shifted material on the night-side of the planet between the polar flows, as the magnetic field funnels some material back towards the planet.

In our models the $\tau = 1$ surface varies from $\approx 1.8R_p$ in the 10G model, to $\approx 1.2R_p$ in the 0G model, along the substellar line. The exact values for the position of the $\tau = 1$ surface in each of our models can be found in Table 2. As previously discussed, when the magnetic field strength of the planet is increased, the size of the deadzone grows. This larger, denser deadzone is then able to absorb more of the incident stellar radiation before it gets lower into the planet’s atmosphere, and as a result the $\tau = 1$ surface is pushed to higher altitudes.

Table 2. The size of the planet’s magnetosphere along the line shown in Fig. 2, chosen as the point where the stellar wind velocity is perpendicular to the shock. B_p is the planet’s magnetic field strength in Gauss, R_m and R_b are distance of the magnetopause and bow shock standoff distance relative to the radius of the planet. R_τ is the position of the $\tau = 1$ surface on the substellar line.

B_p (G)	R_m (R_p)	R_b (R_p)	R_τ (R_p)
0	–	2.2	1.2
1	2.1	3.5	1.4
3	3.5	5.2	1.7
5	4.2	6.0	1.7
10	4.8	6.9	1.8

To quantify the change in the escaping atmosphere in our models, we examine the planetary mass-loss through planes parallel to the orbital plane above and below the planet at $z = \pm 2.5R_p$ versus that loss through the night-side between these planes at $x = 2.5R_p$ (Fig. 4). We can then compare these to the total mass-loss calculated through concentric spheres around the planet to investigate where the planet is losing most of its atmosphere. As expected from Figs 2 and 3, the 0G model loses most of its mass through the night-side, as the stellar wind funnels the escaping atmosphere into a tight comet-like tail centred on the orbital plane. Once a planetary magnetic field is introduced, we begin to see much more mass-loss through polar outflows than through the night-side, with these polar flows contributing to the majority of atmospheric escape for $B_p \geq 3G$. For the 1G model (and the 3G model to a lesser extent) we can see significant difference between the north and south polar flows, which we attribute to the variation in this quasi-steady state solution (see Appendix A). We note also the increase in the total atmospheric escape rate (\dot{m}) seen from the 0 to 10G models (factor of 2). This is caused by the funnelling geometry of the magnetic field which assists in the driving of escape in the polar flows, compared to the predominantly night-side outflow in the 0G model. This is similar to what is seen in stellar wind models with magnetic fields (Vidotto et al. 2009, 2014; Réville et al. 2015; Ó Fionnagáin et al. 2019, 2021; Kavanagh et al. 2019, 2021). However for stronger field strengths ($>3G$) the magnetic field does not cause significant changes to the escape rate, though it does change the observational signatures of this escape, as discussed in Section 4.

Fig. 5 shows the ram (ρu^2), magnetic ($B^2/8\pi$), and thermal ($nk_B T$) pressures in our models along the white line shown in Fig. 2. This is the line where the stellar wind velocity is perpendicular to the bow shock, where the size of the magnetosphere is quantified. As seen in Fig. 5 we find a similar pressure structure to the Earth models of Carolan et al. (2019), and so we use a similar procedure to quantify the size of the magnetosphere in each of our models, given in Table 2. We find that in the stellar wind, ram pressure is the dominant pressure component, while the shocked material in the magnetosheath is dominated by thermal pressure. The bow shock standoff distance can then be found as the point where ram and thermal pressures are balanced. Inside the planetary magnetosphere the dominant pressure component is magnetic, and so the magnetopause is found by the balance of magnetic and thermal pressures. As expected, increasing the magnetic field strength of the planet’s dipole increases the size of the magnetosphere, as increasing the magnetic pressure will push the

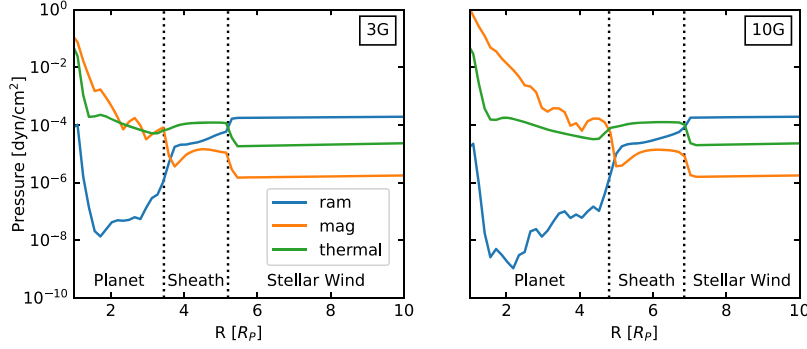


Figure 5. The ram, magnetic, and thermal pressures in two of our models, along the lines marked in left middle and bottom panels of Fig. 2. This line was chosen where the stellar wind velocity is perpendicular to the shock. The black dotted lines mark the position of the magnetopause and bow shock standoff distances, which separate the planetary, magnetosheath, and stellar wind material, respectively.

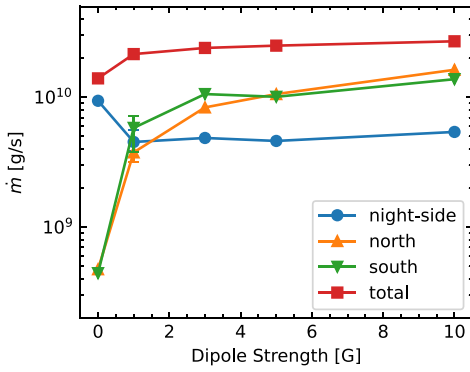


Figure 4. The mass-loss rates of each of our models. The blue circles mark the mass lost through a plane at $x = 2.5R_p$ representing the night-side mass-loss. The orange and green triangles mark the mass lost through planes at $z = 2.5R_p$ and $z = -2.5R_p$, respectively, representing the polar flows. The red squares mark the total mass lost, marking the average mass lost through concentric spheres around the planet. For the 1G model, we plot the mean and variation of the mass-loss rates during the quasi-steady state solution, discussed in Appendix A.

balance of magnetic and thermal pressures further from the planet. Note that due to the lack of intrinsic magnetic field in the 0G model, we cannot identify the magnetopause in this model. In reality it is likely that stellar wind interaction would generate a weak induced magnetic field, which would yield a magnetopause standoff distance $< 1.5R_p$. For all models, we observe a ‘weak’ bow shock, similar to the $30\Omega_\odot$ model from Carolan et al. (2019). This is due to a relatively low mach number of the stellar wind $M_m \approx 1.5$, which causes a jump in density and decrease in velocity by a factor of approx 2.6 (for a strong shock this factor is approximately 4, Spreiter, Summers & Alksne 1966; Gombosi 2004; Balogh & Treumann 2013). We also obtain a relatively thick magnetosheath in our simulations because of this, with the bow shock distance being greater than 1.4 times

the magnetopause standoff distance in each model (1.275 in a strong shock).

4 EFFECT OF MAGNETIC FIELDS: OBSERVATIONAL SIGNATURES

To investigate how magnetic fields affect observational signatures of escape, we calculate transit absorption profile of each of our models in Lyman- α . To do this we use a ray-tracing method similar to Carolan et al. (2021). Placing the observer at positive x , we first calculate the line of sight (LOS) velocity. As our 3D model simulates atmospheric escape in the planet’s reference frame, we must adjust the velocity in our grid to the line-of-sight velocity by $u_{LOS} = -u_x + y\Omega$. As our simulations track the density of neutral hydrogen, we can extract the temperature, density of neutrals, and line-of-sight velocity from our grid and begin the transit calculation.

The frequency (ν) dependent optical depth is given by:

$$\tau_\nu = \int n_n \sigma \phi_\nu dx, \quad (14)$$

where $\sigma = \pi e^2 f / m_e c$ is the absorption cross-section at line centre, and ϕ_ν is the Voigt line profile. $f = 0.416410$ is the oscillator strength for Lyman- α , m_e is the mass of the electron, e is the electron charge, and c is the speed of light. Once the optical depth is calculated we can then find the fraction of incident specific intensity that is transmitted:

$$\frac{I_\nu}{I_*} = e^{-\tau_\nu}. \quad (15)$$

$1 - \frac{I_\nu}{I_*}$ is therefore the fraction of specific intensity that is absorbed. We divide our grid into 201×201 columns and calculate this intensity in 51 velocity bins between -500 and 500 km s^{-1} . The transit depth can then be found as:

$$\Delta F_\nu = \frac{\int \int (1 - e^{-\tau_\nu}) dy dz}{\pi R_*^2}. \quad (16)$$

The transit depth of each model at mid-transit can be seen in Fig. 6.

Even though the variation in \dot{m} is small, varying the strength of the planet’s magnetic field causes significant changes to absorption in Lyman- α . As the comet-like tail in the 0G model is tightly funnelled down the line of sight by the stellar wind, we see significant blue wing absorption in this model. For small magnetic field strengths the

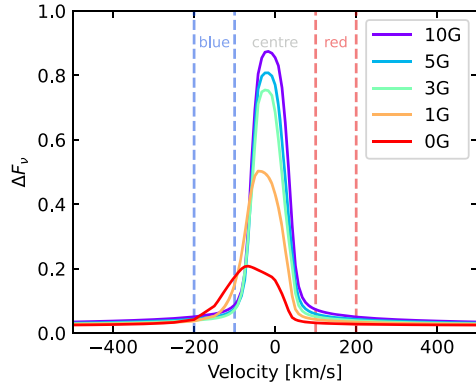


Figure 6. The mid-transit absorption profiles for each of our models, for an impact parameter $b = 0$. The blue and red dashed lines mark the bounds for the integrals of the blue, line centre, and red wing absorptions in Fig. 7.

tail begins to extend further above and below the orbital plane.¹ The magnetic field now introduces a larger obstacle to the stellar wind. As a result the escaping atmosphere is less accelerated along the line of sight, and so we do not see as much blue-shifted absorption.

We see a significant increase in line centre absorption with increasing magnetic field strength. This is due to the growing deadzones around the planet. As the planet’s dipole strength increases, the size of the deadzone increases as shown in Figs 2 and 3. This region contains mostly low velocity, low temperature neutrals, and so as the size of the deadzone grows, so does the line centre absorption.

4.1 Transit asymmetry due to wind–planet magnetic interaction

In Fig. 3, we see asymmetry in the planetary material above and below the orbital plane. This is due to the interaction between the stellar wind and planetary magnetic fields. When the super-alfvénic stellar wind reaches the planet, it is shocked and deflected around the planet. This deflection is what shapes the comet-like tail following the planet. As the stellar wind is shocked to sub-alfvénic velocities, reconnection of field lines can occur, which we see happen just inside the alfvén surface. Due to the orientation of the planetary magnetic field and radial stellar field in our models, the stellar and planetary field lines reconnect at the south pole, below the orbital plane, while the northern planetary field lines are opened. We note that as the upstream stellar wind is super-alfvénic, this reconnection cannot accelerate particles that travel back to the star (this is believed to cause enhanced activity in the star Shkolnik & Llama 2018; Cauley et al. 2019; Folsom et al. 2020; Kavanagh et al. 2021, which could change the properties of the stellar wind). As a result of this reconnection the absorbing neutral material is less extended below the orbital plane, as the bending magnetic field lines at the interface between the stellar wind and escaping atmosphere act as a boundary (see Fig. 3). Above the orbital plane (north pole) there are now more open field lines

¹This is the case where the planet’s dipole axis is perpendicular to the orbital plane. However if the dipole was tilted on the polar plane, the separation between the polar flows and the orbital axis would be reduced see Section 5.1

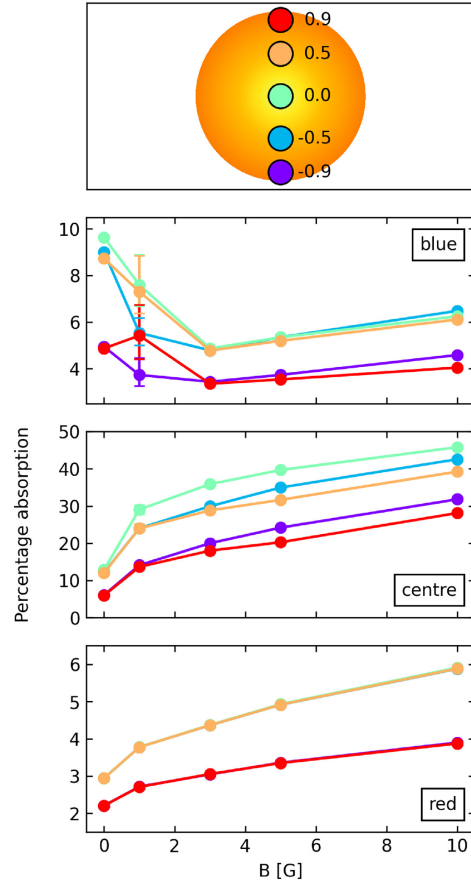


Figure 7. The blue, line centre, and red wing absorptions (marked on Fig. 6) of each of our models for a variety of impact parameters. The top panel illustrates the position of the planet at mid-transit as it transits horizontally across the stellar disc. In the second panel, we plot the mean and variation in the blue wing absorption for the 1G model during its quasi-steady state solution (see Appendix A). Note that there is no such variation in the red wing, or at line centre.

allowing the neutral material to extend further compared below the plane.

Due to the asymmetry in the distribution of absorbing neutrals above and below the orbital plane, we can expect this to affect the absorption profiles depending on the transit geometry of the planet. In Fig. 7, we show the percentage absorptions in the blue, line centre, and red wings of the Lyman- α line shown in Fig. 6, for a variety of impact parameters (b) in the northern and southern hemispheres of the stellar disc.

In the line centre, mid disc ($b = 0$) has the largest absorption, as it maximizes the volume of material within the stellar disc (green curves). In the blue wing we initially see a decrease in absorption for increasing magnetic field strength. As previously mentioned this is because the structure of the comet-like tail moves away from being

funnelled fully along the line of sight on the orbital plane, as the polar outflows perpendicular to the orbital plane are introduced. The most asymmetry between positive and negative impact parameters (see top panel of Fig. 7) is seen in the 1G model. As previously mentioned this model reaches a quasi-steady state, showing some variation in the distribution of material. As we do not see this in other simulations with higher B_p , we believe this is due to the magnetic field not being able to fully break this single comet-like tail structure into the polar outflows and dead-zones we see in other models with higher B_p . During the quasi-steady state solution for this model, a positive impact parameter shows more blue wing absorption than the negative values, suggesting that more high velocity Lyman- α absorption is caused by material under the orbital plane. This is caused by the disparity in the mass lost through the southern pole in this model (see Fig. 4), as the magnetic field begins to break the single comet-like tail structure. We note that depending on the stage during the quasi-steady state variation examined, the velocity of the material under the plane will vary significantly and so this asymmetry will not remain constant (see Appendix A).

For strong planetary fields, we see that blue wing absorption increases with magnetic field strength. As the magnetic field strength increases the size of the magnetosphere increases, allowing more room for absorbing material to accelerate along the polar outflows. As expected from Fig. 3 we see some asymmetry between the positive and negative impact parameters. The negative values yield higher absorption than the positive counterparts. For positive impact parameters the more extended northern flows will lie outside the stellar disc (while it will lie inside the disc for negative impact parameters), yielding less absorption in Lyman- α . This is also the case for absorption in line centre. As there are more neutrals above the plane the negative impact parameters will allow more lower velocity absorbing material to cover the disc than positive values.

There is no asymmetry present in red shifted material when comparing positive and negative impact parameters. From Figs 2 and 3, we can see that most redshifted material lies on the orbital plane between the polar outflows on the night-side of the planet, as a small amount of material falls from the polar outflows back towards the planet. As a result there is no significant difference between the positive and negative impact transits.

5 DISCUSSION

5.1 B-field geometries

As the absorption is related on the geometry of the escaping atmosphere, which is dependent on a combination of B_* and B_p , our results are expected to change for different magnetic field topologies. For example, if B_* had the opposite polarity, then our results for positive and negative impact parameters would be inverted. In this scenario, the reconnection of stellar and planetary field lines now occurs above the orbital plane (as opposed to below, shown in Fig. 3). This would lead to more open field lines below than above the plane. As a result, the distribution of material we currently see in our models would be flipped through the orbital plane, leading to the opposite result for transits with positive and negative impact parameters. Similarly, if the planetary dipole was tilted, the position of reconnection would change. The topology used in this work, where the planetary dipole axis is perpendicular to both the substellar line and direction of transit, yields the greatest difference between positive and negative impact parameter transits. Tilting the dipole towards / away from the star will reduce the vertical distance between the two polar outflows, as rotating the dipole brings the poles closer to the orbital plane. As

a result of this reduced separation, the observed asymmetry between transit geometry would also be reduced. Similarly tilting the dipole towards/away from the transit direction (towards positive y) will reduce asymmetry. Transits close to the edge of the stellar disc now no longer fully remove one of the polar outflows, but rather parts of both, producing less asymmetry between transit geometries.

5.2 No significant change in escape rate

In this work, we find that increasing the planet's magnetic field strength causes a minor increase in the planet's total mass-loss rate (increasing by a factor of 2). This result is contrary to what other works have found for hot Jupiters (e.g. Owen & Adams 2014; Khodachenko et al. 2015; Arakcheev et al. 2017, all found reductions by up to an order of magnitude), and likely caused by difference in the physics included in each model. Similar to other works, we find that the inclusion of magnetic fields creates dead-zones in our models around the equator, where planetary material is held inside the closed field lines. This reduces the mass-loss around the equator, while also causing an increase in the line centre absorption as these dead-zones hold a significant amount of low velocity neutrals. Despite this, all of our models with planetary magnetic fields lose more mass than our 0G model. As previously discussed, in these models more mass is funnelled through the polar flows, leading to two outflows above and below the equatorial dead-zones. Unlike Khodachenko et al. (2015), we do not find suppressed polar winds, where faster adiabatic cooling leads to reduced polar winds. This could be in part due to the inclusion of stellar wind in our model. While Khodachenko et al. (2015) found most mass is lost through the 'wind zone' between the equatorial dead-zones and suppressed polar winds, the inclusion of the stellar wind in our model deflects material from the day-side 'wind zone' towards the night-side comet-like tails. Through this deflection material lost through the day-side 'wind zone' must flow through where the suppressed polar outflows would reside to reach the comet-like tail, leading to no apparent suppression of polar winds in our models. Instead we see an increase in polar outflows when compared to the 0G model. This increased polar flow accompanied by the decreased night-side mass-loss nets an increase in the total mass-loss rate by a factor of 2, though this is not significant enough to affect the time-scale for atmospheric loss. This further emphasizes the importance of considering the stellar wind when modelling atmospheric loss, as it can significantly alter the geometry and rate of atmospheric escape.

5.3 Implications on observations

The results we present in this work have important implications on interpreting transit observations. Despite the mass-loss rate only increasing by a factor of 2, increasing the magnetic field strength greatly alters the absorption line profile. At line centre, the total percentage absorption increases by a factor of 4 at mid-transit, when comparing the 0 and 10G models. The presence of a magnetic field greatly alters the geometry and distribution of absorbing material in the planetary magnetosphere, and so is crucial to consider in order to correctly interpret transit observations. One issue with observing Lyman- α transits is that this line is not observable at line centre, due to both interstellar absorption and geocoronal emission. Recent work has identified the infra-red 10830Å Helium I triplet as an atmospheric escape identifier (e.g. Nortmann et al. 2018; Spake et al. 2018). A popular approach has been to calculate the population of the triplet in post-processing, i.e. a Parker-type wind is used to calculate the bulk properties of the escaping atmosphere and, afterwards, the population

state is calculated (e.g. Oklopčić & Hirata 2018; Lampón et al. 2020; MacLeod & Oklopčić 2021; Dos Santos et al., submitted). There have also been numerous detections of heavier elements in the transmission spectra of exoplanets (e.g. Hoeijmakers et al. 2018, 2019; Gibson et al. 2020; Seidel et al. 2021), with a current popular theory to explain this suggesting that these heavier elements are dragged to these altitude by the escaping hydrogen (Cubillos et al. 2020). There are still many open questions to what the effects of magnetic field would be in the dynamics of heavier particles. For example, given that increasing the dipole strength increases Lyman- α absorption at line centre as more neutral hydrogen is trapped in the dead-zones, we can infer that this will also increase the line centre absorption of other heavier elements if they are well mixed with hydrogen in the escaping fluid. Likewise, the strong hydrogen outflow emerging from the poles could bring heavier elements to high altitudes. If this is the case, we could also expect asymmetries in spectroscopic transits of heavier elements.

5.4 Model limitations

Our simulations neglect the effects of charge exchange and radiation pressure. Radiation pressure from Lyman- α photons has been thought to accelerate neutral atoms to significantly blue-shifted velocities (Bourrier, Ehrenreich & Lecavelier des Etangs 2015; Schneider et al. 2016). However Debrecht et al. (2020) found that radiation pressure alone may not cause significant changes, with Villarreal D'Angelo et al. (2021) finding that if the stellar wind already causes most of this acceleration, the contribution from radiation pressure will be minimal. Though the radiation pressure may have a small impact on the blue wing absorption it will not affect the mass-loss rate, and so we do not expect the inclusion of radiation pressure to significantly alter our models. Charge exchange occurs when a stellar wind proton and a planetary neutral hydrogen atom exchange an electron at the boundary between the stellar wind and escaping atmosphere (Shaikhislamov et al. 2016). Though the number of neutrals remain the same, charge exchange will result in more high velocity neutral atoms thus increasing blue-shifted absorption (Holmström et al. 2008; Tremblin & Chiang 2013; Kislyakova et al. 2014; Bourrier et al. 2016; Shaikhislamov et al. 2016). Though these two processes are unlikely to affect the dynamics of these models, the transit line profiles may change (Cherenkov, Bisikalo & Kosovichev 2018), with Esquivel et al. (2019), Odert et al. (2020) finding a combination of the two being the best fit for observations of HD209458b. One might expect that as a larger magnetosphere provides a larger interaction surface, that charge exchange will become more important for larger magnetic field strengths. However, because most of the low velocity neutrals are trapped in the dead-zones close to the planet, and as the neutrals in the tail are already somewhat blue-shifted, we do not expect charge exchange to significantly alter the trends in absorption line profile that we see with increasing magnetic field strength, as it would only push already blue shifted material to higher velocities.

6 CONCLUSIONS

In this work, we have examined how magnetic fields affect the interaction between the stellar wind and escaping atmosphere. We use newly developed 3D self-consistent radiative magnetohydrodynamic models. Using the same magnetized stellar wind in each model, we vary the planetary dipole strength to examine how the planetary magnetic field affects the interaction with the stellar wind, the mass lost by the planet, and the observational signatures of this

escape. To the best of our knowledge this is the first 3D radiative model capable of simulating the inner most regions of the escaping atmosphere which includes: radiative heating and cooling; cooling from collisions; the planetary magnetic field; magnetized stellar wind; Coriolis & Centrifugal forces; and the force due to tidal gravity.

We performed five simulations, varying the planetary dipole strength from 0 to 10G. We find that increasing the magnetic field strength of the planet greatly alters the structure of material in the magnetosphere. Just as was shown in other works (Owen & Adams 2014; Trammell et al. 2014; Khodachenko et al. 2015; Arakcheev et al. 2017), we found that the planetary magnetic field creates dead-zones, where the closed magnetic field lines around the planet trap material, reducing escape around the equator. This dead-zone grows with magnetic field strength, and is able to absorb more of the incident stellar radiation before it gets lower into the planet's atmosphere. As a result the $\tau = 1$ surface is pushed to higher altitudes when the magnetic field strength is increased. We also presented the novel finding of a double comet-like tail structure, one below and above the orbital plane, caused by the polar outflows. We found that the mass-loss through the poles increases with magnetic field strength, causing an increase in the total atmospheric escape rate. This is due to the interaction with the stellar wind, which deflects day-side atmospheric escape through the poles into this double tail structure, placing further emphasis on the importance of considering the interaction of the escaping atmosphere with the stellar wind when investigating atmospheric escape.

Using the results of our 3D simulations we investigated how changing the planetary magnetic field strength affects the observational signatures of atmospheric escape. We found an increase in line centre absorption with magnetic field strength, as more absorbing material is trapped in the growing dead-zones around the planet. The blue wing absorption initially decreases upon the introduction of the planetary field, as planetary material begins to be launched above and below the orbital plane, instead of being fully funnelled on to the orbital plane by the stellar wind, as seen in the 0G model. As the field strength continues to increase we see the blue wing absorption also increases. Similar to the line centre absorption, the red wing absorption increases with magnetic field strength. We found that most of the red shifted material exists around the night-side orbital plane, as some material falls from the comet-like tails back towards the planet.

Finally, we investigated the asymmetry between positive and negative impact parameters during transit (i.e. if the planet transits in the northern or Southern hemisphere of the star). With the exception of the 1G model (see Appendix A), we find a growing asymmetry in the blue wing absorption with increasing magnetic field strength, with negative impact parameters leading to more absorption. This is caused by the interaction between the planetary dipole and radial stellar magnetic fields. Below the orbital plane, as the stellar wind is shocked back to sub-alfvénic velocities the stellar and planetary magnetic field lines reconnect (note that as the stellar wind is super-alfvénic before this interaction, this cannot affect the upstream stellar wind). Above the plane the opposite occurs, leading to more open planetary field lines. As a result we found that the planetary outflow is more extended above the plane than below for all magnetic field strengths. This causes asymmetry between positive and negative impact parameters, as depending on which comet-like tail is mostly covering the stellar disc during transit, different absorption profiles will be obtained. This work places importance not only on knowledge of the planetary magnetic field, but also on the geometry of its interaction with the stellar wind's field when interpreting observational signatures of atmospheric escape.

ACKNOWLEDGEMENTS

We would like to thank the referee for their constructive review of the manuscript. This project has received funding from the European Research Council (ERC) under the European Union's Horizon 2020 research and innovation programme (grant agreement no. 817540, ASTROFLOW). The authors wish to acknowledge the SFI/HEA Irish Centre for High-End Computing (ICHEC) for the provision of computational facilities and support. This work used the BATS-R-US tools developed at the University of Michigan Center for Space Environment Modelling and made available through the NASA Community Coordinated Modeling Center.

DATA AVAILABILITY

The data described in this article will be shared on reasonable request to the corresponding author.

REFERENCES

- Allan A., Vidotto A. A., 2019, *MNRAS*, 490, 3760
 Arakcheev A. S., Zhilkin A. G., Kaigorodov P. V., Bisikalo D. V., Kosovichev A. G., 2017, *Astron. Rep.*, 61, 932
 Balogh A., Treumann R. A., 2013, *Physics of Collisionless Shocks: Space Plasma Shock Waves*. ISSI Scientific Report Series, Springer, New York. Available at: <http://cds.cern.ch/record/1517899>
 Baraffe I., Selsis F., Chabrier G., Barman T. S., Allard F., Hauschildt P. H., Lammer H., 2004, *A&A*, 419, L13
 Beaugé C., Nesvorný D., 2013, *ApJ*, 763, 12
 Ben-Jaffel L., Ballester G. E., 2013, *A&A*, 553, A52
 Berger T. A., Huber D., Gaidos E., van Saders J. L., Weiss L. M., 2020, *AJ*, 160, 108
 Bisikalo D., Kaygorodov P., Ionov D., Shematovich V., Lammer H., Fossati L., 2013, *ApJ*, 764, 19
 Black J. H., 1981, *MNRAS*, 197, 553
 Bourrier V., Ehrenreich D., Lecavelier des Etangs A., 2015, *A&A*, 582, A65
 Bourrier V., Lecavelier des Etangs A., Ehrenreich D., Tanaka Y. A., Vidotto A. A., 2016, *A&A*, 591, A121
 Bourrier V. et al., 2018, *A&A*, 620, A147
 Carolan S., Vidotto A. A., Loesch C., Coogan P., 2019, *MNRAS*, 489, 5784
 Carolan S., Vidotto A. A., Plavchan P., Villarreal D'Angelo C., Hazra G., 2020, *MNRAS*, 498, L53
 Carolan S., Vidotto A. A., Villarreal D'Angelo C., Hazra G., 2021, *MNRAS*, 500, 3382
 Carroll-Nellenback J., Frank A., Liu B., Quillen A. C., Blackman E. G., Dobbs-Dixon I., 2017, *MNRAS*, 466, 2458
 Cauley P. W., Shkolnik E. L., Llana J., Lanza A. F., 2019, *Nat. Astron.*, 3, 1128
 Cherenkov A. A., Bisikalo D. V., Kosovichev A. G., 2018, *MNRAS*, 475, 605
 Christie D., Arras P., Li Z.-Y., 2016, *ApJ*, 820, 3
 Cubillos P. E., Fossati L., Koskinen T., Young M. E., Salz M., France K., Sreejith A. G., Haswell C. A., 2020, *AJ*, 159, 111
 Debrecht A., Carroll-Nellenback J., Frank A., Blackman E. G., Fossati L., McCann J., Murray-Clay R., 2020, *MNRAS*, 493, 1292
 De Zeeuw D. L., Sazykin S., Wolf R. A., Gombosi T. I., Ridley A. J., Tóth G., 2004, *J. Geophys. Res.*, 109, A12
 Dong C., Jin M., Lingam M., Airapetian V. S., Ma Y., van der Holst B., 2018, *Proc. Natl Acad. Sci.*, 115, 260
 Ehrenreich D. et al., 2015, *Nature*, 522, 459
 Esquivel A., Schneider M., Villarreal D'Angelo C., Sgró M. A., Krapp L., 2019, *MNRAS*, 487, 5788
 Folsom C. P., Ó Fionnagáin D., Fossati L., Vidotto A. A., Moutou C., Petit P., Dragomir D., Donati J. F., 2020, *A&A*, 633, A48
 Fulton B. J. et al., 2017, *AJ*, 154, 109
 Gibson N. P. et al., 2020, *MNRAS*, 493, 2215

- Gombosi T. I., 2004, *Physics of the Space Environment*. Cambridge Univ. Press, Cambridge
 Harbach L. M., Moschou S. P., Garraffo C., Drake J. J., Alvarado-Gómez J. D., Cohen O., Fraschetti F., 2021, *ApJ*, 913, 130
 Hazra G., Vidotto A. A., D'Angelo C. V., 2020, *MNRAS*, 496, 4017
 Hoeijmakers H. J. et al., 2018, *Nature*, 560, 453
 Hoeijmakers H. J. et al., 2019, *A&A*, 627, A165
 Holmström M., Ekenbäck A., Selsis F., Penz T., Lammer H., Wurz P., 2008, *Nature*, 451, 970
 Jensen A. G., Redfield S., Endl M., Cochran W. D., Koesterke L., Barman T., 2012, *ApJ*, 751, 86
 Johnstone C. P. et al., 2015b, *ApJ*, 815, L12
 Johnstone C. P., Güdel M., Lüftinger T., Toth G., Brott I., 2015a, *A&A*, 577, A27
 Kavanagh R. D. et al., 2019, *MNRAS*, 485, 4529
 Kavanagh R. D., Vidotto A. A., Klein B., Jardine M. M., Donati J.-F., Ó Fionnagáin D., 2021, *MNRAS*, 504, 1511
 Khodachenko M. L., Shaikhislamov I. F., Lammer H., Prokopov P. A., 2015, *ApJ*, 813, 50
 Khodachenko M. L., Shaikhislamov I. F., Lammer H., Berezutsky A. G., Miroschnichenko I. B., Rumenskikh M. S., Kislyakova K. G., Dwivedi N. K., 2019, *ApJ*, 885, 67
 Kislyakova K. G. et al., 2014, *A&A*, 562, A116
 Kubyskhina D., Vidotto A. A., Fossati L., Farrell E., 2020, *MNRAS*, 499, 77
 Kulow J. R., France K., Linsky J., Loyd R. O. P., 2014, *ApJ*, 786, 132
 Kurokawa H., Nakamoto T., 2014, *ApJ*, 783, 54
 Lammer H., Selsis F., Ribas I., Guinan E. F., Bauer S. J., Weiss W. W., 2003, *ApJ*, 598, L121
 Lampón M. et al., 2020, *A&A*, 636, A13
 Lecavelier Des Etangs A. et al., 2010, *A&A*, 514, A72
 Lecavelier des Etangs A. et al., 2012, *A&A*, 543, L4
 Lingam M., Loeb A., 2018, *Int. J. Astrobiol.*, 17, 116
 MacLeod M., Oklopčić A., 2021, preprint ([arXiv:2107.07534](https://arxiv.org/abs/2107.07534))
 Matsakos T., Uribe A., Königl A., 2015, *A&A*, 578, A6
 McCann J., Murray-Clay R. A., Kratter K., Krumholz M. R., 2019, *ApJ*, 873, 89
 Murray-Clay R. A., Chiang E. I., Murray N., 2009, *ApJ*, 693, 23
 Nortmann L. et al., 2018, *Science*, 362, 1388
 Odert P. et al., 2020, *A&A*, 638, A49
 Oklopčić A., Hirata C. M., 2018, *ApJ*, 855, L11
 Osterbrock D. E., 1989, *Astrophysics of Gaseous Nebulae and Active Galactic Nuclei*. University Science Books, Melville, NY
 Owen J. E., Adams F. C., 2014, *MNRAS*, 444, 3761
 Owen J. E., Lai D., 2018, *MNRAS*, 479, 5012
 Ó Fionnagáin D. et al., 2019, *MNRAS*, 483, 873
 Ó Fionnagáin D., Vidotto A. A., Petit P., Neiner C., Manchester W. I., Folsom C. P., Hallinan G., 2021, *MNRAS*, 500, 3438
 Pillitteri I., Maggio A., Micela G., Sciortino S., Wolk S. J., Matsakos T., 2015, *ApJ*, 805, 52
 Réville V., Brun A. S., Strugarek A., Matt S. P., Bouvier J., Folsom C. P., Petit P., 2015, *ApJ*, 814, 99
 Rogers J. G., Gupta A., Owen J. E., Schlichting H. E., 2021, *MNRAS*. Available at: <https://doi.org/10.1093/mnras/stab2897>
 Schneider E. M., Esquivel A., Villarreal D'Angelo C. S., Velázquez P. F., Raga A. C., Costa A., 2016, *MNRAS*, 457, 1666
 Seidel J. V. et al., 2021, *A&A*, 653, A73
 Shaikhislamov I. F. et al., 2016, *ApJ*, 832, 173
 Shkolnik E. L., Llana J., 2018, in Deeg H. J., ed., *Signatures of Star-Planet Interactions*. Springer, Berlin, p. 20
 Spake J. J. et al., 2018, *Nature*, 557, 68
 Spreiter J. R., Summers A. L., Alksne A. Y., 1966, *Planet. Space Sci.*, 14, 223
 Tóth G., 1996, *Astrophys. Lett. Commun.*, 34, 245
 Tóth G. et al., 2005, *J. Geophys. Res.*, 110, A12226
 Trammell G. B., Li Z.-Y., Arras P., 2014, *ApJ*, 788, 161
 Tremblin P., Chiang E., 2013, *MNRAS*, 428, 2565
 Vidal-Madjar A., Lecavelier des Etangs A., Désert J.-M., Ballester G., Ferlet R., Hébrard G., Mayor M., 2003, *Nature*, 422, 143

- Vidotto A. A., Cleary A., 2020, *MNRAS*, 494, 2417
 Vidotto A. A., Opher M., Jatenco-Pereira V., Gombosi T. I., 2009, *ApJ*, 703, 1734
 Vidotto A. A. et al., 2014, *MNRAS*, 441, 2361
 Villarreal D'Angelo C., Esquivel A., Schneider M., Sgró M. A., 2018, *MNRAS*, 479, 3115
 Villarreal D'Angelo C., Vidotto A. A., Esquivel A., Hazra G., Youngblood A., 2021, *MNRAS*, 501, 4383
 Yelle R. V., 2004, *Icarus*, 170, 167

APPENDIX: QUASI-STEADY STATE SOLUTIONS

The 1G model (and the 3G model, to a lesser extent) presented in this work does not settle to a fully steady state solution. Instead we find a quasi-steady state where the resulting solution varies periodically with iteration number. Similar quasi-steady state solutions were found by McCann et al. (2019), Carolan et al. (2021), with Christie et al. (2016) demonstrating that the amplitude of the variation in the solution decreases with increasing resolution in the grid.

To illustrate the variation in this model, in Fig. A1 we show how the line-of-sight velocity varies at two points in our grid, one above and below the orbital plane. Above the plane, we can see a small variation in the line-of-sight velocity after iteration 25 000, with a period of 3000–4000 iterations, covering a range of velocities from 0 to -20 km s^{-1} . However below the plane we see a much larger variation, with the velocity ranging from -10 to -125 km s^{-1} , with a period of approximately 5000 iterations. This variation is responsible for the differences in northern/southern escape and absorption in Figs 4 and 7.

The mass-loss rates shown in Fig. 4 for this model are calculated at the final iteration shown in Fig. A1. At this point, we can see that in the quasi-steady state solution, the magnitude of the velocity of material below the plane is much larger than that above the plane. As a result in this model, we obtain a larger difference between mass lost through the north and south poles that what is found in other models.

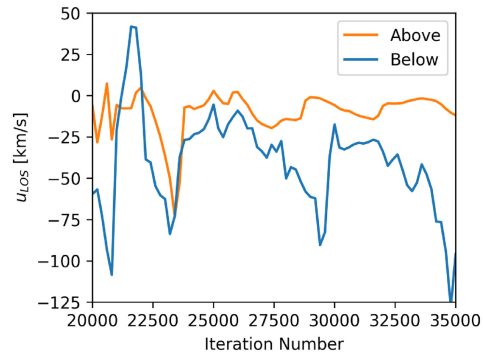


Figure A1. The quasi-steady state variation of the line-of-sight velocity in the 1G model. The two lines refer to points above and below the orbital plane, at X-Z coordinates [6, 3] and [6, -3], respectively. These points lie just within the magnetosonic surface in the left-hand panel of the 1G model in Fig. 3.

Similarly, the effects of the quasi-steady state can be seen in the absorption of planetary material in Fig. 7. As the magnitude of the line-of-sight velocity below the plane it is much larger at this stage in the solution, when the planet transits in the Northern hemisphere of the star we see much more blue wing absorption than when it transits in the south. As we can see from Fig. A1 this difference in absorption will vary depending on the stage of the solution examined (e.g. at iteration 32 000 the velocities above and below are much more similar), and so is not indicative of the overall trend we find in our models: that the asymmetry between mid-transit absorption when transiting above and below the mid-disc will increase with the magnetic field strength of the planet.

This paper has been typeset from a \LaTeX file prepared by the author.